

# University of St Andrews



Full metadata for this thesis is available in  
St Andrews Research Repository  
at:

<http://research-repository.st-andrews.ac.uk/>

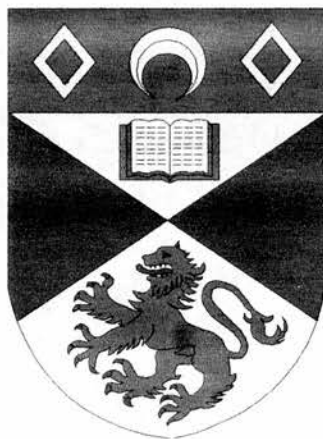
This thesis is protected by original copyright

# SEMICONDUCTOR DIODE LASERS FOR PICOSECOND PULSE GENERATION

Thesis submitted for the degree of Doctor of Philosophy to the University of St. Andrews

by

David M. Hughes, M.Sc., B.Sc.



J.F. Allen Research Laboratories  
Department of Physics and Astronomy  
University of St. Andrews  
North Haugh  
St. Andrews, Fife  
Scotland KY16 9SS

October 1999



$\pi$

E-~~174~~ 174

7

## Declarations

I, David Mason Hughes, hereby certify that this thesis, which is approximately thirty-five thousand words in length, has been written by me, that it is the record of work carried out by me and that it has not been submitted in any previous application for a higher degree.

D.M. Hughes

October 1999

I was admitted as a research student and as a candidate for the degree of Ph.D in February 1993; the higher study for which this is a record was carried out in the University of St. Andrews between 1993 and 1995.

D.M. Hughes

October 1999

I here by certify that the candidate has fulfilled the conditions of the Resolution and Regulations appropriate for the degree of Ph.D in the University of St. Andrews and that the candidate is qualified to submit this thesis in application for that degree.

W. Sibbett

Research Supervisor

October 1999

In submitting this thesis to the University of St. Andrews I understand that I am giving permission for it to be made available for use in accordance with the regulations of the University Library for the time being in force, subject to any copyright vested in the work not being affected thereby. I also understand that the title and abstract will be published, and a copy of the work may be made and supplied to any *bona fide* library or research worker.

D.M. Hughes

October 1999



Barbara

## Abstract

This thesis describes ultrashort pulse production techniques for semiconductor diode lasers. Three methodologies have been considered: active modelocking, gain-switching and forced Q-switching. The advantages and disadvantages of each technique have been examined. Theoretical assessments of the physical processes governing each procedure were outlined as a basis for the construction of simple yet powerful and adaptable computer simulations. These models were used to predict the temporal behavior of a range of semiconductor devices under broad range of operating conditions

An actively modelocked external-cavity InGaAsP device was used to implement a novel dual-wavelength laser. Continuous wavelength tuning was demonstrated over a 0.5 - 55nm range with the possibility of multiple wavelength operation.

Multiple-pulse lasers featured several composite external cavity geometries. Pulse frequencies within a tuning range of 6 - 23GHz were generated using this novel modelocked laser system.

The temporal intensity performance of gain-switched DFB and Fabry-Perot laser was assessed and 20 -30ps single feature optical pulses were routinely generated by direct RF modulation of the laser gain. The theoretical model generated optical intensity profiles showing very good agreement with the experimental results

Forced Q-switching was implemented for a series of multiple-contact InGaAsP and GaAs diode lasers. Output optical powers were enhanced by the saturable absorption provided by the multi-contact geometry and peak powers of up to 100mW were demonstrated for symmetrical pulses of ~15 - 25ps duration.

Pulse timing jitter was considered and distinction made between correlated and uncorrelated timing jitter. Jitter performance was assessed for modelocked, gain-switched and Q-switched regimes. Timing jitter in modelocked lasers was found to be largely correlated (~150fs). Subpicosecond (800fs) jitter was measured at a modulation rate of 2GHz for forced Q-switched multi-contact InGaAsP devices.

# SEMICONDUCTOR DIODE LASERS FOR PICOSECOND PULSE GENERATION

	Page
Declarations	ii
Abstract	iv
Table of contents	v
<b>1. INTRODUCTION</b>	<b>1</b>
1.1 Introduction	1
1.2 Physics of semiconductor lasers	2
1.3 Carrier confinement	5
1.4 Optical confinement	7
1.5 Quantum well lasers	9
1.6 Single frequency lasers	11
1.7 Rate equations	14
1.8 Ultrashort pulse diagnostic techniques	17
<b>2. ACTIVE MODELOCKING OF InGaAsP SEMICONDUCTOR DIODE LASERS</b>	<b>27</b>
2.1 Introduction	27
2.2 Modelocked diode lasers	28
2.3 Theoretical analysis	28
2.4 Modelocking regimes	34
2.5 Active modelocking	35
2.6 Practical modelocked lasers	37
2.7 Subpulse suppression	39
2.8 External cavity lasers	41
2.9 Mode structure of external cavity diode lasers	42
2.10 Spectral performance	44
<b>3. DUAL-WAVELENGTH EXTERNAL-CAVITY SEMICONDUCTOR LASERS</b>	<b>49</b>
3.1 Introduction	49
3.2 The dual-wavelength modelocked laser system	50
3.3 Dual-wavelength oscillation	52
3.4 System stability and noise performance	62
3.5 Relative power distribution	64
3.6 Applications of dual-wavelength systems	67

4. MULTI-PULSING MODELOCKED SEMICONDUCTOR LASERS	72
4.1 Introduction	72
4.2 Three-mirror Fabry-Perot lasers	73
4.3 The offset Michelson cavity configuration	81
4.4 Operating principles of multi-pulsing lasers	82
5. GAIN-SWITCHING OF InGaAsP SEMICONDUCTOR DIODE LASERS	88
5.1 Introduction	88
5.2 Theoretical treatment	89
5.3 Jitter and frequency chirp	100
5.4 Experiment	101
6. FORCED Q-SWITCHING OF MULTIPLE-CONTACT SEMICONDUCTOR DIODE LASERS	111
6.1 Introduction	111
6.2 Q-switching regimes	112
6.3 Theoretical model	115
6.4 Theoretical results	116
6.5 Spectral performance	118
6.6 Experiment	120
6.7 Device development	134
6.8 State-of-the-art Q-switched GaAs lasers	136
7. TIMING JITTER IN ULTRASHORT PULSE SEMICONDUCTOR LASERS	140
7.1 Introduction	140
7.2 Measurement of timing jitter	144
7.3 Noise characterisation of semiconductor diode lasers	149
7.4 Jitter reduction	163
8. GENERAL CONCLUSIONS	167
8.1 Ultrashort pulse semiconductor diode lasers	167
8.2 High-power ultrashort pulse lasers	169
8.3 Pulsewidth reduction techniques	171
8.4 Low jitter in ultrashort pulse lasers	171
Appendices	174
Publications	188
Acknowledgements	189

# Chapter 1

## INTRODUCTION

### 1.1 Introduction

Ultrafast diode lasers are a rapidly growing field of modern optoelectronics in terms of both basic research and applications. It is unquestionably one of the most interesting and promising fields of laser physics. Ultrafast diode lasers offer a vast variety of applications<sup>1-3</sup>, including high-bit-rate optical fibre communication lines, ultrafast optical data processing, optical computing, radar systems and optoelectronic measurement applications and instrumentation.

There have been many recent advances in picosecond pulse generation in diode lasers at a variety of wavelengths including 850, 980, 1300 and 1550nm. Pulse duration ranges from several picoseconds to less than one picosecond at repetition rates of from a few gigahertz up to several hundreds of gigahertz<sup>4,5</sup>. Subsequent pulse compression can result in optical pulse widths of less than 100ps<sup>6,7</sup>. Such pulses have found applications in time-resolved spectroscopic measurements and general electronics applications.

High-speed directly modulated lasers are a key element in optical fibre communications systems. Modulation bandwidths of 20 - 30GHz allow the transmission of optical data at repetition rates in excess of 20Gb/s. Laser structures with low linewidth enhancement factors are capable of transmitting data over distances exceeding several hundreds of kilometres without the need for repeaters. Soliton propagation of diode laser pulses can result in further increase in transmission distance to several thousand kilometres.

The development of a new generation of ultrawideband optoelectronic devices, including optical-sampling oscilloscopes, optoelectronic devices for radar

applications and high-resolution OTDR systems may be facilitated using ultrafast diode lasers<sup>8-11</sup>.

## 1.2 Physics of semiconductor lasers

Semiconductor laser action is achieved by interband electron-hole recombination and the subsequent liberation of photons. When a p-n junction is forward biased by applying an external current, a diffusion of electrons and holes takes place across the junction. These charge carriers recombine in the narrow active region through radiative and non-radiative mechanisms. The radiative recombination of the charge carriers here results in the production of radiation with a rotational frequency  $\omega = E_g/\hbar$ , where  $\hbar$  is Planck's constant and  $E_g$  is the transition energy. Since both energy and wave vector  $k$  must be conserved, direct-gap semiconductor materials are essential for significant radiative recombination. When the injection current exceeds a critical value, a population inversion is achieved and the rate of photon emission due to electron-hole recombination exceeds the rate of absorption due to electron-hole generation<sup>12</sup>.

A commonly used approximation of the exact band structure in semiconductor lasers is the parabolic band model from which the energy versus wave vector and density of states curves may be derived. The electron and hole distributions within the energy bands are described by Fermi-Dirac statistics which define the occupation probability  $f_c$  of an allowed electron with energy  $E_c$  in terms of the quasi-Fermi level of the conduction band,  $F_c$ :

$$f_c(E_c) = \left[ \exp\left(\frac{E_c - F_c}{kT}\right) + 1 \right]^{-1} \quad (1.1)$$

and for holes:

$$f_v(E_v) = \left[ \exp\left(\frac{E_c - F_c}{kT}\right) + 1 \right]^{-1} \quad (1.2)$$

where  $T$  is temperature and  $k$  is Boltzmann's constant.

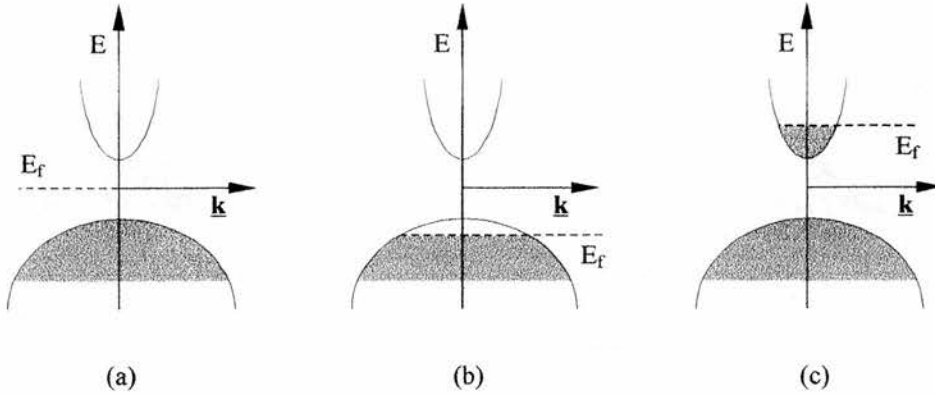


**Figure 1.1.** Energy versus wavevector diagrams for (a) an intrinsic semiconductor for  $T > 0K$ ; (b) a p-type degenerate semiconductor; (c) an n-type degenerate semiconductor.

A graphic summary of the electron and hole distribution under various conditions is presented in Figure 1.1. Figure 1.1 (a) shows an intrinsic material (that is, containing neither donors nor acceptors) in which the electron and hole densities are equal. Figures 1.1 (b) and (c) show semiconductor material with a high level of p-type and n-type dopants respectively. At the heart of the semiconductor injection laser is the p-n junction<sup>13</sup>. Combining the p-type and n-type material produces a doubly degenerate semiconductor (Figure 1.2 (a)). This arrangement results in a condition for which the net stimulated emission is positive, provided equilibrium amongst electrons in each band is sufficient to enable Eqs. 1.1 and 1.2 to be used for  $f_c$  and  $f_v$ . Thus if  $f_c > f_v$  then there must be a net stimulated emission. Since  $E_v = E_c - h\nu$ , the requirement for  $f_c$  to be greater than  $f_v$  is

$$\exp\left[\frac{(E_c - h\nu - F_v)}{kT}\right] > \exp\left[\frac{(E_c - F_c)}{kT}\right] \quad (1.3)$$

or, more simply,

$$F_c - F_v > h\nu \quad (1.4)$$

The condition in Eq. 1.4 states that stimulated emission occurs for all transitions where the photon energy  $h\nu$  is less than the separation of the two quasi-Fermi levels ( $F_c - F_v$ )<sup>14</sup>. Optical feedback is the only other essential requirement for the possibility of laser oscillation. The semiconductor laser can be represented as a four-level laser system as shown in Figure 1.2 (b). Optical gain is demonstrated over a wide wavelength range since the Fermi levels extend well into the bands (Figure 1.2 (a)).

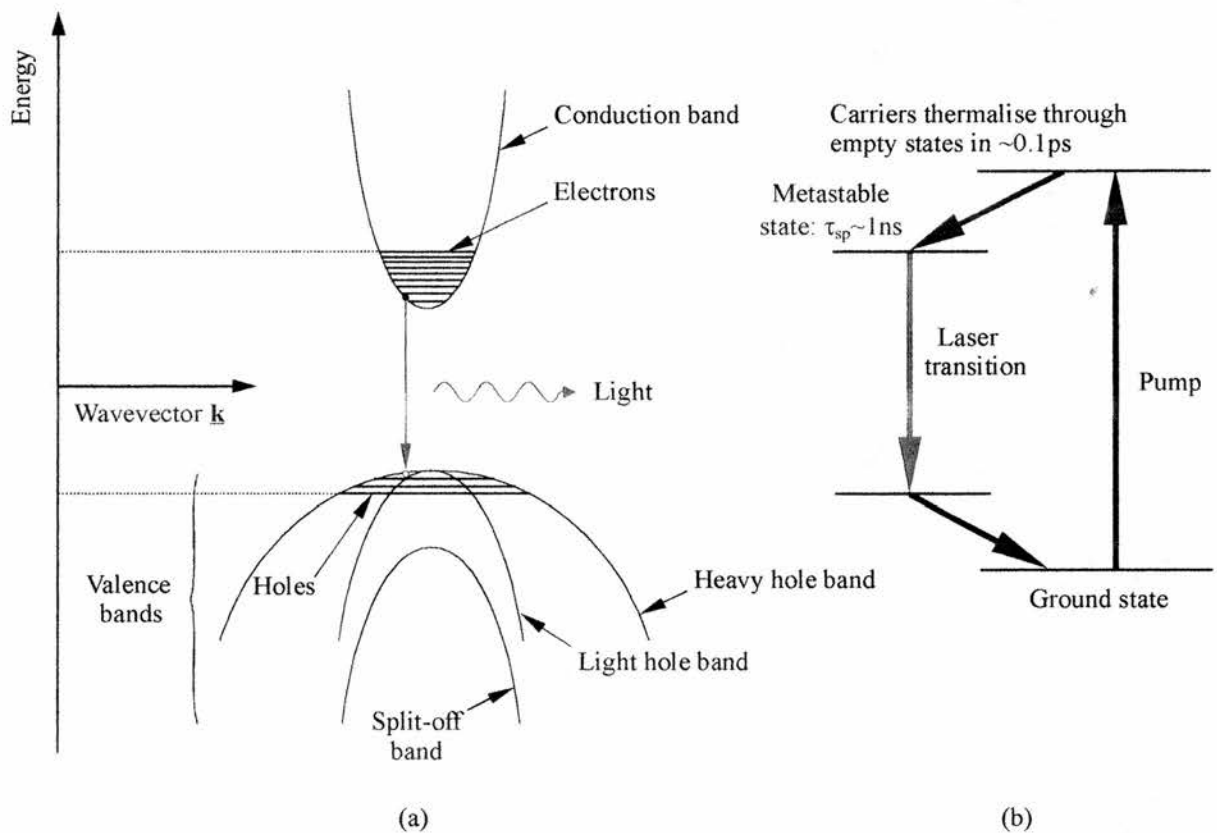


**Figure 1.2.** (a) Energy band diagram of a direct-band-gap semiconductor. Horizontal lines show the filled energy states. Radiative recombination of electrons and holes generates photons. (b) The equivalent four-level laser system.

A doubly degenerate semiconductor gain medium can be realised via optical pumping. This mechanism elevates valence band electrons high into the conduction band where lattice scattering causes relaxation to the band minimum. In a similar way, holes are promoted to the top of the valence band. If external excitation continues, sufficient numbers of electrons will be elevated into the conduction band



such that the probability of stimulated emission eventually becomes higher than the probability of absorption. This situation corresponds to population inversion in the laser medium and is a prerequisite for optical gain. Optical pumping (that is, absorption of radiation higher in energy than the band gap) has been shown to generate a high density of electron-hole pairs in a semiconductor<sup>15</sup>. However the most common means of external excitation is usually provided by injection current<sup>16</sup>.

The semiconductor material used in the active layer of an injection laser must have a direct gap. In a direct semiconductor the minimum of the conduction band has the same wave vector as the maximum of the valence band. Therefore injected electrons prefer to stay near the minimum of the conduction band and the injected holes preferably stay near the maximum of the valence band, so that a direct radiative transition is possible. For an indirect semiconductor, however, the generation of a photon is quite unlikely since this would involve the participation of another particle such as a phonon in order to compensate for the mismatch in the wave vectors.

### 1.3 Carrier confinement

The forward biased, doubly degenerate, direct bandgap p-n junction provides the most convenient method of demonstrating optical gain<sup>12</sup>. Because there is no carrier confinement mechanism, the active region of such homojunctions is  $\sim 100\text{nm}$  and continuous operation at room temperature is inhibited due to the large values of threshold current density ( $J_{\text{th}} \geq 50\text{kA/cm}^2$ ) required. Carrier confinement in the plane perpendicular to the p-n junction may be implemented using heterojunctions<sup>17-19</sup>.

#### 1.3.1 Heterojunction semiconductor lasers

The active region of a heterostructure laser is sandwiched between two cladding layers of semiconductor material which have a relatively wider band-gap producing a double heterojunction (DH). The DH confines the carriers to the active region and prevents non-radiative recombination. Figure 1.3 shows the energy-band diagram of

the forward biased DH.  $E_{g1}$  and  $E_{g2}$  denote the energy gaps of the active and cladding regions respectively. Electrons (from the n-doped layer) and holes (from the p-type region) are injected into the active region under forward bias and are confined in this region by the potential barrier caused by the band-gap difference. Minority carrier concentration in the active layer is greatly enhanced and optical gain is produced there. Thus the current density necessary for laser action is greatly reduced and continuous-wave operation is possible at room temperature<sup>20</sup> when positive optical feedback is introduced into the system via highly reflective cavity mirrors.

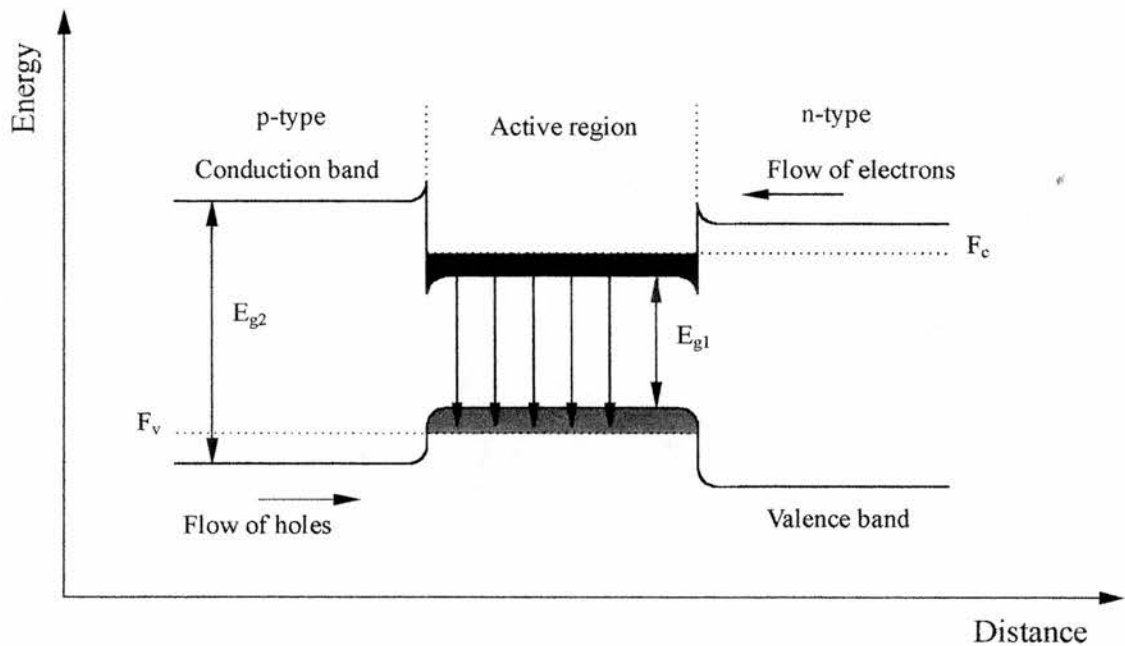


**Figure 1.3.** Energy-band diagram of a double-heterostructure laser under forward bias. Heterobarriers confine the carriers to the active region where they can combine radiatively.

However, such broad-area lasers do not confine the lateral spread of carriers. For this purpose the stripe-geometry contact<sup>21</sup> was developed, whereby carrier injection is restricted to a narrow central section, thus confining the optical mode to a small active region. Stripe widths vary from 2 - 5 $\mu\text{m}$  and narrower stripes restrict laser oscillation to a single transverse mode. The overall result is a reduction in both threshold current density and operating temperature. However, the output beam can

be highly elliptical. Both the gain-guided laser and the index guided laser display strong confinement in the plane parallel to the junction and are shown in Figure 1.5.

### 1.4 Optical confinement

The active region of the heterostructure device has a simultaneously lower band-gap and higher refractive index than the surrounding cladding layers (Figure 1.4 (a) and (b)). This transverse refractive index difference (perpendicular to the junction plane) results in optical confinement close to the active region giving the laser the

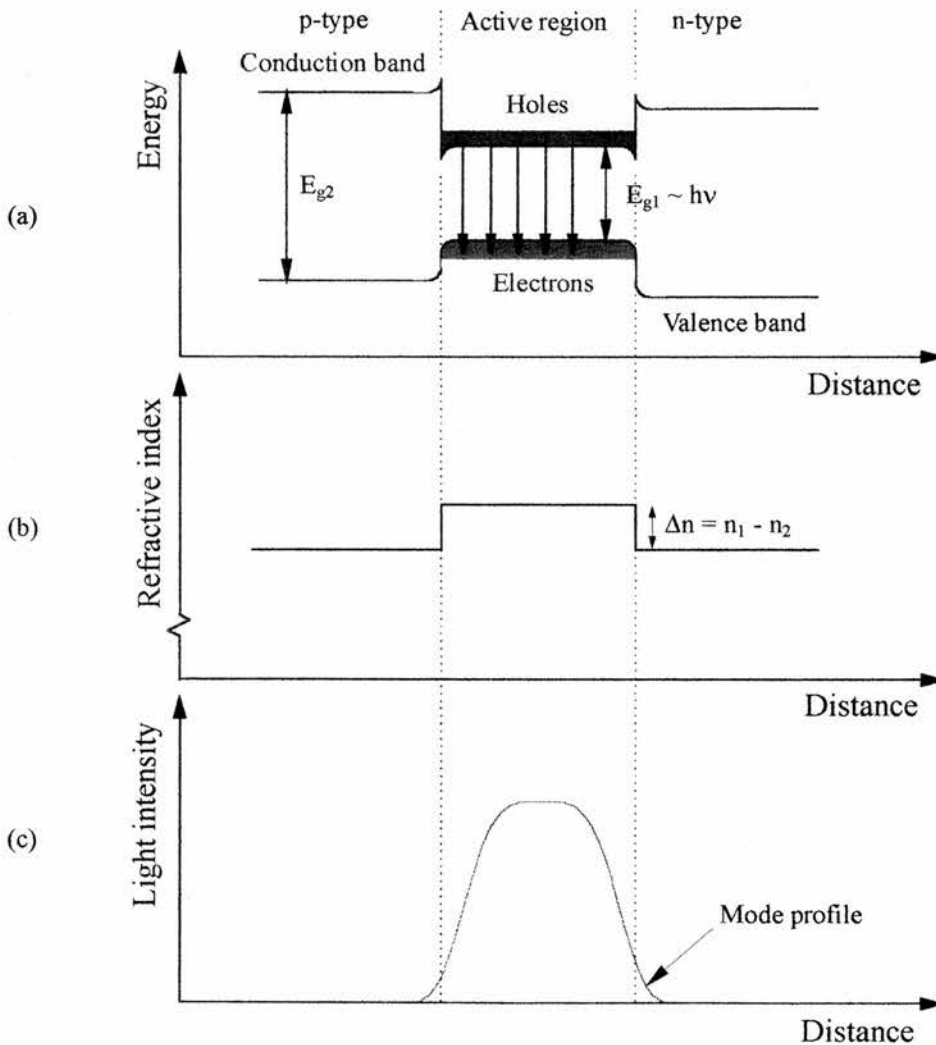


**Figure 1.4.** Confinement of charge carriers and optical mode to the active region of a double heterostructure semiconductor laser. The active layer has a lower band gap and a higher refractive index than those of the cladding layers.

optical features of a dielectric waveguide. The difference in band-gap aids carrier confinement to the active layer where recombination produces optical gain (Figure 1.4 (c)). Optical field confinement may be achieved by laterally varying the effective refractive index, by either changing the shape of the waveguide or the material composition.

Efficient heterostructure operation (with both carrier and optical confinement in the active region) requires careful matching of the lattice constants of the two semiconductor materials. To reduce the formation of lattice defects, the lattice constants of the two materials should match to better than 0.1%. Otherwise, stress and strain in the crystal result in the production and propagation of dislocations in the crystal lattice which cause non-radiative carrier recombination. Radiative quantum efficiency is thus reduced and threshold current density is increased.

Optical field confinement in index-guided lasers (Figure 1.5 (b)) is produced by lateral index steps provided by blocking layers. Lateral carrier confinement is provided by the stripe-geometry contact in gain-guided lasers (Figure 1.5 (a)). Confinement parallel to the junction is due to the nonuniform distribution of both the gain and the refractive index. In the stripe geometry, the refractive index is lower at the centre of the narrow strip through the laser. This produces an antiguiding effect which is only attenuated by the gain profile. Light is generated along the stripe axis,

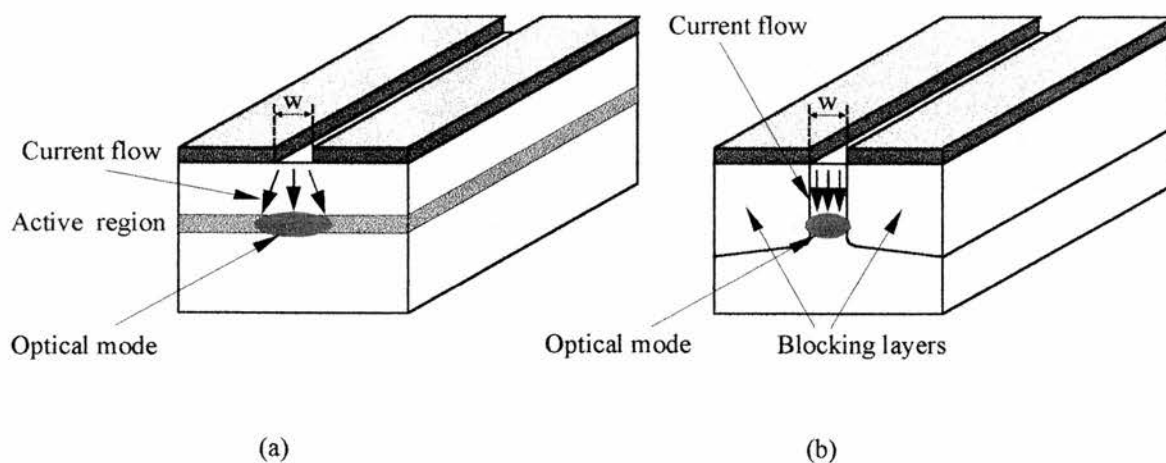


**Figure 1.5.** (a) the gain-guided laser provides poor lateral confinement; (b) the index-guided laser possesses strong lateral confinement. Both lasers give good transverse confinement. Strip width  $w$  varies between 2 - 5  $\mu\text{m}$ .

the optical field is absorbed outwith this region and the field is confined to the stripe region.

### 1.5 Quantum well lasers

Multiquantum-well (MQW) injection lasers in which the active layer has a thickness of less than 10nm have been developed as a result of advances in molecular-beam epitaxy (MBE) and vapour-phase epitaxy (VPE)<sup>22,23</sup>. In these devices the active region comprises a number of ultra-thin layers separated by layers of a greater band-gap. The active layer thickness in QW lasers is comparable to the de Broglie wavelength ( $\lambda = h/p$ ) where  $p$  is the electron momentum. These active layers are sufficiently thin that they give rise to quantum-size effects, produced by the confinement of carriers to the potential wells formed by conduction and valence bands (see Figure 1.6). In the active layer the motion of electrons in the dimension perpendicular to the wells is quantised. This carrier confinement gives rise to a quantisation of the allowed energy levels of the electrons travelling in the direction of confinement.

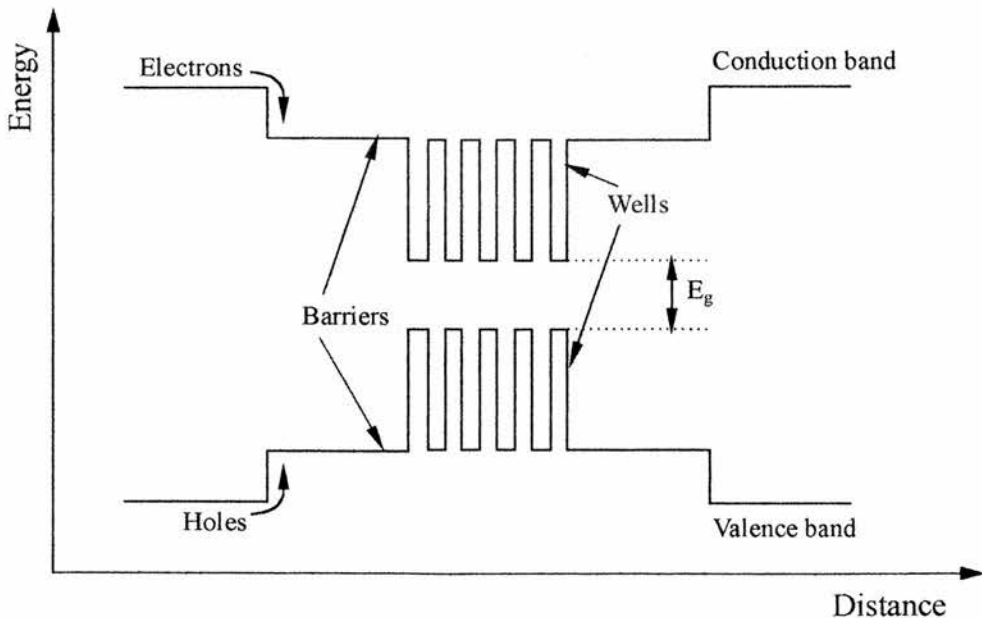


**Figure 1.6.** Multiple quantum well structure band diagram. Holes and electrons have discrete energy levels in the bands.

The lowest energy radiative transition occurs at a photon energy that is considerably higher than the material bandgap. Laser action most often takes place on the transition between the lowest conduction band sub-band and the highest heavy-hole sub-band of the valence band.

However, carriers can move freely in the direction parallel to the heterojunction. The confinement of electrons in one dimension results in a quantisation of allowed energy levels. The result is the step-like density of states function shown in Figure 1.7. Photon energy is dependent on well width and barrier height and on their respective material composition. Consequently, quantum well lasers exhibit improved differential gain and low threshold current densities and improved temperature performance<sup>16,24,25</sup>. When compared to bulk lasers, QW devices provide higher modulation bandwidths, due to their enhanced differential gain. Improved quantum well (and multiple QW) laser performance has resulted in the widespread use of such devices. Quantum wire and quantum box lasers are also under development<sup>26,27</sup>, the active layer being confined in two and three dimensions respectively.

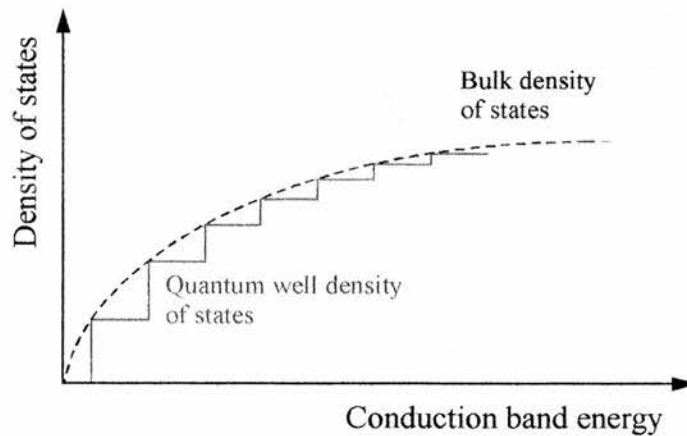


**Figure 1.7.** Schematic for the density of states function for bulk and quantum well lasers. Each step represents a sub-band corresponding to a new discrete energy level.

## 1.6 Single-frequency lasers

The diode laser emits a light beam which has an astigmatic, elliptical cross-section as a result of diffraction from the rectangular cross-section of the active region. The output is generally longitudinal multimode. In conventional FP-type lasers, optical feedback is provided by facet reflections which are the same for all longitudinal modes. Longitudinal mode discrimination is provided only by the gain spectrum itself. Since the gain bandwidth is usually much larger than the longitudinal mode spacing, mode discrimination is poor. One way of improving the mode selectivity is to make the feedback frequency dependent so that the cavity loss changes for different longitudinal modes. One useful method of implementing this solution is by using distributed feedback. Semiconductor lasers employing distributed feedback can be classified into two broad categories: distributed feedback (DFB) lasers and distributed Bragg reflector (DBR) lasers.

### 1.6.1 Distributed feedback (DFB) lasers

The feedback necessary for laser action in a DFB laser<sup>27,28</sup> is achieved by way of a grating region running along the length of the device in close proximity to the active region such that the propagating optical field is affected (Figure 1.8 (a)). Periodic perturbations in the refractive index along the laser cavity provides frequency-selective feedback via backward Bragg scattering. Forward and backward propagating waves are coherently coupled only at the wavelength satisfying the Bragg condition defined by the grating period. However, DFB lasers with uniform gratings and cavities do not oscillate at the Bragg wavelength<sup>29</sup> and two-mode oscillation on either side of the stop-band can occur instead. The dominant mode is established by variations in carrier density along the cavity length and asymmetries in the cavity or at the facets of the device. However, the carrier distribution varies enormously under dynamic drive conditions and the phase and residual facet reflectivity vary significantly. Therefore stronger mode selectivity is necessary for directly modulated devices. Single-mode



oscillation may be realised by introducing a phase shift of  $\pm\pi$  for the cavity round-trip, that is, both counter-propagating waves must experience a  $\pi/2$  or  $\lambda/4$  phase-shift. The laser mode is moved to the Bragg wavelength by phase shifting the diffraction grating by  $\lambda/4$  in the middle of the grating<sup>30,31</sup> (Figure 1.8 (b)) or two  $\lambda/8$  phase shifts situated towards the facets<sup>32</sup>. However  $\lambda/4$  phase-shifted DFB lasers suffer from longitudinal-mode spatial hole burning. DFB lasers also suffer from wavelength chirp when operated at high modulation rates. This is caused by changes in the effective pitch of the grating due to carrier-induced variation in the refractive index of the laser and may be overcome by use of multiple-contact lasers.

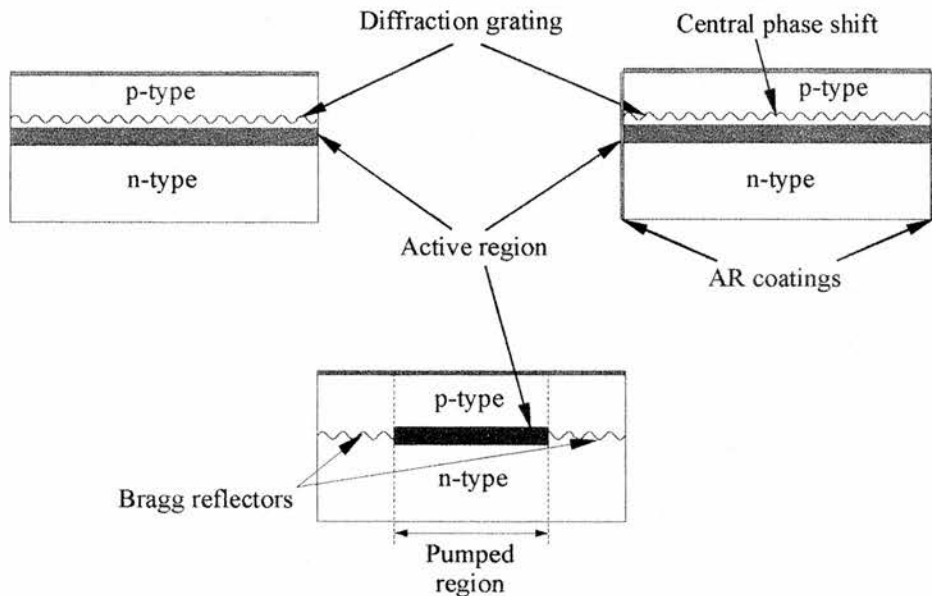


**Figure 1.8.** Schematic of the distributed feedback (DFB) laser (a) without and (b) with a phase shift. (c) shows the distributed Bragg reflector (DBR) laser. All three devices feature integrated mode control. Different refractive indices on opposite sides of the grating result in a periodic index perturbation which is responsible for the distributed feedback

### 1.6.2 Distributed Bragg reflector (DBR) lasers

DBR lasers<sup>33,34</sup> employ diffraction gratings positioned near the cavity ends and distributed feedback is initiated outside the active region as shown in Figure 1.8 (c). First-order gratings are generally formed in the DBR region with a coupling



coefficient of  $\sim 100\text{cm}^{-1}$ . The unpumped corrugated end regions effectively act as wavelength-dependent mirrors whose reflectivity is of DFB origin. A problem inherent in the DBR laser is that when the unpumped active material is used to etch the gratings at both ends, optical losses inside the DBR region are high and the resulting DBR reflectivity is poor. The problem of material loss is can be overcome by using a material for the distributed Bragg reflector that is relatively transparent at the laser wavelength<sup>16</sup>.

The performance of DBR lasers is comparable to that of DFB devices as far as emission characteristics and the dynamic and spectral properties are concerned<sup>34</sup>. The longitudinal mode closest to the Bragg wavelength has the lowest threshold gain and becomes the dominant mode. Because of the significant gain margin ( $\sim 8\text{cm}^{-1}$ ), the other longitudinal modes are suppressed by about 30dB relative to the main mode. In contrast to FP lasers, the longitudinal modes of DBR devices are not equidistant. As a consequence of its spectral purity, DBR lasers are useful as single-frequency sources for optical fibre communications.

### 1.6.3 Multiple-contact lasers

Multiple-contact lasers are now commonly used in picosecond pulse regimes including modelocking<sup>35,36</sup>, active and passive Q-switching<sup>37,38</sup>, wavelength tuning<sup>39</sup>,

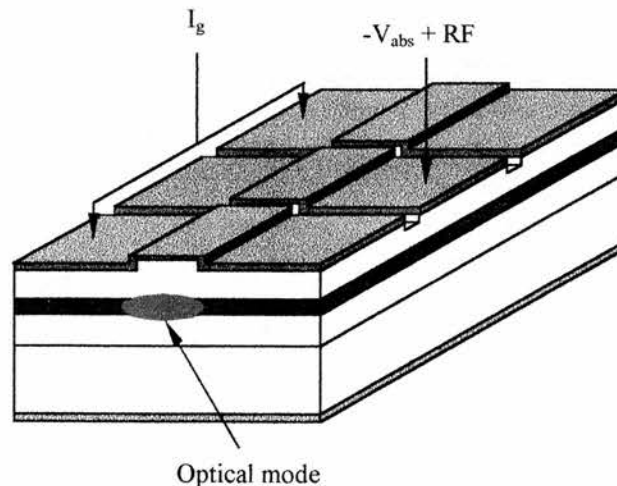


**Figure 1.9.** Basic structure of a three-contact diode laser. Gain and absorber currents can be independently varied.

optical bistability<sup>40,41</sup> and optical time- and wavelength-division multiplexing<sup>42</sup>. A three-contact laser diode is shown in Figure 1.9 although any number of sections may be produced. The upper metallic contact of the device is divided monolithically into three sections and each section can be driven independently. In a multiple-contact device, there is a nonlinear dependence of gain and absorption on carrier concentration and the absorption cross-section is much greater than the gain cross-section. For the forced Q-switched example shown, the two end contacts of the diode are joined together off-chip and are strongly forward biased to provide gain. The centre contact provides absorption and is driven via an RF modulation superimposed on a reverse bias dc voltage. The highly conductive upper semiconductor layer is etched to provide sufficient electrical isolation between the sections as shown in Figure 1.10.

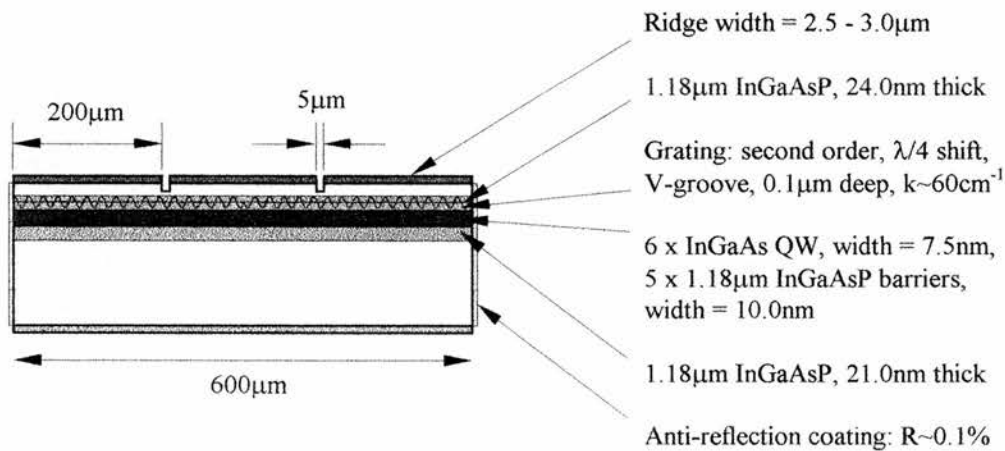


**Figure 1.10.** Schematic of a three-contact ridge-waveguide multi-quantum well distributed feedback laser showing typical structure, dimensions and material composition. Intercontact resistance is 600 - 1000 Ω.

## 1.7 Rate Equations

The dynamic operation of semiconductor diode lasers may be formalised in terms of a set of time-dependent nonlinear rate equations describing the electron and photon densities:

$$\frac{dN}{dt} = \frac{\eta J}{ed} - AN - BN^2 - CN^3 - v_g \frac{dg}{dN} \left[ \frac{N - N_0}{1 + \epsilon P} \right] P \quad (1.5)$$

$$\frac{dP}{dt} = \Gamma \beta BN^2 + \Gamma v_g \frac{dg}{dN} \left[ \frac{N - N_0}{1 + \epsilon P} \right] P - \frac{P}{\tau_p} \quad (1.6)$$

The net change in carrier concentration in the laser per second (Eq. 1.5) is increased by current injection, where  $\eta J$  is the injected current density flowing through the active region,  $d$  is the active layer thickness and  $e$  the electronic charge. Carrier concentration is depleted by the generation of photons via radiative recombination. The recombination rate  $A$  is due to mechanisms such as trap or surface recombination.  $B$  is the radiative recombination coefficient, while  $C$  is related to Auger recombination processes. The last term in Eq. 1.5 is due to stimulated recombination and leads to nonlinear coupling between photons and charge carriers.

The net change in photon density of the oscillating mode per second (Eq. 1.6) is increased by both stimulated and coupled spontaneous emission and is reduced via waveguide losses in the laser and by facet losses. The spontaneous radiative recombination term included in the photon density equation is scaled by a factor  $\beta$  to account for the spectral overlap of the spontaneous emission with the longitudinal modes resulting from stimulated emission. The spontaneous emission coupling coefficient  $\beta$  is small ( $\sim 10^{-4} - 10^{-5}$ ) since only a small part of the spontaneous emission is at the same wavelength as the oscillating mode. The optical confinement factor  $\Gamma$  describes extent to which the optical mode spreads beyond the active region.

The electron rate equations assume that

- i) light amplification by stimulated emission is linear;
- ii) the laser generates monochromatic light;
- iii) carrier and photon densities are constant throughout the laser volume;
- iv) carrier and photon population changes are small on the round-trip time scale;
- v) waveguide and facet losses are combined;

vi) temperature effects are negligible.

Equations 1.5 and 1.6 are used to generate the theoretical models of the temporal dynamics of ultrashort pulse generation in modelocked, gain-switched and Q-switched laser devices described in Chapter 2, 5 and 6 respectively. Values of the laser parameters used are shown in Table 1.1

<i>Symbol</i>	<i>Variable</i>	<i>Value</i>	<i>Unit</i>
A	Non-radiative recombination rate	$1 \times 10^8$	$s^{-1}$
B	Radiative recombination rate	$1 \times 10^{-10}$	$cm^3 s^{-1}$
C	Auger recombination coefficient	$1.3 \times 10^{-28}$	$cm^6 s^{-1}$
$g_0$	Differential gain	$3.1 \times 10^{-6}$	$cm^3 s^{-1}$
d	Active layer thickness	0.18	$\mu m$
e	Electronic charge	$1.602 \times 10^{-19}$	C
h	Planck's constant	$6.626 \times 10^{-34}$	J s
$\hbar$	Planck's constant divided by $2\pi$	$1.055 \times 10^{-34}$	J s
k	Wave vector $2\pi/\lambda_0$	$4.537 \times 10^4$	$cm^{-1}$
k	Boltzmann's constant	$1.381 \times 10^{-23}$	J/K
L	Cavity length	400	$\mu m$
w	Waveguide width	2.5	$\mu m$
t	Time	$1 \times 10^{-12}$	s
$n_g$	Group refractive index	3.7	
$n_t$	Transparency density	$1.1 \times 10^{18}$	$cm^{-3}$
$R_1, R_2$	Mirror reflectivities	0.35	
$\alpha$	Linewidth enhancement factor	0.5	
$\beta$	Spontaneous emission coupling coefficient	$1 \times 10^{-4}$	
$\Gamma$	Optical confinement factor	0.3	
$\lambda_0$	Emission wavelength	1550	nm
$\tau_p$	Photon lifetime		s
$\epsilon$	Nonlinear gain coefficient	$1.7 \times 10^{-17}$	$cm^3$

**Table 1.1.** Laser parameters used throughout the text.

## 1.8 Ultrashort pulse diagnostic techniques

The precise evaluation of picosecond optical pulse structures is a fundamental requirement for the accurate characterisation of semiconductor diode lasers. Two main techniques are available: direct linear-response processes and indirect nonlinear methods. Direct detection is implemented via an electron-optic streak camera or a photodiode/oscilloscope combination. Indirect methods are based on the determination of the second-order autocorrelation function derived by second-harmonic generation (SHG) in a nonlinear crystal.

### 1.8.1 Linear detection of temporal intensity using photodiodes and oscilloscopes

The simplest and most convenient means of measuring the temporal intensity of picosecond laser pulses is via direct detection using the combination of a photodiode and a fast oscilloscope. The time resolution of this method is determined by the combined bandwidth of the photodiode and oscilloscope<sup>43</sup>. The speed of the photodetector is limited by either the carrier recombination time or the carrier transit time. However high-speed diodes having bandwidths in excess of 100GHz have been reported<sup>44,45</sup> and it is the oscilloscope bandwidth which effectively limits the resolvable pulse duration of the system. If the pulse signal is periodic, sampling oscilloscopes may be used. State-of-the-art sampling oscilloscopes have bandwidths as large as 50GHz<sup>46</sup>, corresponding to a risetime of 7ps, whereas optical oscilloscopes enable accurate optical pulse measurement with a time resolution of ~10ps. Thus pulse durations down to a minimum of ~10ps may be readily measured using such photodiode/oscilloscope combinations.

### 1.8.2 Electron-optical chronoscopy using streak cameras

Streak cameras<sup>47</sup> can offer an improved time resolution of  $\sim 500$ fs, an order of magnitude greater than that available via photodiode/oscilloscope combinations. Streak cameras offer

- i) a wide spectral range, from the near infra-red to the X-ray region;
- ii) the ability to directly determine the profile of optical pulses with picosecond and subpicosecond time resolution;
- iii) the capability for two-dimensional analysis, such as time-resolved spectroscopy and spatial measurement.

The streak camera converts data characterising the optical pulse under investigation from the time domain into the spatial domain. It combines the operating principle of a photomultiplier and an oscilloscope<sup>48</sup>. The dynamic operation of streak cameras can be classified into two distinct modes

- i) synchroscan operation at repetition rates  $\geq 100$ MHz<sup>49,50</sup>;
- ii) single-shot scan having a repetition rate of up to several kHz<sup>47,51</sup>.

Figure 1.11 shows a schematic of an electron optic streak image tube. The laser pulse

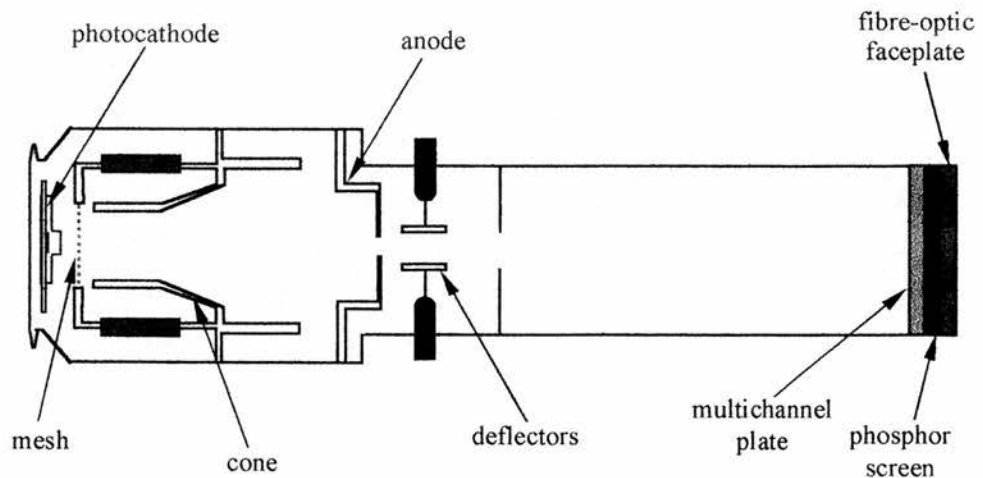


Figure 1.11. Schematic of a Photochron IIA streak image tube.

is focused on the photocathode of the streak tube and a packet of photoelectrons is generated. The temporal distribution of this packet replicated that of the laser pulse intensity. The photoelectrons are then accelerated by the electrostatic field between the photocathode and the mesh and focused onto the output phosphor screen via an electrostatic lens arrangement. The electron packet passes between a pair of deflectors to which a linear, time-varying ramp voltage is applied. The photoelectric signal level produced by the phosphor screen is linearly proportional to the optical intensity of the incident pulse. The ramp voltage produces a streaking effect and the electron distribution is mapped out spatially on the phosphor screen. Thus the temporal distribution of the photoelectrons (derived from the incident pulse) is converted into a spatial distribution on the screen. The image may be subsequently analysed via a readout device such as an optical multichannel analyser (OMA).

Synchroscan (or synchronously repetitive) action<sup>52</sup> is the preferred mode of operation for the assessment of periodic sequences of optical pulses produced by modelocked, gain-switched and Q-switched semiconductor lasers. In this system a repetitive linear deflection voltage which is precisely synchronised to the incident sequence of ultrashort pulses is applied to the deflection plates of the camera. The linear deflection signal is derived from the RF modulation used to drive the laser. For practical implementation of this scheme a high-frequency (e.g.  $\sim 650\text{MHz}$ ) sinusoidal voltage is applied and advantage is taken of the fact that the central  $1/6^{\text{th}}$  of the sinewave period and central half of the amplitude are linear to within 5%. The frequency of the waveform may be chosen to be equal to or an exact harmonic of the RF repetition rate of the laser. In this way the individual streaks of each pulse may be accumulated at a fixed position on the screen thereby producing an effective signal gain with a high detection sensitivity and dynamic range and an enhanced signal-to-noise ratio.

Single-shot cameras having a temporal resolution of  $\sim 300\text{fs}$  have been realised<sup>53</sup> whereas  $\sim 500\text{ps}$  is the current limit of temporal resolution in the synchroscan mode<sup>54</sup>. However, it should be appreciated that the temporal resolution



of a synchroscan streak camera can be limited by accumulating pulse timing jitter between the periodic pulse train and the applied sinusoidal detection signal.

The main limiting factor in the temporal resolution of femtosecond pulses with good dynamic range are space charge effects<sup>55</sup>. These effects may be lessened by reducing the slit length of the streak camera in conjunction with a reduction in the electron-optical magnification, using higher operating voltages or enabling a shorter transit time for the photoelectrons. In addition, the detail of the temporal intensity profile of a streak image can only be deduced when the camera resolution is significantly better than the pulse duration. Thus for an optical pulse duration of 10ps the camera resolution should be 2ps or better.

### 1.8.3 Nonlinear detection via SHG intensity autocorrelation

The most commonly used technique for the measurement of pulse durations of less than one picosecond is that of nonlinear correlation measurement, specifically that of second harmonic generation (SHG) autocorrelation<sup>43,56</sup>. This technique is simple and inexpensive and provides extremely high time resolution down to tens of femtoseconds. However, since this is an indirect technique, the intensity autocorrelation is unable to provide unambiguous information about the pulse shape, particularly its asymmetry and frequency chirping. In particular, higher order correlation functions are required to accurately describe the pulse shape and duration<sup>56</sup>. When applied with interferometric techniques, second order (fringe-resolved) autocorrelation may provide qualitative information about the pulse shape and the frequency chirp of the pulse<sup>57,58</sup>.

In the schematic of Figure 1.12 the standard, real-time, collinear autocorrelator is typical of the basic Michelson interferometer schemes that are generally employed. The E-field of each pulse is split into two components via the 50/50 beamsplitter and the subcomponents are recombined in an optically nonlinear crystal after being retroreflected by corner cube mirrors. The adjustable location of mirror  $M_1$  allows one subcomponent to be temporarily advanced or retarded relative



to its counterpart such that the instantaneous intensity incident upon the nonlinear crystal is a function of their overlap. A variable optical delay can be introduced into one via an electronically driven speaker mounted mirror. Since the second harmonic intensity in the crystal depends quadratically upon the instantaneous intensity of the input, the output of the photomultiplier represents a second order intensity autocorrelation function. The speaker is typically driven at 20 - 60 Hz<sup>59,60</sup> by a rounded sawtooth waveform which enables real-time monitoring of the autocorrelation using an oscilloscope.

A variety of nonlinear materials have been utilised for SHG of ultrashort laser pulses<sup>61</sup>. The lower peak powers of the optical pulses produced by diode lasers mean that it is considerably more difficult to generate the second harmonic in semiconductor devices than, for example, in solid-state lasers. Thus, nonlinear materials having a high nonlinear optical coefficient are required. It has been demonstrated that nonlinear crystals such as  $\text{LiIO}_3$ ,  $\text{KnbO}_3$  and  $\text{KTiOPO}_4$  (KTP) are the best nonlinear materials for frequency doubling of diode laser emission<sup>62-65</sup>.

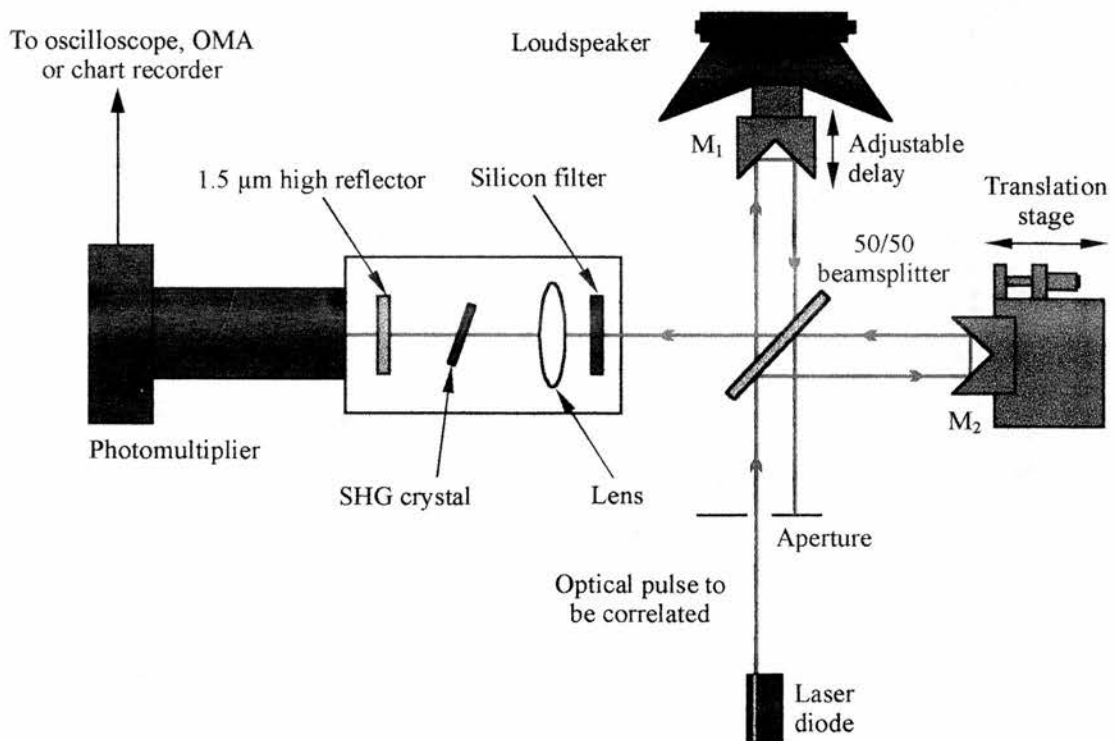


Figure 1.12. Schematic of the SHG autocorrelator.

### 1.8.4 Spectral analysis

In addition to temporal measurements, the optical spectrum of the laser output provides useful information regarding pulse quality. The commercially available optical spectrum analyser is essentially a digitally calibrated scanning monochromator and provides a calibrated video representation of the wavelength characteristics of the laser light. The fibre-coupled Anritsu Wiltron MS96A optical spectrum analyser (OSA) provides a resolution bandwidth of 0.1 - 0.5nm over a wide wavelength range (600 - 1600nm). While the OSA is an extremely versatile diagnostic, it offers a relatively slow means of acquiring and presenting spectral data. Real-time spectral information is provided via a scanning Fabry-Perot Interferometer (SFPI). A 1m Monospek monochromator with a resolution of 1nm and a custom-built scanning FP interferometer may be used in conjunction with an oscilloscope display to record the relatively broad spectral features of picosecond pulse diode lasers.

RF spectrum analysis is provided by a high-speed InGaAs PIN photodiode (~30ps typical response time) in conjunction with a Hewlett-Packard HP70001A RF spectrum analyser having a 0.1 - 22GHz frequency range and a minimum resolution bandwidth of 10Hz. Analysis of the RF spectrum allows evaluation of timing jitter (or phase noise) of the optical pulse train typically using 1<sup>st</sup> and 4<sup>th</sup> harmonics.

### 1.8.5 Additional pulse measurement techniques

Although the synchroscan streak camera and optical spectrum analyser were used almost exclusively in the laboratory, other important characterisation techniques have recently been developed. These include frequency-resolved optical gating (FROG)<sup>52</sup> and frequency-domain phase measurement (FDPM)<sup>57</sup>. In FROG<sup>60,66</sup>, the optical pulse is input into a nonlinear autocorrelator (a SHG autocorrelator, for example) and then passed through a spectrometer. Using iteration techniques, the original pulse may be reconstructed from the resulting spectrogram. For FDPM, a short segment of the optical pulse (sampled using a nonlinear optical element acting

as a time gate<sup>58,60,66-69</sup>) is passed through a spectrometer and the spectrally resolved components of the pulse are cross-correlated with the pulse itself in a SHG crystal. The original pulse is then reconstructed via iteration from the resultant sonograph.

## 1.8 Conclusions

In this chapter the physical process which contribute towards laser action in semiconductor diode laser have been described. The forward biased p-n junction has been described in terms of electron-hole recombination and has been shown to form the basis of the diode laser. The development of the semiconductor laser has been described highlighting such important milestones as the introduction of the heterojunction and methods of confining both the carriers and the optical pulse. Various laser structures including gain-guided and index-guided were contrasted and compared. The quantum well laser was described and single-frequency (DFB and DBR) laser were highlighted. The basis of the computer simulations of subsequent chapters, the nonlinear rate equations, were described.

Characterisation of ultrashort pulses produced by semiconductor diode lasers require diagnostics capable of picosecond timescale resolution. Linear and nonlinear measurement techniques were described which allow the comprehensive characterisation of the modelocked, gain-switched and Q-switched pulses described in subsequent chapters.

**1.8 References**

1. C. Lin, *Optoelectronic Technology and Lightwave Communications Systems*, Van Nostrand Reinhold, New York (1989).
2. J.E. Bowers and M.A. Pollock, *Optical Fibre Telecommunications II*, Academic Press, New York (1988).
3. M.J. Adams, A.G. Steventon, W.J. Devlin and I.D. Henning, *Semiconductor Lasers for Long-Wavelength Optical-Fibre Communications*, P. Peregrinus, London (1987).
4. R.D.T. Lauder, A.C. Tropper, D.C. Hanna, P.P. Vasil'ev, R.V. Penty, I.H. White, S.T. Davey and D. Szebesta, *Electron. Lett.*, **30**, 1298 (1989).
5. M. Asobe, H. Kobayashi and H. Itoh, *Opt. Lett.*, **18**, 1056 (1994).
6. C.F. Lin and C.L. Tang, *Appl. Phys. Lett.*, **63**, 2594 (1993).
7. J.T. Ong, R. Takahashi, M. Tsuchiya, S.-H. Wong, R.T. Sahara, Y. Ogawa and T. Kamiya, *IEEE J. Quantum Electron.*, **QE-29**, 1701 (1993).
8. P.P. Vasil'ev, *Sov. J. Quantum Electron.*, **20**, 207 (1990).
9. C.H. Lee, Ed., *Picosecond Optoelectronic Devices*, Academic Press, Orlando, FL (1984).
10. G. A. Mourou, D.M. Bloom and C.H. Lee, *Picosecond Electronics and Optoelectronics*, Springer, New York (1985).
11. T.C. Sollner and D.M. Bloom, Eds., *OSA Proc. On Picosecond Electronics and Optoelectronics*, Optical Society of America, Washington, DC (1989).
12. N.G. Basov, O.N. Krokhin and Yu. M. Popov, *Sov. Phys. JETP*, **13**, 1320 (1961).
13. S.M. Sze, *Physics of Semiconductor Devices*, Second Ed., John Wiley & Sons, New York (1981).
14. M.G.A. Bernard and G. Duraffourg, *Phys. Status Solidi*, **1**, 699 (1961).
15. R.J. Phelan and R.H. Rediker, *Appl. Phys. Lett.*, **6**, 70 (1965).
16. G.P. Agrawal and N.K. Dutta, *Long-Wavelength Semiconductor Lasers*, Van Nostrand Reinhold, New York (1986).
17. Zh. I. Alferov, V.M. Andreev, E.L. Portnoi and M.K. Trukan, *Sov. Phys. Semcond.*, **3**, 1107 (1970).
18. H. Kroemer, *Proc. IEEE*, **51**, 1782, (1963).
19. I. Hayashi, M.B. Panish and P.W. Foy, *IEEE J. Quantum Electron.*, **QE-5**, 211 (1969).
20. I. Hayashi, M.B. Panish, P.W. Foy and S. Sumski, *Appl. Phys. Lett.*, **17**, 81 (1970).
21. J.C. Dymant, J.E. Ripper and T.H. Zachos, *J. Appl. Phys.*, **40**, 1802 (1969).

22. R. Dingle, W. Wiegmann and C.H. Henry, *Physical Review Letters*, **33**, 827 (1974).
23. P.S. Zory, Ed., *Quantum Well Lasers*, Academic Press, Boston, MA (1993).
24. A. Katz, Ed., *Indium Phosphide and Related Materials: Processing, Devices and Material*, Artech House, Boston, MA. (1992).
25. Y. Arakawa and A. Yariv, *IEEE J. Quantum Electron.*, **21**, 1666 (1985).
26. Y. Arakawa K. Vahala and A. Yariv, *Appl. Phys. Lett.*, **45**, 950 (1984).
27. M. Asada, Y. Yimamoto and Y. Suematsu, *IEEE J. Quantum Electron.*, **22**, 1915 (1986).
28. H. Kogelnik and C.V. Shank, *J. Appl. Phys.*, **43**, 2327 (1972).
29. R.D. Burnham, D.R. Scifres and W. Streifer, *IEEE J. Quantum Electron.*, **11**, 439 (1975).
30. H. Haus and C.V. Shank, *IEEE J. Quantum Electron.*, **12**, 532 (1976).
31. K. Sekartedjo, N. Eda, K. Furuya, F. Koyama and T. Tanbun-Ek, *Electron. Lett.*, **20**, 80 (1984).
32. J.E.A. Whiteaway, B. Garrett, G.H.B. Thompson, A.J. Collar, C.J. Armistead and M.J. Fice, *IEEE J. Quantum Electron.*, **28**, 1277 (1992).
33. F.K. Reinhart, R.A. Logan and C.V. Shank, *Appl. Phys. Lett.*, **27**, 45 (1975).
34. Y. Suematsu, S. Arai and K. Kishino, *J. Lightwave. Tech.*, **1**, 161 (1983).
35. V.N. Morozov, V.V. Nikitin and A.A. Sheronov, *JETP Lett.*, **7**, 256 (1968).
36. P.P. Vasil'ev and A.B. Sergeev, *Electron. Lett.*, **25**, 1049 (1989).
37. T.P. Lee and R.H.R. Roldan, *IEEE J. Quantum Electron.*, **6**, 339 (1970).
38. D.Z. Tsang and J.N. Walpole, *IEEE J. Quantum Electron.*, **19**, 145 (1983).
39. Y. Yoshikuni and G. Motosugi, *J. Lightwave. Tech.*, **5**, 516 (1987).
40. G.J. Lasher, *Solid-State Electronics*, **7**, 707 (1964).
41. N.G. Basov, *IEEE J. Quantum Electron.*, **4**, 855 (1968).
42. H. Kawaguchi, *Proc. IEEE*, **140**, 3, (1993).
43. D.J. Bradley and G.H.C. New, *Proc. IEEE*, **62**, 313, (1974).
44. Y. Chen, S. Williamson, T. Brock, F.W. Smith and A.R. Calawa, *Appl. Phys. Lett.*, **59**, 1984 (1991).
45. S.Y. Chou, Y. Liu, W. Khalil, T.Y. Hsiang and S. Alexandrou, *Appl. Phys. Lett.*, **61**, 819 (1992).
46. J.R. Andrews, "Comparison of Sampling Oscilloscopes with ~35 ps Transition Durations", *Picosecond Electronics and Optoelectronics II*, F.G. Leonburger, C.H. Lee, F. Cappasso and H. Morcos, Eds., Springer, New York, 64 (1987).
47. D.J. Bradley L. Bidby and W.E. Sleat, *Opt. Comm.*, **2**, 391 (1971).
48. Y. Tsuchiya, *IEEE J. Quantum Electron.*, **20**, 1516 (1984).

49. R. Hadland, K. Herbrough and A.E. Huston, *Proc. Of 11<sup>th</sup> International Congress on High-Speed Photography*, Chapman & Hall, London, 107 (1975).
50. M.C. Adams, W.E. Sleat and W. Sibbett, *Opt. Comm.*, **26**, 273 (1978).
51. M. Ya. Schelev, M.C. Richardson and A.J. Alcock, *Appl. Phys. Lett.*, **18**, 354 (1971).
52. W. Sibbett, *Proc. XV<sup>th</sup> International Conf. on High-Speed Photography and Photonics*, **SPIE 21**, 226 (1982).
53. A. Finch, Y. Liu, H. Niu, W. Sibbett, W.E. Sleat, D.S. Walker, Q.L. Yang and H. Zhang, *Ultrafast Phenomena IV*, Springer Series in Chem. Phys., **48**, 159 (1988).
54. A. Finch, W.E. Sleat and W. Sibbett, *Review of Scientific Instruments*, **60**, 839 (1989).
55. Y. Liu and W. Sibbett, *IoP Conference Series*, **121**, 305 (1992).
56. E.P. Ippen and C.V. Shank, "Techniques for Measurements", *Ultrashort Light Pulses*, S.L. Shapiro, Ed., Springer, New York, 83 (1977).
57. J.-C.M. Diels, J.J. Fontaine, I.C. McMichael and F. Simoni, *Applied Optics*, **24**, 1270 (1985).
58. K. Naganuma, K. Mogi and H. Yamada, *IEEE J. Quantum Electron.*, **25**, 1225 (1989).
59. Sala, G.A. Kenney-Wallace and G.E. Hall, *IEEE J. Quantum Electron.*, **16**, 990 (1980).
60. R. Trebino and D. Kane, *J. Opt. Soc. Am. A*, **10**, 1101 (1993).
61. S. Singh, "Nonlinear Optical Materials", *Handbook of Laser Science and Technology*, **3**, M.J. Weber, Ed., CRC Press, Boca Raton, FL, 3 (1986).
62. D. Gloge and T.P. Lee, *J. Appl. Phys.*, **42**, 307 (1971).
63. P.P. Vasil'ev V.N. Morozov and A.B. Sergeev, *Proc. Of the Lebedev Physics Institute*, **185**, 1 (1989).
64. W. Wang, K. Nakagawa, Y. Toda and M. Ohtsu, *Appl. Phys. Lett.*, **61**, 1886 (1992).
65. P. Gunter, P.M. Asbeck and S.K. Kurtz, *Appl. Phys. Lett.*, **35**, 461 (1979).
66. D. Kane and R. Trebino, *IEEE J. Quantum Electron.*, **29**, 571 (1993).
67. G. Taft, A. Rundquist, H. Kapteyn and M. Murnane, *Opt. Lett.*, **7**, 743 (1995).
68. C. Yan and J.-C.M. Diels, *J. Opt. Soc. Am. B*, **8**, 1259 (1991).
69. J. Payne, M. Ramaswamy, J.G. Fugimoto and E.P. Ippen, *Opt. Lett.*, **18**, 1946 (1993).

# Chapter 2

## ACTIVE MODELOCKING OF InGaAsP SEMICONDUCTOR DIODE LASERS

### 2.1. Introduction

There are three established techniques for the generation picosecond pulses using semiconductor diode lasers: gain-switching, modelocking and Q-switching. All involve direct modulation of the laser output by controlling the degree of excitation of the gain medium. The largely linear nature of the light-current characteristic of semiconductor lasers means that the optical output is directly proportional to the drive current over a wide range of currents. The prime advantage of modelocking is that shorter pulses can be generated using this method than those produced by either gain-switching or Q-switching.

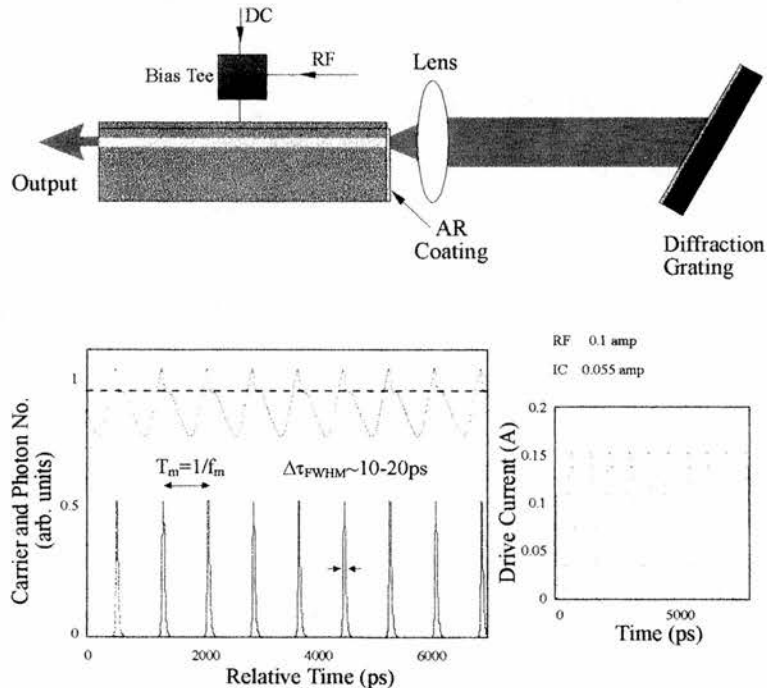


**Figure 2.1.** Schematic representation of ultrashort pulse production by modelocking. A RF signal of frequency equal to the external cavity mode spacing (or some multiple thereof) is superimposed onto a subthreshold dc bias.



## 2.2 Modelocked Diode Lasers

A major disadvantage of modelocking is the greater cavity complexity entailed by the need for an external mirror to define the cavity length. The modulation frequency  $f_m$  is related to the optical path length  $L_m$  by the relationship  $f_m = c/2nL_m$  where  $c$  is the speed of light and  $n$  is the harmonic modelocking number. Therefore extended cavity lengths are required for active modelocking to allow modulation at electrically achievable frequencies. Active modelocking may be realised either by modulating the gain of the laser cavity<sup>1-10</sup> or by modulating the loss of the cavity via an external modulator<sup>11</sup>. To date the shortest pulses have been obtained with active modelocking<sup>8</sup>. A schematic representation of active modelocking using an external cavity diode laser is shown in Figure 2.1. The output was collected and collimated by the lens and the external cavity was terminated by a diffraction grating which also provided wavelength tunability and bandwidth control.

## 2.3 Theoretical analysis

The theoretical treatment of active modelocking has been dealt with comprehensively in the literature<sup>12-21</sup>. However, a brief examination of the modelocking process will be considered in this section. The following analysis will demonstrate that a periodic train of picosecond optical pulses may be generated by fixing the relative phase relationship between the axial cavity modes.

### 2.3.1 Modelocking theory

Consider the simple standing-wave laser cavity shown in Figure 2.2. In principle, as a free running laser, it may have many oscillating modes and light may be generated at specific wavelengths  $\lambda_i$

$$\lambda_i = \frac{2L}{n} \quad n = \text{integer} \quad (2.1)$$



where the  $L$  is the optical path length of the laser resonator and  $\lambda_i$  is the fluorescent linewidth. That is, states exist such that

$$E_2 - E_1 = \frac{hc}{\lambda_i} \quad (2.2)$$

Hence the electric field amplitude of the output laser beam (ignoring the spatial distribution) is given by

$$E(t) = \sum_{n=0}^{N-1} (\mathcal{E}_0)_n \exp i(\omega_n t + \delta_n) \quad (2.3)$$

where  $(\mathcal{E}_0)_n$ ,  $\omega_n$  and  $\delta_n$  are the amplitude, frequency and phase of the  $n^{\text{th}}$  mode. The number of modes,  $N$ , is determined by the available states (fluorescence or lasing linewidth).

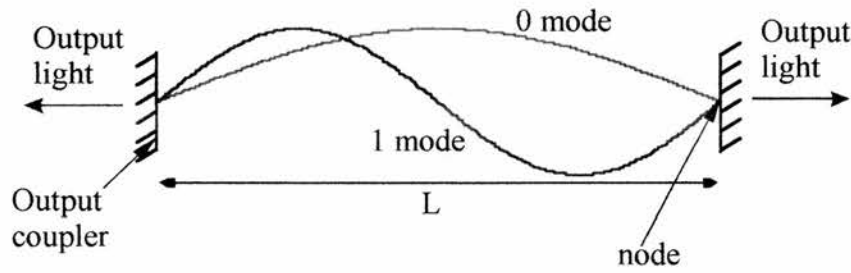


**Figure 2.2.** A simple laser cavity.

Usually each mode is generated independently, has random phase and as such is incoherent. If the modes have no fixed phase relationship the laser output will comprise noise, whose shortest fluctuations will have duration of the order of the inverse oscillating bandwidth. The total intensity  $I_{tot}$  is obtained by the summation of the individual mode intensities: Thus the total light intensity generated is

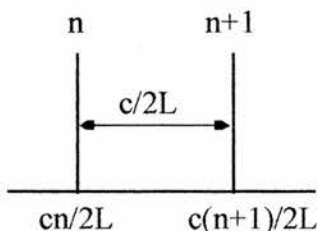
$$I_{tot} = \frac{E^2(t)}{2} = \frac{\sum_0^{N-1} |\mathcal{E}_0|_n^2}{2} \quad (2.4)$$

where cross terms average to zero. However, if it is assumed that these modes can be locked, then  $\delta_n = \delta$ , and

$$E(t) = \mathcal{E}_0 \exp i(\delta) \sum_{n=0}^{N-1} \exp i(\omega_n)t \quad (2.5)$$

assuming also that  $(\mathcal{E}_0)_n = \mathcal{E}_0$  for all  $n$ .

But  $\frac{n\lambda_n}{2} = L$ . Thus, from Figure 2.3, it is clear that



$$f_n = \frac{c}{\lambda_n} = \frac{cn}{2L} \quad (2.6)$$

Figure 2.3. Consecutive modes inside a simple laser cavity.

This implies that the frequency spacing between modes  $\delta\omega = \frac{2\pi c}{2L}$ . Therefore the output of the laser comprises axial cavity modes separated in frequency by  $\delta\omega$ , where

$$\delta\omega = \omega_n - \omega_{n-1} = 2\pi \frac{c}{2L} \quad (2.7)$$

where  $L$  is the optical path length of the laser resonator and  $n$  is the refractive index. Therefore, for the general case given a central frequency  $\omega_c$  and  $N$  modes in the fluorescent linewidth,

$$E(t) = \mathcal{E}_0 \exp(i\delta) \sum_{n=0}^{N-1} \left[ \exp i \left( \omega_c + \frac{N-1}{2} \delta\omega \right) t \right] \exp i(-n\delta\omega)t \quad (2.8)$$

Let

$$\omega_0 = \omega_c + \frac{N-1}{2} \delta\omega \quad (2.9)$$

This implies that

$$E(t) = \mathcal{E}_0 \exp(i\delta) \left[ \sum_{n=0}^{N-1} \left[ \exp i(\omega_0 - n\delta\omega)t \right] \right]$$

$$E(t) = \mathcal{E}_0 \exp i(\omega t_0 + \delta) \sum_{n=0}^{N-1} [\exp i(-\pi n c t/L)]$$

Let  $\phi = \pi c t / L$ . Then

$$E(t) = \mathcal{E}_0 \exp i(\omega t_0 + \delta) [1 + \exp i(-\phi) + \exp i(-2\phi) + \dots + \exp i[-(N-1)\phi]] \quad (2.10)$$

The term  $[1 + \exp i(-\phi) + \exp i(-2\phi) + \dots + \exp i[-(N-1)\phi]]$  is a sinc function, and thus the electric field amplitude may be expressed as

$$\begin{aligned} E(t) &= \mathcal{E}_0 \exp i(\omega t_0 + \delta) \left[ \frac{1 - \exp i(-N\phi)}{1 - \exp i\phi} \right] \\ &= \mathcal{E}_0 \exp i(\omega t_0 + \delta) \left[ \frac{\sin^2\left(\frac{N\phi}{2}\right)}{\sin^2\left(\frac{\phi}{2}\right)} \right] \exp -i\left(\frac{(N-1)\phi}{2}\right) \end{aligned}$$

Therefore total field intensity is

$$I(t) = \frac{\mathcal{E}_0^2}{2} \left[ \frac{\sin^2\left(\frac{N\phi}{2}\right)}{\sin^2\left(\frac{\phi}{2}\right)} \right] \quad (2.11)$$

This function describes a sequence of pulses generated at a rate of  $\frac{1}{2L/c}$ , that is, the round-trip time of the cavity (where  $L$  is the cavity optical path length). If it is now assumed that the duration of the pulses is the time between points of zero intensity adjacent to the peak power point (see Figure 2.4), then when

$$\frac{N\phi}{2} = \pi = \frac{N\pi c t}{2L}$$

$$t_n = \frac{2L}{Nc} \quad (2.12)$$

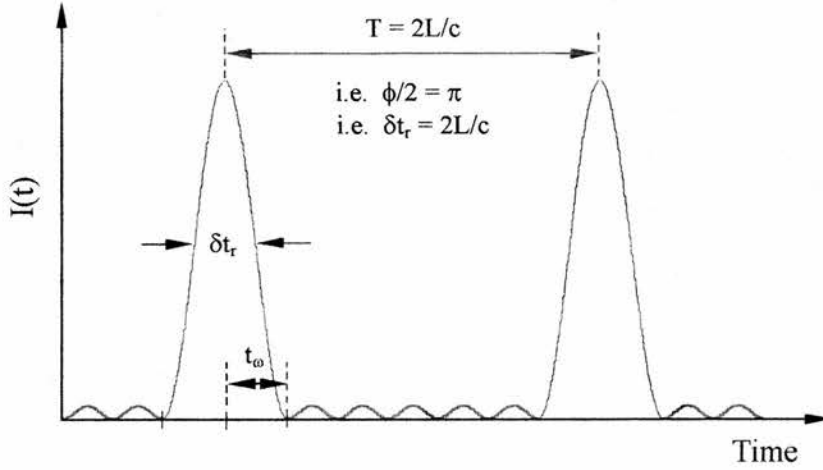


**Figure 2.4.** Total field intensity expressed as a function of time for seven locked modes.

The ratio of the period  $T$  to the pulsewidth  $\delta t$  is equal to the number of locked modes  $N$ . It is also possible to produce several modelocked pulses inside the cavity spaced by a multiple of  $\frac{c}{2L}$ . Figure 2.5 shows the envelope of  $E(t)$  for  $N = 20$ .

### 2.3.2 Homogeneous and inhomogeneously broadened laser gain media

The output of a homogeneously broadened laser comprises one longitudinal cavity mode, assuming the effects of spatial hole-burning are ignored. The reasons for this are twofold: firstly, the spectral lineshape function  $g(\nu)$  describes the response of each individual atom situated in the upper laser level and these are all considered to behave identically. Secondly, in an oscillating laser cannot increase the population inversion beyond the threshold value where the gain per pass equals the losses. Thus, when pumping is increased from below threshold the laser will oscillate at the centre frequency  $\nu_0$ . The gain at other frequencies will remain below threshold, however, so that an ideal homogeneously broadened laser will oscillate only at a single frequency.

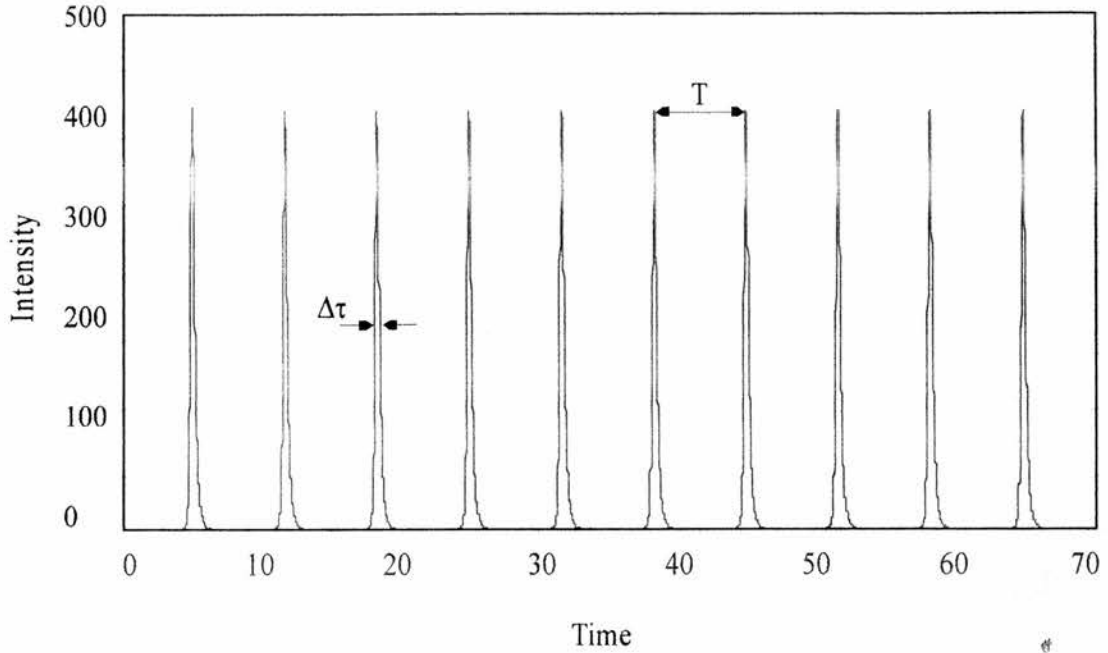


**Figure 2.5.** Ideal modelocking: derived total field intensity is  $I_n = N^2 \epsilon_0^2$  where  $\epsilon_0=1$ ,  $N=20$

In inhomogeneously broadened lasers, where individual atoms are considered to behave differently from one another, the population inversion and gain profile can increase above threshold values at frequencies other than  $\nu_0$ . The gain at  $\nu_0$ , however, remains clamped at the threshold value due to gain saturation. Further pumping may increase the gain at other frequencies until oscillations commence at those frequencies also. This results in a decrease in both the population inversion and the gain to the threshold values. The gain curve therefore acquires depressions or ‘holes’ at these oscillating frequencies: hole burning.

In modelocked lasers, the longitudinal cavity modes of the laser are forced to maintain fixed phase relationships. For inhomogeneously broadened system, the laser will normally oscillate spontaneously in a large number of free-running axial modes, with the mode amplitudes determined primarily by the inhomogeneous saturation and hole-burning properties of the laser transition itself. The primary task of the modulation signal in an inhomogeneously broadened laser is then only to synchronise, or lock into phase, the already oscillating modes. If the modulation frequency is closely tuned to the axial

mode interval, the modulation sidebands will fall directly on the adjoining axial modes and the modulation sidebands will easily pull the adjoining modes into the required frequency and phase relationship.

For an ideal homogeneously broadened system, the laser will oscillate naturally in only one (or a few) preferred axial modes located at line centre. The initially oscillating mode is modulated at a frequency consistent with the intermode spacing and this induces energy transfer to the adjacent modes which then begin to oscillate. These oscillating modes promote further mode generation, effectively pushing the sideband distribution outwards in frequency. A steady-state energy balance is then maintained by the action of the modulation signal in transferring energy from the stronger central modes to the weaker modes in the wings of the gain spectrum. In this way, a significant spectral broadening is apparent during the pulse build-up time (typically a few tens or hundreds of round trip times). Mode generation arises indirectly from the applied modulation signal and so the 'new' modes must theoretically possess a definite phase relationship.

Thus for inhomogeneously broadened lasers, modelocking is achieved by the phase locking of already oscillating modes and by mode generation in homogeneously broadened lasers. In practice, both types of laser are rarely single mode, mainly due to spatial hole burning, hence these modes must first be phase locked before further mode generation can take place.

## 2.4 Modelocking regimes

Modelocked pulses may be generated in semiconductor diode lasers using a number of different techniques: active<sup>22-24</sup>, passive<sup>25-27</sup>, coupled cavity<sup>28,29</sup>, colliding pulse<sup>30-32</sup> and hybrid methods<sup>33-35</sup>. An actively modelocked system is based upon the modulation of the gain (or loss) of the laser using a high-frequency RF signal generator synchronised to the cavity round-trip time. Active modelocking is considered in detail in Section 2.5. Passive modelocking is implemented by using an intracavity saturable absorber (which has high loss for low light intensities but saturates, becoming low loss, for high intensities) with no external modulation. The saturable absorption can be

introduced by either proton bombardment or ion implantation, often at the exit facet. Coupled cavity modelocking features a nonlinear element within the external cavity which enhances the modelocking process and produces a pulse-shortening effect. For semiconductor diode lasers, colliding pulse modelocking (CPM) produces the shortest temporal pulses<sup>36</sup> and is realised by interacting two counter-propagating optical pulses inside the saturable absorber of the laser. Finally, hybrid modelocking can be implemented using a multi-contact laser in conjunction with an external cavity, the gain being modulated by an external RF signal. In this thesis, only active modelocking of single-contact InGaAsP lasers will be considered.

## 2.5 Active Modelocking

The actively modelocked system involves the modulation of the gain (or loss) of the diode laser at a frequency corresponding to the intermodal spacing  $\delta\nu$ . For this regime each spectral mode is driven by the modulation sidebands of its neighbours<sup>37</sup>. Thus the phases of the modes are locked by the external modulation. This implies an inhomogeneously broadened medium where laser modes already exist. If homogeneously broadening applies, the laser modes are initiated in phase by sideband generation. Typical resonator lengths for laser chips are short (300 to 500  $\mu\text{m}$ ) and as a result, axial mode spacing is high ( $\delta\nu$  may exceed 300GHz). Consequently, direct active modelocking of a diode laser is rather difficult, because the frequency range required for modulation is 300 - 500GHz. However the effective cavity length of the device may be increased by placing the diode laser in an external resonator (Figure 2.1) or by using an extended monolithic cavity. Using these techniques the temporal periodicity is increased and active modelocking may be readily achieved.

### 2.5.1 Active modelocking via direct modulation

Active modelocking uses RF current modulation of the laser gain at the intermodal spacing frequency as shown in Figure 2.6. Modulation is normally produced using a sine

wave or comb generator. The standard modelocking technique is to apply a sub-threshold dc bias  $I_0$  and superimpose onto this a RF signal whose frequency equals that of the external cavity mode spacing (or some multiple thereof). Thus, for example, the cavity mode spacing  $\frac{c}{2L}$  (where  $L$  is the optical path length), will be 650MHz for a 23.1cm long laser cavity assuming that the internal diode facet is AR-coated.

The current modulation causes a corresponding modulation in the carrier density around the threshold value  $n_{th}$ . A short temporal window of net gain is created in the laser by selection of appropriate values of dc bias and modulation current amplitude. As a result, it may be implied that the carrier density  $n(t)$  exceeds threshold for an extremely small time period during each modulation cycle. However, a phase difference exists between the applied current modulation and the electron response due to the finite lifetime of the carriers. Although the carrier density is periodic, it comprises a set of harmonics of the modulation frequency  $2\pi/T$ . The fundamental harmonic (at  $2\pi/T$ ) is the most strongly excited Fourier component of the carrier density whilst the harmonics of order  $m$  are reduced by a factor of approximately  $1/m^{38}$ . Modelocking is achieved provided the round-trip time of the laser cavity exactly matches the modulation period  $T$ . That is, the condition

$$T = \frac{1}{\delta\nu} \quad (2.13)$$

is satisfied. The RF modulation frequency is clearly identical to the repetition rate of the modelocked pulses. The pulses will show significant degradation as the modulation frequency is detuned from the resonance condition given in Eq. (2.13). Positive frequency detuning, which produces a delay such that the optical pulse arrives at the laser frequency later than the peak of the current pulse, leads to gradual pulse broadening. Conversely, negative detuning, in which the optical pulse arrives at the laser before the peak of the optical gain, leads to the production of a pulse tail.



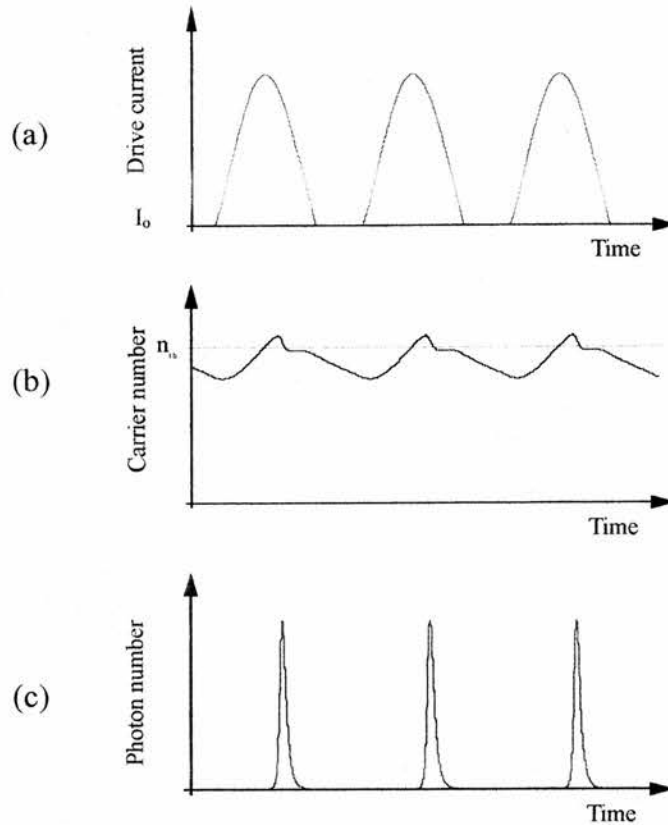


**Figure 2.6.** Theoretical representation of active modelocking of a diode laser using current modulation: (a) drive current waveform; (b) carrier density; (c) optical output against time.

## 2.6 Practical modelocked lasers

Efficient picosecond pulse production in actively modelocked lasers requires that a number of important criteria are met. The first of these is that the laser is driven at high RF amplitudes, typically above 25dBm for efficient modelocking. Secondly, a large modulation bandwidth is required. A third factor is strong coupling to the external cavity is required and this necessitates a high-grade AR coating with facet reflectivity  $<10^{-4}$ . Finally, an almost linear light-current characteristic is essential for the laser.

The modulation frequency is of crucial importance in the production of high-quality ultrashort pulses in modelocked lasers. In the 850nm wavelength region the shortest pulses are produced at a repetition rate  $\sim 1\text{GHz}$ <sup>15,39,40</sup>. However, at 1500nm, 0.6ps pulse

are obtained via high-frequency modelocking (16GHz) as compared with 5-7ps at 2GHz using low-frequency modelocking for the same laser diode<sup>14</sup>. This difference is thought to be due to the larger pulse shaping at higher frequency that occurs during each pass of the laser cavity, accumulative effects that evolve over many round trips of the cavity. Under optimal conditions, locked packets of modes (illustrated in Figure 2.11) are produced at repetition rates of  $\sim 10$ GHz and higher using current modulation only.

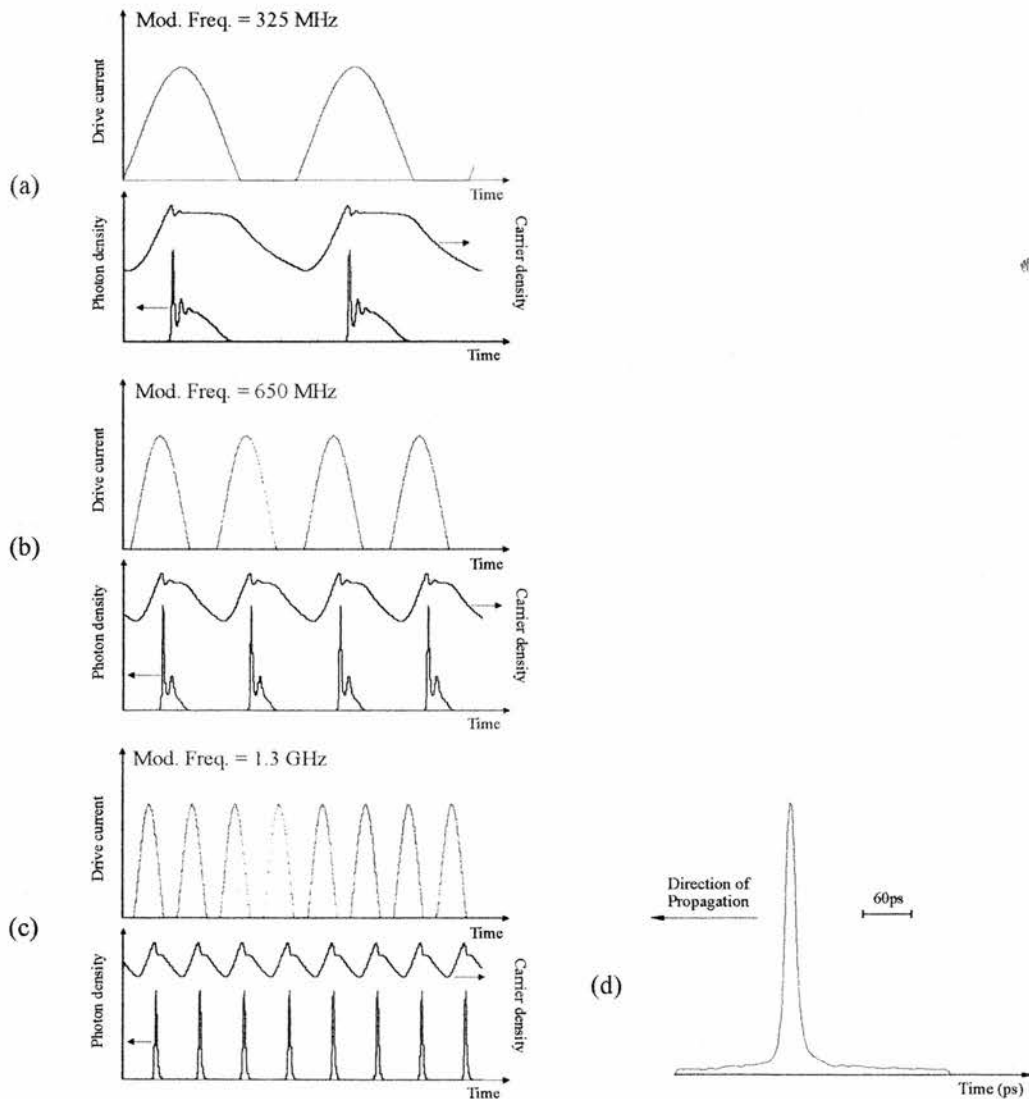


**Figure 2.7.** Theoretical model showing the response of a semiconductor diode laser to strong RF modulation: (a) 325MHz; (b) 650MHz; (c) 1.3GHz. The output from a high-frequency (1.3GHz) actively modelocked laser is shown in (d)

The pulsewidth of actively modelocked pulses decreases with increasing dc bias and increasing amplitude of the high-frequency RF current applied to the laser<sup>15,41</sup>. There is also a simultaneous increase in peak power, but this gradually decreases with increasing pulse repetition rate due to a decrease in the optical gain modulation depth. For InGaAsP devices, typical peak power lies in the range 20 to 50mW for repetition rates from 2 to 20GHz and between 0.5 to 1W at repetition rates <2GHz for GaAlAs diodes<sup>14,15,17</sup>. The dispersion of optical pulses in the diode laser and the finite gain bandwidth of the semiconductor material are generally thought to be the limiting factors on the minimum pulse width.

Figure 2.7 shows the response of a semiconductor diode laser to a current waveform comprising a strong sinusoidal component superimposed on a dc injection current. As the modulation frequency increases the number of satellite pulses decreases until a single 19ps pulse is generated at 1.3GHz.

For high-frequency modulation, subsequent filtering and re-injection of the pulse by the external cavity acts as a seeding signal, the resultant pulse being more coherent. In addition, enhanced gain saturation promotes pulse shortening. This process continues to a steady state where coherent, chirped pulses as short as ~5ps are produced<sup>42</sup>. Low-frequency modulation is characterised by the production of significant satellite pulses as noted above.

## 2.7 Subpulse suppression

Direct modulation of external-cavity modelocked semiconductor diode lasers can often result in the formation of one or more subpulses when the external cavity is adjusted for minimum pulsewidth. Low quality AR coatings can also lead to multiple-pulse output.

Secondary pulse formation is clearly evident in the streak camera profile shown in Figure 2.8. The secondary pulse arises when the pulsewidth of the modelocked pulses becomes less than the laser cavity single-trip time. Multiple pulse formation arises mainly due to dynamic detuning effects and non-ideal AR coatings where a residual

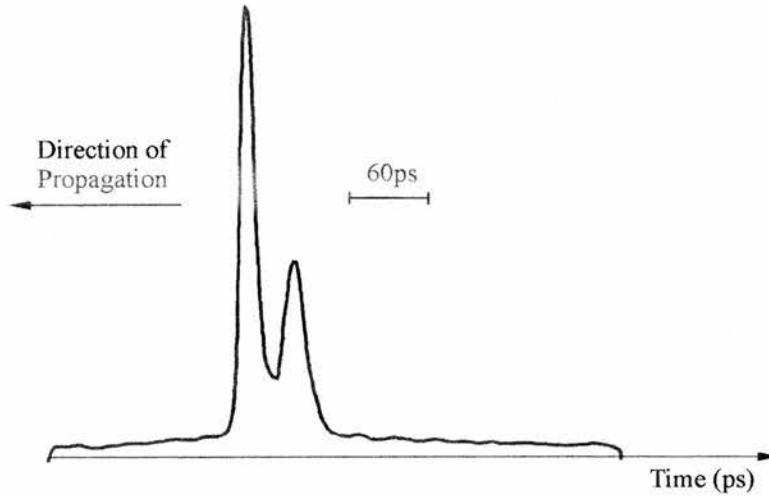


**Figure 2.8.** Temporal output of a modelocked external cavity diode laser. The RF modulation frequency is 650MHz.

reflectivity of even  $10^{-3}$  may give rise to multi-pulsing<sup>43</sup>. It is assumed that the optical pulse occurs a few picoseconds earlier than the peak of the gain (or carrier density) curve at time  $t_0$  as shown in Figure 2.9. The rising edge of the pulse depletes the carrier density via stimulated emission as it passes through the diode and the latter part of the pulse experiences reduced gain. It is this gain saturation which performs the principal pulse shaping operation. The optical pulse is then emitted and the carrier density of the gain medium is significantly reduced. Low frequency modulation of the laser means that there is sufficient time for the carrier density to recover after the initial pulse has exited the gain medium and a secondary pulse may be supported.

When the laser is driven with a large RF drive, the time at which the optical pulse is emitted occurs earlier in the current waveform. The formation of multiple pulses has been reported in several publications<sup>14,44-47</sup>. As the driving current increases, the pulsewidth reduces, but a second pulse is now produced at the cavity round-trip time. Although the AR coating results in a very small residual facet reflectivity, the reflected pulse sees a large gain and may build up to have an amplitude almost as large as the original pulse. Satellite pulse formation may be prevented by ensuring that the net gain experienced by the reflected pulse is negligible and one way of achieving this condition is by the use of multiple contact lasers. In this regime, the longer gain section of the

diode lasers is forward biased while the short section is reverse biased to provide saturable absorption.

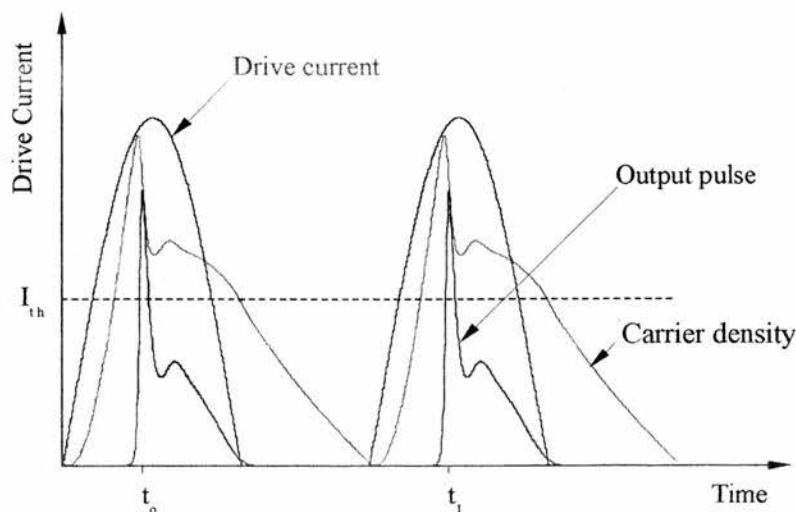


**Figure 2.9.** Multiple pulse formation in external-cavity modelocked diode lasers.

## 2.8 External cavity lasers

Active modelocking is most easily realised by placing the diode laser in an external cavity. Usually a lens is used to collect and collimate the divergent beam produced by the diode laser, and a mirror both defines the length of the external resonator and reflects the beam back to the active region of the device. The most common external resonator configurations are shown in Figure 2.10. The concave mirror geometry illustrated in (d) was used in the first two successful demonstrations of active modelocking<sup>10,48</sup>. The diffraction grating (c) and F-P etalon (b) facilitate tunability and more importantly bandwidth control. The microlensed fibre external cavity<sup>49</sup> (a) allows the production of picosecond optical pulses at relatively higher repetition rates due to potentially shorter cavity lengths. Mirrors may be directly butted<sup>50</sup> on to the end of a cleaved fibre without significant loss; alternatively, an integrated fibre mirror/filter may be employed.

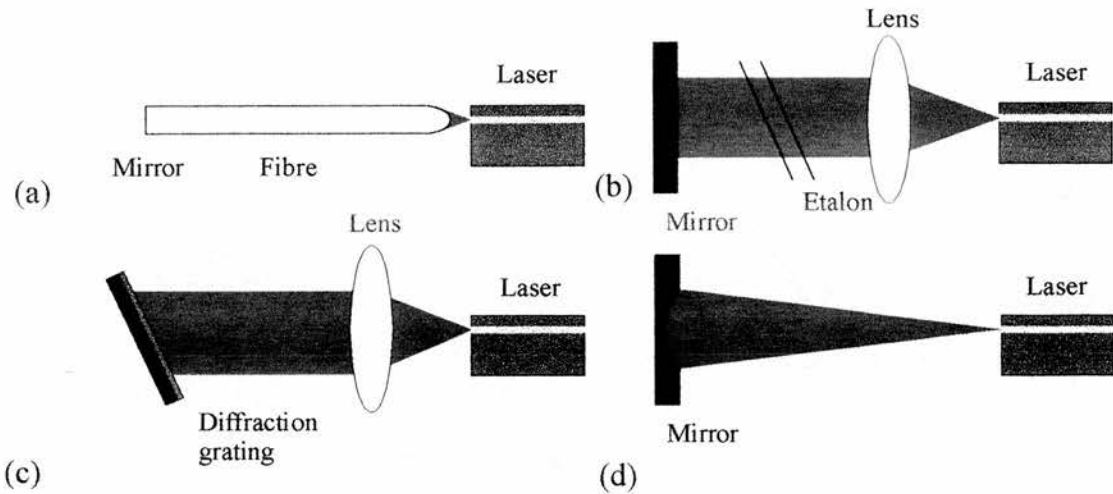


**Figure 2.10.** Modelocked semiconductor diode lasers: typical external cavity configurations incorporating (a) drawn tapered microlensed fibre; (b) etalon; (c) diffraction grating and (d) mirror.

## 2.9 Mode structure of external cavity diode lasers

When a semiconductor diode laser is operated in an external cavity a composite Fabry-Perot resonator effect is produced and this has great influence on the modelocking process such that a complex optical spectrum is created. This complex cavity effect is illustrated in Figure 2.11. A typical laser optical spectrum comprises external-cavity mode packets separated by the laser diode intermodal spacing  $\delta\nu$ . The inner facet reflectivity of the laser chip is entirely responsible for the Fabry-Perot filtering effect of the diode cavity on the resultant spectrum. If a perfect AR coating is applied to the inner facet, then the resultant spectrum is generated by the external cavity which comprises the external laser facet and the external reflector (diffraction grating, mirror or fibre-end). Inner facet reflectivity greatly influences the bandwidth available to be locked by the RF modulation. For example, in the absence of an AR coating, the bandwidth is reduced from the 20 - 30nm intrinsic gain width potentially available for locking to less than the laser cavity mode spacing of 0.3 - 0.4nm.

### 2.9.1 Modelocking in clusters

A temporal sub-structure of modelocked pulses is generated by the Fabry-Perot filtering effect in the diode laser cavity and the resonant current modulation leads to the locking of external cavity modes within each cluster of modes as shown in Figure 2.11. However, the phases of modes belonging to different clusters are randomly distributed and external cavity modes in these clusters are not locked together. As a result, the excited spectral bandwidth exceeds the bandwidth locked by the modulation. This phenomenon, known as modelocking in clusters, was analysed theoretically by Haus<sup>18</sup>, who concluded that for bandwidth-limited pulse generation of less than 20ps with no random temporal sub-structure, the Fabry-Perot filtering effect must be eliminated. The internal Fabry-Perot resonator effect can be suppressed by the reduction of the spectral bandwidth to a single-mode cluster using an external tuning element (Figs. 2.10 (b, c)) or by using either an AR coating<sup>51</sup> (of residual facet reflectivity  $<10^{-4}$ ) on the inner diode facet. Alternatively, angled-stripe amplifier structures may be employed<sup>52</sup>.

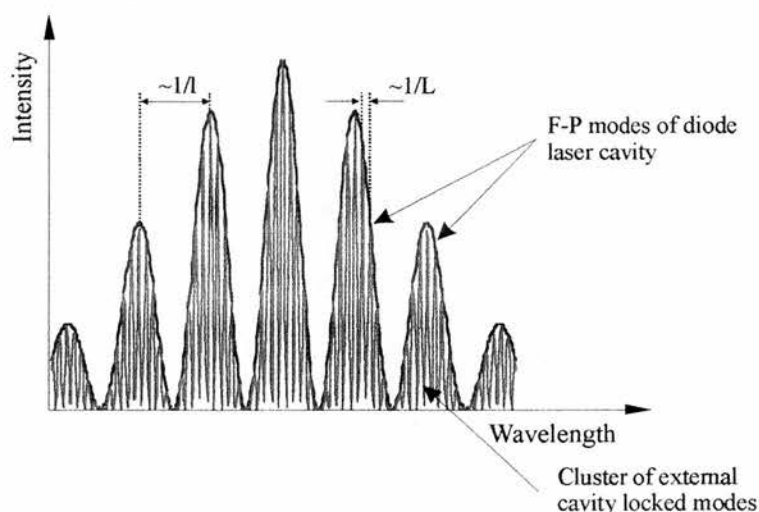


**Figure 2.11.** Modelocking of a laser diode in an external cavity in the absence of an anti reflection coating. Undulation of gain spectrum leads to locking of clusters of modes.  $l$  is the length of the laser diode;  $L$  is the external cavity length.

## 2.10 Spectral performance

In general, the output of almost all semiconductor diode lasers is highly multimode<sup>53,54</sup> due to the inherently large gain bandwidth ( $>50\text{nm}$  for InGaAsP lasers) of the devices. Figure 2.11 shows the optical spectrum of a modelocked diode laser which has no tuning element in the external cavity. There are several methods which may be used to restrict the device to single mode operation. Bandwidth-limited pulses ( $\Delta\tau\Delta\nu\sim 0.3 - 0.6$ ) may be realised<sup>1,39,55-58</sup> either by using a diffraction grating as the cavity reflector (Fig. 2.10(c)) or by placing a FP etalon in the cavity (Fig. 2.10(b)). Coherent photon seeding<sup>59</sup> may also be used to restrict the optical spectrum and allow single mode operation. In addition, DFB lasers<sup>60</sup> allow single longitudinal mode output with linewidths of typically 10MHz under strong pumping conditions.

### 2.10.1 Frequency chirp

The presence of frequency chirp<sup>61</sup> is a problem which is particularly pertinent to modelocked semiconductor diode lasers. Frequency chirp arises as a result of variations in carrier density across the duration of the pulse and the dependence of the refractive index of the active region of the laser upon the carrier density. The chirp content of modelocked diode laser pulses can be evaluated by using a wide variety of techniques including interferometric autocorrelation<sup>62</sup>, cross-correlation<sup>63</sup> or spectro-temporal analysis<sup>64</sup>. The chirp has been shown to be largely linear near the pulse peak with nonlinear components at the pulse extremities<sup>61</sup>. This suggests that the pulses can be compressed using self-phase modulation (SPM) or group-velocity dispersion (GVD) techniques.



## 2.11 Conclusions

In this chapter the behaviour of actively modelocked semiconductor lasers has been outlined. The physical process involved in the generation of modelocked picosecond pulses have been explained and practical consideration was given to the problems of subpulse suppression to enhance the available tuning range of the laser diodes. Modelocked lasers have produced ultrashort (as short as 0.6ps) pulses at very high repetition rates in excess of 300GHz and in this respect are unsurpassed by both Q-switched and gain-switched lasers. There is potential for further increases in the repetition rates since these are determined by the length of the laser cavity. However, as the repetition rate is increased, output power gradually decreases. In general, peak powers of modelocked pulses generated by InGaAsP devices are lower for than those obtained by GaAs lasers. However, output pulses may be amplified up to kilowatt peak power levels using semiconductor travelling-wave optical amplifiers with subsequent pulse compression<sup>65</sup>.

## 2.12 References

1. P.T. Ho, *Electron. Lett.* **5**, 526 (1979).
2. M.B. Holbrook, W. Sleat and D. Bradley, *Appl. Phys. Lett.*, **37**, 59 (1980).
3. J.P. Van der Ziel, "Modelocking of Semiconductor Lasers", in *Semiconductor and Semimetals*, vol. 22B, W.T. Tsang, Ed., New York: Academic (1985).
4. A. Ollsen and C.L. Tang, *IEEE J. Quantum Electron.*, **QE-17**, 1977 (1981).
5. K. Lau and A. Yariv, *Appl. Phys. Lett.*, **46**, 326 (1985).
6. K.Y. Lau and I. Ury, *Appl. Phys. Lett.*, **46**, 1117 (1985).
7. R.S. Tucker, S.K. Korotky, G. Eisenstein, U. Koren, L.W. Stulz and J.J. Veselka, *Electron. Lett.* **21**, 239 (1985).
8. S.W. Corzine, J.E. Bowers, G. Przybylek, U. Koren, B.I. Miller and C.E. Socolich, *Appl. Phys. Lett.*, **52**, 348 (1988).
9. R.S. Tucker, U. Koren, G. Raybon, C.A. Burrus, B.I. Miller, T.L. Koch, G. Eisenstein and A. Shahar, 11<sup>th</sup> IEEE Int. Semiconductor Laser Conf., Boston, MA, paper PD5 (1988).
10. P.T. Ho, L.A. Glasser, E.P. Ippen and H.A. Haas, *Appl. Phys. Lett.* **33**, 241 (1978).
11. A. Morimoto, T. Kobayashi and T. Sueta, *IEEE J. Quantum Electron.*, **QE-24**, 94 (1988).
12. M.S. Demokan, *International J. of Electron.*, **60**, 67 (1986).
13. M. Schell, A.G. Weber, E.H. Bottcher, E. Scholl and D. Bimberg, *IEEE J. Quantum Electron.*, **QE-27**, 402 (1991).
14. J.E. Bowers, P.A. Morton, A. Mar and S.W. Corzine, *IEEE J. Quantum Electron.*, **QE-25**, 1426 (1989).
15. J.P. Van der Ziel, *J. Appl. Phys.*, **52**, 4435 (1981).
16. A.J. Lowery, *IEEE Proc. J.*, **136**, 264 (1989).
17. P.P. Vasil'ev and V.N. Morozov, *Sov. J. Quantum Electron.*, **15**, 211 (1985).
18. H.A. Haus, *J. Appl. Phys.*, **51**, 4042 (1980).
19. K.Y. Lau, *IEEE J. Quantum Electron.*, **QE-26**, 250 (1990).
20. J.C. AuYeung, *IEEE J. Quantum Electron.*, **QE-17**, 398 (1981).
21. G.J. Aspin and J.E. Carrol, *Solid State and Electron Devices*, **3**, 220 (1979).
22. G. Raybon, P.B. Hansen, U. Koren, B.I. Miller, M.G. Young, M. Newkirk, P.P. Iannone, C.A. Burrus, J.C. Centanni and M. Zirngibl, *Electron. Lett.*, **28**, 2220 (1992).
23. D.M. Bird, R.M. Fatah, M.K. Cox, P.D. Constantine, J.C. Regnault and K.H. Cameron, *Electron. Lett.*, **26**, 207 (1990).

24. R.S. Tucker, U. Koren, G. Raybon, C.A. Burrus, B.I. Miller, T.L. Koch and G. Eisenstein, *Electron. Lett.*, **25**, 621 (1991).
25. A.G. Deryagin, D.V. Kuksenkov, V.I. Kuchinskii, E.L. Portnoi and I. Yu. Khrushchev, *Electron. Lett.*, **30**, 309, (1994) Int SL Conf., Hawaii '94, P13.
26. S. Sanders, L. Eng, L. Paslaski and A. Yariv, *Electron. Lett.*, **26**, 310 (1990).
27. D.J. Derickson, R.J. Helkey, A. Mar, J.R. Karin, J.E. Bowers and R.L. Thornton, *IEEE Photon. Technol. Lett.*, **4**, 333 (1992).
28. E.M. Dianov and O.G. Okhotnikov, *IEEE Photon. Technol. Lett.*, **3**, 499 (1991).
29. K. Watanabe, H. Iwamura and Y. Yamamoto, *Opt. Lett.*, **18**, 1642 (1993).
30. Y.K. Chen, M.G. Wu, T. Tanbun-Ek, R.A. Logan and M.A. Chin, *Appl. Phys. Lett.*, **58**, 1253 (1991).
31. M.C. Wu, Y.K. Chen, T. Tanbun-Ek, R.A. Logan and M.A. Chin, *IEEE Photon. Technol. Lett.*, **3**, 874 (1991).
32. J.H. Zarrabi, E.L. Portnoi and A.V. Chelnokov, *Appl. Phys. Lett.*, **59**, 1526 (1991).
33. L.R. Brovelli and H. Jackel, *Electron. Lett.*, **27**, 1104 (1991).
34. P.G. May and M. Bierbaum, *IEEE Photon. Technol. Lett.*, **3**, 296 (1991).
35. P.P. Vasil'ev, V.N. Morozov, Y.M. Popov and A.B. Sergeev, *IEEE J. Quantum Electron.*, **22**, 149 (1986).
36. R.L. Fork, B.I. Green and C.V. Shank, *Appl. Phys. Lett.* **38**, 671 (1981).
37. K.Y. Lau, *J. Lightwave Technol.*, **7**, 400 (1989).
38. H.A. Haus, *Waves and Fields in Optoelectronics*, Prentice-Hall, Englewood Cliffs, NJ (1984).
39. Y.L. Bessonov, A.P. Bogatov, P.P. Vasil'ev, V.N. Morozov and A.B. Sergeev, *Sov. J. Quantum Electron.*, **12**, 1510 (1982).
40. J.C. AuYeung and A.R. Johnson, *Appl. Phys. Lett.* **40**, 112 (1982).
41. P.A. Morton, R.J. Helkey, E. Scholl and D. Bimberg, *IEEE J. Quantum Electron.*, **QE-25**, 2621 (1989).
42. G. Eisenstein, R.S. Tucker, U. Koren and S.K. Korotky, *IEEE J. Quantum Electron.*, **QE-22**, 142 (1986).
43. M. Schell, A.G. Weber, E. Scholl and D. Bimberg, *IEEE J. Quantum Electron.*, **QE-27**, 1661 (1991).
44. J.P. Van der Ziel, R.A. Logan and R.M. Mikulyak, *Appl. Phys. Lett.* **39**, 867 (1981).

45. P.P. Vasil'ev, V.N. Morozov, Yu.M. Popov and A.B. Sergeev, *IEEE J. Quantum Electron.*, **QE-22**, 149 (1986).
46. J.P. Van der Ziel, W.T. Tsang, R.A. Logan, R.M. Mikulyak and W.M. Augustyniak, *Appl. Phys. Lett.* **39**, 525 (1981).
47. H. Yokoyama, H. Ito and H. Inaba, *Appl. Phys. Lett.* **40**, 105 (1982).
48. L.A. Glasser, *Electron. Lett.*, **14**, 725 (1978).
49. G. Wenke and Y. Zhu, *Appl. Opt.*, **22**, 3837 (1983).
50. D. Markuse and J. Stone, *J. Lightwave Tech.*, **LT-4**, 377 (1986).
51. N.A. Olsson, M.G. Olberg, L.D. Tzeng and T. Cella, *Electron. Lett.*, **24**, 569 (1988).
52. W. Rideout, R. Holmstrom, J. LaCourse, E. Meland and W. Powazinik, *Electron. Lett.*, **26**, 37 (1990).
53. G.H.B. Thompson, *Physics of Semiconductor Laser Devices*, Chichester: John Wiley & Sons (1980).
54. R.P. Salathe, *Appl. Phys. Lett.* **20**, 1 (1979).
55. A.J. Lowery, N. Onodera and R.S. Tucker, *IEEE J. Quantum Electron.*, **QE-27**, 2422 (1991).
56. D.J. Bradley, M.B. Holbrook and W.E. Sleat, *IEEE J. Quantum Electron.*, **QE-17**, 658 (1981).
57. P.P. Vasil'ev, V.N. Morozov and A.B. Sergeev, *IEEE J. Quantum Electron.*, **QE-21**, 576 (1985).
58. S. Lundqvist, T. Andreasson and S.T. Eng, *Appl. Phys. Lett.* **43**, 715 (1983).
59. H. Kawaguchi and A.K. Sarwar, *Appl. Phys. Lett.* **62**, 2164 (1993).
60. S. Akiba, M. Usami and K. Utaka, *J. Lightwave Tech.*, **LT-5**, 1564 (1987).
61. C. Lin, C.P. Lee and C.A. Burrus, *Appl. Phys. Lett.* **42**, 141 (1983).
62. K.L. Sala, G.A. Kenny-Wallace and G.E. Hall, *IEEE J. Quantum Electron.*, **QE-16**, 990 (1980).
63. J.-C.M. Diels, J.J. Fontaine, I.C. McMichael and F. Simoni, *Appl. Opt.*, **24**, 1270 (1985).
64. A.S. Hou, R.S. Tucker and E.P. Ippen, *Ultrafast Phenomena VII*, C.B. Harris, E.P. Ippen, G.A. Mourou and A.H. Zewail, Eds., Berlin: Springer, 14 (1990).
65. P.J. Delfyett, L.T. Florez, N. Stoffel, T. Gmitter, C. Andreadakis, Y. Silverberg, J.P. Heritage and G.A. Alphonse, *IEEE J. Quantum Electron.*, **QE-28**, 2203 (1992).

# Chapter 3

## DUAL-WAVELENGTH EXTERNAL-CAVITY SEMICONDUCTOR LASERS

### 3.1. Introduction

Wavelength multiplexing offers great potential for increasing the information capacity of single-mode optical fibres, and also enhances system design and flexibility<sup>1-5</sup>. Implementation of multiple wavelength sources has until now involved the use of either separate light sources for each channel which are then combined using a wavelength multiplexing component<sup>6</sup>, or by using hybrid dual-wavelength semiconductor lasers<sup>7</sup>. Alternative laser designs have also been reported which produce tuneable multiple wavelength operation from a single gain medium. The most notable of these include a multichannel grating cavity (MGC) laser which comprises an external-cavity laser incorporating an array of reflective light modulators to electronically select the single operating wavelength of the device<sup>8</sup>. A second example is a tuneable acousto-optic filter in conjunction with an AO modulator inside an external-cavity GaAlAs semiconductor laser<sup>9</sup>. A third possibility is a compound fibre-ring cavity with a single erbium-doped fibre amplifier where each constituent cavity has a separate bandpass filter and attenuator<sup>10</sup>. Such laser configurations all have limitations in terms of system complexity and in their ability to produce multiple wavelength operation in both continuous-wave (cw) and modelocked regimes. Problems are also anticipated in generating synchronised pulse trains from the fibre-based laser of ref.10 since cavity length adjustment is problematic and each cavity may require a separate modelocking element due to the long upper-state lifetime typical of erbium-doped fibres.

In this chapter a simple optical arrangement capable of pulsed and cw dual-wavelength operation using a single semiconductor laser is described. The two

wavelength components, which are spatially overlapped and of the same polarisation, may be independently tuned over a large spectral range, which is limited only by the laser gain spectrum. This wavelength tunability highlights the added flexibility of this laser system and its potential as a test source for laboratory based optical transmission experimentation and for a variety of measurements of the characteristics of opto-electronic components.

### 3.2. The dual-wavelength modelocked laser system

The laser source was a single-contact buried-heterostructure InGaAsP Fabry-Perot semiconductor diode. The diode back facet was coated with a two-layer, broadband, anti-reflection coating (residual reflectivity  $\sim 0.12\%$ ). The cleaved front facet was uncoated giving a reflectivity of  $\sim 35\%$ . Light output from the AR coated facet was optically coupled into the external cavity via a x20 microscope objective lens (N.A. = 0.5) as shown in Figure 3.1. The external-cavity laser threshold current was measured at 20mA at 1563nm. Variation of the threshold current with wavelength for a single-grating external cavity is shown in Figure 3.2. The dual-wavelength laser configuration comprised a 50/50 beamsplitter giving two independent cavity arms (arm A and arm B). Each arm was terminated with a

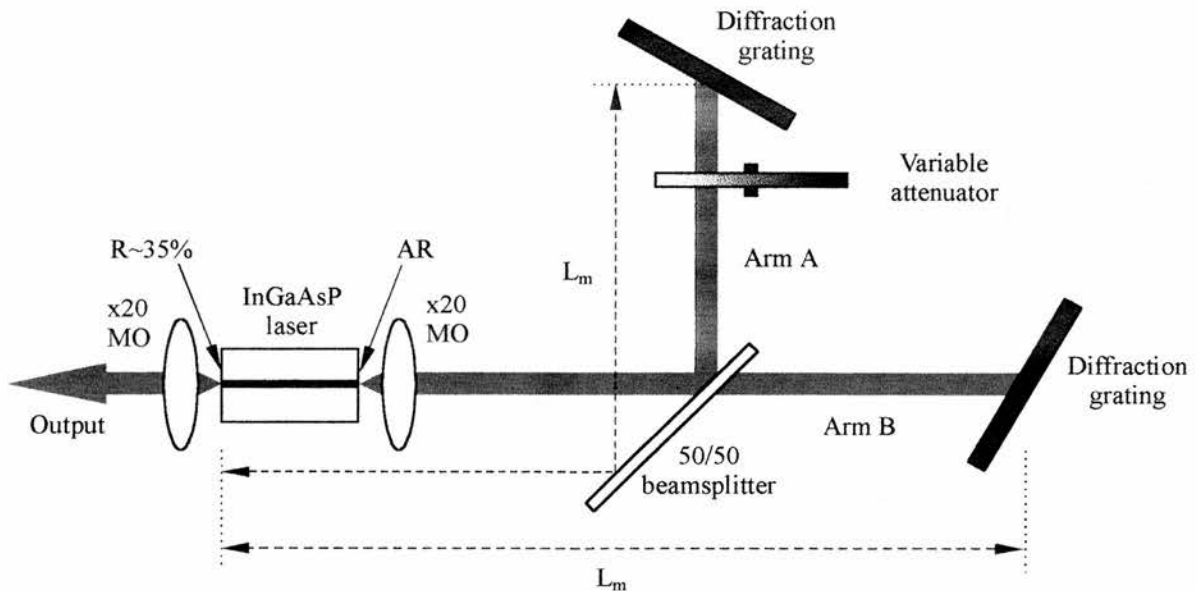
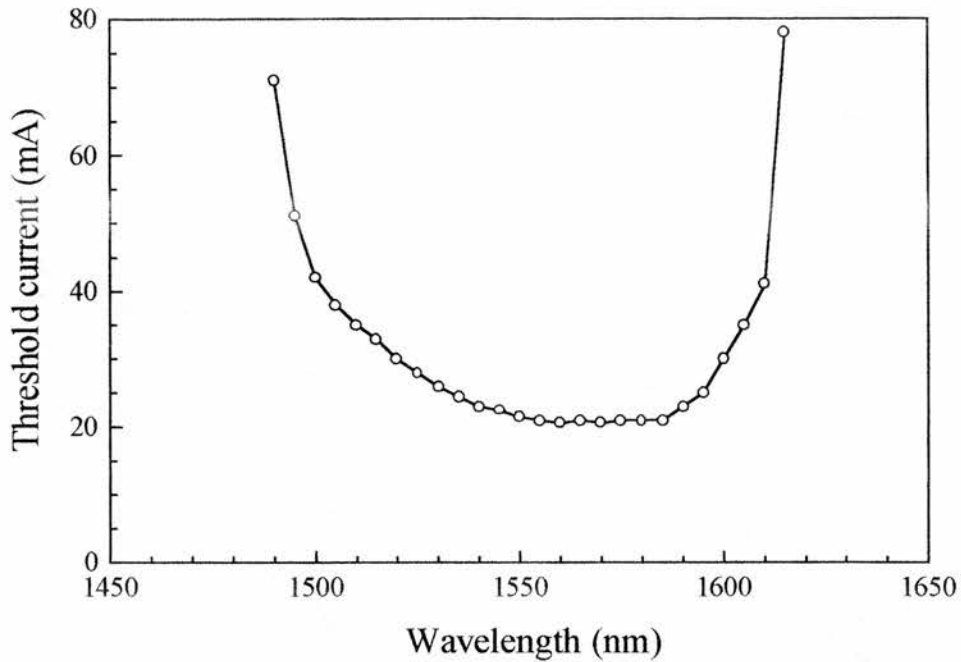


Figure 3.1. Experimental layout for the production of dual-wavelength modelocked pulses.



**Figure 3.2.** Variation of threshold current with wavelength for single-cavity operation. Wavelength selectivity is achieved via the terminating diffraction grating.

diffraction grating (600 lines/mm, blaze wavelength =  $1.6\mu\text{m}$ ) giving independent wavelength selectivity and tunability.

Active modelocking was realised by superimposing a strong RF modulation signal onto a sub-threshold dc bias current<sup>11</sup>. A modulation frequency of 640MHz was chosen corresponding to the 2nd harmonic modelocking frequency for a cavity length  $L_m$  of approximately 47.0cm. A 20dBm RF modulation was applied and dc current was varied between 14 and 33mA because of the current dependence of the oscillation wavelength. Initially each cavity was separately modelocked while the alternate cavity was blocked to ensure that the optical path length of each arm was identical. The oscillation wavelength of each laser cavity (observed using a scanning Fabry-Perot interferometer) was tuned to the semiconductor laser gain peak such that the external cavity operated as a Michelson interferometer. In this interferometric regime the threshold current was reduced to  $\sim 20\text{mA}$  and the laser output demonstrated acute sensitivity to small variations in the path length of the two coupled cavities. (Variation of  $\sim 0.4\mu\text{m}$  in cavity length was sufficient to produce



complete switching of the interferometer from transmission to reflection). Dual-wavelength operation was then implemented via independent tuning of either, or both, diffraction gratings. A variable attenuator was introduced into the cavity arm exhibiting the lower threshold in order to reduce the possibility of either wavelength component dominating the laser output. Thus the output power of each wavelength component was equalised by collimating onto the gratings. The attenuation was routinely adjusted to counteract cavity misalignment effects produced by environmental disturbances (section 3.4).

### 3.3. Dual-wavelength oscillation

The performance of the laser system was evaluated to determine the spectral separation of the two wavelength components, the temporal quality of output

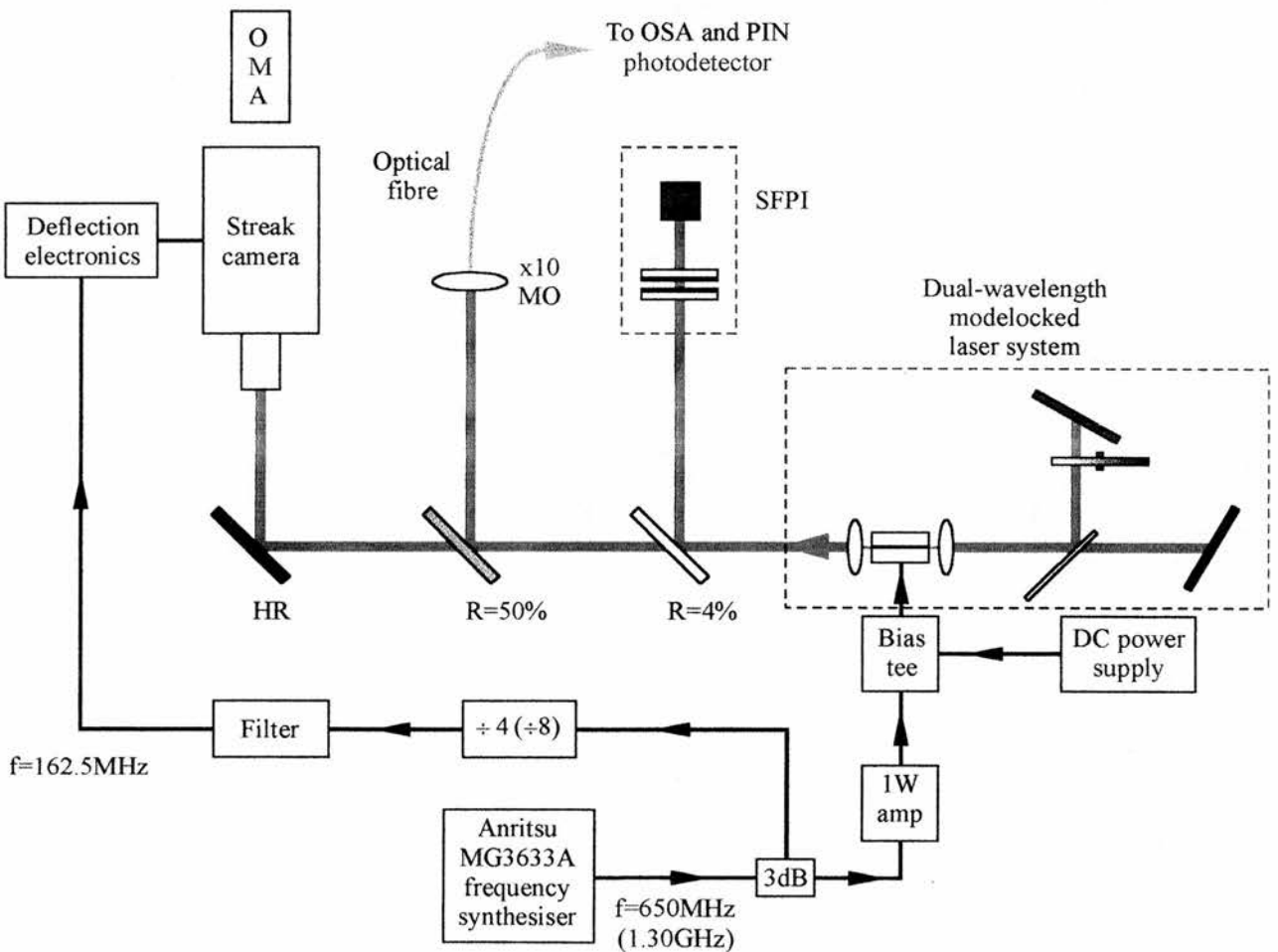


Figure 3.3. Experimental layout and diagnostics for the dual-wavelength external-cavity laser.



modelocked pulses, and the system stability. The diagnostic regime is shown in Figure 3.3.

### 3.3.1 Spectral and temporal characteristics

The external-cavity diffraction gratings were adjusted to initiate dual-wavelength oscillation at 1558 and 1563nm. Spectral and temporal profiles for dual-wavelength operation are shown in Figs 3.4 (c) and (f) respectively. Corresponding traces for single wavelength operation at 1558nm are illustrated in Figs 3.4 (a) and (d) respectively. Operational characteristics at 1563nm are given in Figs 3.4 (b) and (e).

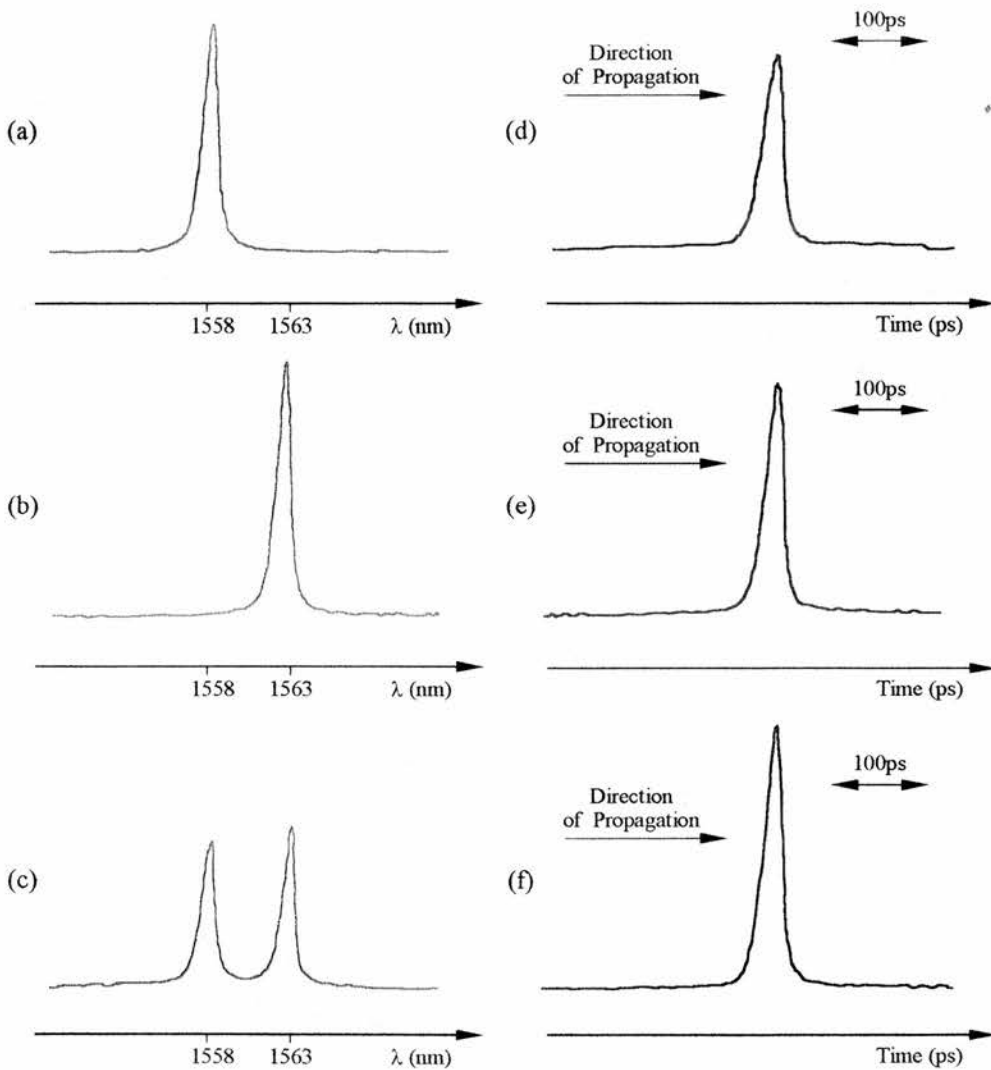


**Figure 3.4.** Dual-wavelength modelocked laser operation at 640MHz: spectral and temporal profiles at 1558nm (a) & (d); 1563nm (b) & (e); dual-wavelength operation at 1558nm & 1563nm (c) & (f).

Since laser oscillation was produced simultaneously at two separate wavelengths, interferometric effects (section 3.3.3) were eliminated, and in this way the sensitivity of the laser to environmental factors was substantially reduced. Adjustment of the variable attenuator in the low-loss cavity arm provided continuous optical power equalisation in both wavelength components. In general, an increase in power in one wavelength component induced a corresponding reduction in the second component such that the total output power virtually unchanged at 23mW (sections 3.5 and 3.6). Output power of equal proportion for each wavelength was maintained throughout at ~23mW.

Spectral and temporal characteristics of the laser were recorded using the scanning Fabry-Perot interferometer or OSA and synchronously operating streak camera<sup>7</sup> systems. Dual-wavelength spectral and temporal profiles are shown in Figures 3.4(c) and (f) respectively. Optical pulse duration was in the 15 to 25ps range. Output pulse characteristics remained unchanged over a number of hours with the implementation of neither active or passive stabilisation.

Figures 3.4(a) and (d) show the optical and temporal profiles for single cavity operation for which the short wavelength component alone (1558nm) was allowed to oscillate. No apparent shift in either wavelength or temporal position was observed. The temporal profile and pulsewidth were unchanged during the transition from single to dual-wavelength operation (see Figures 3.4(d) and (f)). Similar behaviour was also observed when the long wavelength component was permitted to oscillate in isolation as shown in Figures 3.4(b) and (e).

Cavity length equalisation was maintained at all times since any relative time delay between the two pulses entering the gain medium produced either poor pulse quality or single-wavelength oscillation only. For large relative delays the leading pulse depleted the gain sufficiently such that the delayed pulse was unable to persist and single-wavelength output was generated. For small changes in the length of one cavity arm, dual-wavelength operation was maintained. However positive detuning in a single arm produced pulse broadening and decreased peak power whilst negative detuning resulted in satellite pulsation as shown in Figure. 3.5. It should be

noted that the above phenomena are a general feature of actively-modelocked lasers and are not specific to the dual-wavelength systems.

### **3.3.2 High-frequency operation: long and short pulses**

Figure 3.6 shows the temporal and spectral profiles for active modelocking at 1.28GHz. Both cavity arms were positively detuned to produce broad or long pulses (~12ps duration). Temporal pulse profiles for single- and dual-wavelength operation are shown in Figure 3.6(a), (b) and (c). As before, there was minimal change in pulse profile for dual-wavelength operation. Spectral performance is shown in Figure 3.6(d): spectral separation was 8nm with power distributed equally between the two pulses. Peak output power was 82mW and the time-bandwidth product  $\Delta\tau \Delta\nu = 0.38$ .

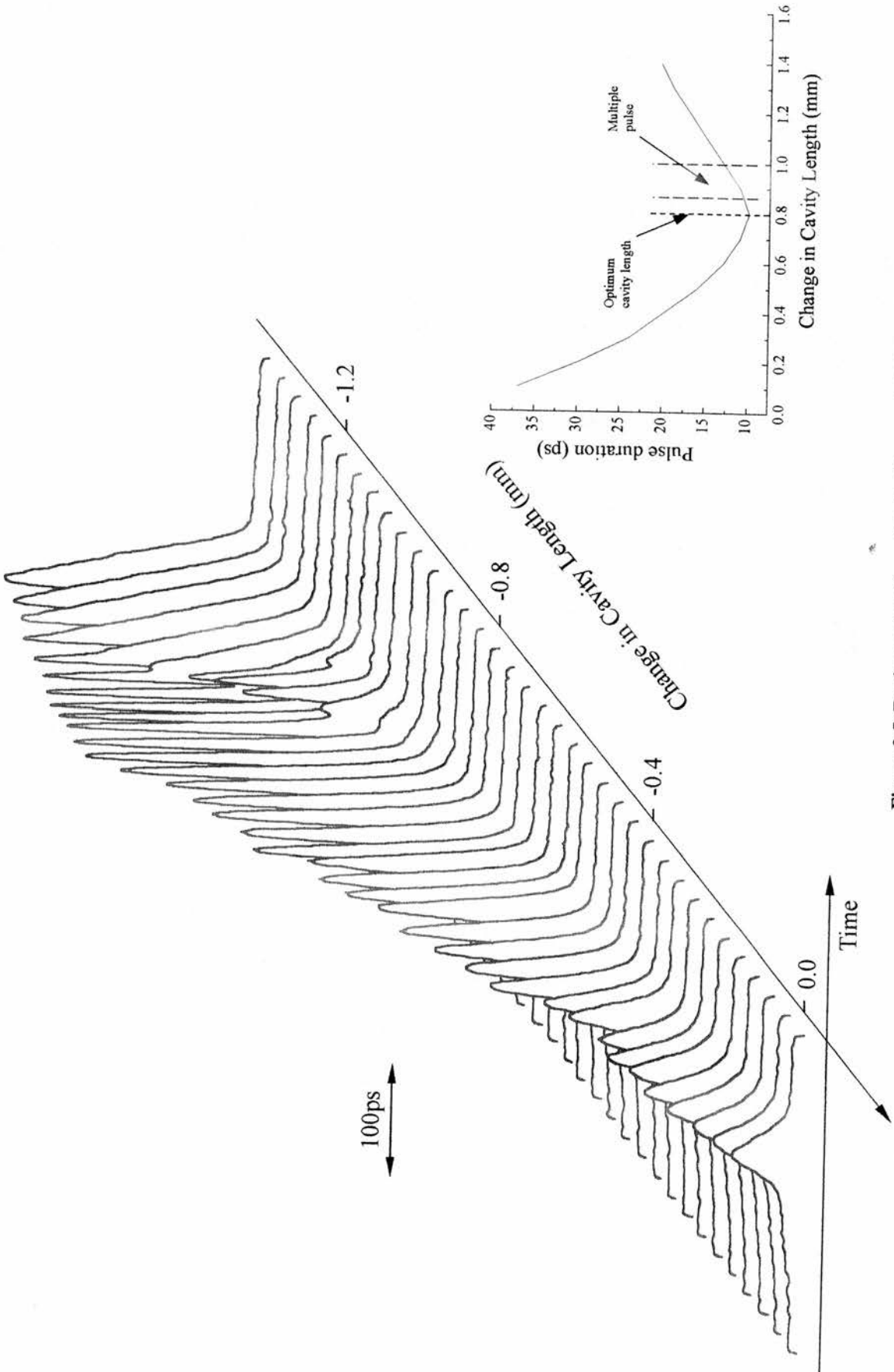
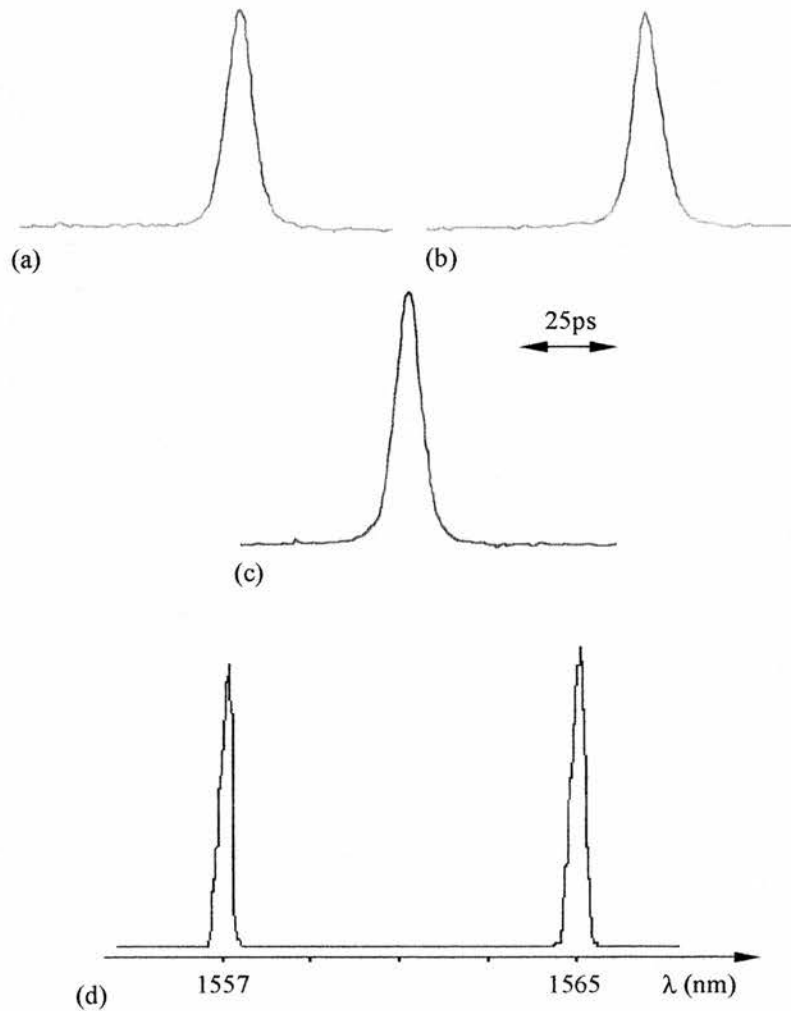


Figure 3.5. Dual-wavelength modelocked laser at 1.28GHz: single arm detuning.



**Figure 3.6.** Dual-wavelength modelocking at 1.28GHz: long pulse. Temporal profiles (a) arm A (1557nm); (b) arm B (1565nm); (c) arm A & arm B (dual-wavelength operation); (d) spectral output.

Short pulse operation at 1.28GHz is shown in Figure 3.7. In this case, both cavities were detuned to produce the shortest possible pulsewidth ( $\sim 4$ ps). Temporal pulse profiles for arm A, arm B and for dual-wavelength operation are shown in Figures 3.7(a), (b) and (c) respectively. Spectral separation in this case was 14.1nm with even power distribution between the two wavelengths (Figure 3.7(d)).

The system was then adjusted to produce a long pulse in arm A and a short pulse in arm B. The arm having the lower threshold current (arm B) dominates and the variable attenuator is placed in this arm. The output is a short temporal pulse at

1565nm (Fig. 3.8). As loss is introduced into arm B via the attenuator, the power distribution between the two arms is altered. The increasing influence of the long pulse in arm A (1557nm) results in dual-wavelength operation and pulse broadening, although the long pulse in arm B still dominates. This process continues, with a gradual shift in power distribution from arm B to arm A. Finally, the short pulse in arm B is completely attenuated and the output is a broad, single-wavelength temporal pulse at 1557nm produced by arm A. Spectral separation was 8nm and the relative power distribution between the two wavelength components is illustrated in Figure 3.8(b).

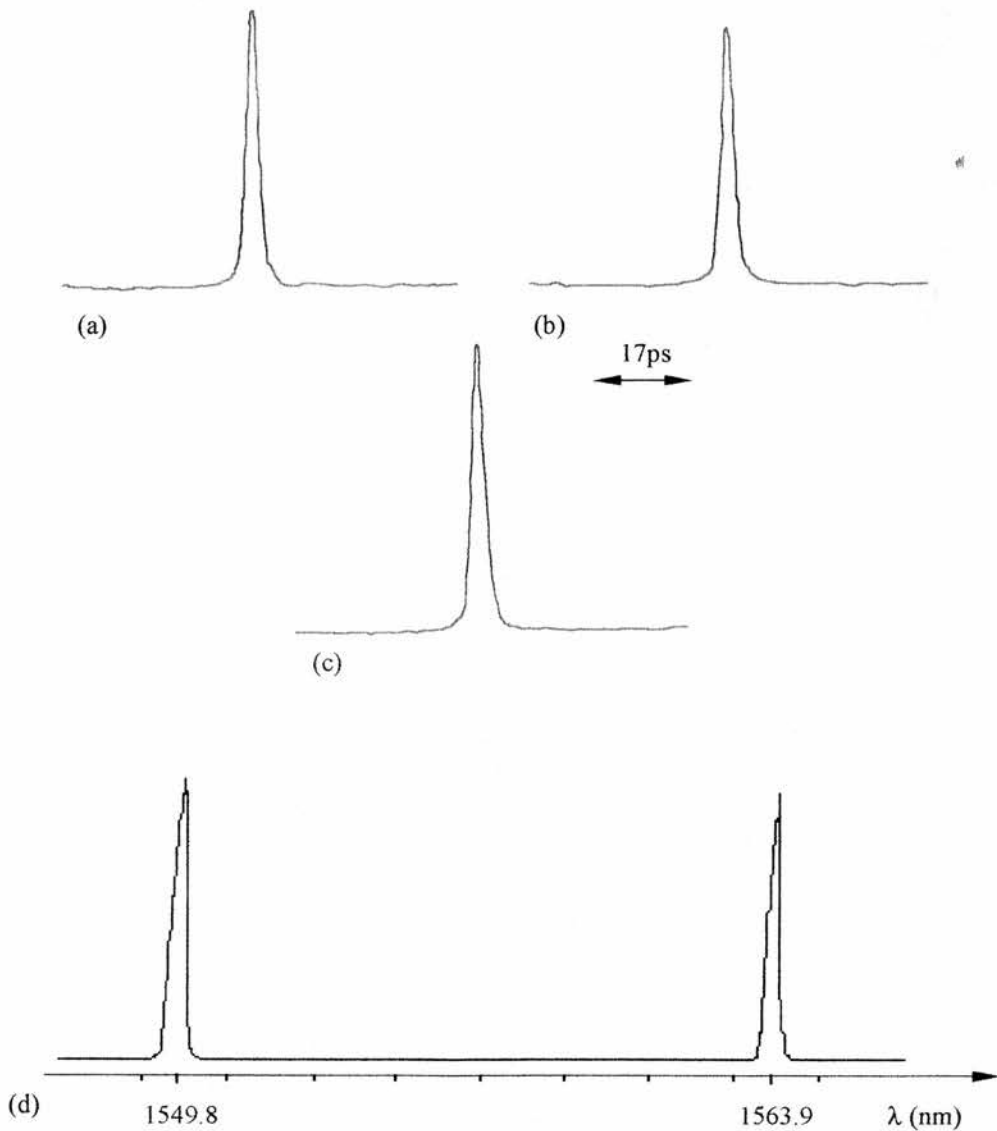


**Figure 3.7.** Dual-wavelength modelocking at 1.28GHz: short pulse. Temporal profiles (a) arm A (149.8nm); (b) arm B (1563.9nm); (c) arm A & arm B (dual-wavelength operation); (d) spectral output.

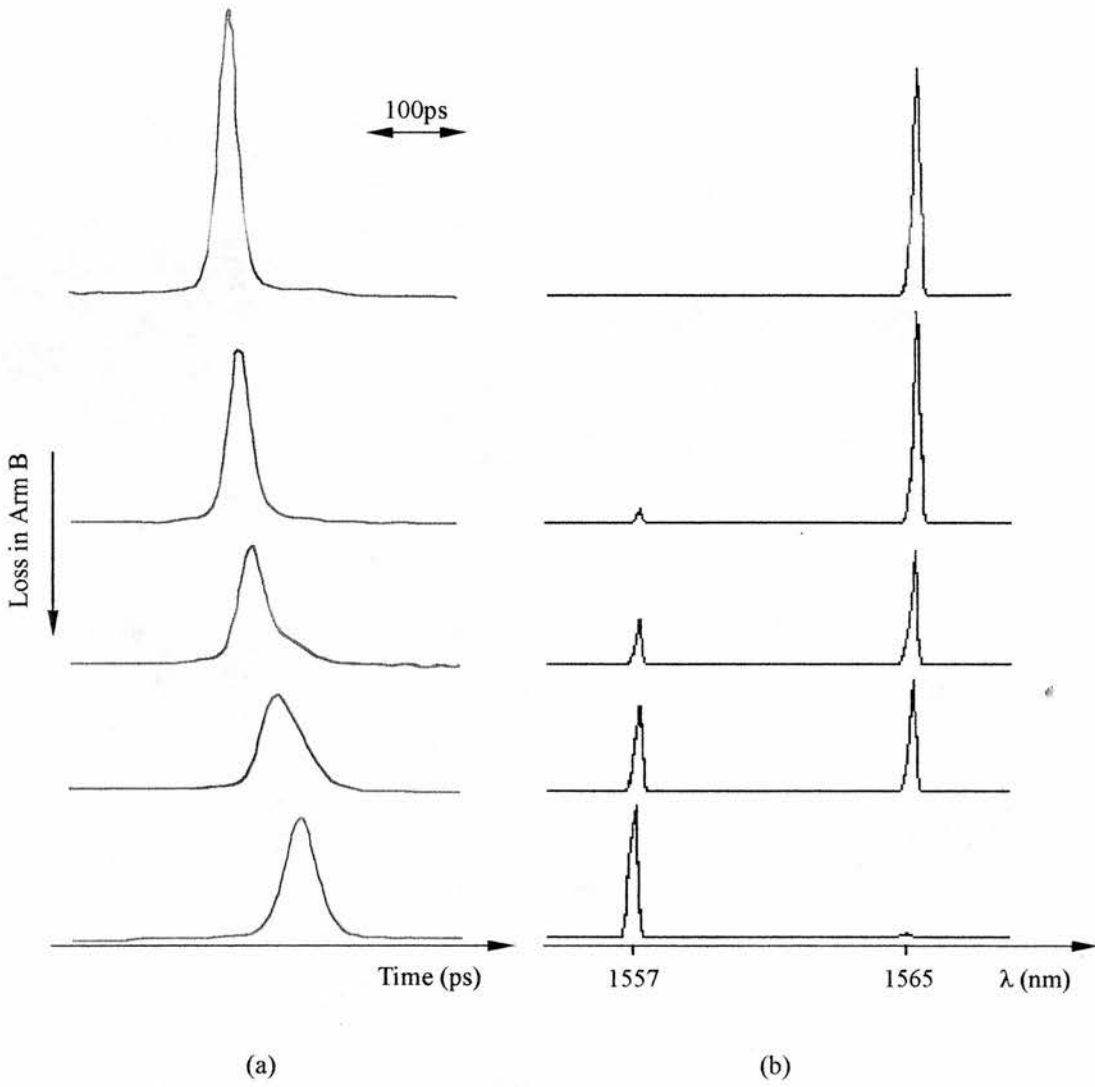


**Figure 3.8.** Dual-wavelength modelocking at 1.28GHz: long and short pulse. Temporal (a) and spectral (b) profiles for laser oscillation at 1557 and 1565nm. Starting with a short pulse at 1565nm in arm B and no contribution from arm A, loss is slowly introduced into arm B. There is a gradual shift in power distribution between arms A and B until a long pulse is produced at 1557nm in arm A when arm B is completely blocked.

### 3.3.3 Spectral separation

A gradual increase in the separation of the two wavelength components was achieved via diffraction grating rotation. Maximum spectral separation was determined by the symmetrical location of the two oscillating wavelength components at either side of the semiconductor gain envelope. A dc bias current increase resulted in an associated increase in the spectral gain window of the laser diode and maximum wavelength separation was increased. For a drive current of 30mA the maximum separation was 55nm. An alternative method of assessing the tuning range was realised by tuning the lower loss cavity arm to the peak of the semiconductor laser gain while the grating in the second arm was aligned to select a range of wavelength settings. Again, by balancing the effective round-trip loss for each wavelength component, a maximum spectral separation of ~55nm was obtained, at a bias current of 33mA. Minimum spectral separation was also examined since this parameter governs important optical communication issues relating to demultiplexing capability and signal crosstalk. As previously described, symmetrical variation of the two wavelength components about the gain peak produced a minimum wavelength separation of 0.5nm. A separation of 0.16nm was measured using the Fabry-Perot interferometer. Since the minimum spectral separation of the two wavelength components of the output was limited only by the pulse bandwidth, a separation of 0.5nm represents the point where the extremities of the two spectral components begin to overlap.

### 3.3.4 CW operation: wavelength tuning

A similar continuous wavelength tuning range was for non-modelocked, or continuous-wave operation, although the relative stability of the two wavelength components was inferior to that of the modelocked case. Single arm adjustment of the system produced a tuning range of 71nm for an injection current of 45mA (Figure 3.9) compared with 108nm for the same current for the single cavity laser (Figure 3.2).



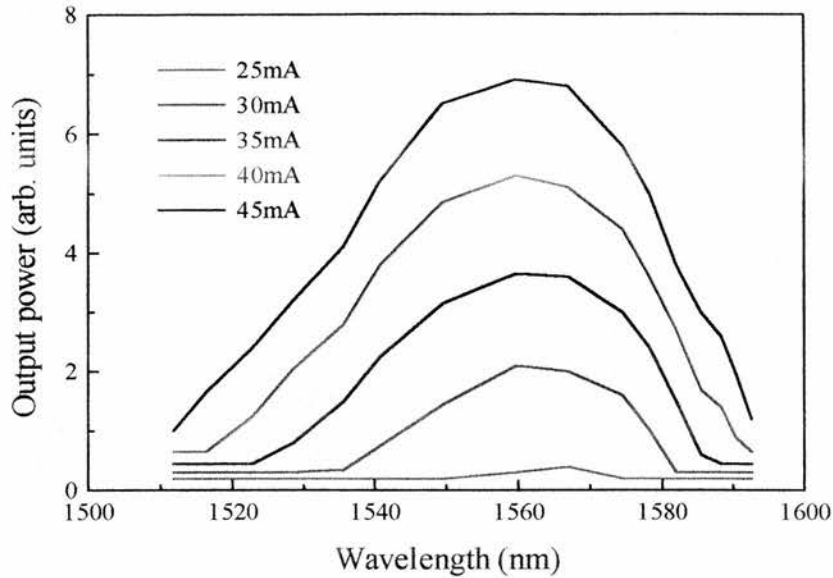


**Figure 3.9.** CW laser: single arm tuning. The tuning range is 1512 - 1593nm at  $I = 45\text{mA}$  (1500 - 1608nm at  $I = 45\text{mA}$  without the beamsplitter).

Comparison of the relative tuning range of both arms is shown in Figure 3.10. Dual-wavelength operation was possible for wavelength separations of up to 80nm. A typical spectral output obtained in the cw mode of operation is shown in Figure 3.11 where the two oscillating wavelength components are centred at 1565.8 and 1567.3nm respectively, and the uneven power distribution between each spectral component reflects the non-optimum adjustment of the intracavity attenuator. It is anticipated that the spectral separation can be made sufficiently small such that a fast photodiode/spectrum analyser arrangement could be used to measure the electrical beat signal, thus enabling the unambiguous measurement of small spectral separations. Further analysis of dual-wavelength semiconductor laser systems operating at very small spectral separation would enable details of the dynamics of the gain medium to be investigated. Such a system, suitably amplified, would also provide a useful source of high-speed microwave and/or mm-wave radiation.

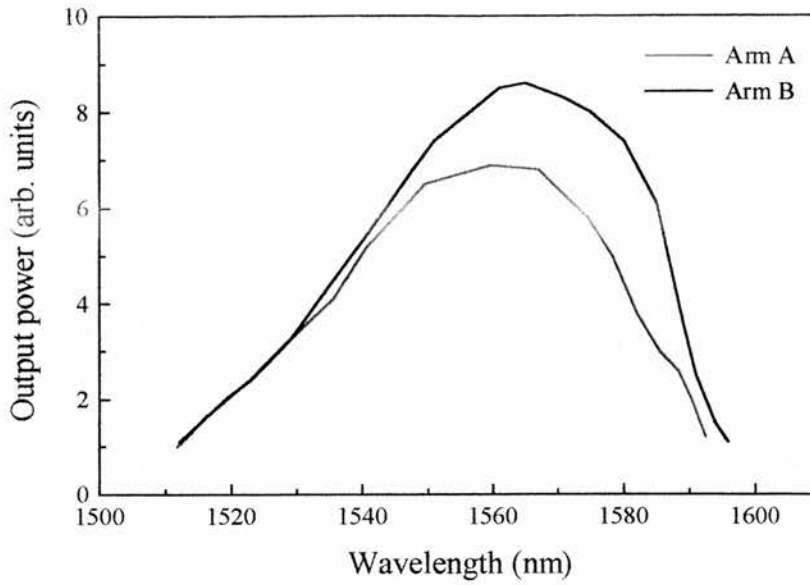


**Figure 3.10.** Comparison of arm A and arm B tuning for  $I = 45\text{mA}$ . Dual-wavelength oscillation is possible over wavelength separations of up to 80nm

### 3.4 System stability and noise performance

The output power stability is an important feature of the performance of any laser system, and this is particularly true for dual-wavelength lasers. For this reason the total and relative power stability of the two-colour semiconductor laser was examined. A simple enclosure protected the laser system from atmospheric turbulence and this arrangement significantly improved the cw laser stability to the extent that performance was comparable to that of the unprotected modelocked system. System stability was investigated by splitting the output beam into two components. One component was detected directly using a photodetector and served as a indicator of the total optical power. The second beam was monitored via a monochromator/photodetector combination which measured power fluctuations in one arm of the dual-wavelength laser. Thus, the relative power of both wavelength components was measured and compared with the total output power. Figure. 3.12 details the short and long term stability of the output power of the dual-wavelength laser, where the upper trace represents the total output power, and the lower trace

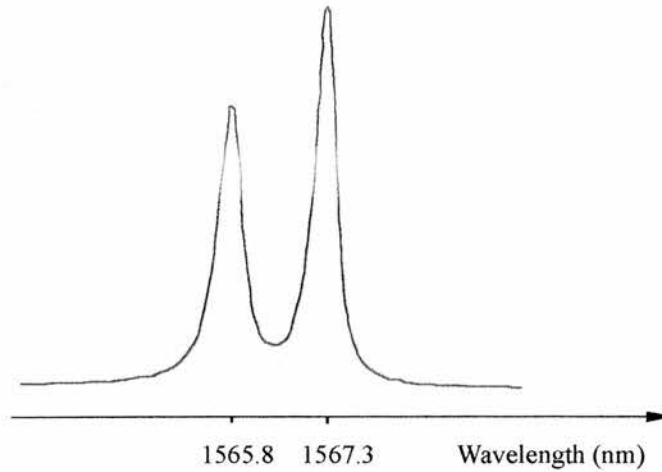


**Figure 3.11.** Spectral output in the continuous-wave regime. Wavelength separation,  $\Delta\lambda=1.5\text{nm}$  for a bias current of 30mA. The unequal power content at each wavelength shows the variation in power distribution possible by simple attenuator adjustment.

indicates the simultaneously recorded power of the long-wavelength component (1563nm). Scan times of 10ms (Figure 3.12(a)) and 1000s (Figure 3.12(b)) clearly illustrate that dual-wavelength oscillation does not involve significant power instability. However, this is merely an indication of the stability of the laser environment: only the addition of the enclosure contributed towards system stability.

Inherent instability can exist in this type of external-cavity laser. However, such instability was apparent only when the laser was misaligned or was subjected to a deliberately unstable environment (Figure 3.13). A scan time of 200ms was used for data acquisition during the application of a mechanical disturbance to the optical bench. It can be clearly seen that the fluctuations of the total output power were considerably smaller than the percentage change in the power of the monitored wavelength component. It is clear that the mechanical disturbance substantially altered the power distribution between the two wavelength components whereas the total output power was influenced to a lesser extent.

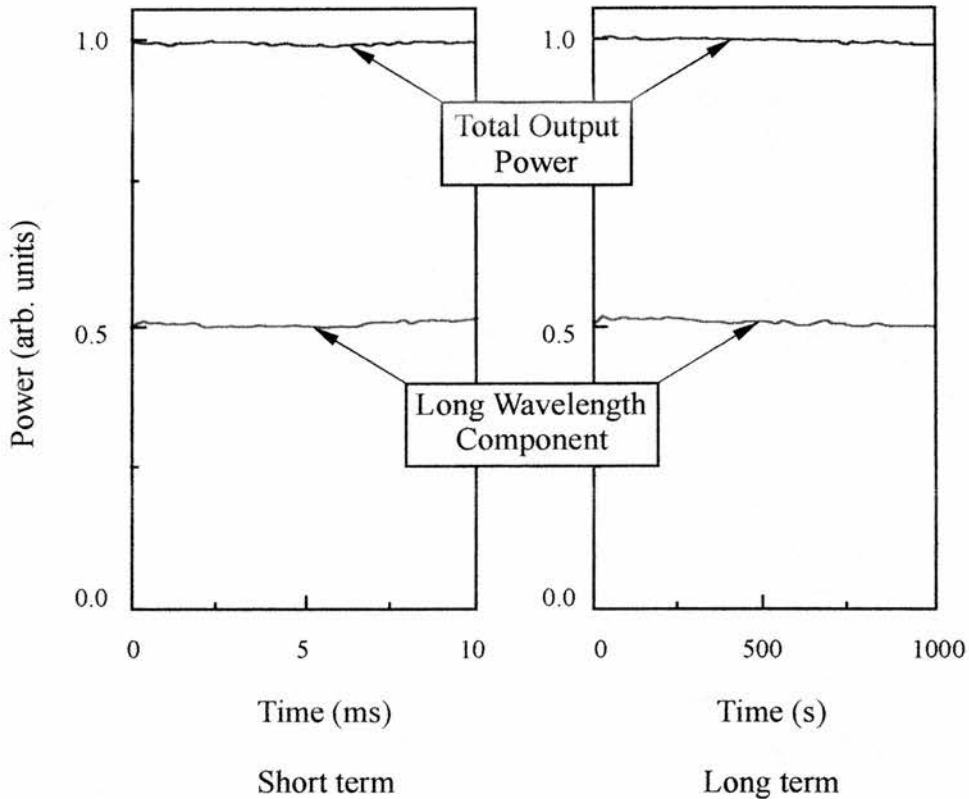


**Figure 3.12.** Stability of total and long-wavelength (1563nm) output power during scan times of 10ms (short term) and 1000s (long term). The short-wavelength component is 1553nm.

### 3.5 Relative power distribution

By altering the attenuation in one cavity arm the power distribution between the two wavelength components may be continuously varied. Slow variation in attenuation allowed comparison of the relative power in each wavelength component as a function of total output power (Figure 3.14). Two general conclusions may be drawn:

- i) Dual wavelength oscillation is not restricted to a subset of relative power distributions of the two wavelength components. Lack of sensitivity of dual-wavelength oscillation to relative cavity loss reduces the relative power

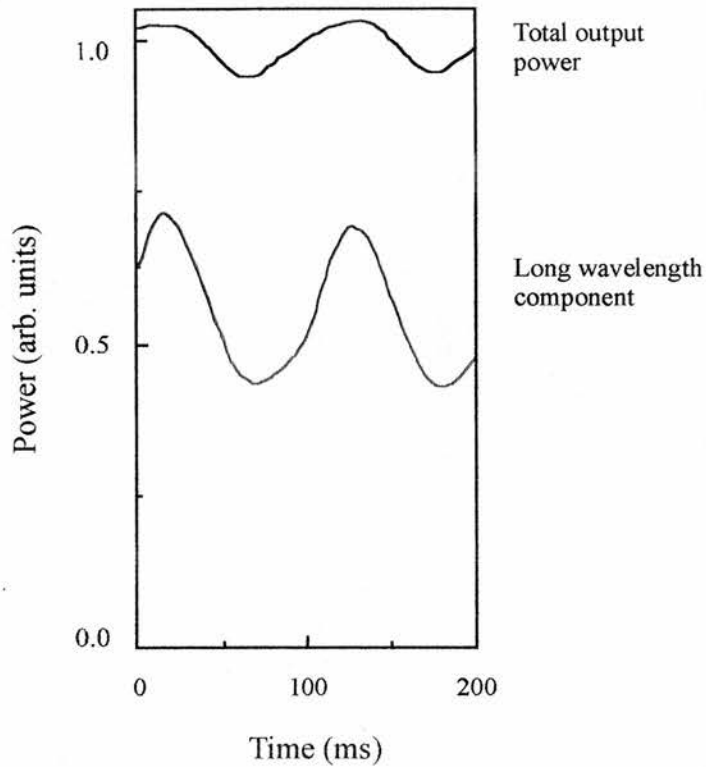


**Figure 3.13.** Output power stability with perturbation. Power fluctuation in the long-wavelength component is significantly higher than that of the total power level indicating a redistribution of power between each wavelength component.

distribution fluctuations to the point where a stable output can be achieved via simple environmental stabilisation/isolation. Cavity alignment and tuning were easily implemented.

- ii) Dual-wavelength oscillation generally produced a decrease in total output power as compared to single-wavelength oscillation. In this case, maximum power decrease was found to be  $\sim 20\%$ , when the ratio of the power of the two wavelength components was 0.8:0.2.

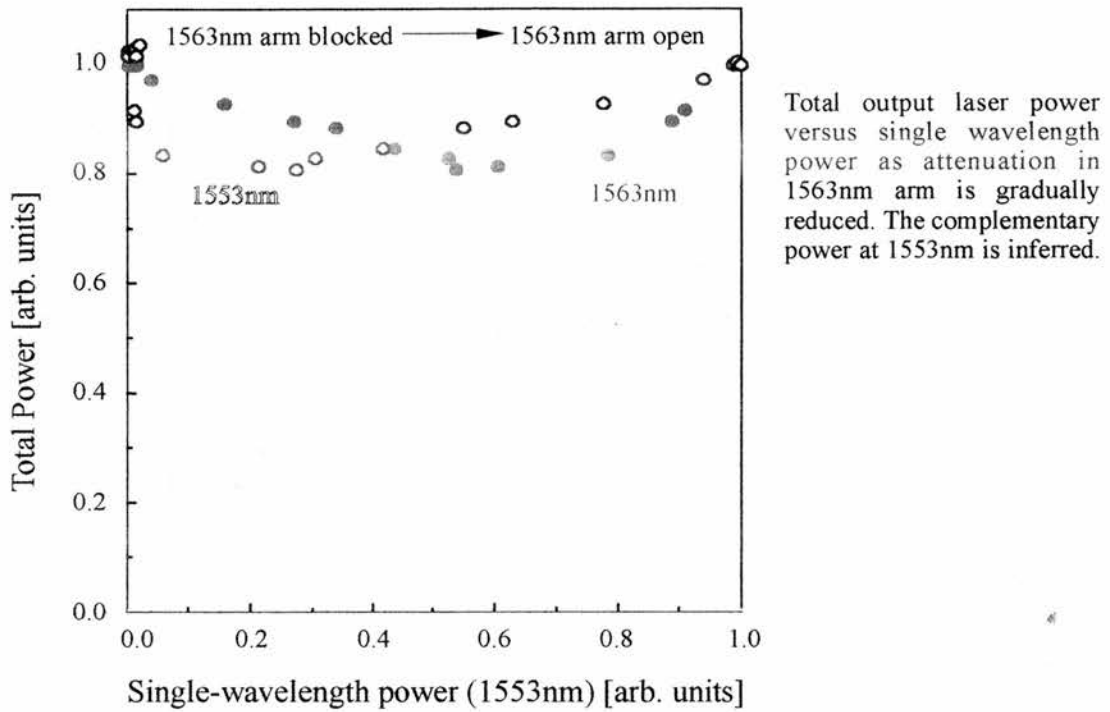


**Figure 3.14.** Variation of total output power with single-wavelength power as attenuation is altered in then low-loss cavity.

The decrease in total output power and the power distribution at which minimum output is achieved is thought to be linked to the different threshold currents and slope efficiencies of the laser at these two wavelengths. Thus the dual-wavelength laser characteristics reflects an average of the characteristics of the laser oscillating in single-wavelength mode at each individual wavelength. Figure 3.15 shows the relative power distribution for dual-wavelength operation. The oscillation spectrum changed with intra-cavity loss and as this was varied the relative power distribution altered.

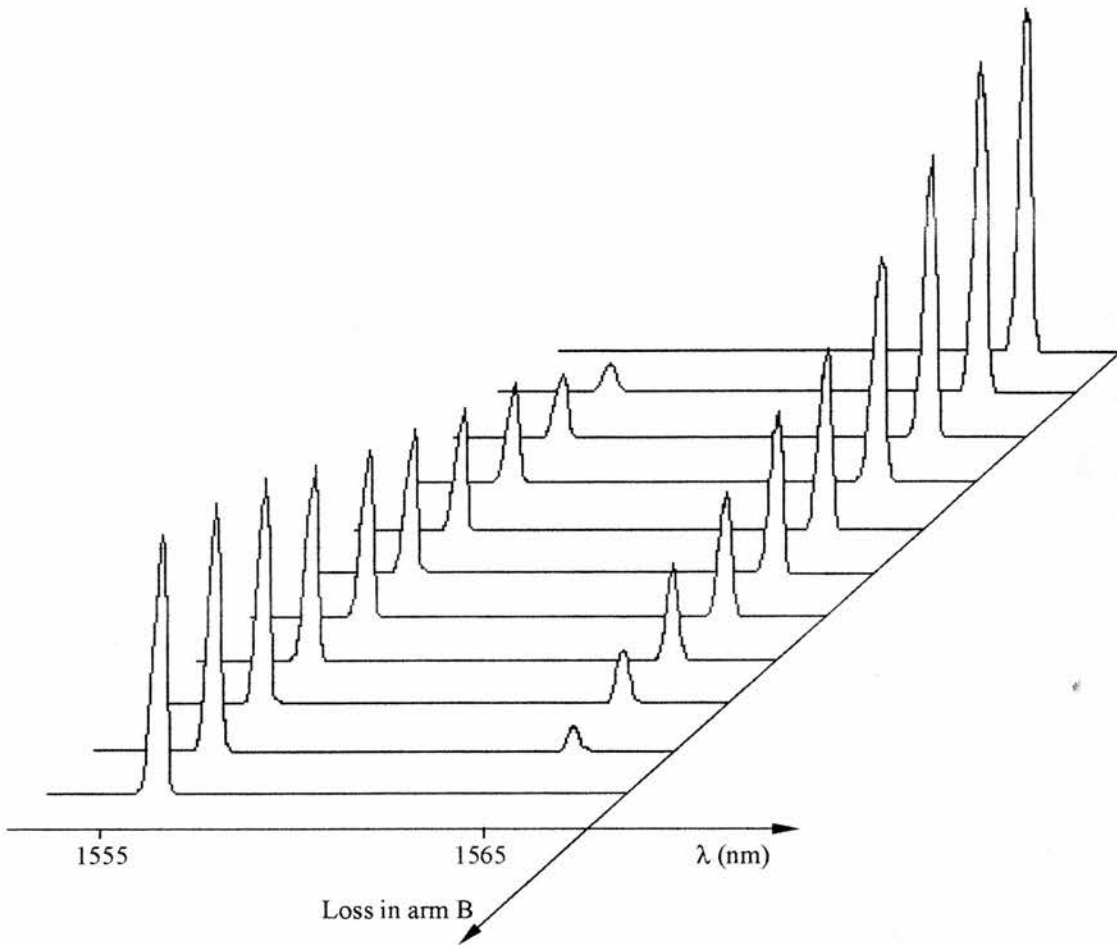


**Figure 3.15.** Relative power distribution for dual-wavelength operation. Dual-wavelength oscillation is (a) not restricted to some subset of relative power distributions and (b) insensitive to cavity loss.

### 3.6. Applications of dual-wavelength laser systems

#### 3.6.1 Multiple-wavelength oscillation

It is envisaged that the design principles of the dual-wavelength laser may be extended to provide multiple-wavelength oscillation from a single semiconductor laser by using additional beamsplitters and diffraction gratings. Differing beam-splitting ratios would be preferable to avoid the need for large attenuation of the lower loss cavities and to allow equalisation of individual round-trip losses. Applying the strong coupling criterion suggested in ref.13, only two wavelength components

were obtained when the internal semiconductor laser facet reflectivity was 1%. As many as eight simultaneously oscillating wavelength components are theoretically possible assuming that facet reflectivity is reduced to 0.1% (50/50 beamsplitters and equal loss subcavities are also assumed). Alternatively the dual-wavelength laser could be expanded to into a multiple-wavelength laser by using a single dispersive element such as an intra-cavity prism (or diffraction grating as shown in Figure 3.16) to define a specific low-loss beam path for each wavelength component. Multi-component output would then be implemented by retroreflection of each wavelength component. In this way, stable, simultaneous oscillation on three discrete wavelength components may be observed (Figure 3.17).

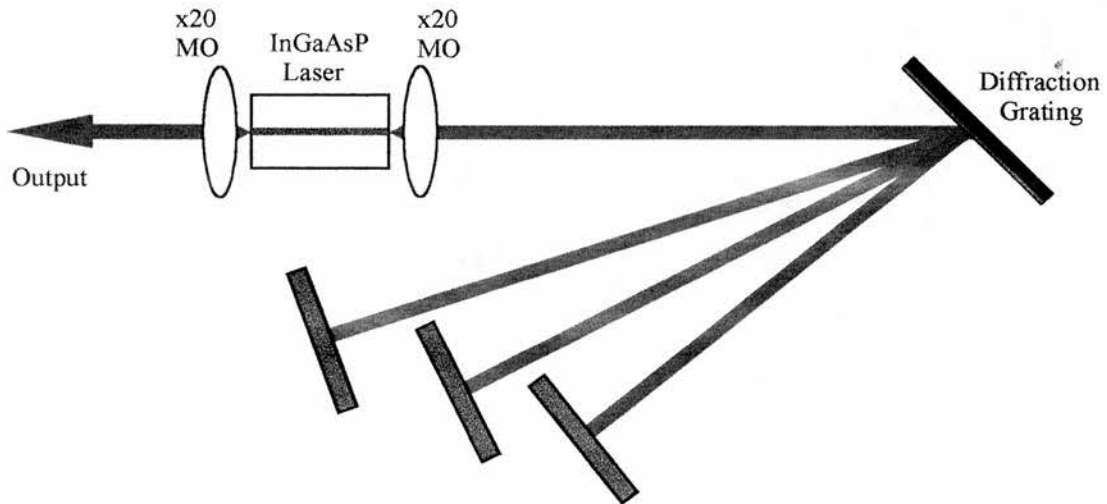


**Figure 3.16.** Multi-wavelength oscillation is possible using a single diffraction grating.



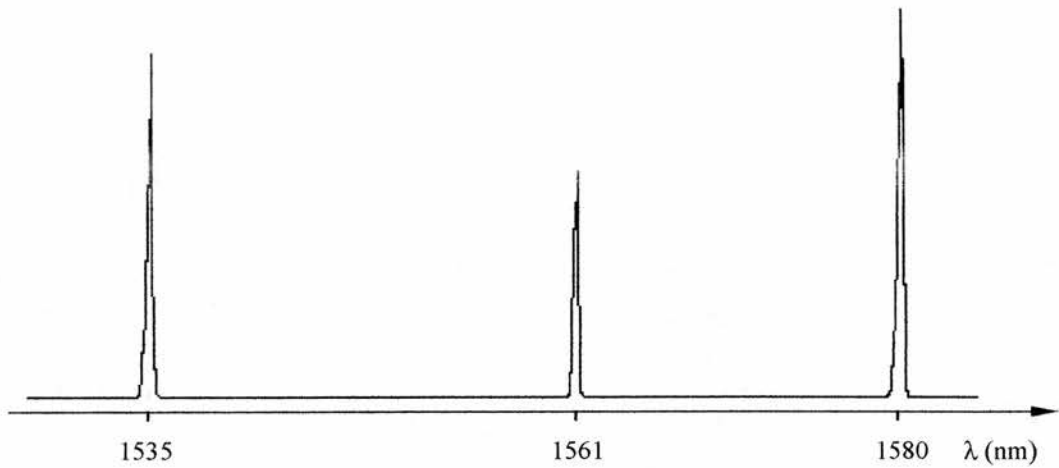


**Figure 6.17.** Simultaneous oscillation at three discrete wavelengths over a tuning range of 45nm.

### 3.6.2 Optical communications

For optical communication applications the laser system requires that information be imposed on each transmitted wavelength component independently. However, for the dual-wavelength laser this procedure would not be simple or practical, although fibre-based wavelength selective modulators have been developed<sup>14,15</sup> which can provide a method of imposing useful information on to the output signals generated by such laser sources. The limitation of this approach results from the bandwidth and wavelength selectivity characteristics of these modulators, hence there is little advantage to be gained by using the dual-wavelength laser over established multiple-wavelength generation techniques incorporating separate laser sources. However, there are specific communications-based applications where the inherent synchronism of the dual-wavelength output from this device is advantageous. For example, two separate data sets could be simultaneously transmitted through an optical fibre using via the two distinct wavelengths.

### 3.6.3 Alternative laser systems

The principle of dual-wavelength operation of broad gain spectrum lasers is not new and has been developed for other laser systems such as erbium-doped fibre-ring lasers<sup>10</sup>. Future designs need only incorporate compound cavity configurations with wavelength selective and variable attenuation components to allow equalisation (or adjustment; see section 3.4) of round-trip loss for each cavity element. The dual-wavelength semiconductor laser is highly stable and performs efficiently for a homogeneous gain medium.

Dual-wavelength operation (in both pulsed and cw regimes) in Ti:sapphire laser systems has also been demonstrated<sup>16</sup>. The saturation behaviour is significantly different from the semiconductor laser described above, due to the long upper-state lifetime of the Ti:sapphire laser, with the result that the two wavelength components can be modelocked or made to oscillate independently in cw mode.

### 3.7. Conclusions

Dual-wavelength operation of an external-cavity semiconductor laser arrangement has been described. Generation of both non-modelocked and modelocked dual-wavelength output signals has been demonstrated over a continuously tuneable wavelength range of 0.5nm to 55nm. Due to the short photon lifetime of the semiconductor laser the pulses produced were necessarily temporally overlapped and this inherent synchronism may prove useful in future experimental applications. The dual-wavelength laser system provides a convenient test source for the development of other optical devices and systems, and the simple principles involved may be incorporated for other lasers where generation of multiple wavelength components is considered advantageous.

### 3.8 References

1. G.E. Wickens, D.M. Spirit and L.C. Blank, *Electron. Lett.*, **27**, 973 (1991).
2. T.S. Kinsel and R.T. Denton, *Proc. IRE*, **56**, 146 (1968).
3. R.S. Tucker and G. Eisenstein, *J. Lightwave Technol.*, **LT-6**, 1737 (1988).
4. A. Alping, T. Anderson, R. Tell and S.T. Eng, *Electron. Lett.*, **18**, 422 (1982).
5. R.S. Tucker, G. Eisenstein, S.K. Korotky, L.L. Bulh, J.J. Veselka, G. Raybon, B.L. Kasper and R.C. Alferness, *Electron. Lett.*, **23**, 1270 (1987).
6. H. Ishio, J. Minowa and K. Nosu, *J. Lightwave Technol.*, **LT-2**, 448 (1988).
7. L.A. Koszi and N.A. Olsson, *Electron. Lett.*, **22**, 1102 (1986).
8. P.A. Kirkby, *J. Lightwave Technol.*, **LT-8**, 202 (1984).
9. G. Coquin, K.W. Cheung and M.M. Choy, *IEEE J. Quantum Electron.*, **QE-9**, 563 (1972).
10. H. Okamura and K. Iwatsuki, *Electron. Lett.*, **28**, 401 (1992).
11. G. Eisenstein, R.S. Tucker, U. Koren and S.K. Korotky, *IEEE J. Quantum Electron.*, **QE-22**, 142 (1986).
12. W. Sibbett, *Proc. 15th Int. Conf. on High Speed Photography and Photonics*, **SPIE 348**, 15 (1982).
13. K-Y. Liou, J.K. Jhee, G. Eisenstein, R.S. Tucker, R.T. Ku, T.M. Shen, U.K. Chakrabarti and P.J. Anthony, *Appl. Phys. Lett.*, **48**, 1039 (1986).
14. M. Wilkinson, J.R. Hill and S.A. Cassidy, *Electron. Lett.*, **27**, 979 (1991).
15. G. Fawcett, W. Johnstone, I. Andonovic, D.J. Bone, T. Harvey, N. Carter and T.G. Ryan, *Electron. Lett.*, **29**, 985 (1992).
16. J.M. Evans, D.E. Spence, D. Burns and W. Sibbett, *Opt. Lett.*, **18**, 1074 (1993).

# Chapter 4

## MULTI-PULSING MODELOCKED SEMICONDUCTOR LASERS

### 4.1. Introduction

Modelocked semiconductor lasers have been the subject of much research interest and have undergone great development since the first successful demonstration by Ho *et al* in 1978<sup>1</sup>. Active and passively modelocked systems have been shown to produce high fidelity ultrashort pulses over a wide range of wavelengths including 850nm<sup>2-9</sup>, 1.3 $\mu$ m<sup>10-12</sup> and 1.5 $\mu$ m<sup>7,13-15</sup> using a variety of configurations and techniques. Pulse duration is generally in the 1-10ps range, although a few examples of sub-picosecond output pulses have also been reported<sup>16</sup>. Active modelocking whereby an external RF signal is used for gain/loss modulation of a single-contact laser is the most popular approach. In recent years, fuelled by the demands of high capacity optical telecommunications applications,<sup>17</sup> there has been a trend towards semiconductor laser systems operating at very high frequencies. This requires the use of low capacitance devices<sup>18</sup> with correspondingly high modulation bandwidths. Special attention must be given to impedance matching of the high frequency modulation signals into such low impedance loads.

In this chapter, laser configurations are described whereby multi-GHz pulse sequences are produced using a standard semiconductor laser diode in conjunction with relatively low frequency modulation drive signals. Although the output comprises synchronised groups of high frequency pulses, such lasers may find use in many laboratory applications such as test sources in the characterisation of high-speed optoelectronic components.

The multi-pulsing modelocked lasers detailed in this chapter have variable configurations although basic operating principles are common to each. In section

4.2, the multi-pulsing behaviour of three-mirror Fabry-Perot (3M-FP), external-cavity laser systems are described. The 3M-FP configuration allows cavity parameter assessment and thus provides a convenient platform for the understanding of the formation and characteristics of modelocked multi-pulse generation. In section 4.3 an alternative laser geometry, the offset-Michelson cavity, is detailed. The relationship between the cavity configuration and the temporal gain profile and their effect on the multiple pulse output is outlined in section 4.4.

#### 4.2. Three-mirror Fabry-Perot lasers

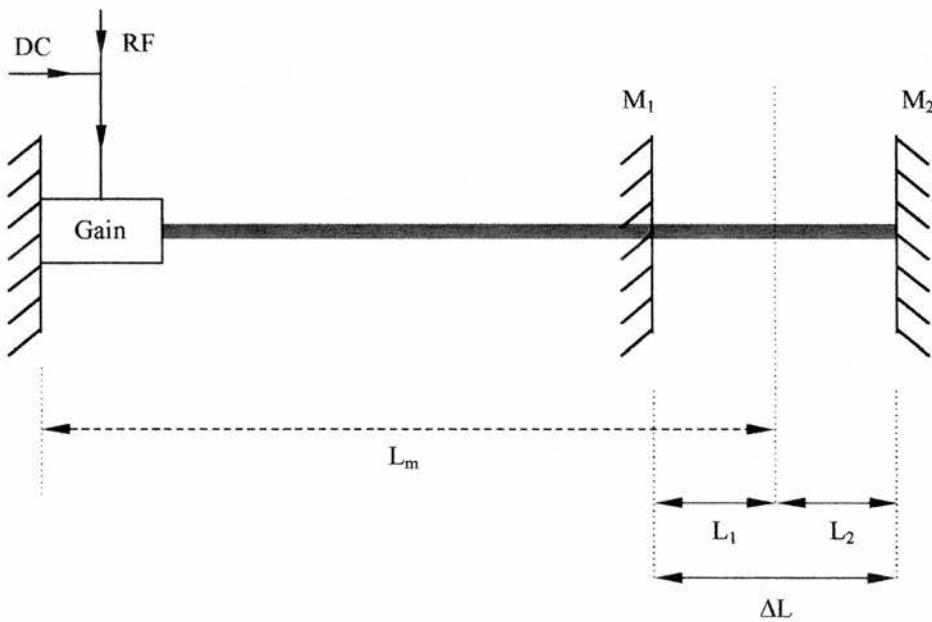


**Figure 4.1** Basic components of the three mirror Fabry-Perot laser cavity.

##### 4.2.1 Cavity configuration

The basic cavity configuration is the three-mirror Fabry-Perot (3M-FP) geometry illustrated in Figure 4.1. The optical path length  $L_m$  denotes the position at which a standard two-mirror, external-cavity semiconductor laser produces optimally modelocked pulses and is related to the frequency  $f_m$  of the modulation signal by:

$$L_m = \frac{c}{2nf_m} \tag{4.1}$$

where  $c$  is the speed of light and  $n$  the harmonic modelocking number. For a chosen modulation frequency,  $L_m$  is the optimum length for this cavity geometry, as the cavity length is a crucial factor in the operation of the multi-pulsing laser. Lengths  $L_1$  and  $L_2$  denote the relative displacement of the mirrors  $M_1$  and  $M_2$  from the synchronous modelocking position  $L_m$ .

**4.2.2 Multiple-pulse modelocking: experimental parameters**

The InGaAsP semiconductor laser used was a buried heterostructure Fabry-

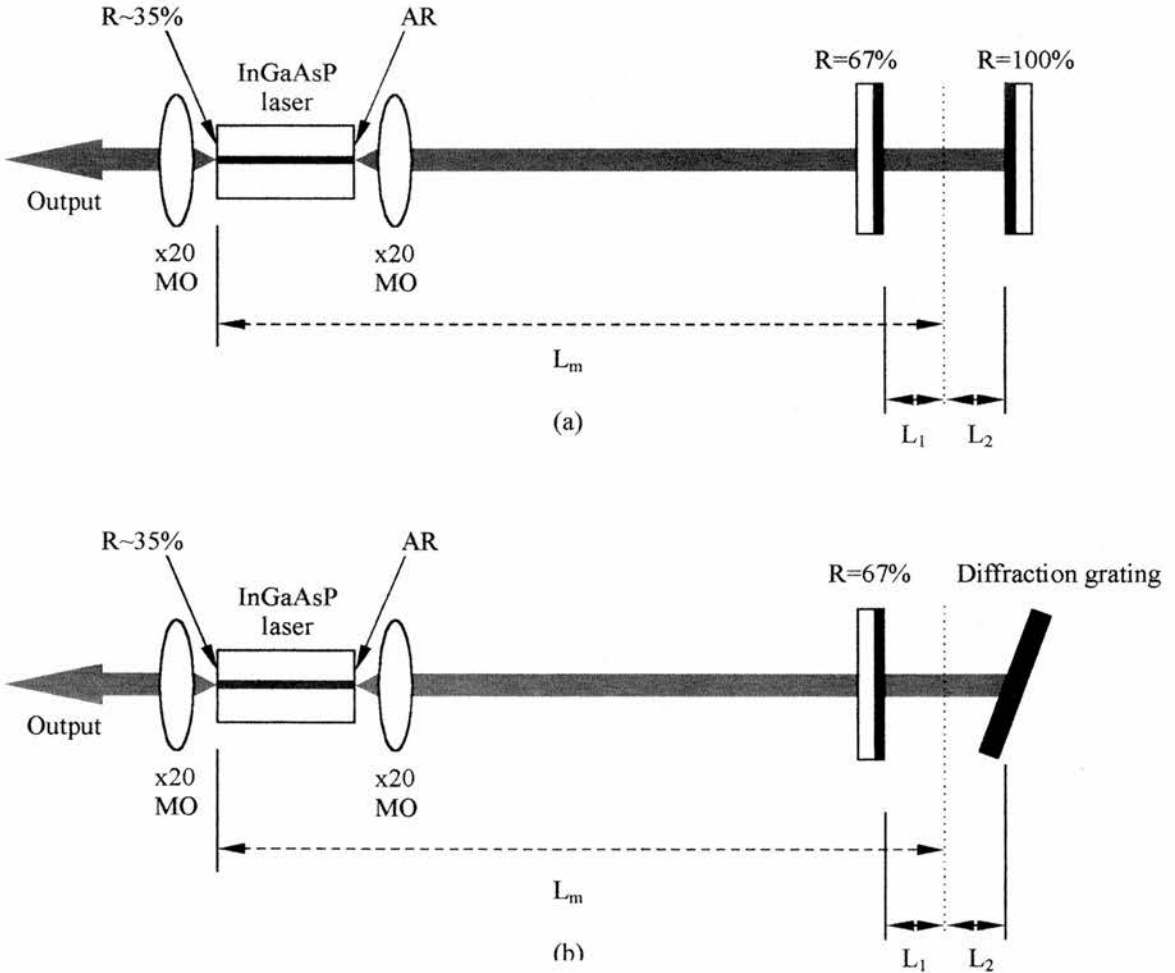


**Figure 4.2.** Two experimental arrangements for the 3M-FP laser. The diffraction grating is included to provide bandwidth limitation and wavelength tuning.

Perot device with a two-layer broadband anti-reflection (AR) coating applied to the cavity facet. Residual reflectivity of the AR-coated facet was  $\sim 0.12\%$ . The cleaved output facet was uncoated and had a reflectivity of  $\sim 35\%$ . Light output from the AR-coated facet was coupled into the external cavity via a  $\times 20$  microscope objective lens (N.A. = 0.5) as shown in Figure 4.2(a). External-cavity mirror reflectivities were 67% (mirror  $M_1$ ) and  $\sim 100\%$  (mirror  $M_2$ ). The laser threshold current for this cavity configuration was 20.0mA at 1560nm.

An alternative cavity configuration, shown in Figure 4.2(b), incorporates a diffraction grating to reduce oscillation bandwidth and facilitate wavelength tunability. The performance of this arrangement was found to be identical to the plane mirror counterpart. However, the original configuration (Figure 4.2(a)) enabled simplified measurement of the cavity parameters and so was adopted for the investigation of the multi-pulsing laser characteristics.

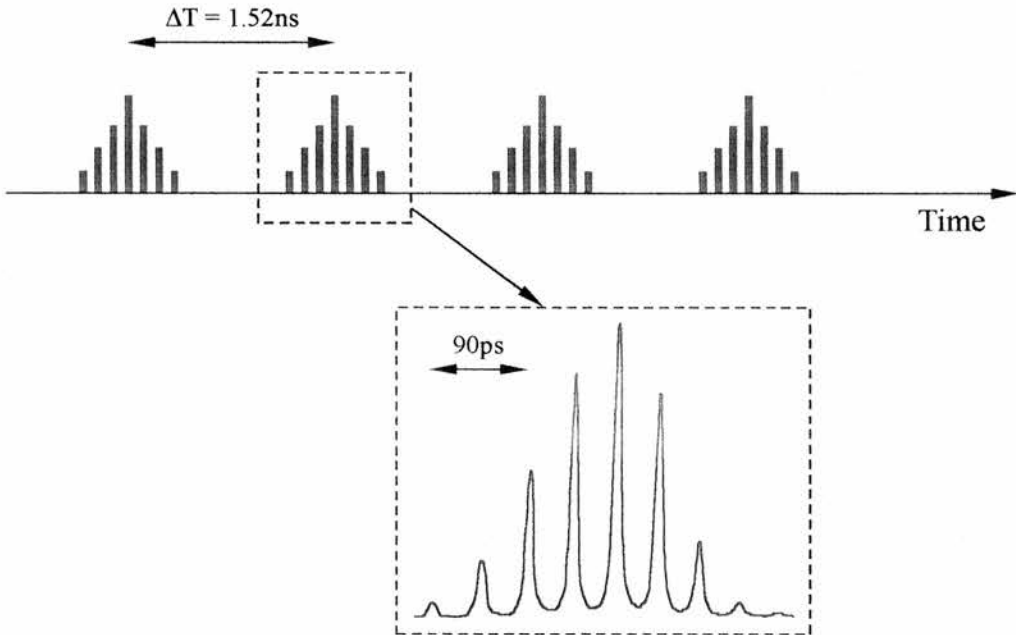


**Figure 4.3.** Schematic representation of long-term output from the multi-pulse laser. The insert shows details of the individual pulse group measured by the streak camera.

The 3M-FP laser was modelocked by superimposing a strong RF modulation signal onto a dc bias current using a bias tee. A modulation frequency of 656MHz was chosen, corresponding to the second harmonic modelocking frequency for a cavity

NO INFORMATION  
AVAILABLE ON  
ETALON FINESSE

length  $L_m$  of 45.7cm. A 20dBm RF varied between 15 and 40mA. The  $M_1$  and  $M_2$  were then adjusted, the laser operating streak camera system<sup>19</sup>. Mirror positioning the two cavity mirrors. A spectrum from the 3M-FP laser is shown in Figure 4.3

was  
 $M_1$   
isly  
ctly  
put

### 4.2.3 Relative mirror displacement

Multiple-pulse operation was initiated for a wide range of relative displacements from the nominal position defined by  $L_m$ . Graphs shown in Figure 4.4 (a) to (d) detail the relationship between the relative mirror displacements  $L_1$  and  $L_2$  necessary for the maintenance of multi-pulsing output for a variety of cavity configurations. Straight-line fits for these data sets indicate that multi-pulse output is possible when mirror separations  $L_1$  and  $L_2$  are governed by the following relationship:

$$\frac{L_1}{L_2} = m \quad L_2 \neq 0, \infty \quad (4.2)$$

Where  $m$  is  $\dots, 5, 4, 3, 2, 1, 0, 1/2, 1/3, 1/4, 1/5, \dots$ . This relationship was verified experimentally for values of  $m$  from 4 through to  $1/2$ . Deviation from this criterion resulted in detuning behaviour similar to that observed in conventional modelocked semiconductor lasers. In the multi-pulsing case subpulses were created after each main pulse and the temporal output of the laser is rather confused for very small mirror displacements from the optimum position.

The pulse separation  $\Delta T$  within the high frequency pulse sequences was determined as a function of the separation of the external-cavity mirrors  $\Delta L (= L_1 + L_2)$  and examples are plotted in Figures 4.5 (a) to (d). A linear relation was obtained and parameter  $m$  was found to have further significance in determining the pulse frequency of the multiple-pulse laser. The relationship describing the multiple-pulse frequency was:



$$(L_m - L)_1 = \frac{c}{2nf_p} = k(L_m + L_2) \quad (4.3)$$

where  $k = (1 + m)$  for  $L_1 > L_2$  and  $k = (1 + 1/m)$  for  $L_1 < L_2$ .

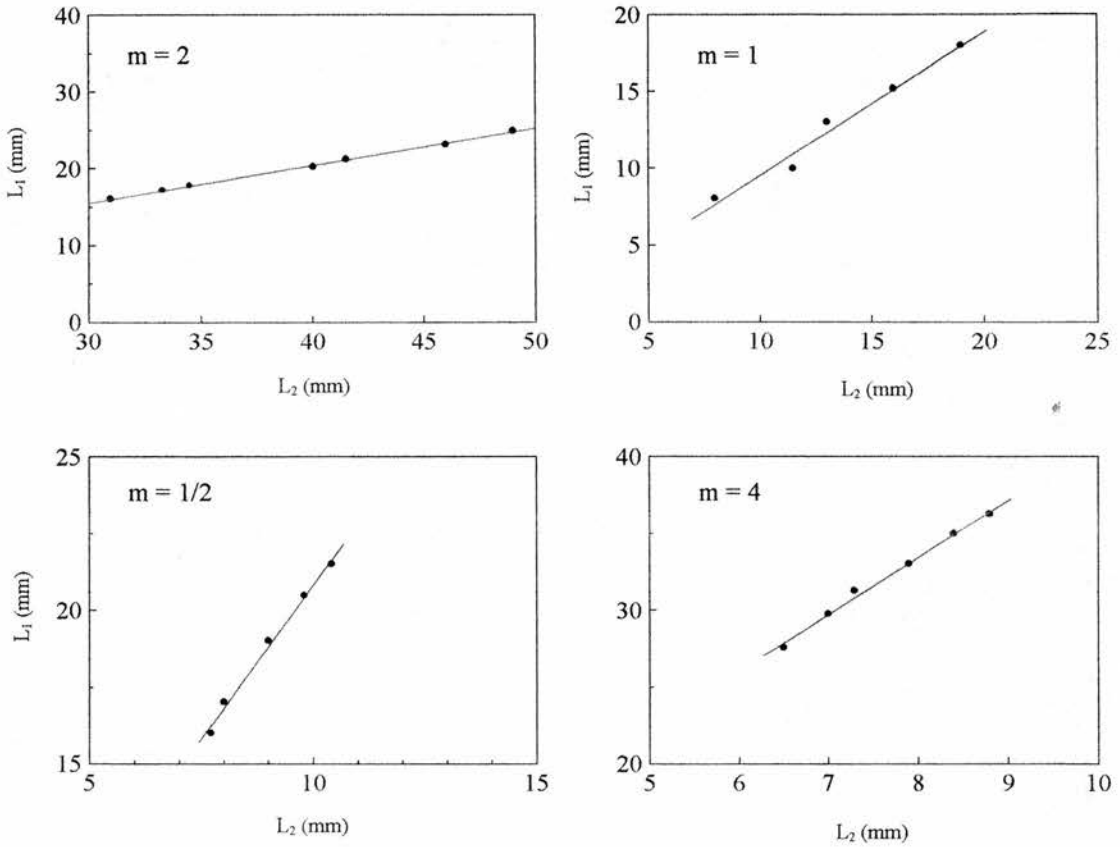


**Figure 4.4.** Relationship between relative mirror displacements  $L_1$  and  $L_2$  for multiple-pulse output.

#### 4.2.4 Multiple-pulse frequency tuning

The pulse frequency,  $f_p$  may be continuously tuned by varying the external cavity mirror separation in order to satisfy the relationship expressed in Eq. 4.2. Thus for continuous tuning, Eq. 4.2 may be modified to give

$$\frac{\Delta L_1}{\Delta L_2} = \frac{L_1}{L_2} \quad (4.4)$$

where  $\Delta L_{1,2}$  represents the change in the relative displacements  $L_{1,2}$  respectively. In this way pulse frequencies in the range 6 - 23GHz were obtained using different laser geometries for different  $m$  values, although any specific configuration could be tuned about a centre frequency by  $\sim 5 - 10$ GHz. A high frequency limit was imposed by the proximity of mirror  $M_1$  to the plane defined by  $L_m$  (for  $L_2$  kept constant) and in practice this was restricted to  $\sim 8 - 10$ mm. As mirror  $M_1$  approached  $L_m$  the pulses congregated together until the output resembled a broad pulse which was modulated by the effects of the two external-cavity mirrors. Pulses were reduced with

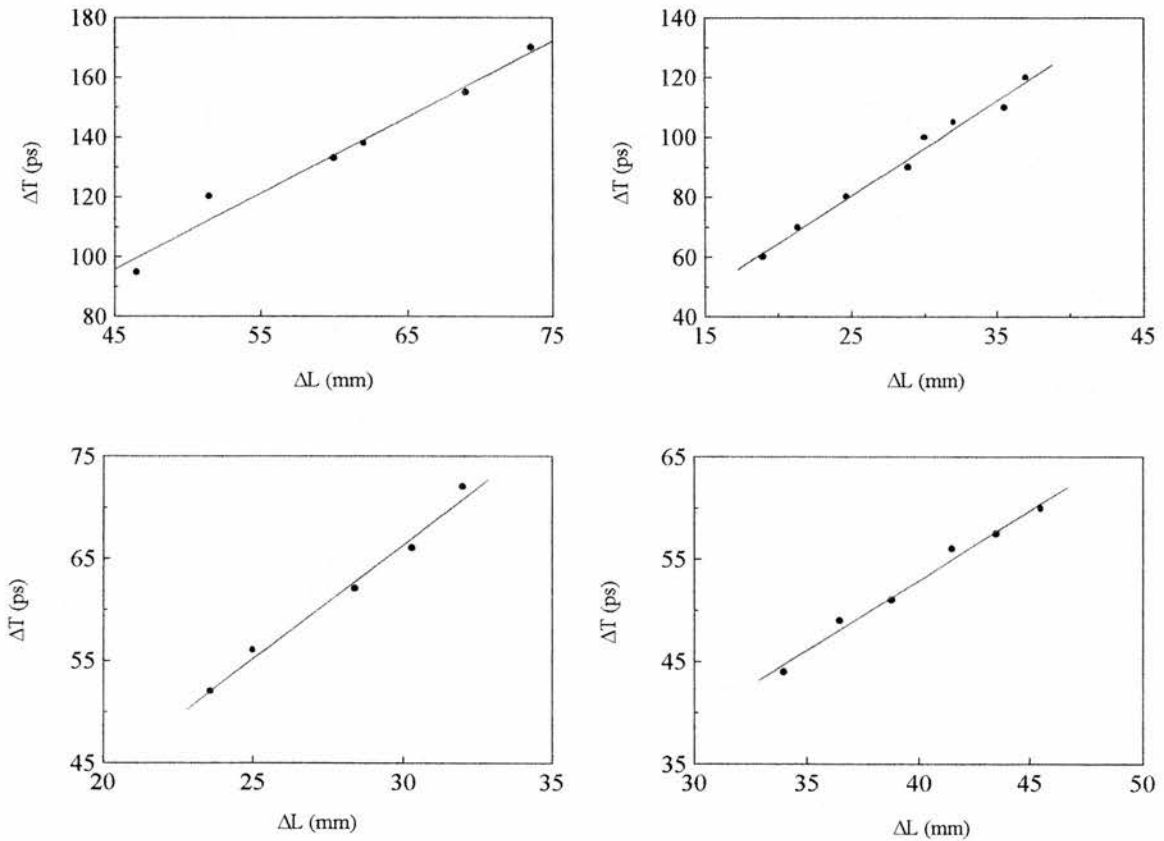


**Figure 4.5.** Variation of pulse spacing (within the high-frequency pulse packet) with external cavity mirror separation.

decreasing mirror separation until eventually no modulation was evident. This indicated that the inner external-cavity mirror was required to be positioned such that a broad, low intensity pulse was promoted in the initial pulse formation process. This then allowed the laser output properties to be dominated by the effects of the two cavity mirrors. If the internal mirror was placed too close to position  $L_m$  then laser output was produced similar to that generated by the single-mirror modelocked laser, the effects of the second mirror being reduced as mirror  $M_1$  approached position  $L_m$ .

The low frequency limit of multiple-pulse frequency tuning was governed by the temporal extent of the gain window created by the modulation signal waveform. If the mirror separation is increased sufficiently then eventually only one pulse is sustained by the gain medium. However, this proved not to be the case for these laser systems because many pulses were simultaneously synchronised with the modulation signal. For the laser in question the maximum obtainable gain window was  $\sim 400$ ps, therefore the maximum pulse separation was  $< 200$ ps and hence the multiple-pulse frequency limit was  $> 5$ GHz. However, such low frequency output tended to comprise

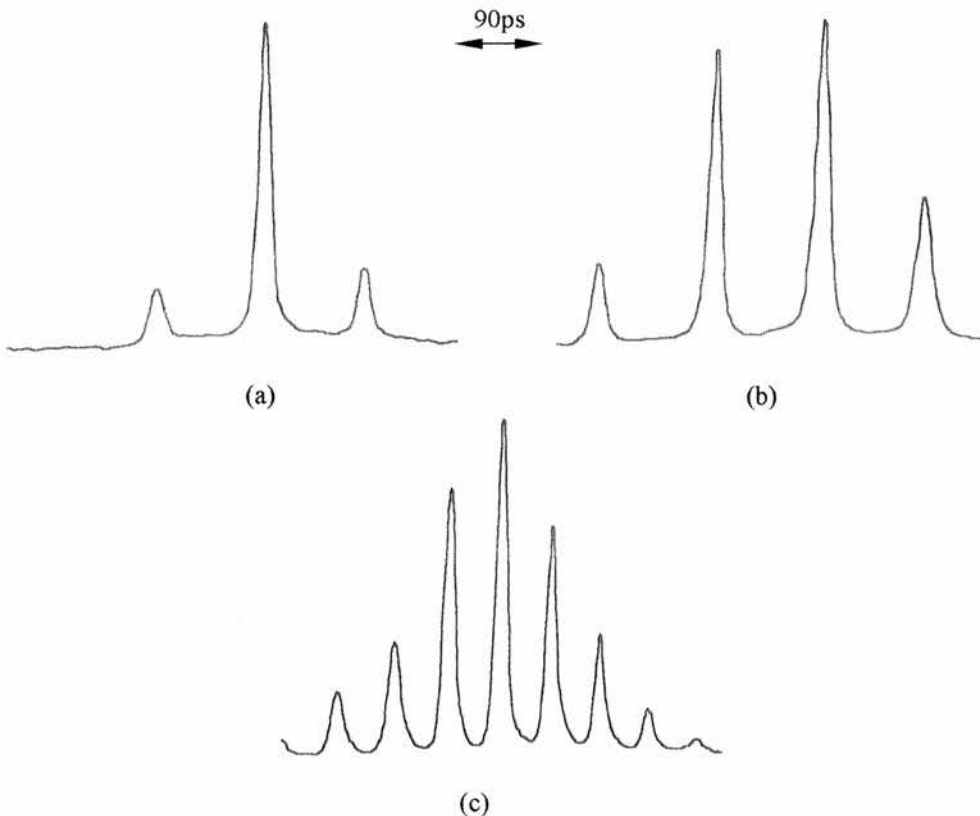


**Figure 4.6.** Streak camera traces showing typical temporal intensity profiles for the 3M-FP multiple-pulse laser where  $m = 1$ .

only three pulses with one high intensity pulse at the centre of the gain window and two substantially lower intensity pulses close to the extremes of the temporal gain.

Examples of typical temporal intensity profiles from the 3M-FP multi-pulsing laser where  $m = 1$  are included in Figure 4.6. At low dc injection currents as few as three pulses were obtained (Figure 4.6(a)). On increasing the dc bias the temporal extent of the gain window created by the composite modulation signal increased and, as shown in Figure 4.6(b), the number of pulses increased. A reduction in cavity mirror separation resulted in pulsing at higher frequency as shown in Figure 4.6(c). It should be noted that the pulse duration obtained in multi-pulse mode were shorter than those obtained via conventional modelocking using a single external-cavity mirror. This phenomenon may be understood by the fact that higher injection currents were used for the multi-pulsing laser without the output being degraded by the noisy subpulse generation arising from gain recovery effects<sup>9</sup>.

#### 4.2.5 Special case: $m = 0$ ( $L_2 \neq 0, \infty$ )

A special case exists in the 3M-FP cavity configuration whereby continuous pulse frequency tuning is possible by moving a single mirror (Figure 4.7). This arrangement corresponds to the  $m = 0$  condition detailed in section 4.2.3 where mirror  $M_1$  is placed at position  $L_m$ . The deviation of the experimental points from the line  $L_2 = 0$  was partly induced through experimental uncertainty in the allocation of a precise position for  $L_m$ . This includes a systematic error, the correction of which would tend to shift the zero of the  $L_2$  axis towards the mean of the experimental data. However, this correction was insufficient to account for the  $\sim 0.5\text{mm}$  deviation, and it is suggested that the main source of the error was due to the difficulty in determining  $L_m$  by optimising the modelocked output when using only one mirror,  $M_1$ . Since the optimum cavity length depends on injection current level and because the output pulse properties are relatively insensitive to cavity detuning, errors in the accurate determination of the position of  $L_m$  inevitably arose. The evidence obtained from further mirror configurations and the basic operating principle involved tends to suggest that the mean position of  $L_2$  measured in this case should be zero. The

gradient of the pulse separation versus mirror separation plot (Figure 4.7(b)) is 6.6ps/mm and this figure is in good agreement with the value of 6.67ps/mm obtained via Eq. 4.3.

Finally, it should be noted that this operating condition was unique to the three mirror Fabry-Perot cavity and was due to the effects of multiple reflections within the two external cavity mirrors. Other cavity variants which do not promote these subcavity effects cannot sustain a multi-pulsing output for  $m = 0$ .

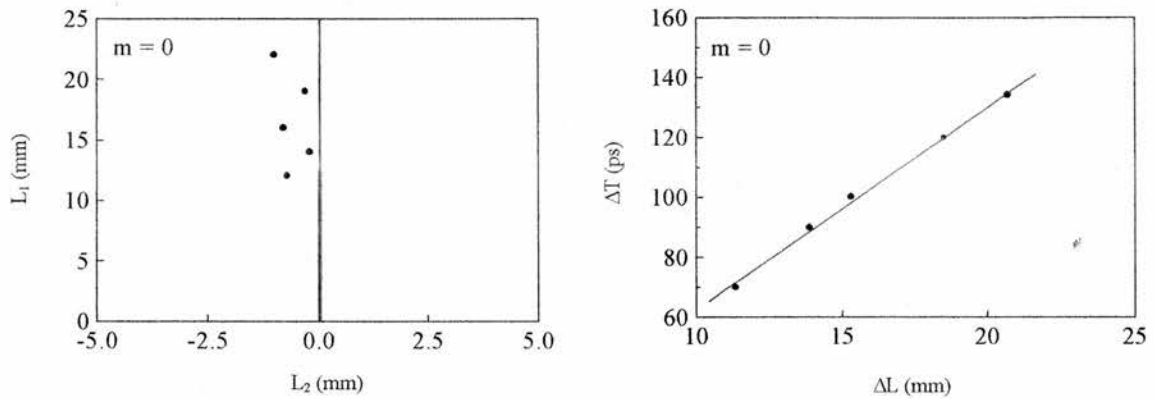


**Figure 4.7.** For  $m = 0$ ; (a) relationship between relative mirror displacements  $L_1$  and  $L_2$ ; (b) variation of pulse spacing with external-cavity mirror separation.

### 4.3. The offset Michelson cavity configuration

The Michelson cavity configuration shown schematically in Figure 4.8 was used to further develop the multiple-pulse technique. The same nomenclature was used to describe the relative positions of mirrors  $M_1$  and  $M_2$ , but for this configuration, each arm had a separate  $L_m$  position. Both positions were determined by optimisation of the modelocked pulses produced by one arm whilst the other was blocked. The mirror displacements  $L_1$  and  $L_2$  were then adjusted until multiple-pulse output was obtained. As before, it was found that the relative mirror displacements satisfied the criteria of Eqs. 4.2 and 4.3 for the 3M-FP cavity.

Substituting a diffraction grating for a cavity mirror produced no significant degradation of the multi-pulse output. However wavelength tuning and bandwidth

reduction were facilitated.

The Michelson cavity sustained multiple-pulse output for a wide range of values of  $m$  (Figure 4.9).

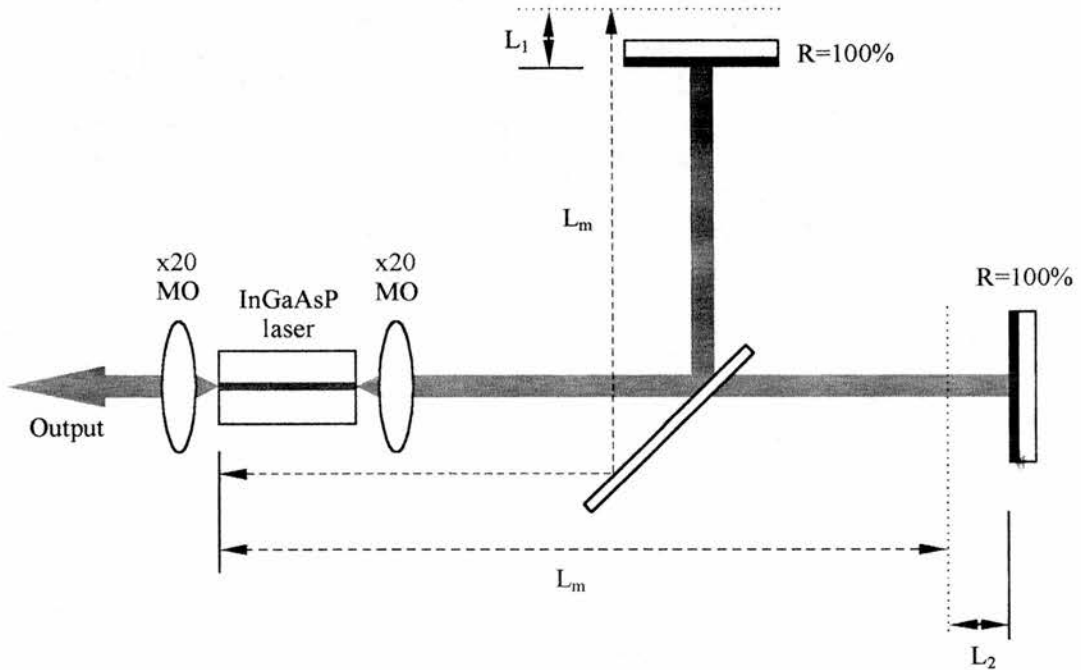


**Figure 4.8.** The offset Michelson cavity configuration.

#### 4.4. Operating principles of multi-pulsing lasers

The schematic diagram of Figure 4.10(a) details the energy transfer processes responsible for the generation of multiple-pulse output from the 3M-FP laser cavity. The ordinate of Figure 4.10 denotes local time with respect to the applied modulation signal. The output of a conventional modelocked laser with one external cavity mirror placed at  $L_m$  (Figure 4.10(b)) is included for comparison using the same representation. For the three-mirror cavity the geometry dictates that the energy of each pulse is transferred both backwards and forwards within the local time frame of the modulation signal. In the figure, a pair of adjacent pulses (displaced by  $\Delta L$  for the pulse sequence to be maintained), are considered over three consecutive round trips of the laser resonator. It is the requirement for a second pulse, which is

responsible for the form of Eqs. 4.2 and 4.3. Thus, when  $L_1 = L_2$  the output comprises two intersecting pulse groups which are independent apart from coupling due to the gain medium. Further, for any mirror combination the number of intersecting pulse groups is equal to  $k$  (defined in Eq. 4.3) due to the same mechanism.

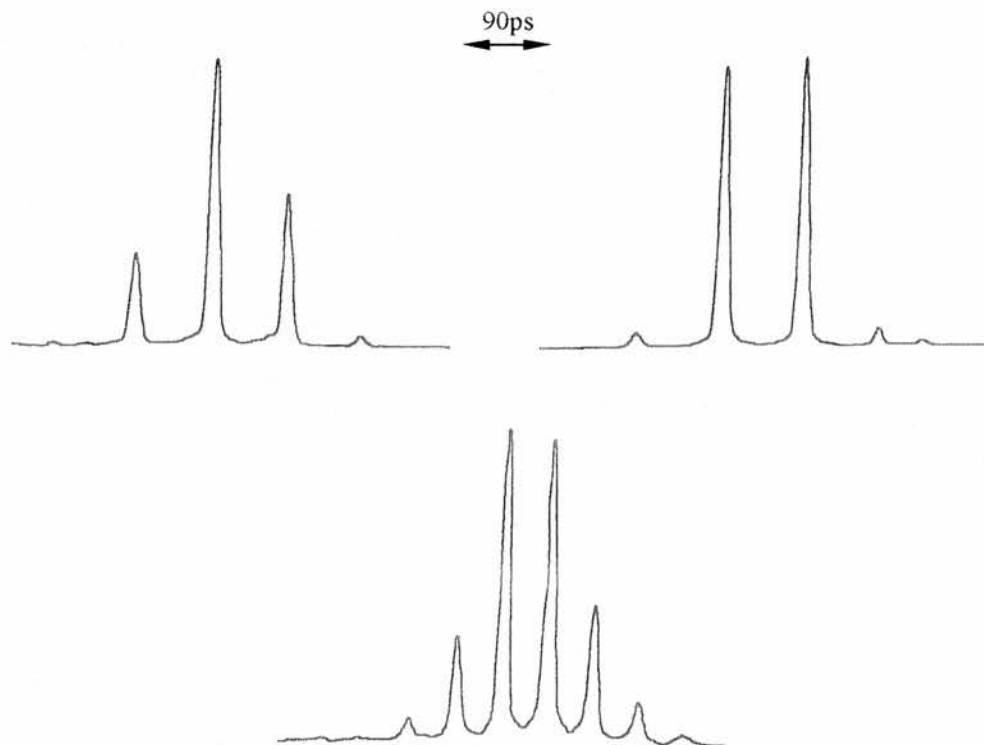


**Figure 4.9.** Streak camera traces showing typical temporal intensity profiles for the offset Michelson cavity configuration multiple-pulse laser.

When mirror  $M_1$  is positioned at  $L_m$  (that is, for  $L_1 = 0$ ), energy can only be shifted forward in time and this is insufficient to access the multiple pulsing regime described above. However, this situation can be configured in the three-mirror Fabry-Perot cavity since each pulse undergoes multiple transitions of the subcavity formed by the two mirrors. Therefore this resonant effect serves to delay a portion of the pulse energy by the required time interval such that the cavity behaves exactly the same as in the more general case of Figure 4.10(a). In this scenario, however, the multiple pulsing frequency can be continuously tuned by varying the position of mirror  $M_1$  since the expression given in Eq. 4.4 can be satisfied for almost all values of  $L_1$  ( $L_1 \neq 0, \infty$ ). Thus multipulsing takes place when the frequency of the RF

drive supports modelocked operation in both the laser cavity of length ( $L_m - L_1$ ) and that of length ( $L_m + L_2$ ).

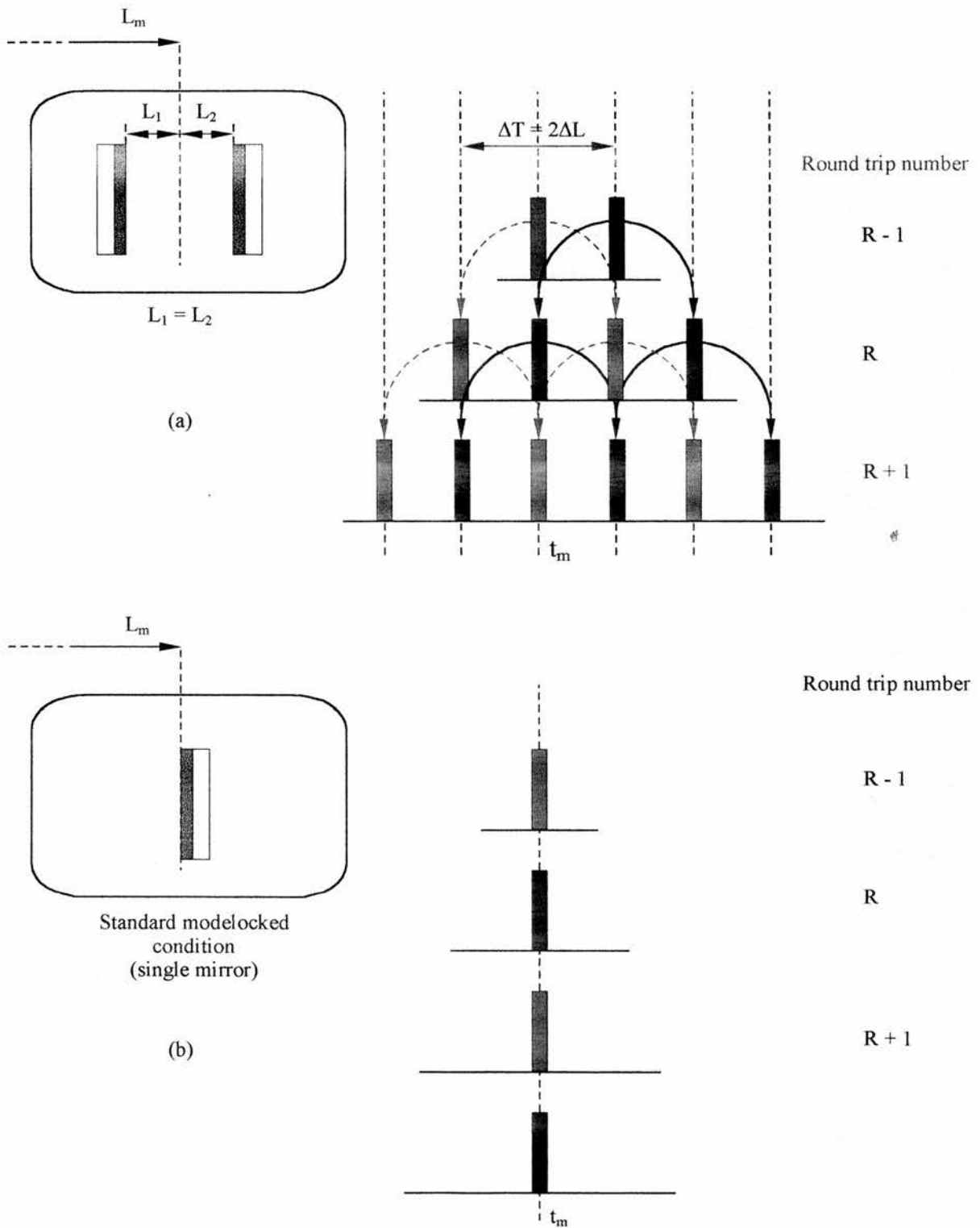
The total number of pulses emitted by the multi-pulsing laser is ultimately determined by the extent of the gain window induced by the applied modulation signal. Although pulse energy is constantly redistributed, only those pulses incident on the semiconductor laser when gain is present can persist. The steady state then marks the balance between the temporal extent of the gain window and the energy transfer processes.

Figure 4.11 shows the spectral output of (a) the three-mirror Fabry-Perot cavity laser system and (b) the three-mirror offset Michelson cavity.

#### 4.5. Conclusions

Multiple-pulse modelocked operation of several composite external-cavity semiconductor laser geometries has been described. Pulse frequencies within a tuning range of 6 - 23GHz were obtained via adjustment of the separation of the two external-cavity mirrors from the position  $L_m$  defined by the single mirror modelocking geometry. Empirical relationships were found for the relative mirror positions necessary for multi-pulsing and for the related pulse frequency. These expressions were explained using a simple pulse evolution model where energy transfer between pulses plays a key role in the introduction of the synchronisation required for sustained modelocking.





**Figure 4.10.** Schematic of the energy transfer processes responsible for multiple pulse formation for the 3M-FP laser cavity (a). The output of a conventional modelocked laser using a single external cavity mirror is shown in (b).

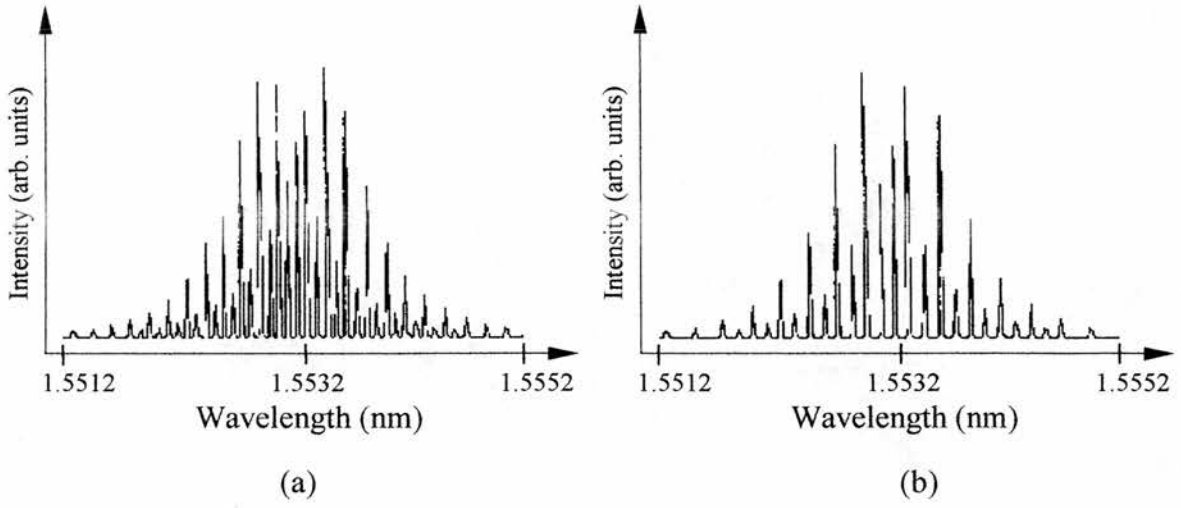


**Figure 4.11.** Spectral performance of (a) the three-mirror Fabry-Perot cavity laser system and (b) the three-mirror offset Michelson cavity.

## 4.6 References

1. P.T. Ho, L.A. Glasser, E.P. Ippen and H.A. Haus, *Appl. Phys. Lett.*, **33**, 241 (1978).
2. M.B. Holbrook, W. Sleat and D. Bradley, *Appl. Phys. Lett.*, **37**, 59 (1980).
3. P.P. Vasil'ev, V.N. Morozov and A.B. Sergeev, *IEEE J. Quantum Electron.*, **QE-21**, 576 (1985).
4. J.P. Van der Ziel, R.A. Logan and R.M. Mikulyak, *Appl. Phys. Lett.*, **39**, 867 (1981).
5. P.P. Vasil'ev, V.N. Morozov, Yu.M. Popov and A.B. Sergeev, *IEEE J. Quantum Electron.*, **QE-22**, 149 (1986).
6. J.P. Van der Ziel, W.T. Tsang, R.A. Logan, R.M. Mikulyak and W.M. Augustiniak, *Appl. Phys. Lett.*, **39**, 525 (1981).
7. D.J. Derickson, R.J. Helkey, A. Mar, J.K. Karin, J.G. Wasserbauer and J.E. Bowers, *IEEE J. Quantum Electron.*, **QE-28**, 2186 (1992).
8. Y. Silverberg, P.W. Smith, D.J. Eilenberger, D.A.B. Miller A.C. Gossard and W. Wiegman, *Optics Letters*, **9**, 507 (1984).
9. D.J. Derickson, P.A. Morton, J.E. Bowers and R.L. Thornton, *Appl. Phys. Lett.*, **59**, 3372 (1991).
10. J.T.K. Chang and J.I. Vukusic, *IEEE J. Quantum Electron.*, **QE-23**, 1329 (1987).
11. J.E. Bowers, P.A. Morton, A. Mar and S.W. Corzine, *IEEE J. Quantum Electron.*, **QE-25**, 1426 (1989).
12. A.G. Weber, M. Schell, G. Fischbeck and D. Bimberg, *IEEE J. Quantum Electron.*, **QE-28**, 2220 (1992).
13. G. Eisenstein, R. Tucker, U. Koren and S. Korotky, *IEEE J. Quantum Electron.*, **QE-22**, 142 (1986).
14. Y.K. Chen, M.G. Wu, T. Tanbun-Ek, R.A. Logan and M.A. Chin, *Appl. Phys. Lett.*, **58**, 1253 (1991).
15. Y.K. Chen and M.G. Wu, *IEEE J. Quantum Electron.*, **QE-28**, 2176 (1992).
16. E.P. Ippen, D.J. Eilenberger and R.W. Dixon, *Appl. Phys. Lett.*, **37**, 267 (1980).
17. L. F. Mollenauer, M. J. Neubelt, S. G. Evangelides, J. P. Gordon, J. R. Simpson and L. G. Cohen, *Opt. Lett.*, **15**, 1203 (1990).
18. J.E. Bowers, U. Koren, B.I. Miller, C. Socolich and W.Y. Wan, *Electron. Lett.*, **24**, 1263 (1988).
19. J. Chen, W. Sibbett and J. I. Vukusic, *Optics Commun.*, **38**, 427 (1984).

# Chapter 5

## GAIN-SWITCHING OF InGaAsP SEMICONDUCTOR DIODE LASERS

### 5.1 Introduction

Semiconductor diode lasers typically generate 10-20ps pulses under modelocked operation. However, this method has the significant disadvantage of requiring an external cavity. In this chapter a second method of ultrashort pulse generation is discussed: gain-switching. Gain-switching is achieved by fast switching of the optical gain by drive current modulation and may be implemented using lasers of any structure. Unlike modelocking, this method requires no external cavity and has the added advantage of producing optical pulses with high peak powers at high repetition rates. The repetition rate may be varied simply by altering the RF frequency of the drive source (see Figure 5.1)

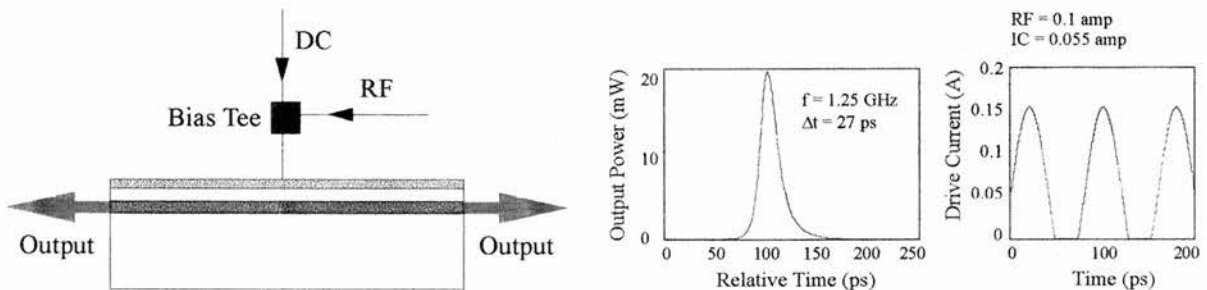


**Figure 5.1.** Schematic representation of ultrashort pulse production via gain-switching. The RF modulation current is superimposed on the dc injection current to give picosecond output pulses.

Onodera *et al*<sup>1</sup> reported the first example of single wavelength, bandwidth-limited optical pulses from a gain-switched InGaAsP DFB device. This was achieved by driving the laser with a high RF modulation superimposed on the dc bias current. The pulsewidth was demonstrated to be continuously controllable over a range of two or three times the modulation frequency. A minimum pulsewidth of 26ps was produced

at 500MHz and the duration-bandwidth product ( $\Delta\tau\Delta\nu$ ) for the pulses varied between 0.32 and 0.44 assuming Lorentzian pulse shapes. Following this breakthrough, gain-switched DFB lasers have been widely used for the production of single wavelength low-chirp picosecond (25-30ps) pulses<sup>2-4</sup>.

## 5.2 Theoretical Treatment

The modulation of laser cavity loss (proposed by Hellwarth in 1961<sup>5</sup>), was the first reported technique used to produce large bursts of radiation from a laser. The principle of gain-switching was developed from the relaxation oscillations observed when a diode laser was activated from below threshold using electrical pulses having a fast leading edge. It was observed that the duration of the resultant optical pulses was significantly shorter than the electrical pulses which produced them<sup>6</sup>. Gain-switching is a process whereby the first 'spike' of the relaxation oscillation is excited by an electrical pulse which is then terminated before subsequent spikes are produced<sup>7</sup>. Very high repetition rates are possible because the photon lifetime is of the order of a few picoseconds inside the laser cavity. This implies that the electrical pulsewidth should be very short ( $\sim 10^{-9}$  -  $10^{-12}$  seconds) and such pulses may be supplied using comb generators<sup>8,9</sup>, picosecond photoconductive switches<sup>10,11</sup> or avalanche transistor generators<sup>12</sup>. Typical electrical pulsewidths are in the range of 25 to 1000ps. However, gain-switched picosecond pulses can also be produced by modulating a diode biased below threshold with a large RF signals at subgigahertz frequencies<sup>13,14</sup>.

Figure 5.2 illustrates the ultrashort pulse generation process in semiconductor diode lasers using gain-switching. The computer simulation shows the RF modulation superimposed on a dc bias (Figure 5.2 (a)). Dc bias  $I_0$  may be above or below threshold. Above threshold, the laser operates in cw mode. Below threshold laser action is impeded until the RF signal increases the injected carrier density above the threshold density (Fig 5.2 (b)). As the excitation pulse increases the gain above threshold, carrier density rises above  $n_{th}$ , light builds up in the cavity and optical output is produced. The rapidly increasing light signal saturates the gain via

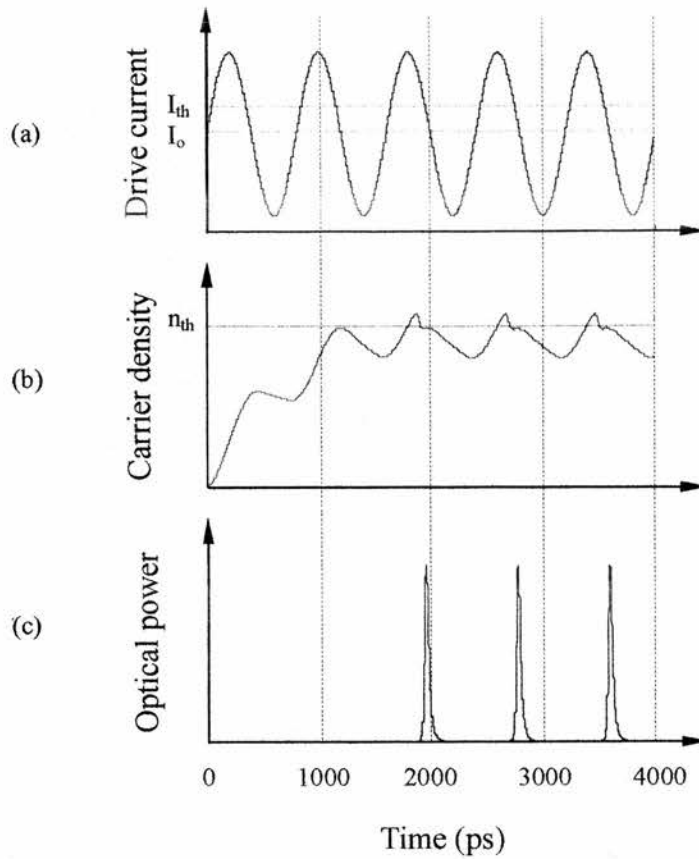


**Figure 5.2.** Gain-switching: computer model of the temporal evolution of (a) the applied current; (b) carrier density; (c) output pulses.

stimulated emission, carrier density growth is repressed and laser oscillation ceases as the carrier density is pulled below threshold. If the excitation waveform (and hence the gain) is strong enough to take the carrier density above threshold for a significant period of time then the gain can recover and satellite pulses or subpulses can occur. Typically, the theoretical output pulse is asymmetric, the leading edge of the pulse being 23-50% shorter than the trailing edge. This is because the mechanisms which act on the leading and trailing edges of the pulse are usually different in origin.

The dynamic performance of gain-switched pulses in a semiconductor diode lasers may be formalised in terms of carrier and photon rate equations which connect the carrier density  $N$  in the cavity with the photon density  $P$ .

$$\frac{dN}{dt} = \frac{\eta J}{ed} - AN - BN^2 - CN^3 - v_g \frac{dg}{dN} \left[ \frac{N - N_o}{1 + \epsilon P} \right] P \quad (5.1)$$

$$\frac{dP}{dt} = \Gamma \beta BN^2 - \Gamma v_g \frac{dg}{dN} \left[ \frac{N - N_o}{1 + \epsilon P} \right] P - \frac{P}{\tau_p} \quad (5.2)$$

where  $e$  is the electron charge,  $d$  the active layer depth and  $v_g$  is the group velocity.

The spontaneous radiative recombination term included in the photon density equation is scaled by a factor  $\beta$ , the spontaneous coupling factor. The optical confinement factor  $\Gamma$  describes the spatial overlap of the optical mode with the active region. The photon density  $P$  is increased through the coupled spontaneous and stimulated emission, and is depleted via waveguide loss and loss at the facets. In a Fabry-Perot laser the losses can be characterised in terms of the lifetime  $\tau_p$ :

$$\tau_p^{-1} = v_g \left\{ \ln(1/R^2)/2L + \alpha_i \right\} \quad (5.3)$$

Losses at the facet depend on the logarithm of the facet reflectivity  $R$  as the optical intensity will increase exponentially along the length  $L$  of the cavity. Both facet and waveguide losses ( $\alpha_i$ ) are assumed to be combined. Such an approximation is valid only when carrier and photon population changes are small on a round-trip time scale. Carrier and photon densities are also assumed to be spatially non-variant. A summary of laser parameters used to generate the theoretical model are given in Table 5.1.

Gain-switched picosecond pulses have been produced at several important wavelengths: 1550nm<sup>15,16,17</sup>, 1300nm<sup>11,17,22</sup> and 850nm<sup>8-10,12,13</sup>. Pulse widths may be measured, for example using a streak camera or a oscilloscope/photodiode combination with picosecond resolution. Peak power values of gain-switched optical pulses typically lie in the range 10 to 100mW at 1550nm<sup>16,17</sup> and 0.1 to 1W for GaAs lasers<sup>11,13,14</sup>. Enhanced nonlinear gain compression accounts for the relatively low peak power values of InGaAsP devices.

<i>Variable</i>	<i>Symbol</i>	<i>Value</i>	<i>Unit</i>
Wavelength	$\lambda$	1500	nm
Waveguide width	w	3.5	$\mu\text{m}$
Active layer thickness	d	0.18	$\mu\text{m}$
Cavity length	L	400	$\mu\text{m}$
Confinement factor	$\Gamma$	0.35	
Differential gain	$g_0$	$3 \times 10^{-16}$	$\text{cm}^2$
Transparency density	T	$1.1 \times 10^{18}$	$\text{cm}^{-3}$
Nonradiative recombination rate	A	$1 \times 10^8$	$\text{sec}^{-1}$
Radiative recombination rate	B	$1 \times 10^{-10}$	$\text{cm}^3 \text{s}^{-1}$
Auger coefficient	C	$1.3 \times 10^{-28}$	$\text{cm}^6 \text{s}^{-1}$
Spontaneous emission coupling coefficient	$\beta$	$1 \times 10^{-4}$	
Mirror loss	$\alpha_{\text{mirror}}$	45	$\text{cm}^{-1}$
Nonlinear gain coefficient	$\epsilon$	$2 \times 10^{-17}$	$\text{cm}^3$
Internal loss	$\alpha_{\text{int}}$	40	$\text{cm}^{-1}$

**Table 5.1** Laser parameters used for theoretical modelling of the gain-switching regime.

*MathCad* computer simulations were generated (see Appendices) using the semiconductor laser rate equations 5.1 and 5.2 in order to model the performance of carrier density, output power and pulsewidth of a given laser for a wide variety of drive currents and device parameters. It was assumed that the gain was proportional to the carrier concentration. The rate equations are single mode, that is, carrier and photon densities are presumed to be spatially nonvariant. It is also assumed that the laser operates in a single spatial mode. Facet and waveguide losses are combined. For gain-switching, the current density  $J(t)$  is taken as a train of short electrical pulses.

Figure 5.3 shows that the calculated peak power and pulsewidth vary with changes in the amplitude of the RF drive current. The cw threshold of the laser is 33mA, and so the maximum value of the ratio  $I_1/I_{th}$  is less than 5. Above this value, gain recovery takes place and satellite pulses are generated. Pulse repetition rate is



1.3GHz. From Figure 5.3 it is clear that as the current amplitude increases, peak power increases whilst the pulsewidth decreases. Pulsewidth is typically in the range 20 to 35ps. Variation of pulsewidth and peak power over a range of dc bias currents is shown in Figure 5.4. Again, the RF frequency is 1.3 GHz. For a given value of RF current, there is an optimum sub-threshold dc bias current for which the pulsewidth is minimised. As the RF frequency increases, the reduction in drive current pulsewidth minimises the difference between threshold and the optimal dc bias, eventually becoming zero at very high frequencies<sup>11</sup>. Pulse generation suffers increasing delay, peak power decreases and pulsewidth decreases with dc bias when the diode is operated below this optimal bias condition.

Gain compression has a profound effect on both peak power and the FWHM value of the optical pulses and as a result Figures 5.3 and 5.4 are shown for a nonlinear gain coefficient  $\epsilon$  of 0 and  $2 \times 10^{-17} \text{cm}^3$ . The nonlinear gain coefficient is defined as  $\epsilon = dg/dn$ , where  $g$  is the gain and  $n$  is the carrier density of the device. Pulsewidth variation and change in peak power are plotted as a function of  $\epsilon$  in Figure 5.5. Dc bias is 20mA and the RF current amplitude is 140mA at a frequency of 1.3 GHz. As the nonlinear gain coefficient is reduced, peak power increases and the pulse narrows because the nonlinear gain in gain-switched diode lasers is a major limiting factor on the maximum achievable peak power and the minimum possible pulsewidth.

The effect of linear gain variation on peak power and pulsewidth is illustrated in Figure 5.6. Dc bias is 15mA and the RF frequency is 1.3GHz at 115mA. Increasing the linear gain results in optical pulses having both greater peak power and shorter pulsewidth, due to the fact that the initial carrier density inversion is greater for higher values of linear gain.

Figure 5.7 illustrates the detrimental effect that an increase in RF frequency beyond  $\sim 1.3\text{GHz}$  has on both the pulsewidth and peak power of gain-switched pulses. In the case shown, dc bias is 25mA for two values of RF current amplitude (100mA and 140mA). Pulse degradation (peak power reduction and temporal broadening) occurs as a result of decreasing modulation depth of the carrier density with increasing frequency. The reduction of carrier density modulation depth at higher frequencies is more clearly illustrated in Figure 5.8. Here drive current, carrier density

and output power are shown for three different values of RF frequency. The dc bias is 15mA and RF drive current amplitude is 100mA.

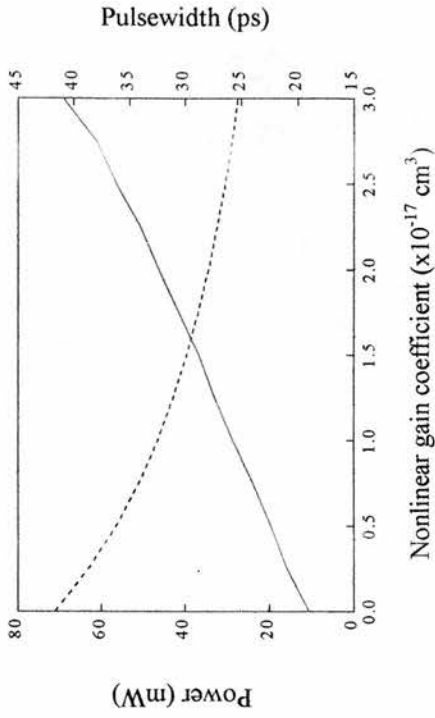


Figure 5.5. Effect of variation in nonlinear gain coefficient on peak power (dotted line) and pulsewidth.

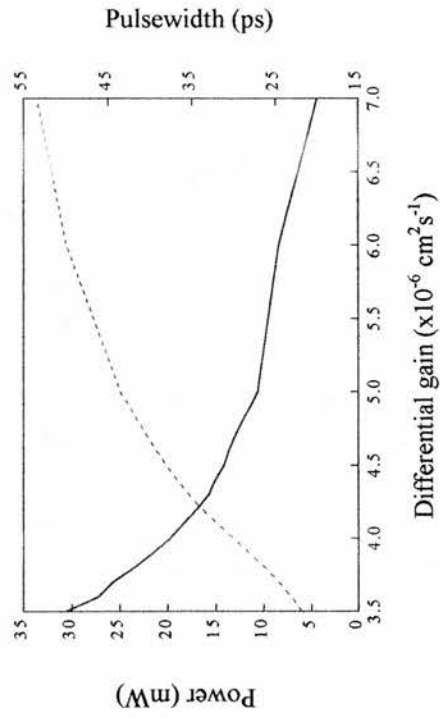


Figure 5.6. Calculated peak power (dotted line) and pulsewidth (solid line) as a function of differential gain coefficient  $g_0$ . Dc bias is 15mA, RF amplitude current is 115mA and nonlinear gain coefficient is  $2 \times 10^{-17} \text{ cm}^{-3}$ .

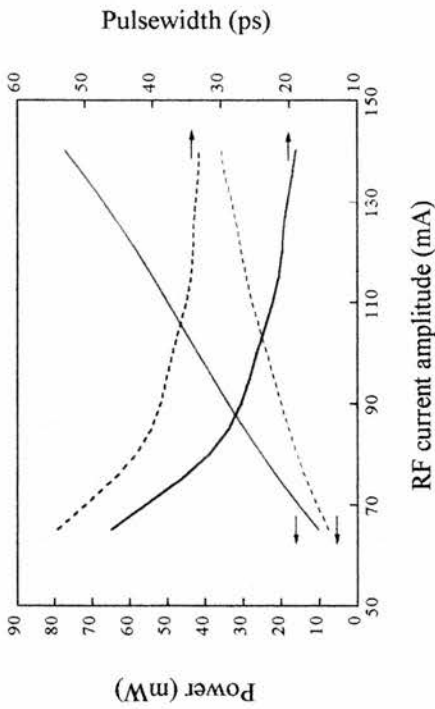


Figure 5.3. Peak power and pulsewidth variation for different values of RF drive current amplitude. Dc bias is 25mA. The nonlinear gain coefficient  $\epsilon$  is 0 (solid line) and  $2 \times 10^{-17} \text{ cm}^{-3}$  (dotted line).

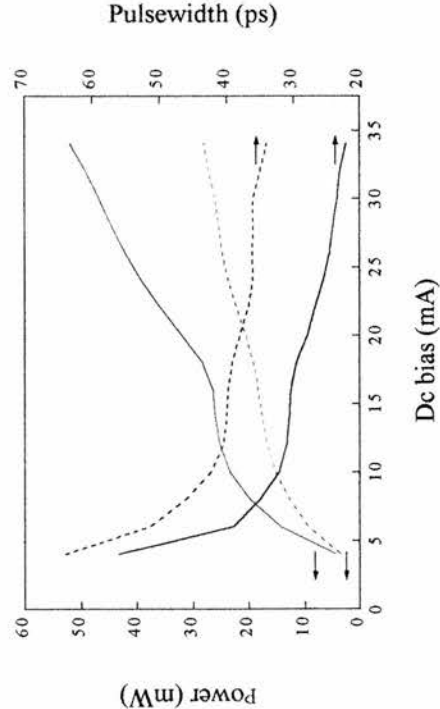
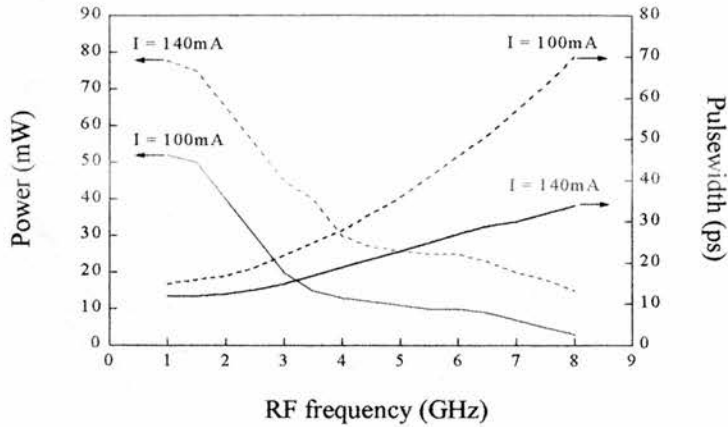


Figure 5.4. Variation of calculated peak power and pulsewidth with dc bias. The RF current amplitude is 100mA. The nonlinear gain coefficient  $\epsilon$  is 0 (solid line) and  $2 \times 10^{-17} \text{ cm}^{-3}$  (dotted line).



**Figure 5.7.** Variation in peak power and pulsewidth as a function of drive current frequency.

Figure 5.9 shows the variation of the drive current, carrier density and optical output for three values of dc bias current (25, 40 and 55mA) for constant RF drive conditions (650MHz; 100mA). Carrier density modulation depth is high and shows only a small reduction as the dc bias is increased. Output power and pulsewidth both show marked improvement.

The modulation depth of the carrier density remains constant in Figure 5.10. Three values of RF current amplitude are shown for a dc bias of 25mA. The RF frequency is 650MHz. As before it is clear that there is an increase in output power and a reduction in pulsewidth.

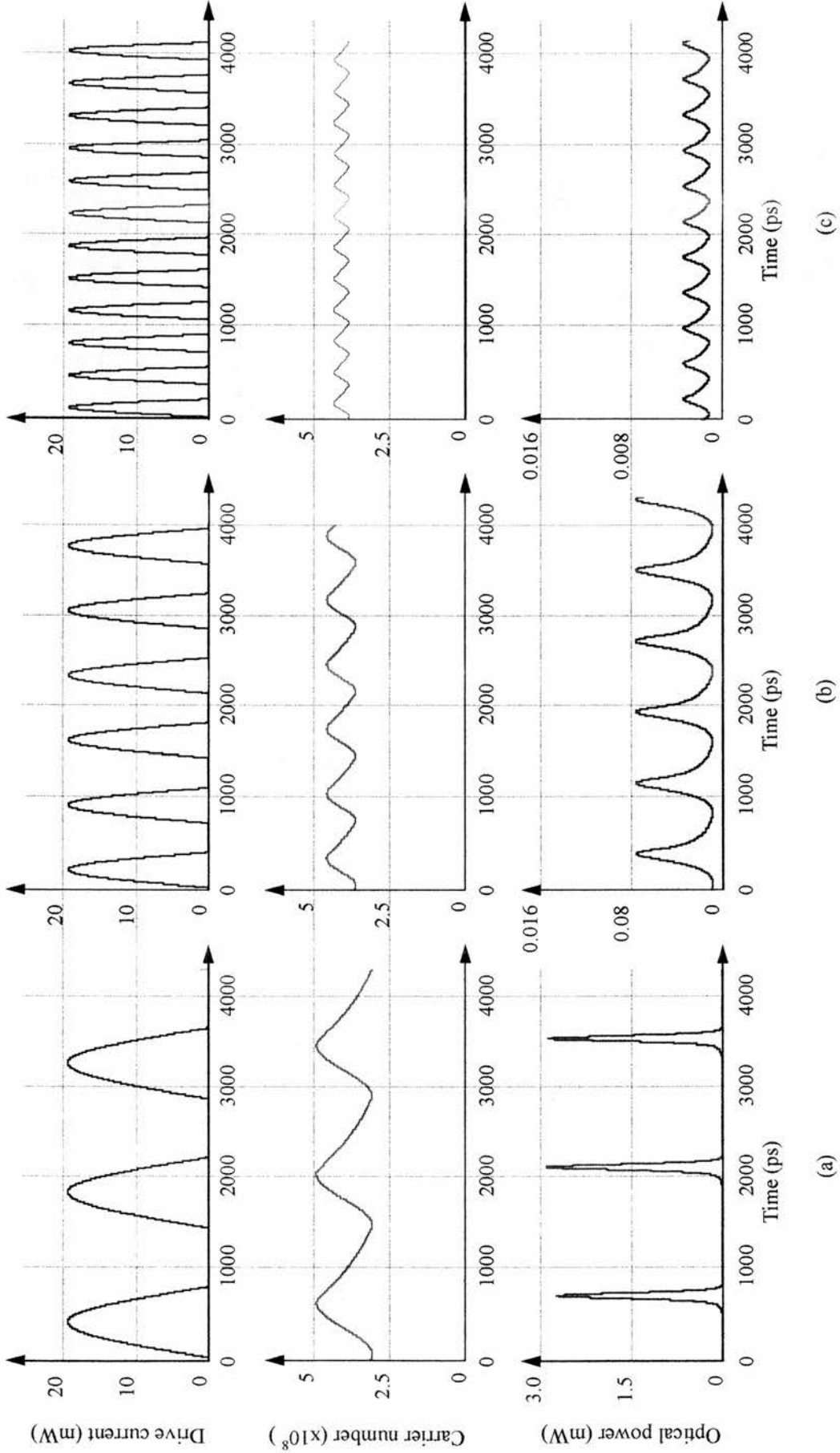
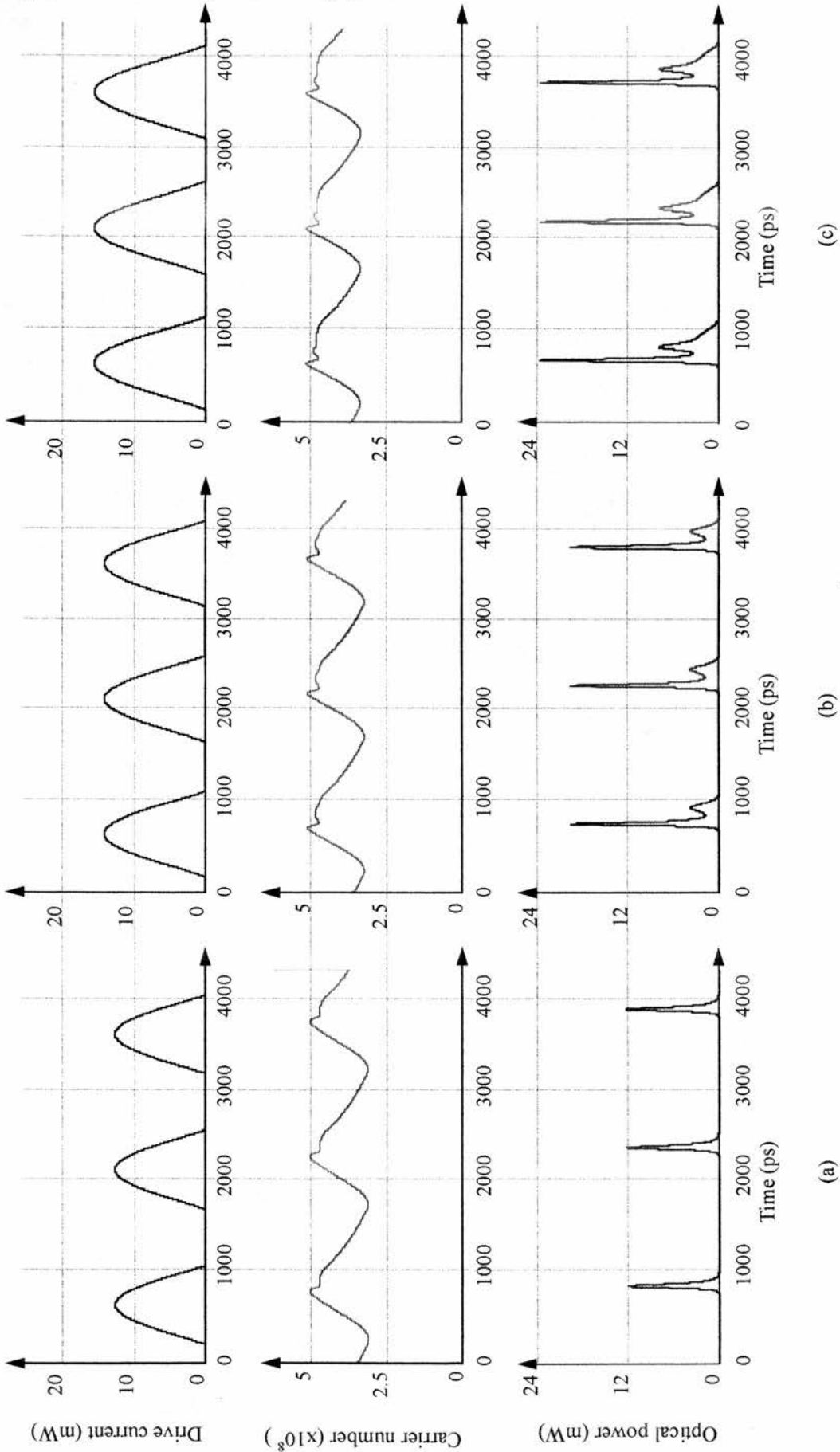


Figure 5.8. Temporal variation of drive current, carrier density and optical output for a range of RF drive frequencies: (a) 650MHz; (b) 1.3GHz; (c) 2.6GHz. Pulsewidth increases, output power decreases and carrier density modulation depth decreases with increasing frequency



**Figure 5.9.** Temporal variation of drive current, carrier density and optical power for a range of dc bias current amplitude: (a) 25mA; (b) 40mA; (c) 55mA. Pulsewidth decreases, peak power increases and carrier density modulation depth decreases with increasing dc bias.

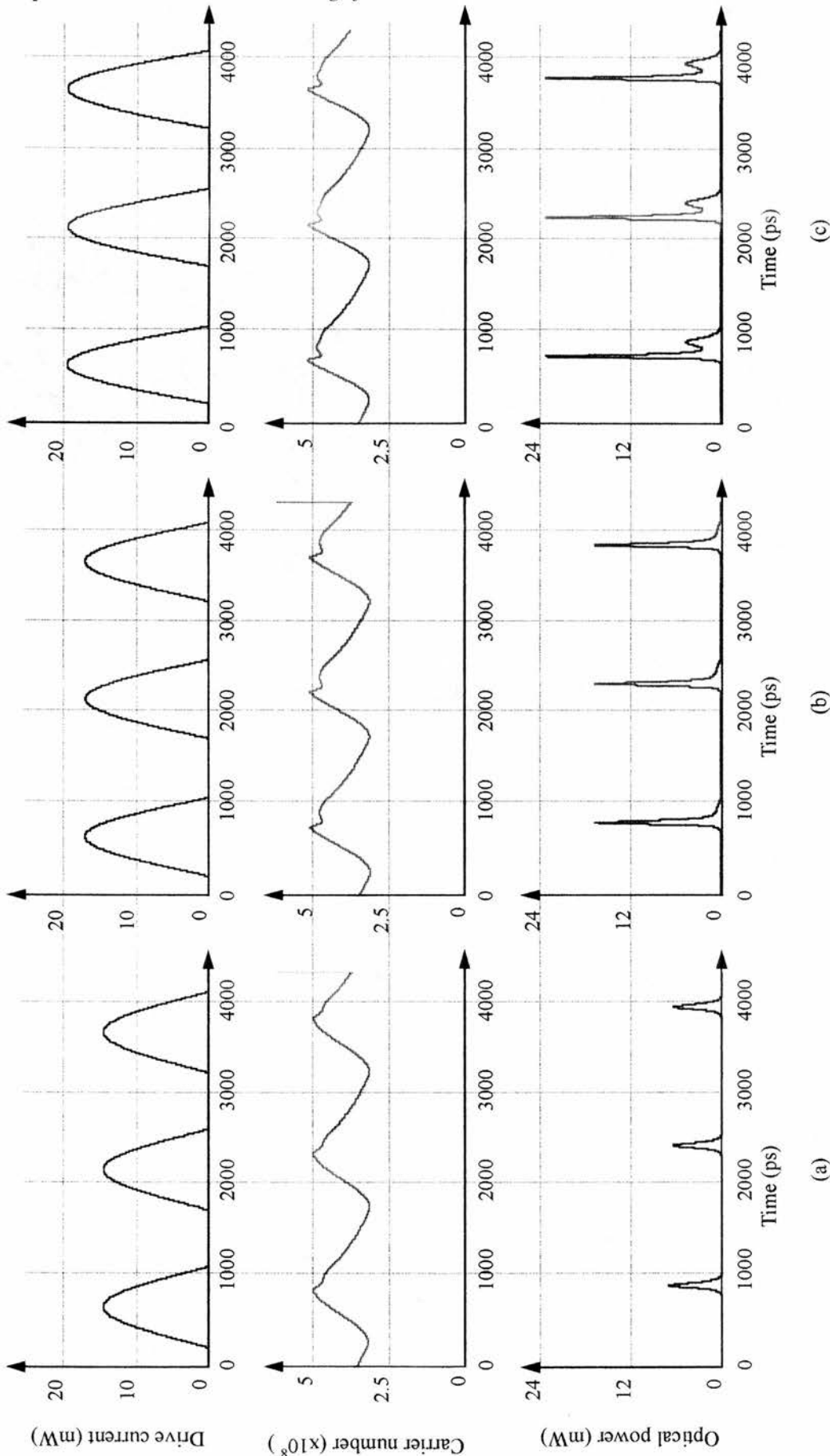


Figure 5.10. Temporal variation of drive current, carrier density and optical power for a range of RF currents: (a) 70mA; (b) 110mA; (c) 150mA. Pulse peak power increases and pulsewidth decreases as RF current increases. The modulation rate is 650MHz, dc bias is 25mA.

### 5.3 Jitter and frequency chirp

Although gain-switching is a simple and attractive means of producing high repetition rate, high peak power optical pulses in diode lasers, the technique suffers from several inherent weaknesses. Because the build-up of each pulse starts from randomly generated spontaneous photons, gain-switched pulses exhibit random fluctuations of the photon density in the laser cavity. This results in the excitation of many randomly phased axial modes producing an output which is in essence a noise burst. As a result, gain-switched lasers are susceptible to significant amounts of timing jitter (see Chapter 7).

A second problem that is especially relevant to bulk gain-switched lasers is the presence of frequency chirp<sup>18</sup>. Frequency chirp (or spectral broadening) is defined as the rate of change of the instantaneous frequency of the optical pulse. It arises as a result of variations of the carrier density which may cause the injection current to saturate the gain across the duration of the pulse. These variations can have considerable influence on the waveguiding of the laser and hence the effective refractive index of the guided wave. Laser chirp is usually characterised by calculating the duration-bandwidth product of the pulse and comparing the result with  $\Delta\tau\Delta\nu$  products for bandwidth limited pulses of a particular shape.

The problem of frequency chirp may be of reduced significance, however, with the development of single- and multiple-contact quantum-well lasers having a linewidth enhancement factor  $\alpha < 2$  (typical values of  $\alpha$  in most lasers lie in the range 3 to 5<sup>19</sup>). Apart from reducing frequency chirp, gain-switched QW lasers have the additional effect of reducing pulsewidth. By optimising the barrier thickness and the number of quantum wells, pulses less than 2ps have been reported<sup>20</sup>.



### 5.4 Experiment

Gain-switching was applied to two single-contact InGaAsP laser devices operating at 1550nm:

- i) a bulk,  $\lambda/4$  phase shifted, buried heterostructure DFB laser;
- ii) a bulk, buried heterostructure Fabry-Perot laser.

Both lasers were 400 $\mu\text{m}$  long with an 0.18 $\mu\text{m}$  active layer depth and 3.5 $\mu\text{m}$  ridge waveguides. The spontaneous emission coupling coefficient was  $1 \times 10^{-4}$ . The two lasers were antireflection (AR) coated.

Figure 5.11 shows the experimental arrangement used in the characterisation of gain-switched diodes. Laser output was monitored via a high speed InGaAs PIN photodiode (30ps response time) and RF spectrum analyser combination and an ultrafast synchroscan streak camera. An Anritsu MS96A optical spectrum analyser

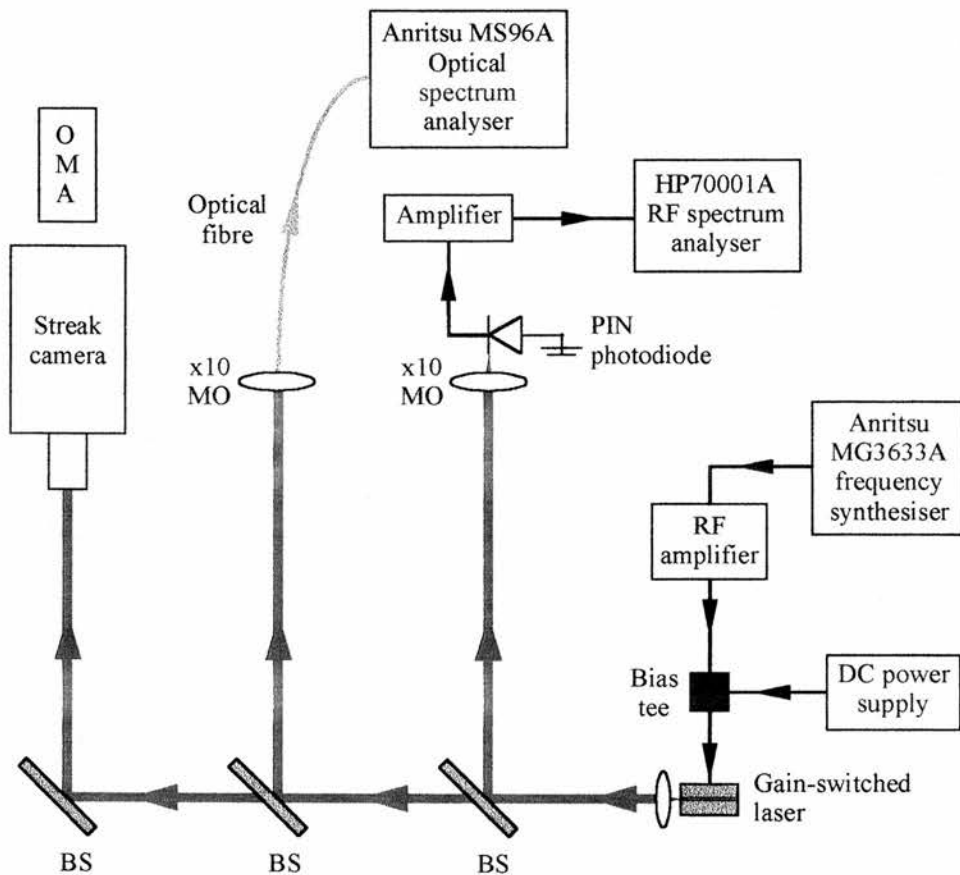


**Figure 5.11.** Experimental layout for the characterisation of gain-switched semiconductor lasers.

enabled the spectral characteristics of the lasers to be evaluated. Temperature control was by peltier cooling with an operating temperature of  $(16 \pm 0.1)^\circ\text{C}$  constantly maintained. Impedance matching was achieved via a  $47\Omega$  series resistor.

#### 5.4.1 Bulk, $\lambda/4$ phase shifted, buried heterostructure DFB laser

Gain-switched ultrashort pulse generation was implemented by superimposing a 650MHz RF modulation upon a dc bias current. A wide range of operating conditions were considered:

- i) three values of RF power were used to drive the gain: 11, 17 and 23dBm;
- ii) five values of dc bias current were generated for each value of RF power: 6, 9, 12, 15 and 18mA. The dc threshold was 33mA.

From the streak camera traces shown in Figure 5.12, the following characteristics of gain-switching were observed:

- i) as the dc bias current was increased, the laser demonstrated prominent relaxation oscillation behaviour, that is, with one or two satellite pulses. The number of relaxation peaks decreased with decreasing dc bias; eventually at a low bias only one gain-switched pulse was generated.
- ii) as the injection current was increased, the main pulse power saturated. Further pumping only served to enhance the subpulse or tail which resulted in the formation of a long wavelength spike on the optical spectrum (Figure 5.13).
- iii) the turn on delay preceding the relaxation oscillation decreased with increasing bias.
- iv) when only one gain-switched pulse was generated, the pulse width decreased with increasing bias until the secondary pulse appeared.

It can be seen from Fig. 5.12 that for a given value of RF power the pulses were seen to “walk forward” in time with increasing dc bias. This phenomenon was produced as a result of the superimposition of the RF signal onto the dc bias current. The threshold for laser oscillation was constant, but as the dc bias was increased, the RF sinusoid passed threshold earlier in the cycle and produced output pulses at an earlier time. The same effect was produced by increasing the RF power for a given dc bias current. At high RF, if the injection current was increased, the pulse formed earlier in time; but as the peak power increased the gain  $G$  saturated and the peak power of the pulse was limited. This process is known as gain saturation.

Typical spectral output is illustrated in Figure 5.13. For an injection current of 6mA there was no subpulse on the temporal output and the corresponding optical spectrum was clean (Figure 5.13(a)). As the injection current increased the main pulse power saturated and secondary pulses began to form. Further pumping only served to enhance the subpulse or tail which resulted in the formation of a long wavelength spike on the spectrum (Figures 5.13(a) and (b))

The DFB laser was also biased to produce optimum spectral output. Streak camera pulse and their corresponding “spikeless” spectra for such operating conditions are shown in Fig. 5.14 (a) and (b) respectively. Pulses were typically in the 25-40ps range and are in very good agreement with theoretical predictions (Fig 5.14(c)). It should be noted that the operating conditions which produce optimal spectral output simultaneously give rise to short, asymmetric temporal pulses with no subpulsing.

#### 5.4.2 Bulk, buried heterostructure Fabry-Perot laser

The single-contact Fabry-Perot laser was gain-switched as follows:

- i) the dc injection current was varied between 65 and 100mA, the dc threshold current for oscillation being around 114mA.
- ii) superimposed on each dc current were a series of three RF power values: 13, 8 and 3dBm.
- iii) as in the case of the DFB laser, the RF modulation frequency was 650MHz.

Pulse profiles obtained for each value of RF power are shown in Fig. 5.15(a). The characteristics are comparable with those obtained for the DFB laser and there was significant subpulsing in all three cases for currents above 85mA as a result of gain recovery. Pulsewidth decreased and peak power increased with both increasing RF power\* and increasing dc bias. The optical spectrum was highly multi-mode<sup>11,13,21</sup> the number of excited modes being dependent on the RF modulation frequency, the pumping conditions, the device structure and the spontaneous emission factor  $\beta$ . Theoretical temporal pulse profiles were produced for the experimental conditions listed above and are shown in Fig 5.15(b). As in the case of the DFB laser there is excellent agreement between theory and experiment.

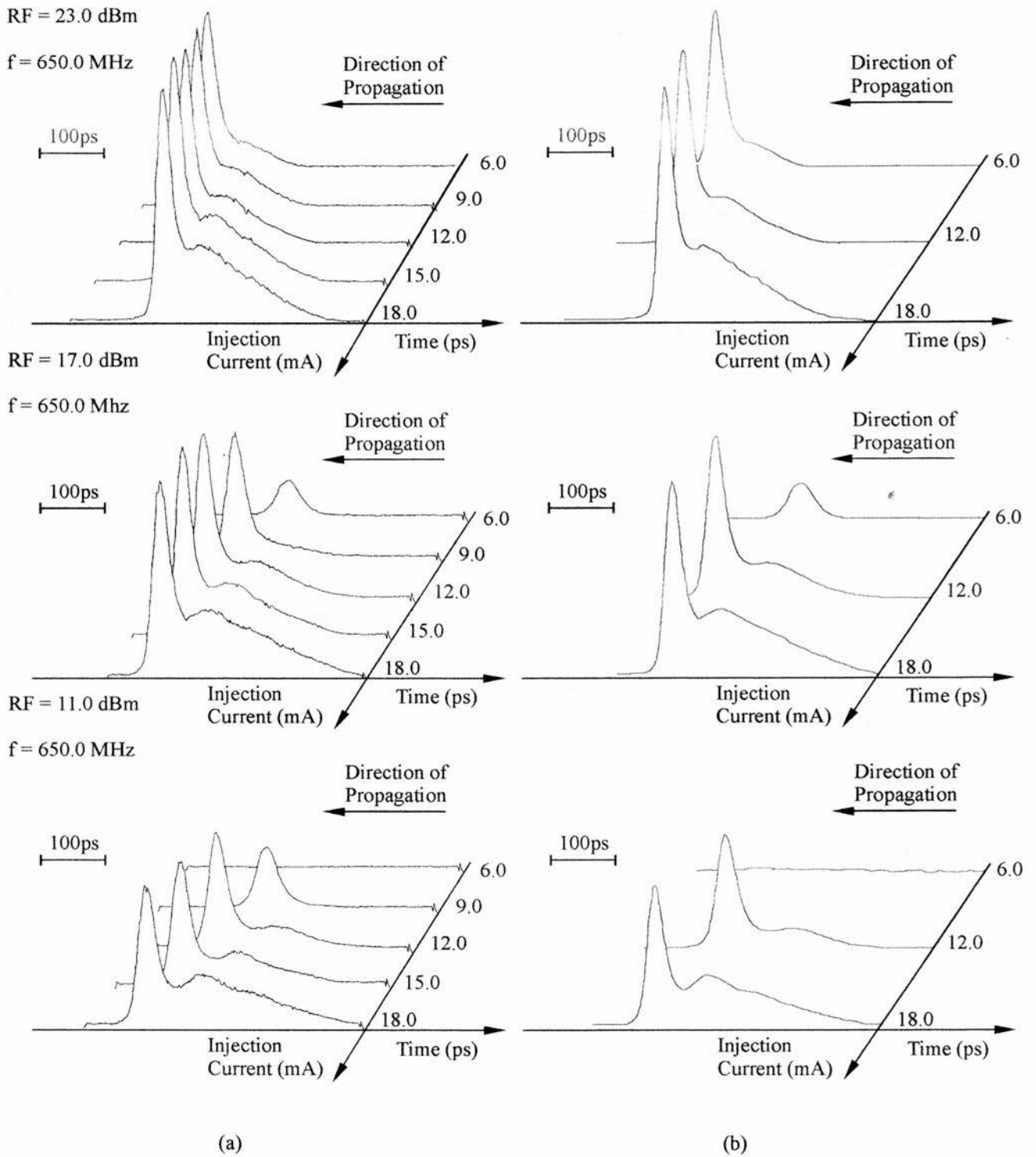
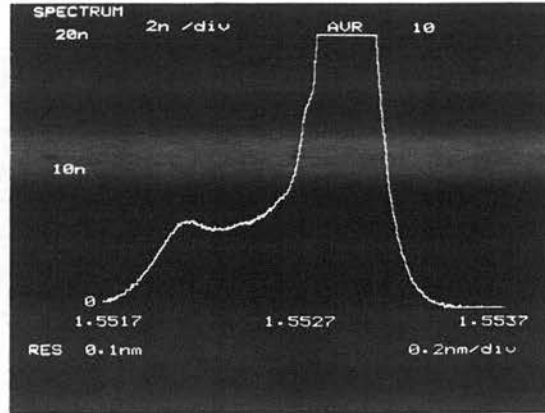
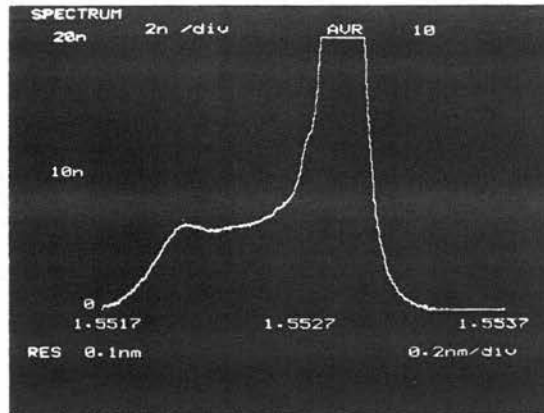


**Figure 5.12** Temporal pulse profile vs. injection current for a gain-switched, bulk,  $\lambda/4$  phase shifted, buried heterostructure DFB laser operating at 650MHz for several values of RF drive. Theoretical pulses (b) show good agreement with those obtained experimentally (a).

(a) Injection current = 18.0 mA



(b) Injection current = 12.0 mA



(c) Injection current = 6.0 mA

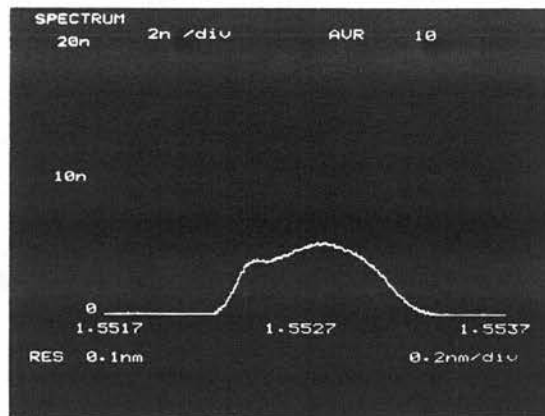


**Figure 5.13.** Optical spectra for a gain-switched, bulk,  $\lambda/4$  phase shifted, buried heterostructure DFB laser modulated at 650MHz.

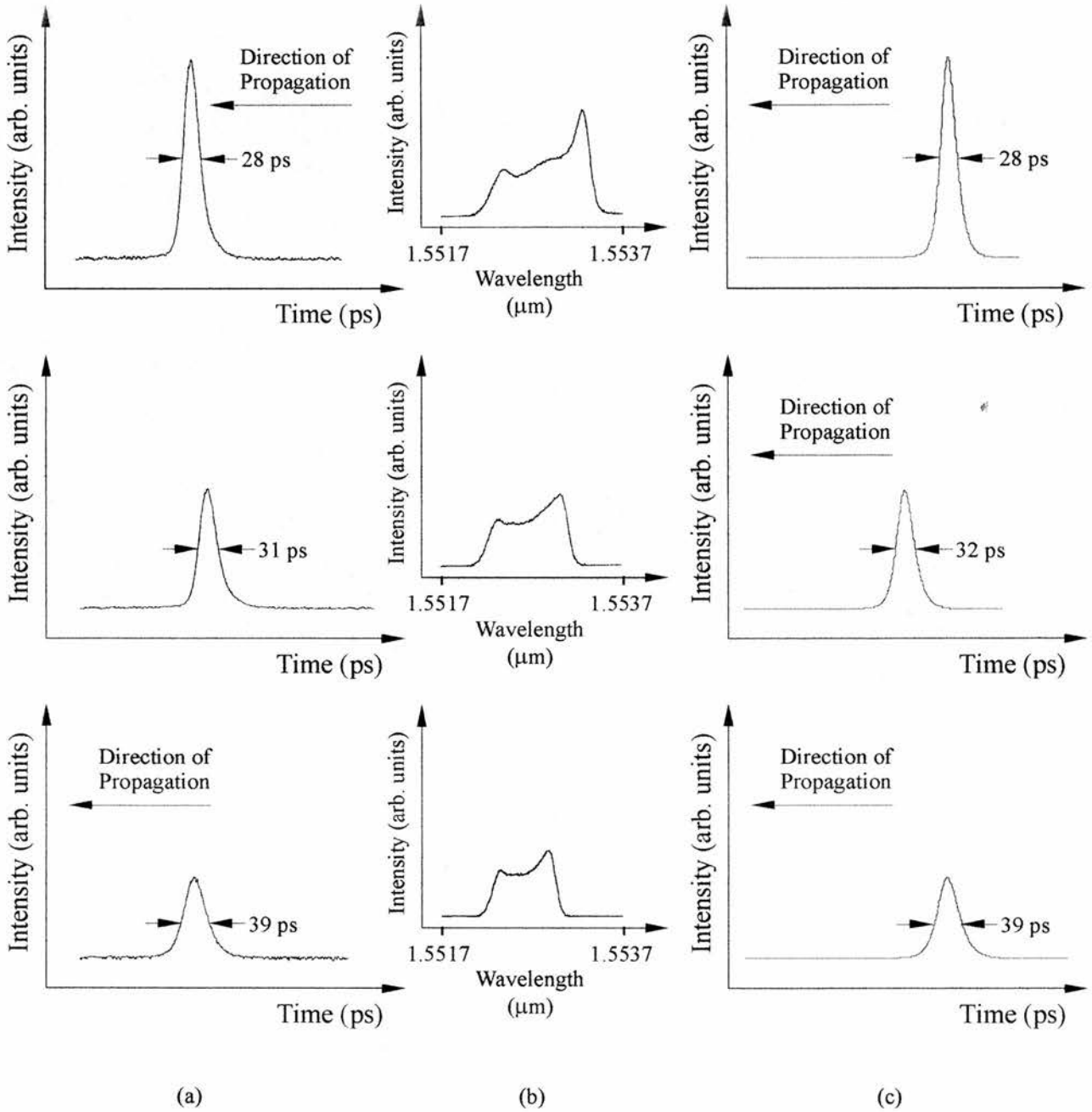


**Figure 5.14** Temporal pulse profiles (a) and corresponding optical spectra (b) for “spikeless” or clean spectral operating conditions. Three RF power scenarios are considered: 23dBm; 17dBm and 13dBm. Theoretical temporal pulses are compared in (c)

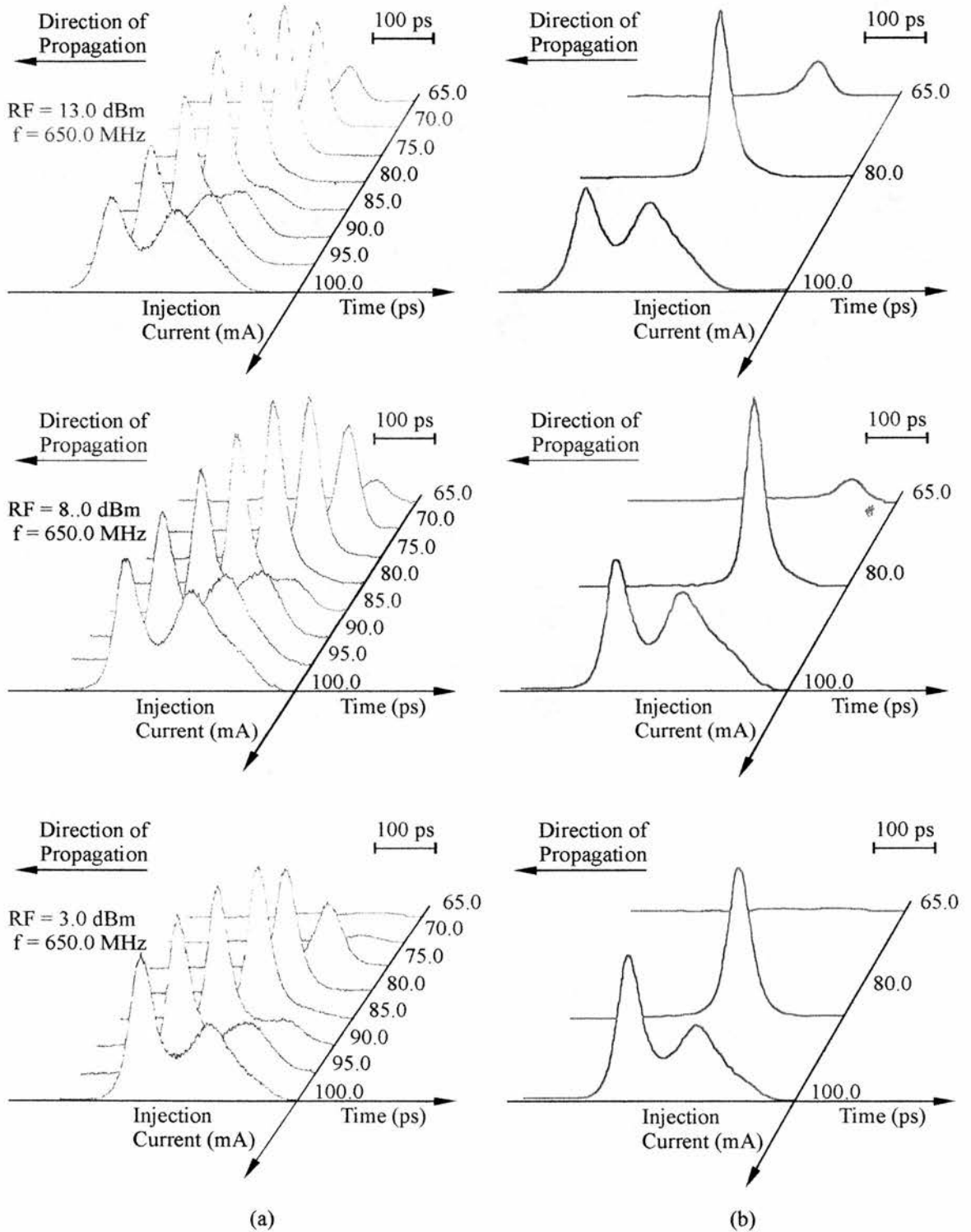


**Figure 5.15.** Temporal pulse profile as a function of gain section bias current for a gain switched, bulk, buried heterostructure Fabry-Perot laser operating at 650MHz for several values of RF drive. Theoretical pulses (b) show good agreement with those obtained experimentally (a).



## 5.5 Conclusions

In this chapter a description of the principles of gain-switching in semiconductor diode lasers has been given. A detailed theoretical model was developed (using nonlinear rate equations) to predict the temporal behaviour of gain-switched lasers for a wide range of operating conditions. A variety of gain-switched InGaAsP lasers were characterised experimentally and were shown to behave as predicted.

It has been shown that gain-switching is a very simple technique which, unlike modelocking, requires no external cavity. Moreover, the repetition rate of the optical pulses can be readily altered simply by changing the frequency of the RF drive. Unlike Q-switching, gain-switching can be implemented using diode lasers of any structure. Despite these advantages, gain-switching suffers from a number of drawbacks. The first of these is that it requires high RF modulation powers to drive the process and this can reduce the effective lifetime of the device. Pulse durations are limited to 20-30ps (i.e., of the order of several cavity round-trip times) because the pulsewidth is linearly related to the cavity length of the laser. Frequency chirp is also problematic in gain-switched lasers as a result of variations of the carrier density. This problem may be of reduced significance, however, with the development of quantum-well lasers.

A third method of picosecond pulse generation in semiconductor diode lasers is Q-switching. This method allows the production of ultrashort pulses having peak power several orders of magnitude greater than those produced by modelocking or gain-switching methodologies. However, specially fabricated devices are required for the Q-switching process which is analysed and discussed in Chapter 6.

## 5.6 References

1. N. Onodera N, H. Ito and H. Inaba, *Appl. Phys. Lett.*, **45**, 843 (1984).
2. C. Lin and T.L. Koch, *Electron. Lett.*, **21**, 958 (1985).
3. H. Sundaresan and G.E. Wickens, *Electron. Lett.*, **26**, 725 (1990).
4. I.H. White, P.S. Griffin, M.J. Fice and G.E.A. Whiteaway, *Electron. Lett.*, **28**, 1257 (1992).
5. R.W. Hellwarth, *Advances in Quantum Electronics*, J.R. Singer, Ed., New York: Columbia University Press, 334 (1961).
6. N.G. Basov, V.N. Morozov, V.V. Nikitin and A.S. Semenov, *Sov. Phys. Semcond.*, **1**, 1305 (1968).
7. K.Y. Lau, *Appl. Phys. Lett.*, **52**, 257 (1988).
8. C. Lin, L. Liu, T.C. Damen, D.J. Eilenberger and R.L. Hartman, *Electron. Lett.*, **15**, 600 (1980).
9. T. Kobayashi, A. Yoshikawa, A. Morimoto, Y. Aoki and K. Sueta, *Tech. Digest Papers 11<sup>th</sup> Int. Quan. Electron. Conf.*, **W1** (1980).
10. E.O. Gobel, G. Veith, J. Kuhl, H.-U. Habermeier, K. Lubke and A. Perger, *Appl. Phys. Lett.*, **42**, 25 (1983).
11. P.M. Downey, J.E. Bowers, R.S. Tucker and E. Agyekum, *IEEE J. Quan. Electron.*, **QE-23**, 1039 (1987).
12. D. Bimberg, K. Ketterer, H.E. Scholl and H.P. Vollmer, *Electron. Lett.*, **20**, 34 (1984).
13. H. Ito, H. Yokoyama, S. Murata and H. Inaba, *Electron. Lett.*, **15**, 738 (1979).
14. J. AuYeung, *Appl. Phys. Lett.*, **38**, 308 (1981).
15. C. Lin and J.E. Bowers, *Electron. Lett.*, **21**, 1200 (1985).
16. I.H. White, D.F.G. Gallacher, M. Osinski and D. Bowley, *Electron. Lett.*, **21**, 197 (1985).
17. L.Chusseau, J.M. Xie, L. Du villaret, J.M. Lourtioz, A. Accard and J.-P.Hebert, *Electron. Lett.*, **26**, 1085 (1990).
18. D. Bimberg, K. Ketterer, H.E. Scholl and H.P. Vollmer, *Electron. Lett.*, **20**, 343 (1984).
19. C. Lin, T.P. Lee and C.A. Burrus, *Appl. Phys. Lett.*, **42**, 141 (1983).
20. M. Osinski and J. Buus, *IEEE J. Quan. Electron.*, **QE-23**, 9 (1987).
21. T. Sogawa and A. Arakawa, *IEEE J. Quan. Electron.*, **QE-27**, 1648 (1991).
22. P. Liu, C. Lin, I.P. Kaminow and J.J. Hsieh, *IEEE J. Quan. Electron.*, **QE-17**, 671 (1981).

# Chapter 6

## FORCED Q-SWITCHING OF MULTIPLE-CONTACT SEMICONDUCTOR DIODE LASERS

### 6.1 Introduction

Active modelocking can generate shorter pulsewidths (10 - 50ps) than those produced using either gain-switching, Q-switching or other modelocking methods, but it has the significant disadvantage of requiring an external cavity. Although peak pulse powers of 60mW have been routinely measured using this technique, reduced pulse energies of 0.3 pJ are typical<sup>1</sup>. Gain-switching of multi-contact devices<sup>2-4</sup> generates low-linewidth ultrashort pulses (20-30ps), but typical pulse powers are

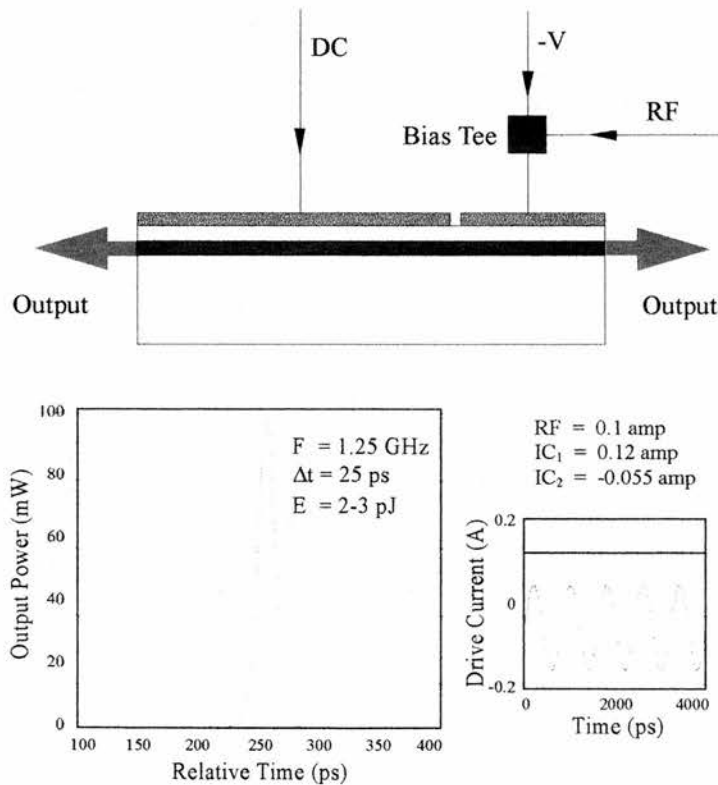


**Figure 6.1.** Schematic representation of ultrashort pulse production via forced Q switching using a two contact InGaAsP device. The long gain section is strongly forward biased using dc current. The short absorber contact is driven by superimposing a strong RF modulation onto a reverse dc bias.

limited to around 10mW, with corresponding pulse energies of 0.3pJ. However, many optoelectronic and communications applications require high-power picosecond pulses at the 1300 and 1550nm wavelength regions. Despite the fact that Q-switching requires the use of specially fabricated diode laser chips, this technique allows the generation of ultrashort pulses having peak powers greatly in excess of those obtained by modelocking and gain-switching. For example, peak pulse powers of 80mW and pulse energies of 2.1pJ are possible for 26ps pulses at repetition rates of 1.25GHz using forced Q-switching<sup>5</sup>.

Figure 6.1 shows a schematic of a forced Q-switched laser. The long (gain) section is strongly forward biased and laser oscillation is frustrated via current control of the short (absorber) section. The quality, Q, of the resonator is switched by superimposing a strong RF modulation onto a reverse bias dc current.

## 6.2 Q-switching regimes

The principle of Q-switching is illustrated in Figure 6.2. While the laser population inversion (or gain) builds up, a low Q (or high loss) cavity frustrates laser oscillation and carrier depletion of the population inversion is minimal. As the carrier density in the laser reaches its peak, the cavity is rapidly switched to a high Q state, such that stimulated emission builds up quickly, the population is depleted and the stored energy is emitted in the form of an ultrashort optical pulse. Population depletion continues until either the loss recovers (due to high pumping conditions) or the cavity is switched to a low Q.

Q-switching is an excellent technique for the generation of high power, high energy picosecond optical pulses from diode lasers. There are two main techniques by which this approach may be realised: passive and active Q-switching.

### 6.2.1 Passive Q-switching

Passive Q-switching<sup>6-8</sup> employs an arrangement with a reversible saturable absorber located in the laser cavity. There is no external modulation source, the repetition rate, pulsewidth and peak power of the optical pulse being determined by

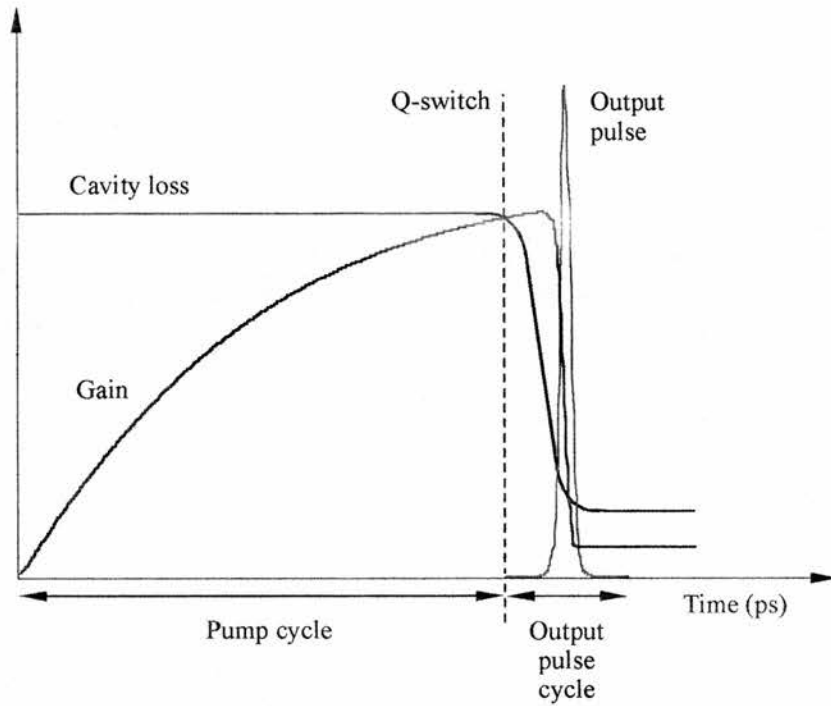


**Figure 6.2.** Schematic illustration of Q switching showing the temporal evolution of cavity loss (or Q), gain (or inversion) and the output laser pulse.

the pumping conditions and the laser parameters. It has been shown<sup>9,10</sup> that for effective passive Q-switching, the ratio of the differential gain of the amplifier section should be less than the differential loss of the absorber; i.e.,  $\frac{dg/dn}{da/dn} < 1$ . Also, the carrier lifetime of the absorber section should be less than that of the gain section of the laser<sup>9-11</sup> (that is,  $\frac{\tau_g}{\tau_a} > 1$ ). Recovery of the absorber relies on spontaneous recombination of excited electron-hole pairs and absorber lifetime. Thus  $\tau_a$  may be minimised by proton bombardment of the laser material near the facets<sup>7,12</sup> to introduce a small area of saturable absorption with an extremely short carrier lifetime. Alternatively, ion implantation may be used to produce saturable absorption<sup>13</sup>. A third option is to employ multi-contact device structures<sup>5,14-26</sup>.

### 6.2.2 Active Q-switching

Active Q-switching is initiated when the switching is implemented via an external source, usually an optical or electrical drive. It is normally realised using multiple-contact devices, the most common geometry being a three-contact laser<sup>17</sup> having a long section strongly forward biased to provide gain, a short modulator section reverse biased to generate optical loss and a passive waveguide section between the two. In this regime, the pulse repetition rate is determined by an external RF source. Figure 6.3 illustrates active (forced) Q-switching in which the RF signal is applied to a reverse-biased absorber section while inversion is established in a longer gain section. Only the actively Q-switched regime will be considered in this thesis, specifically forced Q-switching.

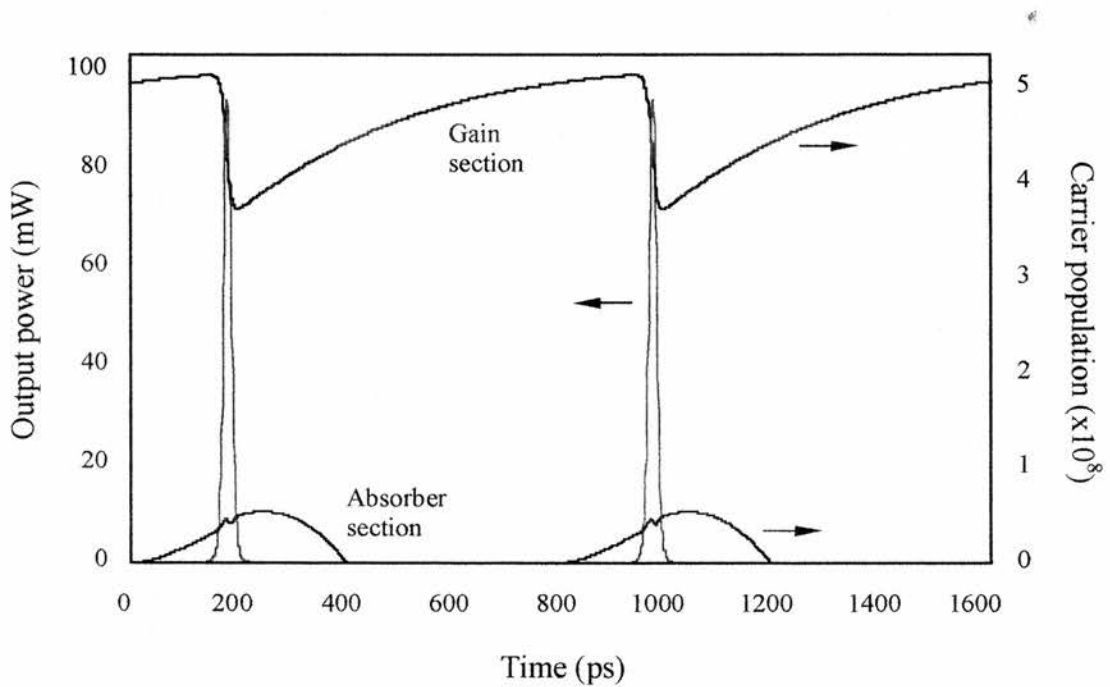


**Figure 6.3.** Schematic illustration of carrier dynamics and optical output for a two-contact forced Q-switched laser. The long (gain) section is strongly forward biased and the short section is driven by superimposing a strong RF modulation onto a reverse bias injection current.

### 6.3 Theoretical model

The schematic diagram of an actively Q-switched two-contact laser is shown in Figure 6.1. The laser is divided into two sections with different pumping currents  $I_1$  (for the longer gain section) and  $I_2$  (into the short absorber section). The absorber section is driven by a strong RF modulation superimposed onto a reverse biased dc current. A set of carrier and photon rate equations can be used to describe the dynamic performance of the laser system. For a two-contact laser system:

$$\frac{dN_1}{dt} = \frac{\eta I_1}{ed} - AN_1 - B_1 N_1^2 - C_1 N_1^3 - v_g \frac{dg}{dN_1} \left[ \frac{N_1 - N_0}{1 + \epsilon_1 P} \right] P \quad (6.1)$$

$$\frac{dN_2}{dt} = \frac{\eta I_2}{ed} - AN_2 - B_2 N_2^2 - C_2 N_2^3 - v_g \frac{dg}{dN_2} \left[ \frac{N_2 - N_0}{1 + \epsilon_2 P} \right] P \quad (6.2)$$

$$\frac{dP}{dt} = \Gamma \beta (B_1 N_1^2 + B_2 N_2^2) - \Gamma v_g \left\{ \frac{dg}{dN_1} \left[ \frac{N_1 - N_0}{1 + \epsilon_1 P} \right] + \frac{dg}{dN_2} \left[ \frac{N_2 - N_0}{1 + \epsilon_2 P} \right] \right\} P - \frac{P}{\tau_p} \quad (6.3)$$

*MathCad* computer simulations were generated (see Appendices) using the semiconductor laser rate equations 6.1, 6.2 and 6.3 in order to model the performance of carrier density, output power and pulsewidth of a given laser for a wide variety of drive currents and device parameters. Here, the rate equations were developed for photon density in the laser cavity and two carrier densities in each of two parts of the diode were adopted for modelling the two-section devices. Similar assumptions were made as in the case of the gain-switching model. Typical values used in the numerical model are similar to those used for the simulation of gain-switched lasers shown in Table 5.1.

## 6.4 Theoretical results

Figure 6.3 shows a typical calculated temporal dependence of the carrier densities and the output power in the gain and absorber sections of the laser. The gain section is strongly forward biased and laser oscillation is frustrated by the reverse biased absorber section and laser action is impeded. As the RF signal increases, the injected carrier density of the absorber rises above threshold, the resonator Q is switched and optical output is produced. The rapidly increasing light signal saturates the gain via stimulated emission, carrier density growth is repressed and laser oscillation ceases as the carrier density is pulled below threshold. When the ultrashort pulse is emitted, stimulated emission is the dominant mechanism and the contribution of all other processes, including spontaneous emission, carrier pumping and recombination are negligible. The RF modulation then decreases the absorber carrier density and the gain recovers through threshold due to current injection. If the RF signal is strong enough to increase the carrier density above threshold for a significant period of time then the gain can recover sufficiently quickly and subpulsing can occur.

Peak output power is determined by the peak carrier concentration in the gain section just before Q-switching. Because of the strong depletion of carriers caused by the optical pulse, clean Q-switched pulses may be produced without any trailing structure or satellite pulses. Carrier population in the gain region during Q-switching typically varies between  $(2.0 \text{ to } 5.5) \times 10^{18} \text{ cm}^{-3}$ . Thus, a strong dynamic gain saturation, a low level of carrier density just after pulse emission and an additional loss due to the absorber are the principal requirements for the generation of output pulses having clean intensity profiles. Typically, the pulse shape is asymmetrical, the leading edge of the pulse being 30 - 50% shorter than the trailing edge. The pulse repetition rate is determined solely by the frequency of the RF modulation.

Figure 6.4 illustrates the variation of pulsewidth and peak power as the amplitude of the RF modulation is varied. The simulated device was a  $400\mu\text{m}$  ( $300\mu\text{m}$  gain section,  $100\mu\text{m}$  absorber), two-contact InGaAsP device modulated at 650MHz. The figure shows the strong effect of the RF amplitude on the peak power



and the minimal influence on pulsewidth. In this case calculations indicate pulsewidths between 10 to 20ps. Typical values of peak power are predicted to lie between 80 and 300mW.

Data relating to the variation of pulsewidth and peak power with applied gain section dc bias  $I_1$  are shown in Figure 6.5 for the device described above. Threshold current was measured at 15mA at a modulation frequency of 650MHz. The figure predicts that peak power will increase and pulsewidth will reduce as the gain bias is increased. A typical pulsewidth lies in the range of 10 to 20ps. Peak powers range between 200 and 400mW.

The parameters in Figures 6.4 and 6.5 are plotted for two values of the nonlinear gain coefficient,  $\epsilon$ . Gain compression has a strong influence on both peak power and pulsewidth. This effect is demonstrated in Figure 6.6 where peak power and pulsewidth are plotted as a function of  $\epsilon$ . The gain bias is 120mA, absorber bias – 55mA, RF amplitude 200mA and the repetition rate 1.3GHz. The peak power decreases and pulsewidth increases with nonlinear gain saturation. This is an extremely important observation because the nonlinear gain sets the limit for the minimum achievable pulsewidth and the maximum attainable power of the Q-switched pulses.

Another important parameter which significantly affects the laser dynamics is the differential gain coefficient,  $g_0$  (or  $dg/dN$ ). Figure 6.7 illustrates the dependence of the parameters of Q-switched laser pulses on  $g_0$ . This figure shows that pulsewidth decreases and peak power increases as the differential gain coefficient is increased. Consequently, the generation of shorter, higher power output pulses require devices having high values of differential gain. Thus Q-switched multi-quantum well (MQW) lasers have greater potential to produce such pulses than bulk devices, but nonlinear gain saturation effects must be simultaneously minimised.

## 6.5 Spectral performance

Q-switching may excite many longitudinal modes in the diode laser cavity as a consequence of the dynamic overshoot of electron concentration and the variation of carrier density during optical pulse emission. For a Q-switched laser, typical optical spectra comprise several longitudinal modes<sup>6,7,20</sup>. A typical optical spectrum of a Q-switched laser is very similar to that of a gain-switched laser.

Single frequency lasers (for example, distributed Bragg reflector (DBR) or distributed feedback (DFB) lasers<sup>3,24</sup>) allow reduction of the spectral bandwidth of Q-switched optical pulses. Alternatively, good spectral control of Q-switched Fabry-Perot lasers may be achieved by placing the laser in a diffraction-grating-based external cavity. Good spectral control is possible at the expense of a significant reduction in peak power and a degree of pulse broadening

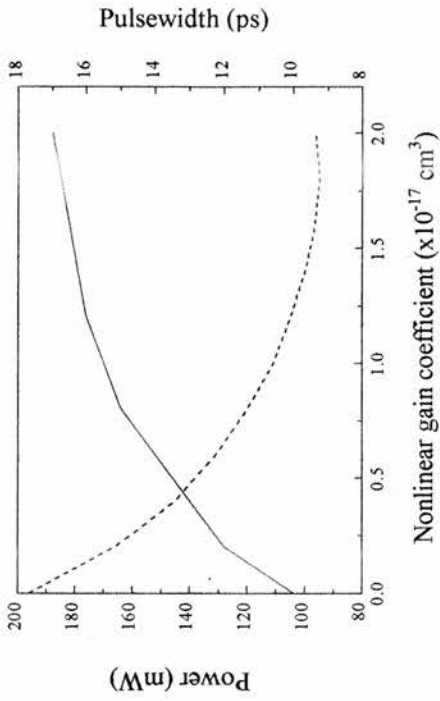


Figure 6.6. Effect of variation in nonlinear gain coefficient E on peak power (dotted line) and pulsewidth (solid line).

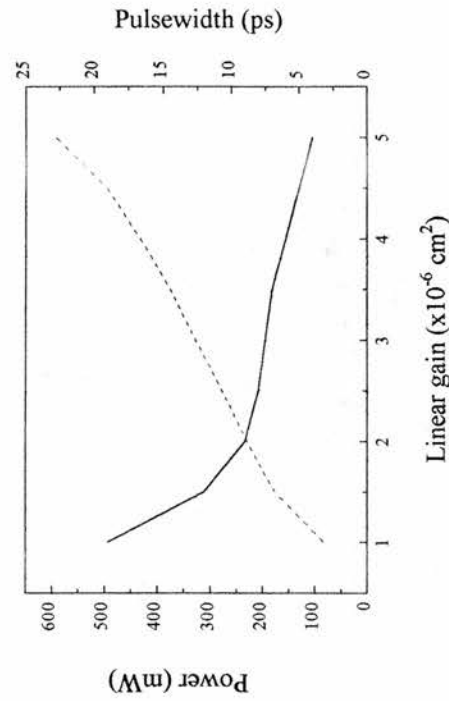


Figure 6.7. Calculated peak power (dotted line) and pulsewidth (solid line) as a function of linear gain coefficient G.

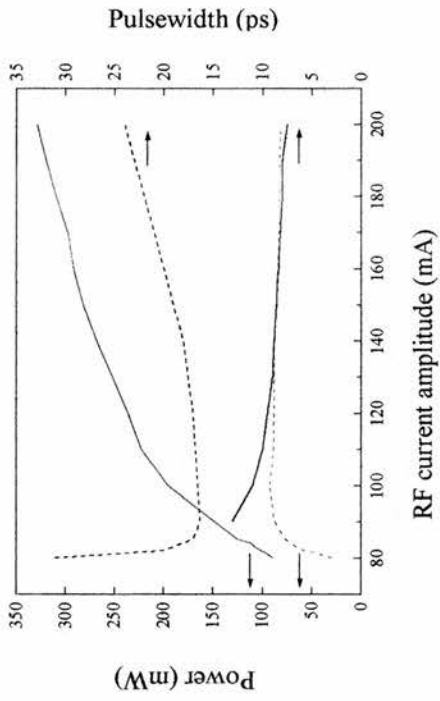


Figure 6.4. Peak power and pulsewidth variation for different values of RF drive current amplitude. The nonlinear gain coefficient E is 0 (solid line) and  $2 \times 10^{-17} \text{ cm}^3$  (dotted line).

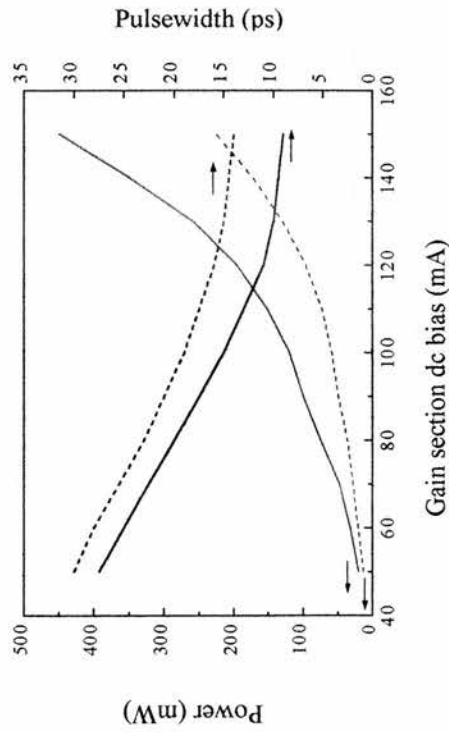


Figure 6.5. Variation of calculated peak power and pulsewidth with gain section dc bias. The nonlinear gain coefficient E is 0 (solid line) and  $2 \times 10^{-17} \text{ cm}^3$  (dotted line).

## 6.6 Experiment

Forced Q-switching was applied to three multi-contact diode lasers (see Fig 1.9 for the basic structure of a 3-contact device):

- i) a 405 $\mu\text{m}$  long, two-contact, Fabry-Perot (FP), multi-quantum well (MQW) device comprising six InGaAsP quantum wells and five barriers. The 300 $\mu\text{m}$  contact was forward biased to provide gain and the 100 $\mu\text{m}$  section supplied absorption. This device operated at a nominal wavelength of 1550nm.
- ii) a 410 $\mu\text{m}$  long, three-contact, FP, MQW device consisting of six InGaAsP quantum wells and five barriers. Contact geometry was 100/200/100 $\mu\text{m}$ . The longer central section was biased to provide gain and the two end (absorber) contacts were joined together electrically off-chip to give a gain/absorber ratio of 1:1. This device also operated at 1550nm.
- iii) a 250 $\mu\text{m}$  long, three-contact, bulk, DFB, GaAs device operating at 880nm. Laser contact geometry was 100/40/100 $\mu\text{m}$ . The two end-contacts were joined off-chip and formed the gain section. The small central contact provided absorption.

Contact separation in all three cases was 5 $\mu\text{m}$ . Antireflection coatings on one facet provided a residual reflectivity of less than 0.1%. The output facet had a reflectivity of 35%.

Forced Q-switching of multi-contact structures involved the application of a strong forward bias dc current to the gain section of the device. Laser oscillation was frustrated via current control of the absorber section: the resonator Q was switched by

applying a strong radio-frequency (RF) modulation in conjunction with a reverse bias dc current.

Figure 6.8 shows the experimental arrangement used for the characterisation of Q-switched diodes. The temporal output from the laser was monitored via an ultrafast synchroscan streak camera and an optical multi-channel analyser (OMA). The streak camera resolution was 5ps. An Anritsu MG3633A synthesised signal generator was used to drive both the laser device and the streak camera system. An Anritsu MS96A optical spectrum analyser enabled the spectral characteristics of the

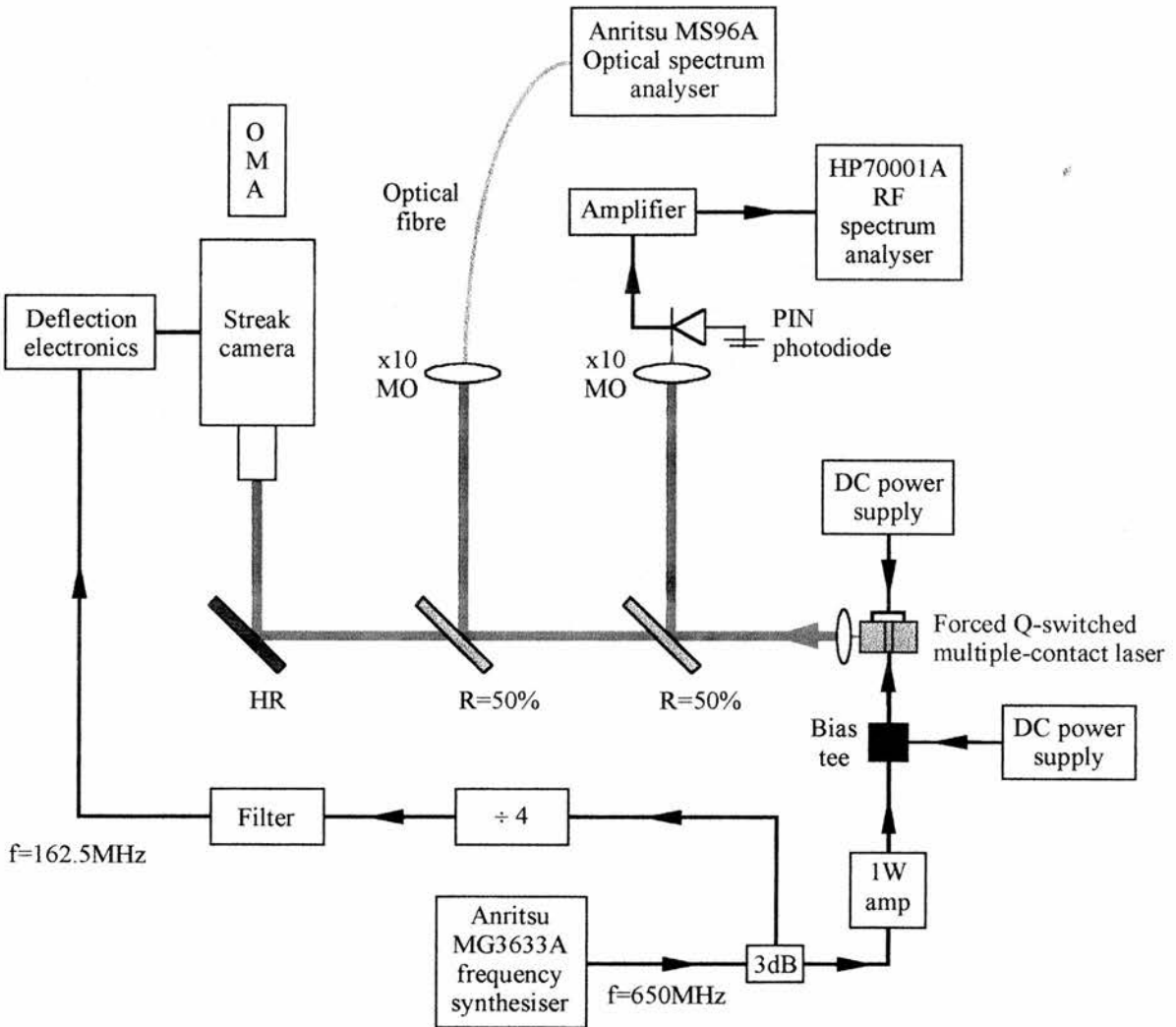


Figure 6.8 Experimental arrangement for the operation and characterisation of forced Q-switched multi-contact semiconductor diode lasers.

lasers to be evaluated. Temperature control was by Peltier cooling and an operating temperature of  $(16 \pm 0.1)^\circ\text{C}$  was sustained. Impedance matching was achieved via a  $47\Omega$  series resistor.

### 6.6.1 Two-contact MQW InGaAsP FP laser (100/300 $\mu\text{m}$ )

Forced Q-switching was implemented by providing forward dc bias to the (300 $\mu\text{m}$ ) gain contact while RF modulation was superimposed onto a reverse dc bias and applied to the (100 $\mu\text{m}$ ) absorber contact. A wide range of operating conditions were examined:

- i) three values of RF modulation: 3, 0 and -3dBm.
- ii) a series of gain section bias currents were applied:  $I_1 = 40, 50$  and  $60\text{mA}$  for each RF modulation setting.
- iii) absorber current  $I_2$  was adjusted between +1 and -3.5mA for each gain section bias current.
- iv) the RF modulation frequency was 650MHz.

Streak camera data illustrating temporal output are shown in Figure 6.9 (i)(a), (ii) and (iii). It is clear that an increase in gain section bias current ( $I_1$ ) leads directly to an increase in peak output power and a reduction in pulsewidth as predicted by Figure 6.5. For example, for a gain section bias of 60mA, absorber bias of -1.27V at 0dBm, the output pulsewidth was 24ps with an average power of 1.8mW and a peak power of 61mW (Figure 6.9 (ii)). However, a further increase in gain bias led to the formation of secondary pulses as the peak power saturated. Further increase in pumping served only to encourage the onset of a parasitic subpulse or trailing edge feature. When only one discrete pulse was generated, the pulsewidth decreased with increasing bias until the secondary pulse appeared.

By increasing the RF power, shorter pulsewidths with higher peak powers were achieved. For a given RF power and gain bias, it was possible to adjust the absorber bias to give the desired degree of symmetry in the output waveform,

decreasing the rise time of the front edge and removing unwanted satellite pulses. As was the case for gain-switching, the Q-switched pulses advanced forward in time as the gain bias current was increased. The pulsewidths increased and peak powers decreased with decreasing RF amplitude as predicted by Figure 6.4. Theoretically simulated output pulses are shown for all three values of gain bias for the laser operating at 3dBm (Figure 6.9 (i)(b)) and show excellent agreement with experimental results thereby reinforcing the validity and accuracy of the simple theoretical model. Figures 6.9 (ii) and (iii) show temporal intensity performance for laser operation at RF powers of 0dBm and -3dBm respectively.

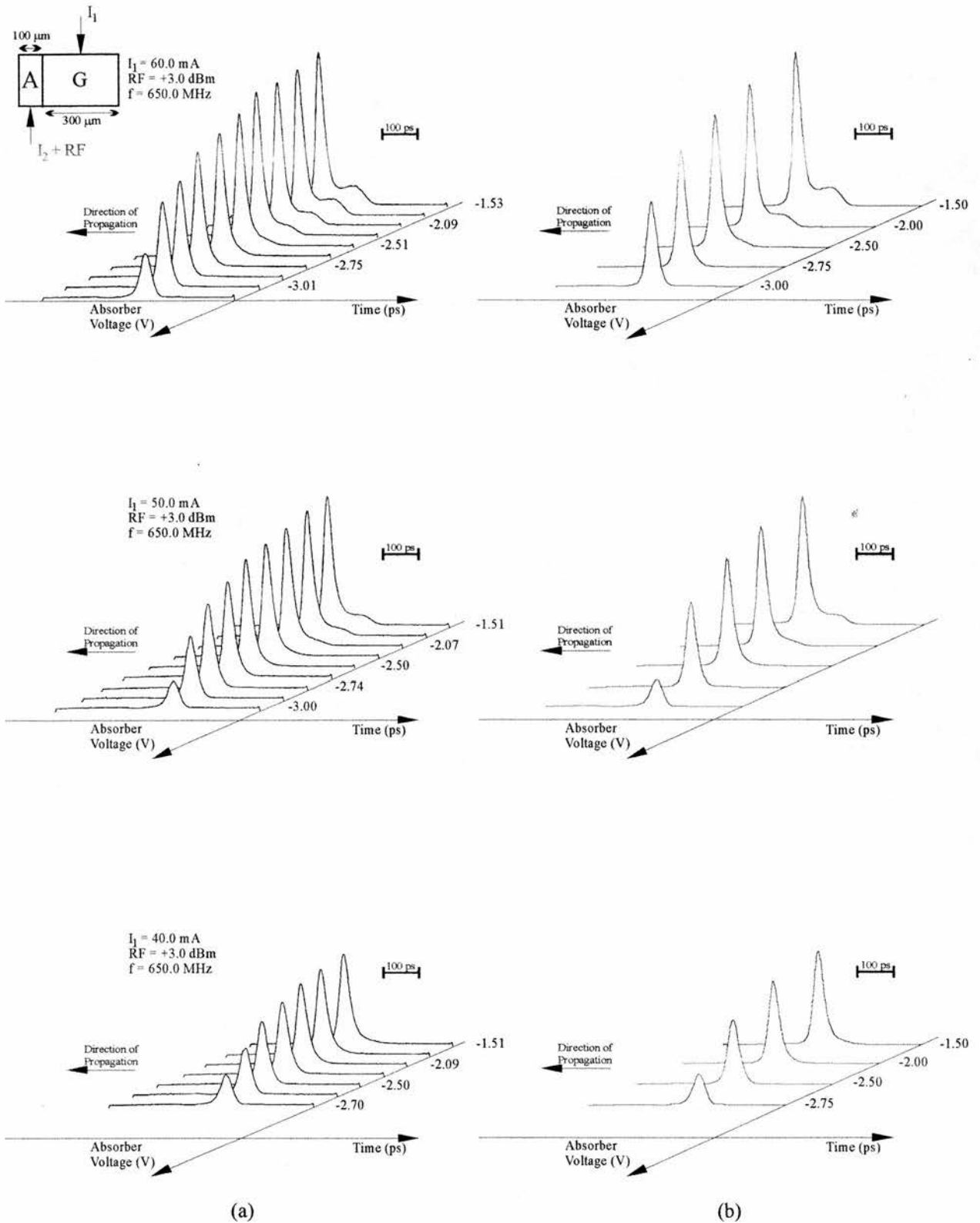


**Figure 6.9 (i).** Temporal pulse profile as a function of absorber voltage for a forced Q-switched, MQW, 2-contact, Fabry-Perot InGaAsP laser operating at 650 MHz, 3dBm absorber modulation for several values of gain current. Experimental results are shown on the left (a) with corresponding theoretical profiles on the right (b). There is extremely good agreement between the experimental and theoretical traces.



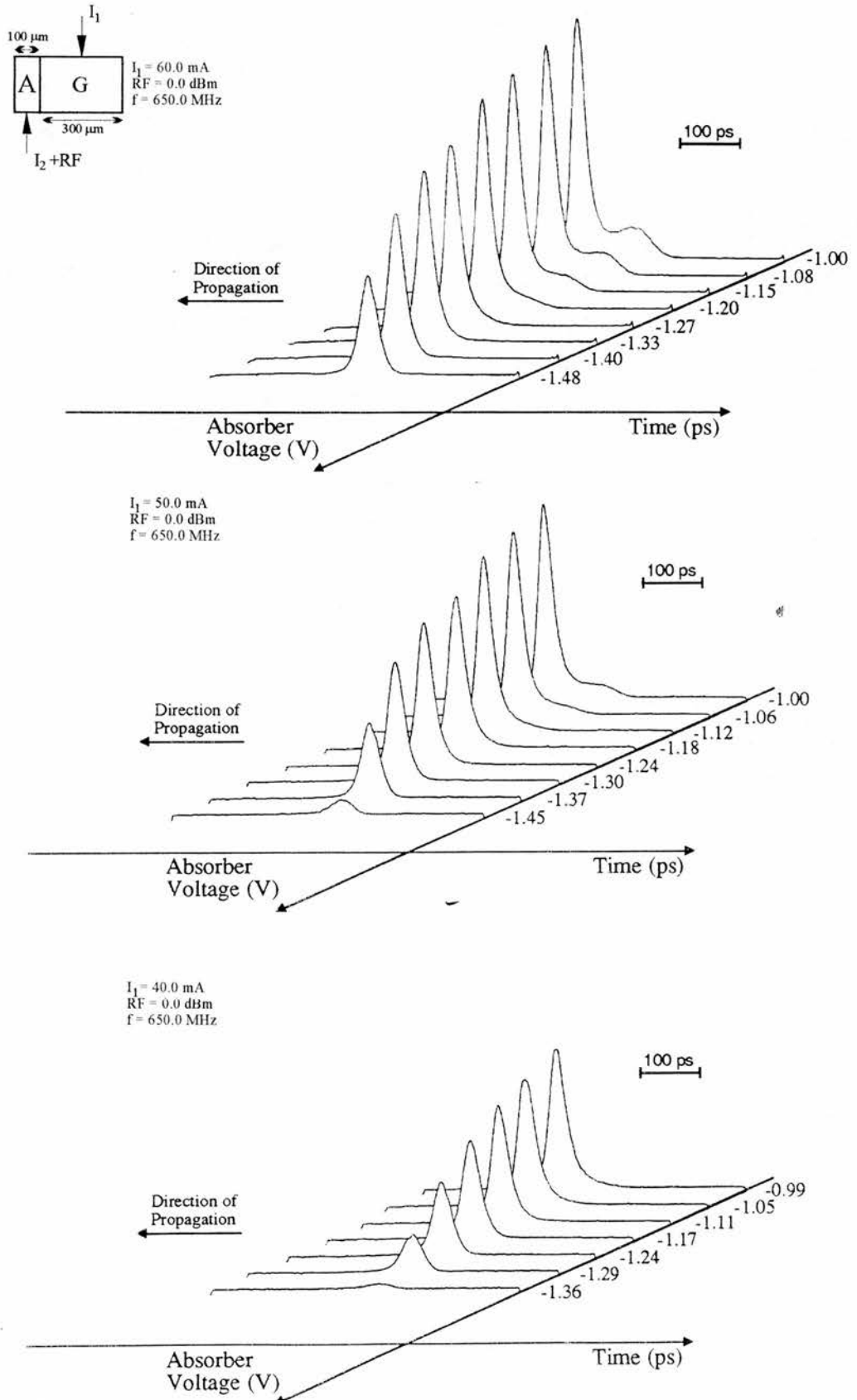


**Figure 6.9 (ii).** Temporal pulse profile as a function of absorber voltage for a forced Q-switched, MQW, 2-contact, Fabry-Perot InGaAsP laser operating at 650 MHz, 0dBm absorber modulation for several values of gain current.

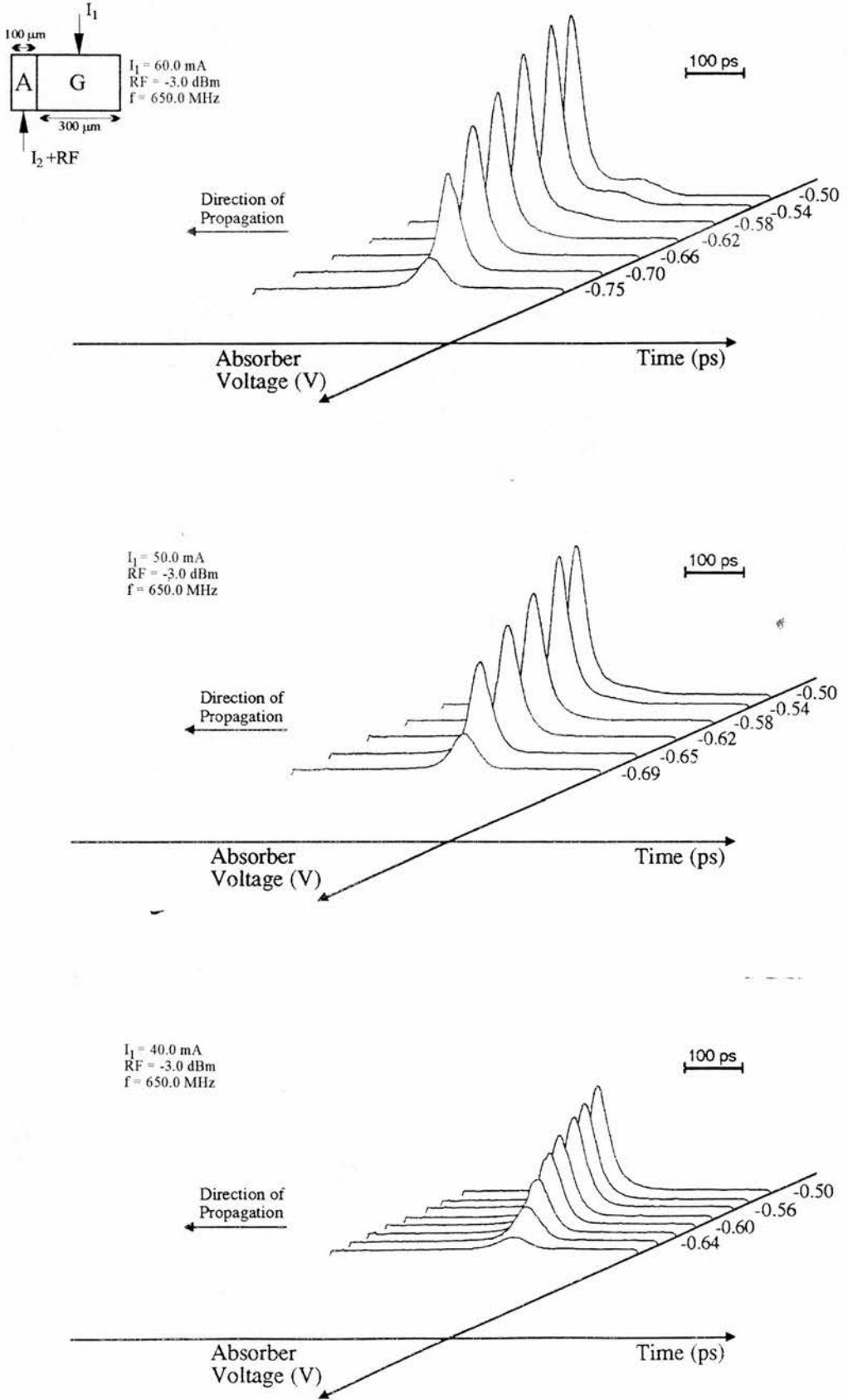


**Figure 6.9 (iii).** Temporal pulse profile as a function of absorber voltage for a forced Q-switched, MQW, 2-contact, Fabry-Perot InGaAsP laser operating at 650 MHz, -3dBm absorber modulation for several values of gain current.

### 6.6.2 Three-contact MQW InGaAsP FP laser (100/200/100 $\mu\text{m}$ )

For the three-contact device, the two 100 $\mu\text{m}$  end contacts were joined off-chip and formed the absorber section. As before, a comprehensive set of operating conditions were considered:

- i) three values of RF modulation: 3, 0 and -3dBm.
- ii) three values of gain current,  $I_1$ : 80, 60 and 40mA for each value of RF modulation.
- iii) absorber current  $I_2$  was varied between +1 and -6mA and the corresponding absorber voltage measured.
- iv) the repetition rate was 650MHz.

Streak camera data showing temporal intensity profiles were obtained for the above parameters and are shown in Figure 6.10 (i)(a), (ii) and (iii). These data are similar to that generated by the two-contact device in that increasing the gain bias and increasing the RF power resulting in shorter pulsewidths and higher peak powers. For this device, a gain section bias of 80mA, absorber bias of -2.77V at 3dBm, produced an output pulsewidth of 23ps with an average power of 2.6mW and a peak power of 92mW. Theoretical output pulses are shown for the three values of gain bias for the laser operating at 3dBm (Figure 6.10 (i)(b)) and, as before, show excellent agreement with experimental results. Figures 6.10 (ii) and (iii) show temporal intensity performance for laser operation at RF powers of 0dBm and -3dBm respectively.

This device was also driven using centre-contact modulation. In this instance, the two 100 $\mu\text{m}$  end contacts formed the gain section and were injected with an 80mA bias current. The 200 $\mu\text{m}$  central absorber contact was driven with a 3dBm RF modulation superimposed onto a series of reverse bias currents. Streak camera traces for the pulses produced in this laser arrangement are shown in Figure 6.10 (iv). These traces are similar to those obtained using end-contact modulation under identical conditions: peak power is maintained although pulsewidth shows a slight increase. For centre contact modulation, a gain section bias of 80mA, absorber bias of -2.76V at

3dBm, this laser produced output pulsewidths of 28ps with an average power of 2.5mW and a peak power of 75mW. The computer model also coped well with these bias conditions: simulated intensity profiles are shown in Figure 6.10 (iv)(b) and show excellent agreement with the experimentally generated pulses.

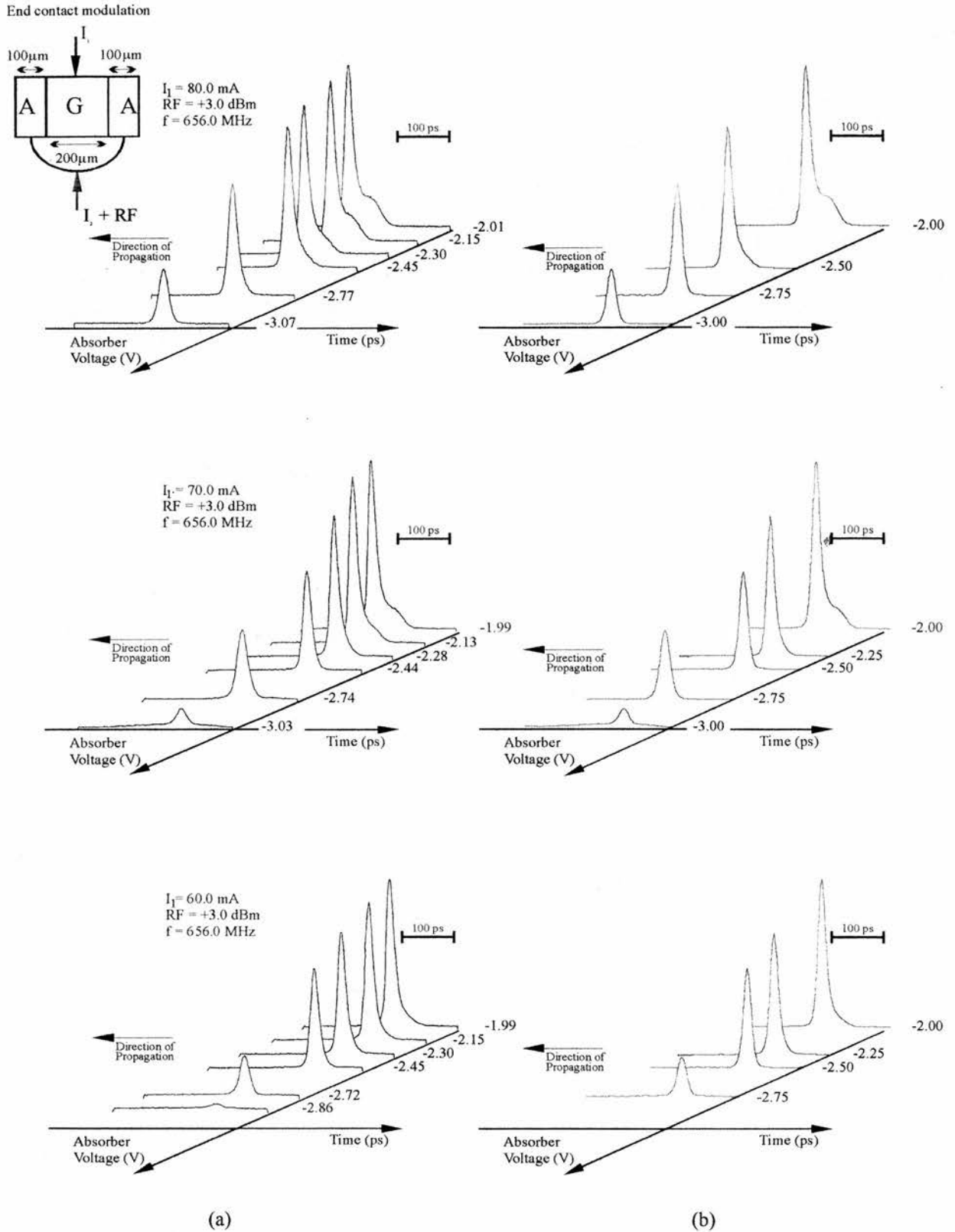


**Figure 6.10 (i).** Temporal pulse profile as a function of absorber voltage for a forced Q-switched, MQW, 3-contact, Fabry-Perot InGaAsP laser operating at 656 MHz, 3dBm absorber modulation for several values of gain current. Experimental results are shown on the left (a) with corresponding theoretical profiles on the right (b).

Chapter 6 Forced Q-Switching of Multiple-Contact Semiconductor Diode Lasers

End contact modulation

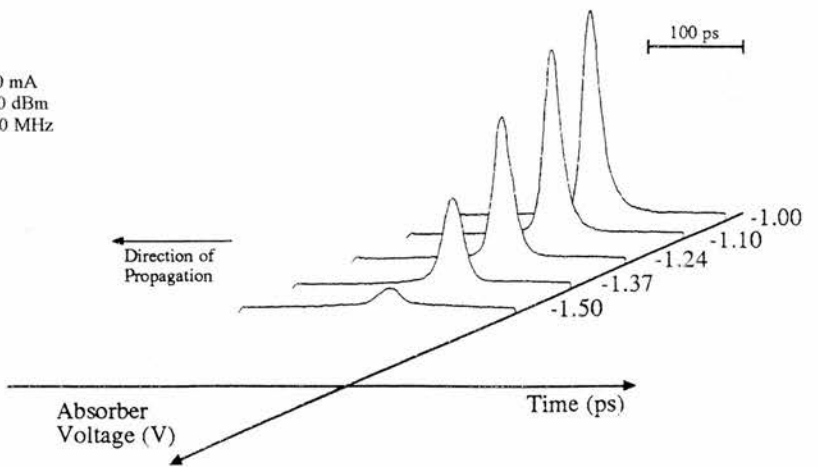
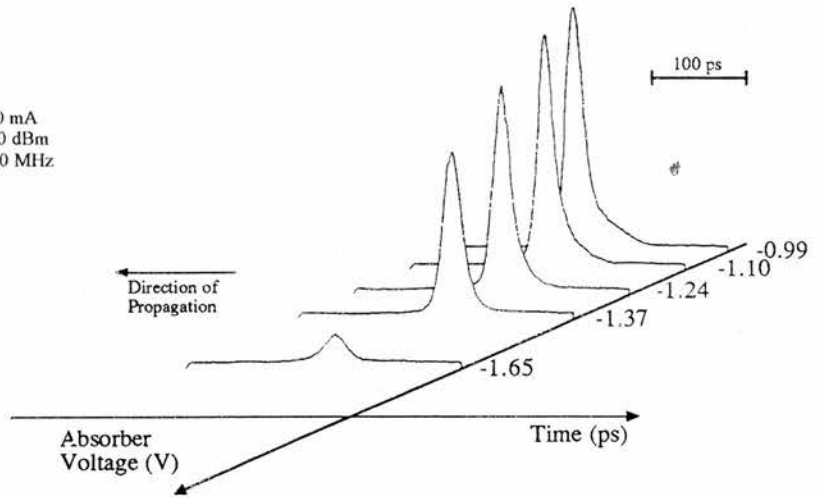
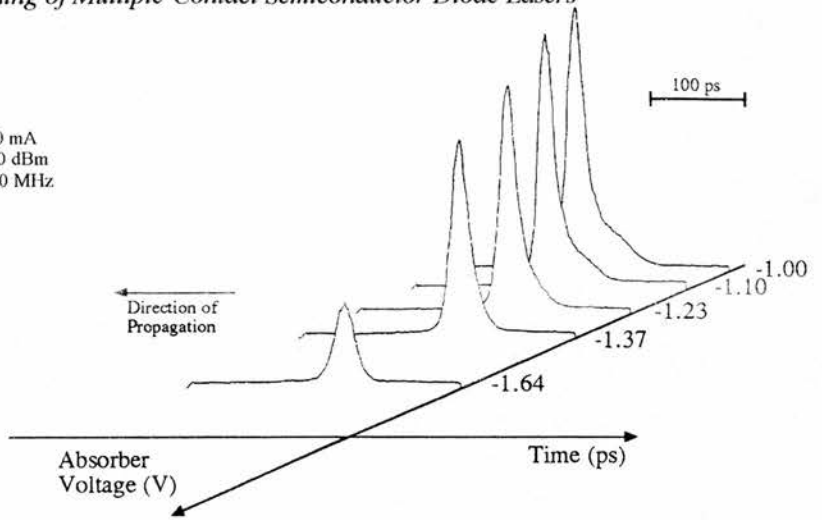
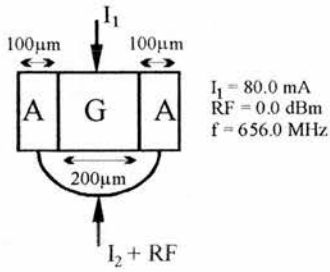
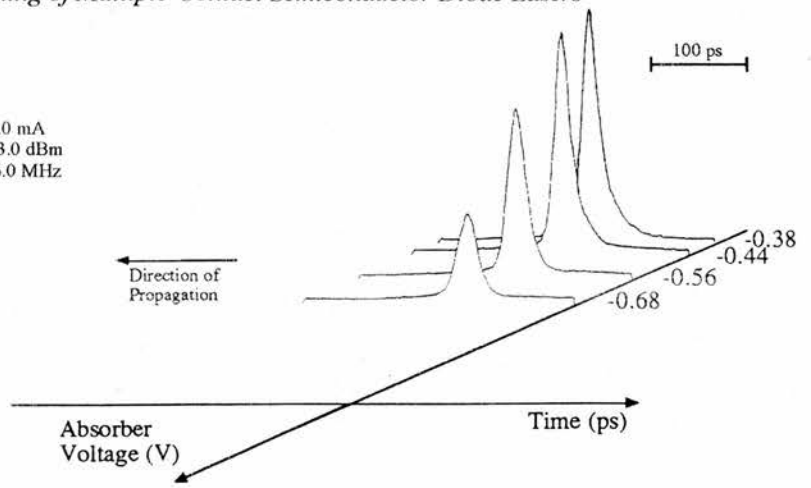
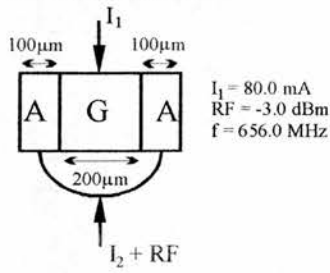


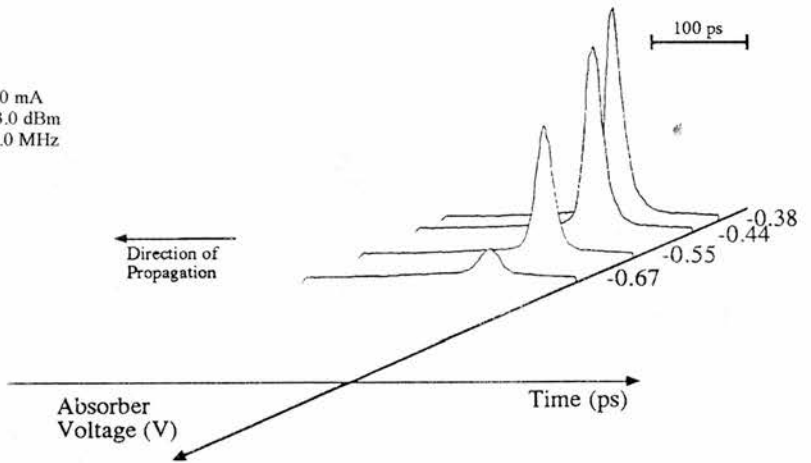
Figure 6.10 (ii). Temporal pulse profile as a function of absorber voltage for a forced Q-switched, MQW, 3-contact, Fabry-Perot InGaAsP laser operating at 656 MHz, 0dBm absorber modulation for several values of gain current.

Chapter 6 Forced Q-Switching of Multiple-Contact Semiconductor Diode Lasers

End contact modulation



$I_1 = 70.0 \text{ mA}$   
 $\text{RF} = -3.0 \text{ dBm}$   
 $f = 656.0 \text{ MHz}$



$I_1 = 60.0 \text{ mA}$   
 $\text{RF} = -3.0 \text{ dBm}$   
 $f = 656.0 \text{ MHz}$

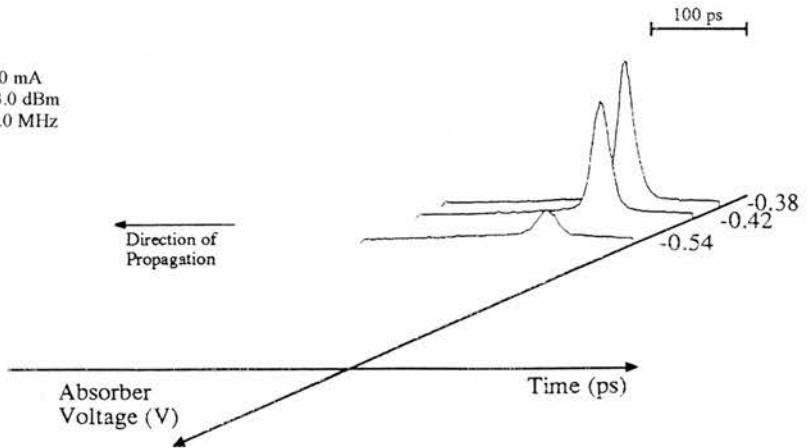
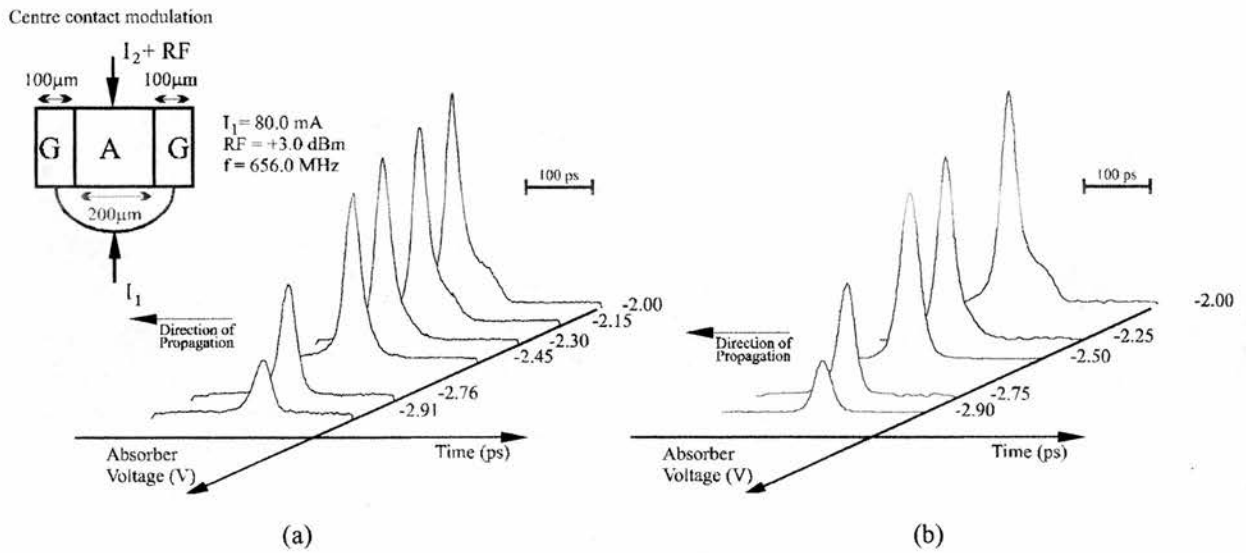


Figure 6.10 (iii). Temporal pulse profile as a function of absorber voltage for a forced Q-switched, MQW, 3-contact, Fabry-Perot InGaAsP laser operating at 656 MHz, -3dBm absorber modulation for several values of gain current.



**Figure 6.10 (iv).** Temporal pulse profile as a function of absorber voltage for a forced Q-switched, MQW, 3-contact, Fabry-Perot InGaAsP laser operating at 656 MHz, 3dBm absorber modulation for several values of gain current. In this case, RF modulation is applied to the long centre contact. Experimental results are shown on the left (a) with corresponding theoretical profiles on the right (b).



### 6.6.3 Three-contact bulk GaAs DFB laser (100/40/100 $\mu$ m)

The two end contacts of this device were joined together off-chip to form the gain section. The laser was driven using this arrangement due to the device geometry. Typically, the smallest contact is biased to form the absorber, in this case producing a gain/absorber ratio of 200:40 or 5:1. The 100/200/100 $\mu$ m device illustrated in Fig 6.10(i) was operated with a gain/absorber ratio of 200:200 or 1:1, so either the single central contact or the two connected end contacts could have formed the gain section. Operating conditions were as follows:

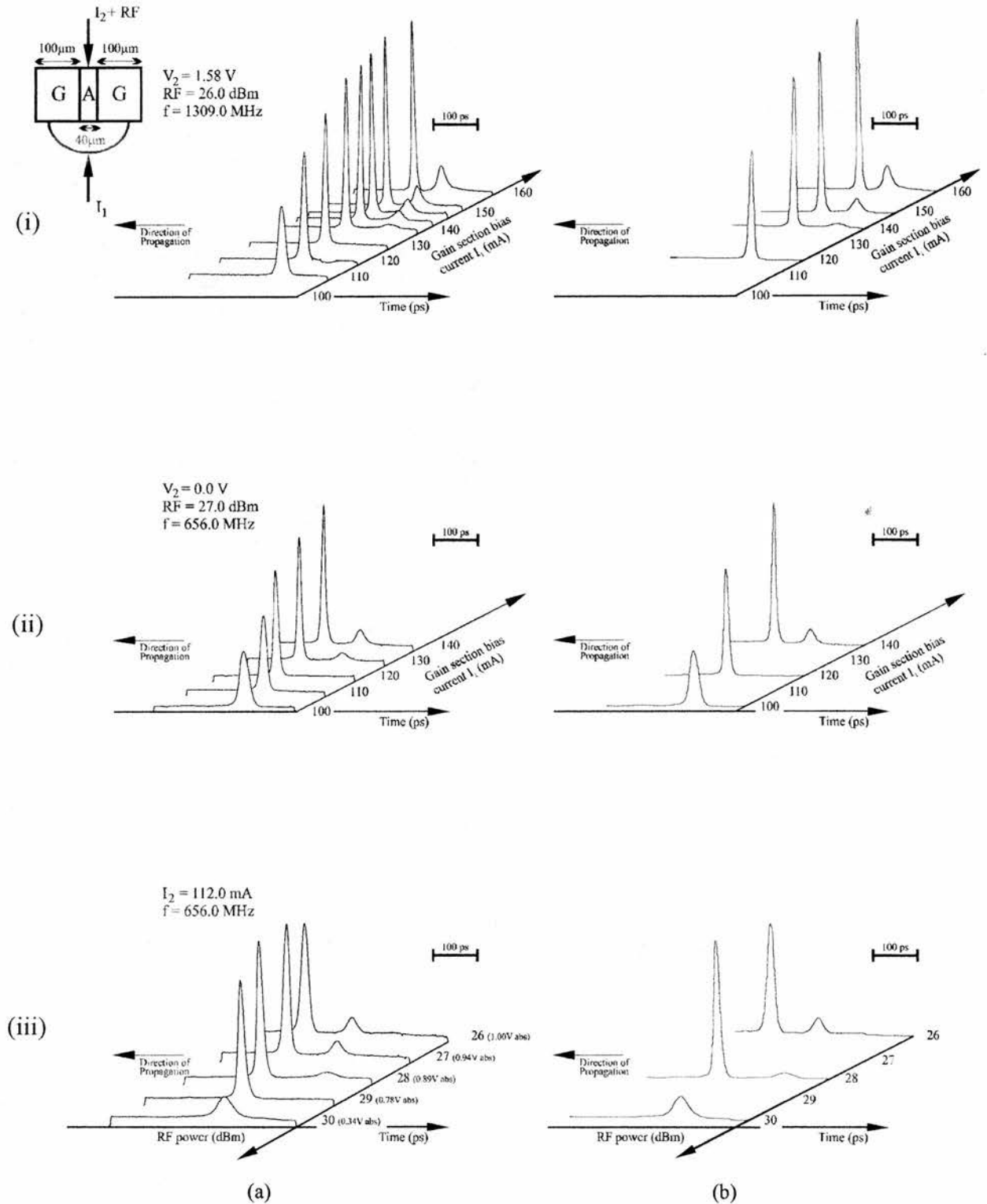
- i) the gain section bias current was varied between 100 and 160mA for an absorber section bias of 1.5V, 26dBm. RF frequency was 1309MHz.
- ii) gain section bias current was varied between 100 and 140mA for an absorber section bias of 0.0V, 27dBm. RF frequency was 656MHz.
- iii) for a gain section bias current of 112mA, the RF power was varied between 26 and 30dBm at a frequency of 656MHz.

Figure 6.11 shows the output pulse dependence on bias conditions. Figures 6.11 (i), (ii) and (iii) correspond to the operating regimes detailed above. Pulsewidths and peak powers for the GaAs device show significant improvement on InGaAsP devices. This is primarily due to the increased level of gain compression provided by the gallium arsenide material. Also, the narrower band gap of InGaAsP devices leads to significant levels of Auger recombination which limit peak power. For example, for a gain section bias of 120mA, absorber bias of 0V at 27dBm, 656MHz, the output pulsewidth was 18ps with an average power of 19.2mW and a peak power of 650mW (see Figure 6.11 (ii)(a)). A 15ps pulse with a peak power of 900mW (average power 26.5mW) was achieved at an operating frequency of 1.309GHz (with a gain section bias of 130mA) as shown in Figure 6.11 (i)(a). Secondary pulses were generated only at higher gain-section bias levels. These were eliminated either by increasing the level of reverse bias supplied to the absorber contact or by increasing the amplitude of the

RF modulation for a given gain section bias current (Figure 6.11 (iii)(a)). Theoretical output pulse traces for each of the above operating regimes were developed and are shown in Figure 6.11 (b). As before the results produced by the model were in very good agreement with the experimental data and indicates the flexibility of the model in coping with a variety of semiconductor materials and device structures.

### **6.7 Device development**

However, the supply of test laser devices (from Bath University) were limited, and as a result, it was not possible to carry out the planned systematic study. Despite these limitations, this work illustrates very clearly the key operational (and analytical) features of these Q-switched diode laser structures.



**Figure 6.11.** Forced Q-switched, bulk, 3-contact, FP GaAs laser: temporal pulse profile as a function of gain section bias current for two absorber section bias conditions (i) 1.58V modulated at 1309MHz, 26dBm; (ii) 0V modulated at 656MHz, 27dBm; (iii) shows the variation of the pulse profile with RF power. Experimental results are shown on the left (a) with corresponding theoretical profiles on the right (b).

### 6.8 State-of-the-art Q-switched GaAs lasers

Structure, pulse duration, peak power and repetition rate as reported in the literature.

Q-switching regime	FWHM (ps)	Peak Power (W)	Repetition rate	Reference
Modified Q-switching - double pulse technique	5	10	1.0 - 18.5 GHz	20
Passive Q-switching - straight guide	35	0.2	1.0 GHz	27
Passive Q-switching - diffraction grating cavity	20	0.75	40 MHz	23
RF locked self Q-switching - straight guide	17	1	2.5 GHz	29
Passive Q-switching - tapered laser	8 -15	5.6 - 6.6	1.0 MHz	28
Transverse mode switched - broad area laser	40	140	<kHz	25
Active Q-switching - broad area laser	24	1.3	1.5 GHz	21
Optical Q-switching – straight guide, broad area laser	21	6	500 Hz	22
Passive Q-switching - broad area laser	40	7.5	400 MHz	26

**Table 6.1.** State-of-the-art Q-switched GaAs lasers.

## 6.9 Conclusions

In this chapter a description of the principles governing Q-switching in semiconductor diode lasers has been presented. Further, a simple theoretical model was developed (from nonlinear rate equations) to predict the temporal behaviour of forced Q-switched multi-contact lasers for a wide range of operating conditions. A series of Q-switched InGaAsP and GaAs lasers were characterised experimentally and were shown to behave largely as predicted.

Forced Q-switching has been shown to be a very straightforward and practical technique which, although requiring multiple-contact device geometry, provides great enhancement in pulse energy over that achieved by either gain-switching or modelocking. As with gain-switching, the repetition rate of the optical pulses is dependent only on the frequency of the absorber contact RF drive. However, the presence of the absorber section implies greater cavity losses than for gain-switched lasers. As a result, higher injection currents and carrier density levels are required for optical output. Consequently, the peak power of the Q-switched pulse is significantly greater than that produced by gain-switching or modelocking. Peak powers of ~900mW have been demonstrated at modulation rates of 1.309GHz with the potential for performance greater than 1W using optimised high-power laser structures such as the 'bow-tie' or tapered-geometry laser<sup>28</sup>.

Ultrashort pulse generation using gain-switched methods results in poor timing jitter performance, but the timing jitter is reduced with increasing pulse power. Therefore, forced Q-switching of diode lasers can be used to produce high peak power pulses with low timing jitter characteristics. In Chapter 7 the origin and nature of timing jitter will be examined for modelocked, gain-switched and Q-switched devices. Routes towards jitter improvement will also be discussed.

## 6.10 References

1. G.Eisenstein, R.S. Tucker, S.K. Korotky, U. Koren, J.J. Veselka, L.W. Stulz, R.M. Jopson and K.L. Hall, *Electron. Lett.*, **21**, 173 (1985).
2. H. Sunderason and G.E. Wickers, *Electron. Lett.*, **26**, 725 (1990).
3. I.H. White, P.S. Griffin, M.J. Fice and J.E.A. Whiteaway, *Electron. Lett.*, **28**, 1257 (1992).
4. J.-M. Lourtios, L. Chusseau, E. Brun, J.-P. Hamaide, D. Lesterlin and F. Leblond, *Electron. Lett.*, **28**, 1499 (1992).
5. K.A. Williams, D. Burns, I.H. White, W. Sibbett and M.J. Fice, *IEEE Photon. Technol. Lett.*, **5**, 867 (1993).
6. N.G. Basov, *IEEE J. Quantum Electron.*, **QE-4**, 855 (1968).
7. T.P. Lee and R.H. Roldan, *IEEE J. Quantum Electron.*, **QE-6**, 339 (1970).
8. C. Harder, K.Y. Lau and A. Yariv, *IEEE J. Quantum Electron.*, **QE-18**, 1351 (1982).
9. R.W. Dixon and W.B. Joyce, *IEEE J. Quantum Electron.*, **QE-15**, 470 (1979).
10. M. Ueno and R. Lang, *J. Appl. Phys.*, **58**, 1689 (1985).
11. J.P. Van der Ziel, T.W. Tsang, R.A. Logan and W.M. Augustyniak, *Appl. Phys. Lett.*, **39**, 376 (1981).
12. L.A. Volkov, A.L. Guriev, V.G. Danil'chenko, A.G. Deryagin, D.V. Kuksenkov, V.I. Kuchinskii, E.L. Portnoi and V.B. Smirnitskii, *Sov. Technol. Lett.*, **15**, 497 (1989).
13. Zh. I. Alferov, A.B. Zhuravlev, E.L. Portnoi and N.M. Stel'makh, *Sov. Tech. Phys. Lett.*, **12**, 1093 (1986).
14. T. Tsukada and C.L. Tang, *IEEE J. Quantum Electron.*, **QE-13**, 37 (1977).
15. H. Ito, N. Onodera, K. Gen-Ei and H. Inaba, *Electron. Lett.*, **17**, 15 (1981).
16. K. Kitayama and S. Wang, *Appl. Phys. Lett.*, **44**, 571 (1984).
17. D.Z. Tsang and J.N. Walpole, *IEEE J. Quantum Electron.*, **QE-19**, 145 (1983).
18. D.Z. Tsang, J.N. Walpole, Z.L. Liau, S.H. Groves and V. Diadiuk, *Appl. Phys. Lett.*, **45**, 205 (1984).
19. Y. Arakawa, A. Larsson, A. Paslaski and A. Yariv, *Appl. Phys. Lett.*, **48**, 561 (1986).
20. P.P. Vasil'ev, *IEEE J. Quantum Electron.*, **QE-24**, 2386 (1988).
21. J. O'Gormann, A.F.J. Level and W.S. Hobson, *Electron. Lett.*, **27**, 13 (1991).
22. B.J. Thedrez, S.E. Sadow, Y.Q. Liu, C. Wood, R. Wilson and C.H. Lee, *IEEE Photon. Technol. Lett.*, **5**, 19 (1993).

23. S. Bouchoule, N. Stelmakh, M. Cavelier and J.-M. Lourtioz, *IEEE J. Quantum Electron.* **QE-29**, 1693 (1993).
24. P.P. Vasil'ev, I.H. White and M.J. Fice, *Electron. Lett.*, **29**, 561 (1993).
25. F.P. Volpe, V. Gorfinkel, J.Sola and G. Kompa, CLEO, paper CWC4, (1994).
26. P.Gavrilovic, N. Stelmakh, J.H. Zarrabi and D.M. Beyea, *Electron. Lett.*, **31**, 1154 (1995).
27. A. Finch, W.E. Sleat and W. Sibbett, *Review of Scientific Instruments*, **31**, 839 (1989).
28. K.A. Williams, J. Sarna, I.H. White, R.V. Penty, I. Middlemast, T. Ryan, F.R. Laughton and J.S. Roberts, *Electron. Lett.*, **30**, 320 (1994).
29. P.P. Vasil'ev, I.H. White, D.Burns and W.Sibbett, *Electron. Lett.*, **29**, 1594 (1993).

# Chapter 7

## TIMING JITTER IN ULTRASHORT PULSE SEMICONDUCTOR LASERS

### 7.1. Introduction

Semiconductor laser diodes are now widely used to generate picosecond optical pulses at GHz repetition rates. When such devices are used in communication systems or diagnostic experiments, the variations in the amplitude (pulse energy fluctuations) and phase (timing jitter) characteristics of the laser pulse train are of great importance. Correlated and uncorrelated timing jitter of ultrashort optical pulses generated via modelocked, gain-switched and Q-switched laser diodes have been extensively studied<sup>1-18</sup>. Correlated jitter is produced largely by the drive electronics whereas uncorrelated jitter originates from random fluctuations in photon density.

#### 7.1.1. Timing jitter in external-cavity modelocked lasers

In addition to offering the shortest pulsewidths of the three pulse production techniques, external-cavity modelocked lasers also exhibit the lowest levels of timing jitter. Low timing jitter requires a low level of spontaneous emission at turn-on to reduce the variance of pulse emission times. However, the continuous presence of stimulated emission in the external cavity and the effective filtering action of wavelength selective cavity elements reduce the contribution of spontaneous emission. The overall effect is a reduction in absolute timing jitter due mainly to lower levels of uncorrelated jitter. Correlated jitter remains largely unchanged (although extremely low) and is dominated by long-term fluctuations in the modulating frequency produced by the RF drive oscillator<sup>10,11,19,20</sup>. External-cavity modelocking gives lower values of timing jitter than the comparable monolithic cavity device. For either monolithic or external-cavity



devices, active modelocking gives the lowest jitter level, followed by hybrid and passive modelocking. Thus, external-cavity active modelocking produces the lowest uncorrelated timing jitter (65fs)<sup>11</sup> followed by the hybrid (980fs)<sup>20</sup> and passive (12.2ps)<sup>19</sup> techniques. Corresponding values for the monolithic cavity case are 530fs<sup>11</sup>, 1.13ps<sup>19</sup> and 12.5ps<sup>20</sup>. Figure 7.1 shows the phase noise spectral density  $L(f)$  for a variety of multi-contact, multi-quantum well GaAs modelocked lasers characterised by Derickson *et al*<sup>11,19,20</sup>.

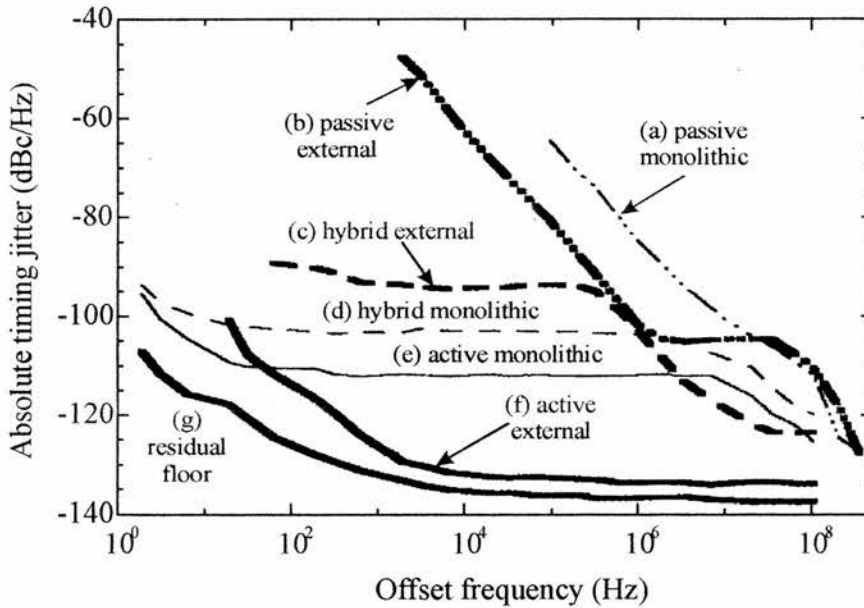


**Figure 7.1.** Absolute timing jitter  $L(f)$  as a function of frequency offset for six types of modelocked laser. [Source: 20.]

### 7.1.2. Timing jitter in gain-switched lasers

For gain-switching, the start-up process of each pulse is stochastic in nature and leads to fluctuations in pulse energy and the turn-on delay time from pulse to pulse. Consequently, uncorrelated jitter in gain-switched lasers decreases with increasing spontaneous emission levels as a result of increased bias current<sup>5</sup>. Weber *et al* demonstrated the effect of increased drive current on timing jitter for one DFB laser and three FP lasers (see Figure 7.2). The Fabry-Perot devices exhibit lower levels of timing jitter (<5 ps) than DFB lasers (>20 ps) since the FP spectrum is highly multimode. This

leads to enhanced spontaneous emission capture which in turn leads to a reduction in the variance of the pulse build-up times.

Timing jitter also decreases as the amplitude of the RF modulation current increases<sup>18</sup>. In addition, pulse build-up times can be enhanced and timing jitter minimised by increasing the RF modulation frequency. Increasing the drive current and the RF power leads to an increase in peak power and a corresponding decrease in timing jitter. However, increasing one or both of these drive parameters invariably leads to the formation of one or more satellite pulses. The peak power saturates and timing jitter quenches (and increases) when the tail (or subpulse) becomes dominant. If pumping

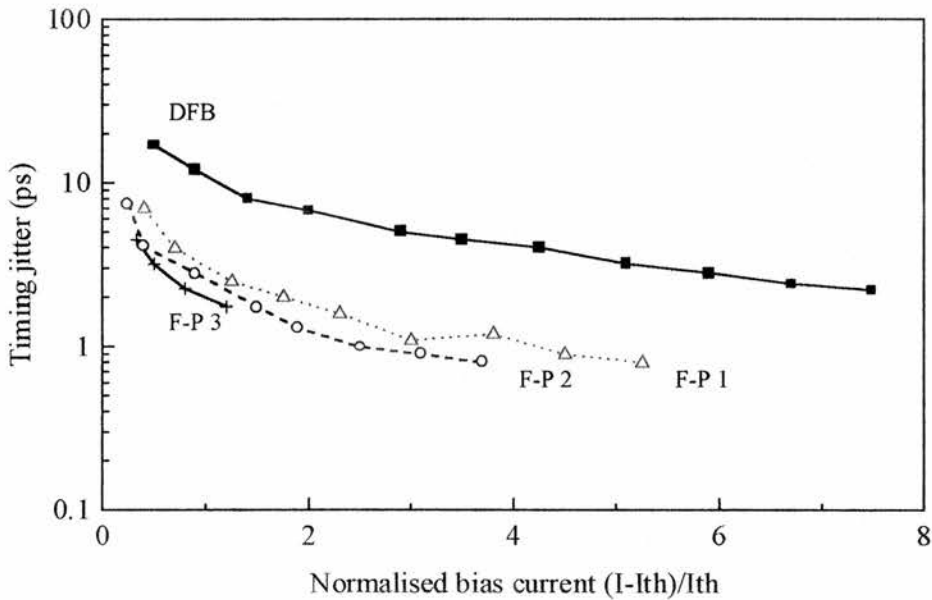


**Figure 7.2.** Timing jitter for one DFB and three F-P laser diodes as a function of normalised bias current. The threshold current of all four diodes lay between 24 and 27mA. A range of drive conditions were delivered by biasing with 10ns pulses at a modulation rate of 50kHz. [Source: 5.]

continues then timing jitter will increase due to the pulse tail influencing carrier concentration experienced in the next pumping cycle. Therefore, timing jitter cannot be considered without reference to other pulse parameters such as peak power, pulsewidth and spectral performance.

However, secondary pulse generation (because of red shift chirping) at high bias conditions may be eliminated by optical filtering and linear compression as described by Jinno<sup>13</sup>. Here, two gain-switched DFB lasers are considered and are modulated with a very strong RF signal superimposed onto a dc current biased slightly above threshold. Timing jitter is reduced to  $<1$  ps at 5GHz for clean operating conditions as shown in Figure 7.3.

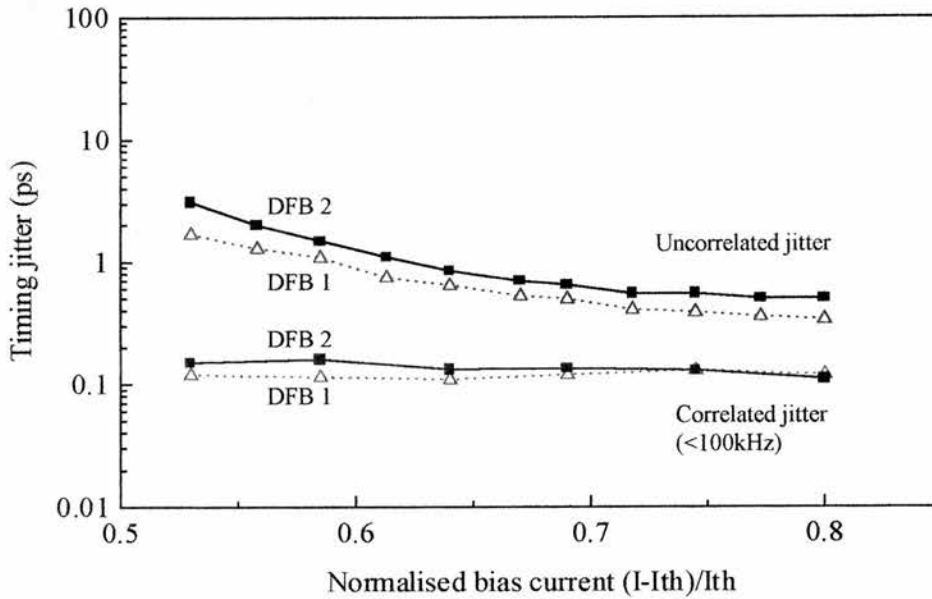


**Figure 7.3.** Timing jitter for two gain-switched DFB laser diodes as a function of normalised bias current. Threshold currents for LD1 and LD2 were 20mA and 24mA respectively. Both diodes were modulated by a 21.5dBm, 5GHz signal. The pulses were filtered and compressed to trim their spectra and reduce chirping. [Source: 13.]

### 7.1.3. Timing jitter in Q-switched lasers

Since timing jitter is shown to decrease with increasing peak power, the high peak powers and pulse energies generated by Q-switching produce low levels of timing jitter. As for gain-switching, forced Q-switched FP lasers exhibit lower levels of timing jitter than DFB devices due to the larger spontaneous emission capture by the laser modes. Timing jitter may be reduced by increasing either the level of the dc bias current, the

amplitude of the RF modulation or the frequency of the RF modulation. An increase in either or any of these parameters produces a corresponding increase in carrier concentration and thus in the spontaneous emission coupling to the laser mode prior to pulse turn-on. Peak power is directly proportional to carrier concentration<sup>18</sup>.

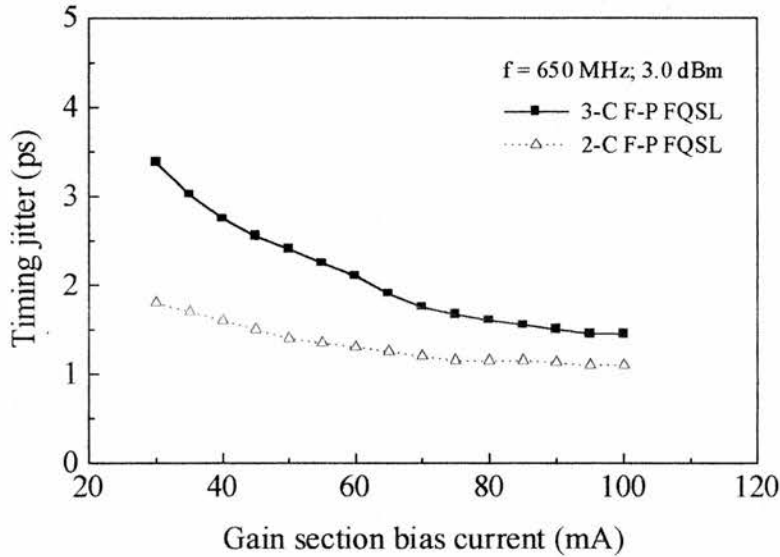


**Figure 7.4.** Uncorrelated timing jitter for two multi-contact forced Q-switched laser diodes as a function of gain section bias current. i) a 3-contact MQW FP InGaAsP diode with contact geometry 100/200/100 $\mu\text{m}$ ; ii) a 2-contact MQW FP InGaAsP diode with contact geometry 300/100 $\mu\text{m}$ . [Source; 18.]

## 7.2 Measurement of timing jitter

There are two different experimental approaches which may be followed to investigate timing jitter of optical pulse trains. These pulse sequences are converted to electrical pulse trains at the modulation frequency by fast photodetectors and may be evaluated by either direct temporal assessment via a sampling oscilloscope and a PC employed as a multichannel analyser (as used by Weber *et al*<sup>5</sup>) or the frequency domain technique where the phase noise sidebands are integrated to the time domain<sup>12</sup>. The spectral technique is preferred since it allows discrimination between correlated jitter produced by the drive electronics and uncorrelated jitter of the laser.

7.2.1. Frequency domain analysis: correlated timing jitter

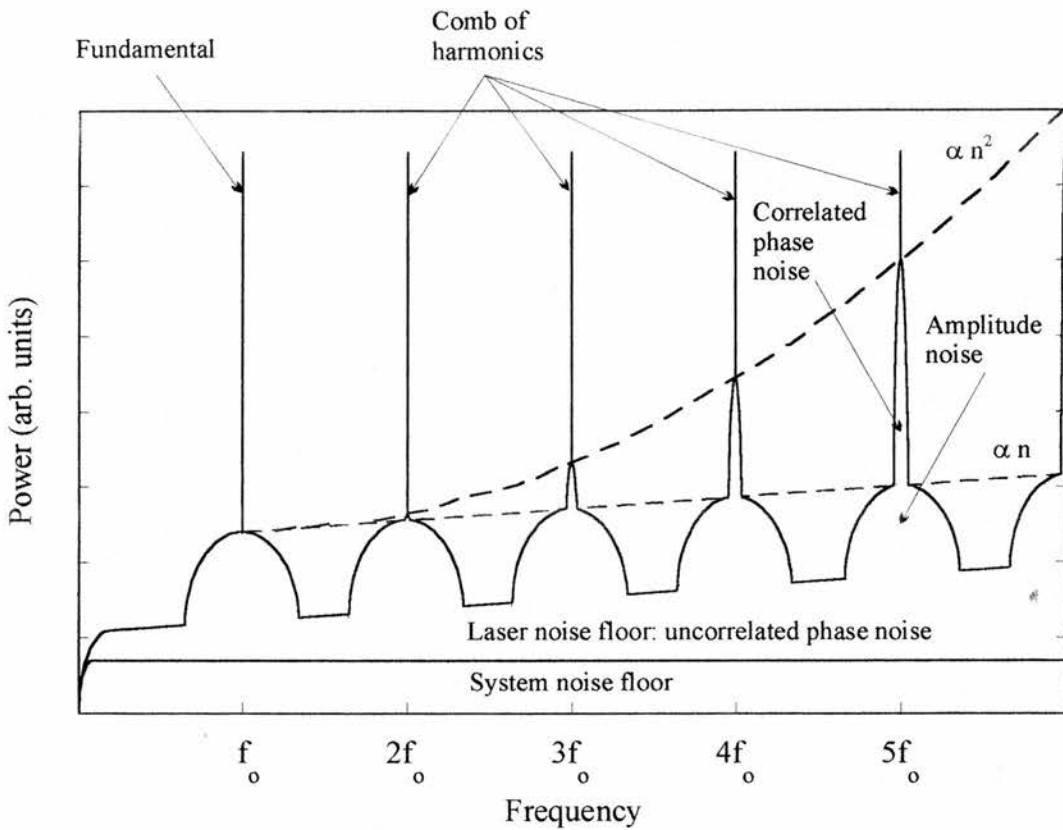


**Figure 7.5.** Schematic of a typical RF spectrum of a train of ultrashort pulses after spectral analysis.  $f_0$  is the repetition rate of the optical pulses. Amplitude noise is independent of frequency while phase noise shows a quadratic increase with harmonic number. [Source: 12.]

The intensity of a periodic train of short Gaussian optical pulses can be approximated by the expression<sup>8,9</sup>

$$P(t) = P_0 T_1 (1 + N(t)) \sum_{n=-\infty}^{n=+\infty} \left[ \frac{1}{\sqrt{2\pi} \sigma_t} \exp\left(-\frac{(t - T_0 - nT_1 - J(t))^2}{2\sigma_t^2}\right) \right] \quad (7.1)$$

where  $P(t)$  is the laser intensity,  $P_0$  is the power level of the beam,  $T_1$  is the pulse repetition period,  $\sigma_t$  is the rms pulse duration,  $N(t)$  is the normalised pulse-intensity variation,  $J(t)$  is the timing fluctuation of the pulse train,  $T_0$  is the static timing offset of the pulse train and  $n$  is the harmonic number. Taking the Fourier transform of the laser

intensity  $P(t)$  (approximated to second order in  $n\omega_1\sigma_J$ ) produces the power spectral density  $S_p(\omega)$ .

$$S_p(\omega) = P_{av}^2 \exp(-\omega^2\sigma_t^2) \sum_{n=-\infty}^{n=+\infty} \left[ (1 - n^2\omega_1^2\sigma_J^2) 2\pi\delta(\omega - n\omega_1) + (1 - n\omega_1^2\sigma_J^2) S_N(\omega - n\omega_1) + n^2\omega_1^2 S_J(\omega - n\omega_1) \right] \quad (7.2)$$

where  $\sigma_J$  is the rms timing jitter,  $\omega_1 = 2\pi/T_1$ ,  $S_N(\omega)$  is the power spectral density of the relative amplitude fluctuation and  $S_J(\omega)$  is the power spectral density of the pulse train timing jitter.

The timing jitter technique used here employs a frequency domain analysis of the Fourier components of the optical pulse train. The power spectrum of the laser under investigation is recorded by a high-speed photodetector and wide bandwidth electronic spectrum analyser<sup>8,22</sup>. A typical power spectrum is illustrated in Fig. 7.5. The spectrum comprises: i) a sequence of delta function frequency components (comb of harmonics) at multiples of the pulse repetition rate  $f_0$ ; ii) amplitude noise sidebands which attend each delta function. Each  $\delta$ -function component rests on these relatively broad pedestals (double-sided noise bands); iii) close-in correlated phase noise sidebands which accompany each Fourier component. These noise bands may result from fluctuations in the pulse intensity (amplitude noise bands) and/or from random variations in the pulse repetition rate (phase noise bands)<sup>6</sup>. Amplitude noise sidebands  $S_N(\omega - n\omega_1)$  (the power spectral density of the pulse intensity variation) are directly proportional to the intensity of the  $\delta$ -function which defines each component and are independent of the harmonic number  $n$ , while the phase noise sidebands  $(n\omega_1)^2 S_J(\omega - n\omega_1)$  increase as  $n^2$ .

By measuring  $S(\omega)$  the attendant phase noise may be extracted assuming the amplitude noise and the system noise floor remain constant over the nominal frequency range. Phase noise is negligible at harmonics of sufficiently low order and here amplitude noise predominates and is readily assessed. Phase noise sidebands have power proportional to the square of the harmonic number  $n$  and are dominant at high order harmonics. Thus, a photodetector/spectrum analyser combination having a large

bandwidth is essential for optimum system performance. The spectral density of the timing jitter is determined by the relative power of the laser harmonic and its associated sidebands. At extremely high harmonics, (7.2) is inaccurate because of spectral terms related to pulsewidth fluctuations and higher order terms in  $n\omega_1\sigma_J$ .

For a specific frequency interval  $f_l$  to  $f_h$ , the rms amplitude fluctuation is<sup>8</sup>

$$\sigma_A[f_l, f_h] = \sqrt{\langle A(t)^2 \rangle} = \sqrt{\frac{P_n}{P_c}} \quad (7.3)$$

$$\text{where } P_n = \int_{nf_o - f_l}^{nf_o + f_h} \frac{2P(f)}{1.2 \times RB} df \quad (7.4)$$

Where  $P(f)$  is the continuous part of the power spectral density relative to the envelope of discrete lines. Thus,

$$\sigma_A[f_l, f_h] = \sqrt{\frac{P_n}{P_c} \frac{\Delta f}{RB}} \quad (7.5)$$

where  $\Delta f$  is the noise bandwidth,  $P_n$  and  $P_c$  are the power of the  $n^{\text{th}}$  harmonic and the maximum of the phase noise sideband at the  $n^{\text{th}}$  harmonic respectively and  $RB$  is the resolution bandwidth of the spectrum analyser. Similarly, correlated phase noise is

$$\sigma_{J(C)}[f_l, f_h] = \sqrt{\langle J(t)^2 \rangle} = \frac{1}{\sqrt{2\pi} nf_o} \sqrt{\frac{P_n}{P_c} \frac{\Delta f}{RB}} \quad (7.6)$$

Since each harmonic component has a constant intensity, an increase in phase noise produces a decrease in the peak level of the delta function component of  $S(\omega)$  and hence a proportionate change in the amplitude noise sidebands. Using the spectral analysis technique, it has been demonstrated that correlated jitter in Q-switched<sup>15,17</sup>, gain-switched<sup>6,14,17</sup> and modelocked<sup>6-10,21</sup> lasers is compatible with the phase noise of the laser drive electronics and has been found to be  $\sim 0.2\text{ps}^{13}$ .

### 7.2.2 Spectral domain analysis: uncorrelated timing jitter

Uncorrelated timing jitter is of particular significance in gain-switched and Q-switched lasers. As for correlated timing jitter, uncorrelated phase noise increases in magnitude with the square of the harmonic number  $n$ . In gain-switching, some uncorrelated jitter is inherent in the turn-on transients. The origin of this type of timing jitter is attributed to transient fluctuations of the optical power during the turn-on process of the laser. The optical pulses generated by gain-switching are built up from spontaneous emission. The stochastic character of this process leads to fluctuations of the pulse energy and the turn-on delay time from one pulse to the next. This is because pulse-to-pulse phase memory is not retained in Q-switched and gain-switched lasers and phase variations result in wideband noise.

The power spectral density (Eq. (7.2)) may also be expressed as<sup>12</sup>

$$S_p(\omega) \approx \frac{P_{\text{ave}}^2 |F(\omega)|^2}{T} \left[ \sigma_A^2 + \sigma_J^2 \omega^2 + \omega_1 \sum_{n=-\infty}^{n=+\infty} \delta(\omega - \omega_n) \right] \quad (7.7)$$

where  $\omega_1 = 2\pi/T$  is the pulse repetition frequency,  $\omega_n = n\omega_1$  is the  $n^{\text{th}}$  harmonic and  $|F(\omega)|$  is the Fourier transform of the Gaussian  $e^{-\omega^2 \sigma_t^2}$ . As explained previously, the function represents a sequence of delta functions, an accompanying series of amplitude-noise sidebands and a set of phase noise sidebands which attend each component. In this instance, the jitter term  $\sigma_J$  is proportional to  $\omega^2$ . If  $P(\omega)$  is defined as the continuous part of the power spectral density relative to the envelope of discrete lines, then in the approximation of Eq. (7.7)  $\omega_1 P(\omega) = \sigma_A^2 + \sigma_J^2 \omega^2$ . Then uncorrelated jitter is given by<sup>12</sup>

$$\Rightarrow \sigma_{J(\text{uc})} = \frac{1}{2\pi f \sqrt{(n^2 + 1/12)}} \sqrt{\frac{P_n}{P_c} \frac{f}{RB}} \quad (7.8)$$



Using the expressions for correlated and uncorrelated timing jitter given in Eqs. (7.6) and (7.8) respectively, the noise content of specific laser systems may be identified by analysing the frequency domain elements and subsequent Fourier transforms to the time domain using a high-speed photodiode and RF spectrum analyser combination. Amplitude noise can be determined by examining the sidebands around the fundamental harmonic, where only amplitude noise is present, and the phase noise can be extracted from the noise sidebands attending higher harmonics of the pulse repetition frequency

#### 7.4 Noise characterisation of semiconductor diode lasers

The experimental layout used to measure timing jitter is shown in Figure 7.5. The laser and synchroscan streak camera system were simultaneously driven by the RF signal generator and the output pulses illuminated the InGaAs PIN photodetector which had an 8GHz bandwidth in excess of 22GHz. Processing by the optical spectrum analyser transformed the electrical power spectrum into the frequency domain as a periodic set of Fourier components spaced at the RF frequency  $f_0 = T^{-1}$ . The HP70001A analyser used in experiment had a frequency range of 0.1 - 22GHz and a minimum resolution bandwidth of 10Hz. The need for post-amplification of the photodiode signal and limitations arising from the noise floor of the spectrum analyser reduced the overall bandwidth of the detection system to 4.2GHz.

##### 7.4.1 Timing jitter in actively modelocked semiconductor diode lasers

Actively modelocked external cavity semiconductor diode lasers not only exhibit the lowest levels of timing jitter of all the modelocking regimes, they also provide significantly lower levels of jitter than gain-switched or Q-switched lasers. These low jitter levels are dominated by the noise correlated to the modulating source since there is a negligible contribution of uncorrelated noise due to strong coupling between spectral modes. To achieve low pulse-to-pulse jitter in modelocked lasers, devices with low levels of spontaneous emission noise are essential. The level of spontaneous emission noise

increases with the number of longitudinal modes in the laser emission spectrum and with the gain level in the semiconductor laser amplifier<sup>11</sup>.

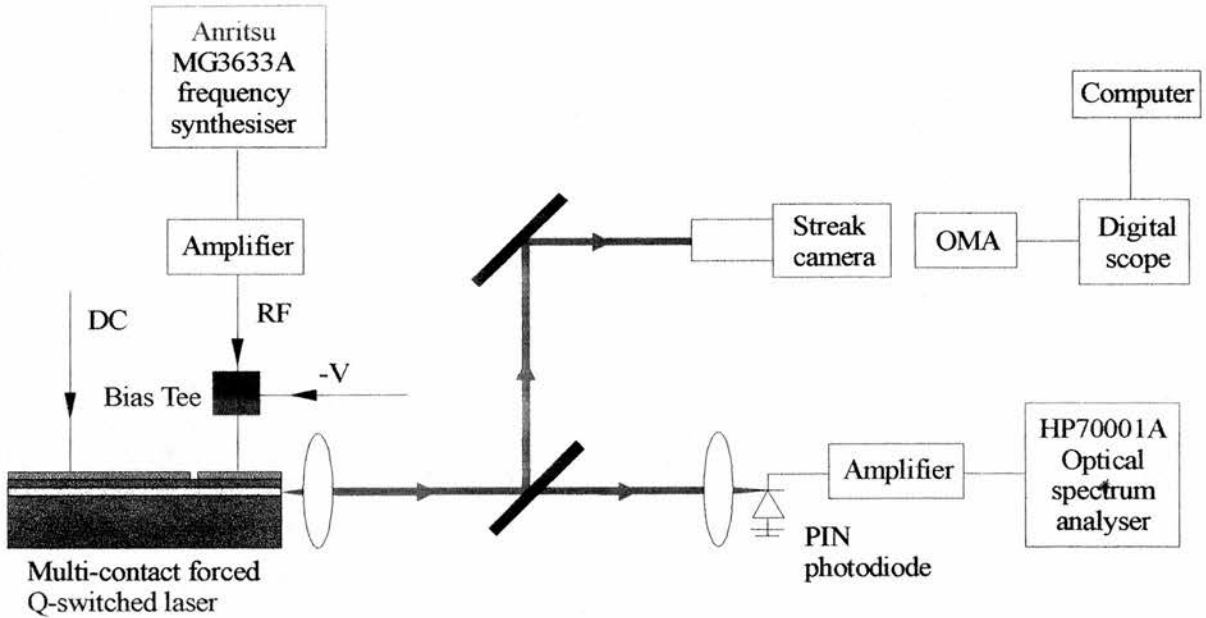


**Figure 7.6.** Experimental layout for the measurement of timing jitter of forced Q-switched semiconductor lasers. A similar arrangement was also used to assess the noise performance of gain-switched and modelocked systems.

#### 7.4.2 Actively modelocked external-cavity dual-wavelength InGaAsP laser

The phase noise and amplitude noise components are separated out using the  $n^2$  dependence of the phase noise and the single sideband phase noise power spectrum  $L_J(f)$  was plotted. This is a log/log graph of the ratio of the power in the noise sideband in a 1Hz bandwidth to the power in the carrier. Units are dBc/Hz. Figure 7.7 shows the single sideband phase noise spectra for both single-wavelength and dual-wavelength operation calculated from the first and third harmonics of the pulse train.

The rms timing jitter  $\sigma_J$  in any frequency interval  $[f_l, f_h]$  was then obtained by linearising the single-sideband noise spectrum and integrating it over the interval then applying the relation given in Eq. (7.9). The rms phase noise is simply  $\phi_{rms} = 2\pi f_o \sigma_J$ ,

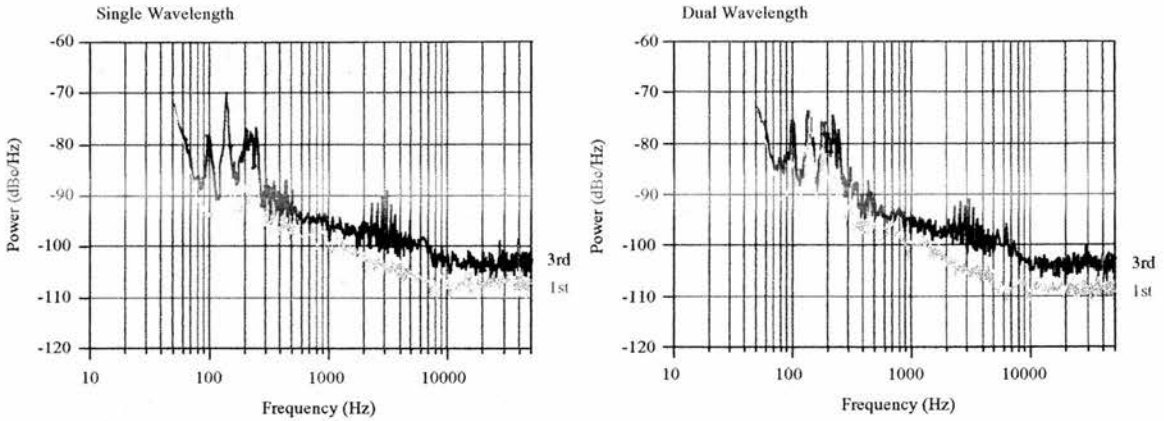


**Figure 7.7.** Single sideband power spectra (calculated using 1<sup>st</sup> and 3<sup>rd</sup> harmonics) for single-wavelength and dual wavelength operation of a dual-wavelength, external-cavity, actively modelocked InGaAsP laser system.

where  $f_o$  is the fundamental frequency (i.e., the RF drive frequency). Data obtained via the photodiode/spectrum analyser combination was processed via a portable computer system operating an in-house software package. The resulting phase noise performance for single- $\lambda$  and dual- $\lambda$  operation is shown in Figure 7.8. The rms timing jitter was measured at 81fs in the 50 - 500Hz frequency range and 50fs for the 500Hz - 5kHz frequency band for single-wavelength operation. Corresponding values for dual-wavelength operation were 83fs and 49fs respectively. From these figures, it is clear that phase noise was no greater for dual- $\lambda$  operation. These figures compare well with those obtained by Derickson *et al*<sup>20</sup> for actively-modelocked external cavity systems (65fs).

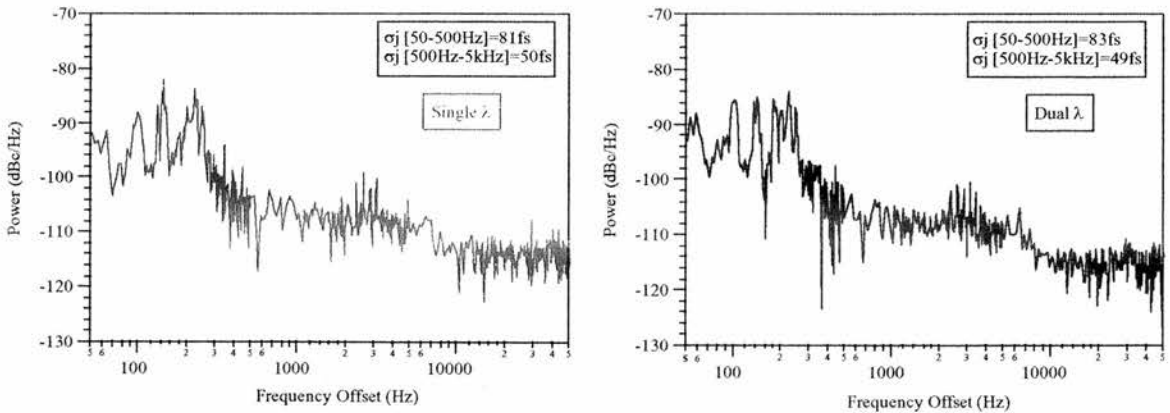


**Figure 7.8.** Single sideband phase noise for the actively modelocked dual-wavelength laser system. Phase noise performance is given for single-wavelength and dual-wavelength operation.

Excess amplitude noise was also evaluated and results are shown for both modes of operation in Figure 7.9. Although excess amplitude noise was evident, it was primarily related to environmental conditions and as a consequence was virtually unchanged for dual- $\lambda$  operation.

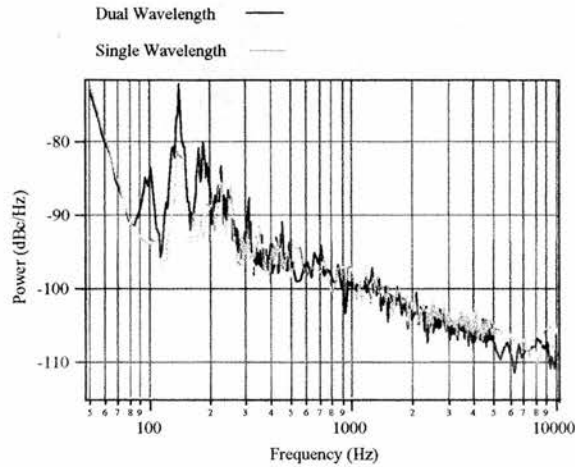


**Figure 7.9.** Excess amplitude noise for the actively modelocked dual-wavelength laser system. Noise performance is given for single-wavelength and dual-wavelength operation.

### 7.4.3 Timing jitter in gain-switched lasers

Timing jitter was evaluated for the two gain-switched lasers examined in Chapter 5: a single-contact bulk InGaAsP DFB device and a single-contact bulk InGaAsP Fabry-Perot diode. Both lasers were operated at 650 MHz for a variety of bias conditions (Figures 5.12 and 5.15). Timing jitter, pulse duration and pulse energy were simultaneously determined using the experimental arrangement shown in Figure 7.6.

### 7.4.4 Gain-switched single-contact DFB laser

RF spectrum analysis revealed that the noise was more or less uniform between the harmonics indicating that it was largely uncorrelated. From the power spectrum data set (using second and fourth harmonics) jitter values calculated using (7.13) are shown in Figure 7.10 as a function of bias current for several values of RF power. Correlated

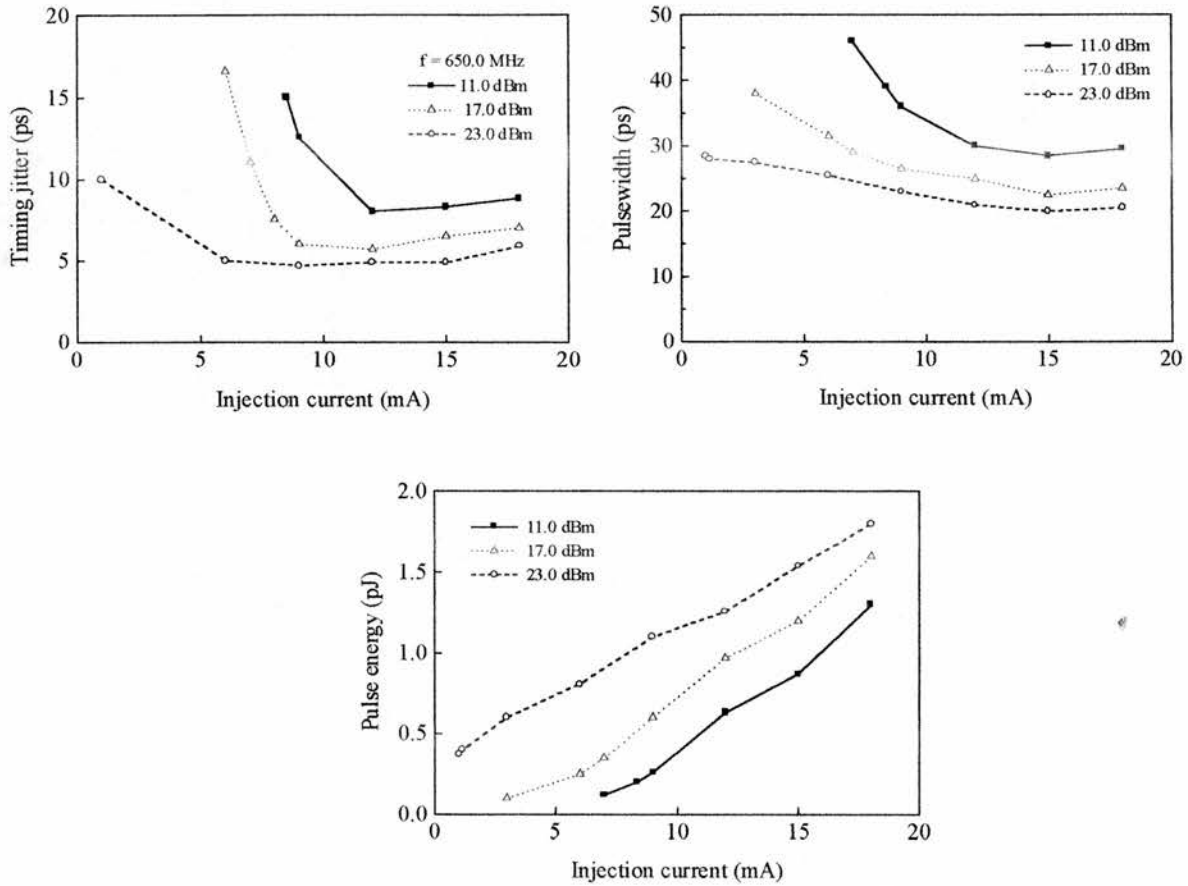


**Figure 7.10.** Timing jitter, pulse duration and pulse energy as a function of bias current for a gain-switched single-contact bulk InGaAsP DFB laser. The modulation frequency was 650 MHz for several values of RF drive.

timing jitter was independent of bias conditions and was negligible ( $< 0.15$ ps) due to the efficient performance of the Anritsu RF generator. Uncorrelated jitter derived from the spontaneous character of laser emission and decreased from 10 - 15ps to 5 - 8ps as the injection current increased. As the injection current was increased the main pulse power saturated. Further pumping only served to enhance the subpulse or tail which resulted in the formation of a long wavelength spike on the spectrum. As the subpulse became dominant, timing jitter quenched and then increased. As pumping continued then timing jitter was increased due to the influence of the pulse tail on carrier concentration of the next pump cycle. Thus, timing jitter decreased as pulse peak power increased. Timing jitter was greater than 10ps for all operating conditions for the single mode DFB laser.

These figures compare well with those obtained by Weber *et al*<sup>5</sup> for low frequency gain switching of DFB devices (10-20ps).

However, for optimum pulse conditions (that is, in the case of single pulse output with 'spikeless' or clean spectra [see Figure 5.14]) timing jitter was greater than 15ps. Pulse timing jitter was also shown to decrease with increasing RF modulation falling from 29.2ps (at 8.39mA, 11dBm) through 20.8ps (6.99mA, 17dBm) to 14.7ps (1.15mA, 23dBm) for the optimum pulse conditions given in Figure 5.14.

Pulse duration decreased with increasing bias current, falling from 30 - 50ps to 20 - 30ps as the current increases from threshold (7.6mA) to 15mA. Pulwidth also decreased with increasing RF modulation as previously noted in Chapter 5.

Pulse energy increased with both increasing bias current and RF modulation, rising from 0.3 - 1.0pJ just above threshold to 1.25 - 1.75pJ at twice this value. Thus, for optimum operating conditions (1.15mA at 23dBm) timing jitter was 14.7ps, pulwidth 28ps and pulse energy 0.4pJ. Thus short, single pulse output with a clean optical spectrum may be obtained only at the expense of low pulse energy and high levels of timing jitter.

#### 7.4.5 Gain-switched single-contact Fabry-Perot laser

Using second and fourth power spectrum harmonics, values of timing jitter were obtained for the data set given in Figure 5.15. These are shown (along with values of pulwidth and pulse energy) as a function of bias current in Figure 7.11.

For the FP laser, uncorrelated jitter decreased from 10 - 15ps to a minimum of 2 - 3ps as the bias current was increased. This corresponds to an increase in peak power with increasing bias current (see Figure 5.15). As in the case of the DFB laser, timing jitter decreased as peak power increased. As before, timing jitter was quenched when the subpulse or tail appeared. Jitter continued to increase (to 3.5 - 6ps) as the power in the subpulse increased. Pulse timing jitter also decreased with increasing RF modulation power. Fabry-Perot lasers have lower timing jitter (< 5ps) than DFB lasers since the FP spectrum is highly multi-mode. This condition leads to enhanced spontaneous emission

capture probability which in turn leads to a reduction in the variance of build-up times. These figures compare well with those obtained by Weber *et al*<sup>5</sup> for F-P devices (1-10ps).

Variation in pulse duration followed a similar pattern to that of the timing jitter. Pulswidth initially decreased with increasing bias current to a minimum of  $\sim 30$ ps and steadily increased (to  $\sim 60$ ps) after peak power saturation and subsequent subpulse domination. Pulswidth decreased with increasing RF modulation power as before.

Pulse energy increased linearly with increasing bias current from 0.1 - 0.5pJ at 70mA to 1.5 - 2pJ at a bias of 100mA. At high bias currents much of the pulse energy appeared in the subpulse or tail as shown in Figure 5.15.

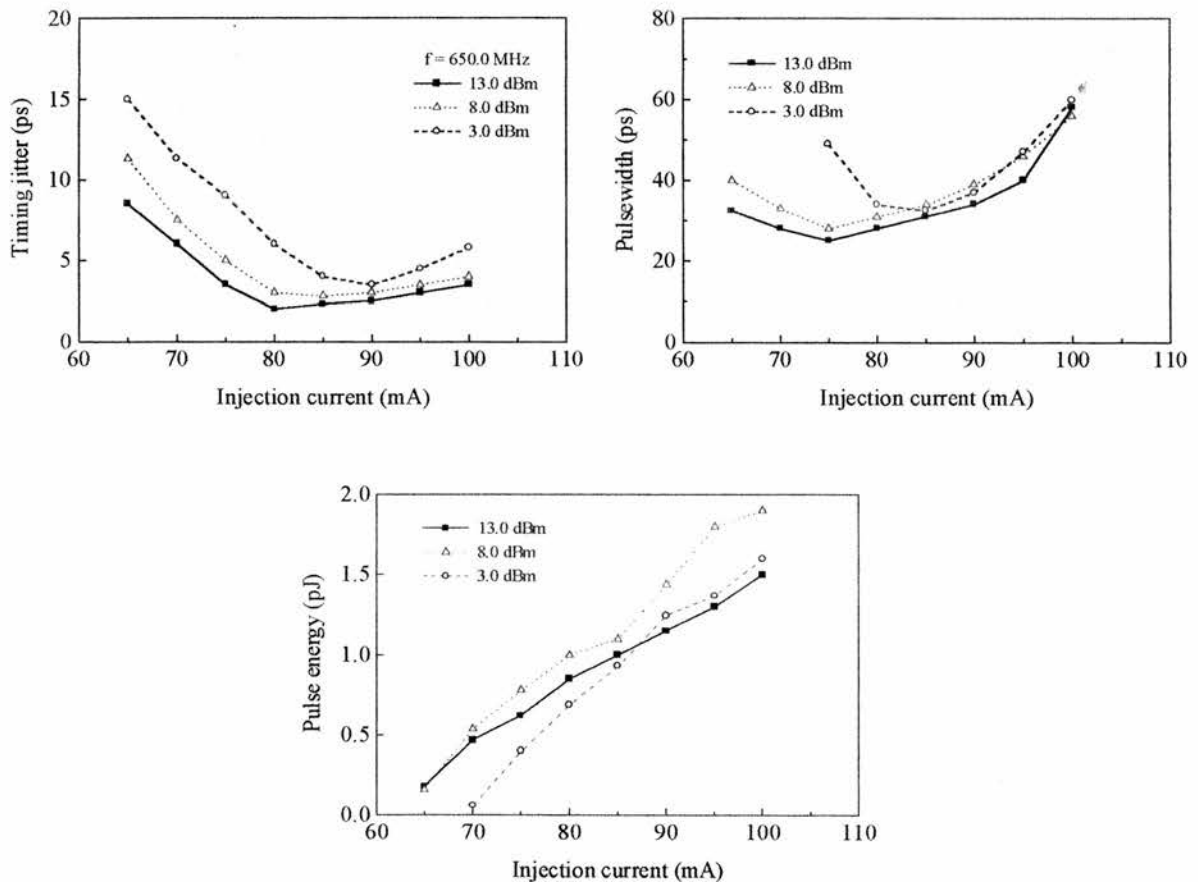


**Figure 7.11.** Timing jitter, pulse duration and pulse energy as a function of bias current for a gain-switched single-contact bulk InGaAsP Fabry-Perot laser. The modulation frequency was 650 MHz for several values of RF drive.



### 7.4.6 Timing jitter in forced Q-switched lasers

Timing jitter was assessed primarily for the two-contact (300/100 $\mu\text{m}$ ) MQW InGaAsP FP device and the three-contact (100/40/100 $\mu\text{m}$ ) bulk GaAs FP laser detailed in Chapter 6. Both diodes were operated at a modulation frequency of 650 MHz and 1309 MHz for a wide range of bias conditions. Timing jitter, pulse duration and pulse energy were simultaneously determined using the instrumentation shown in Figure 7.6.

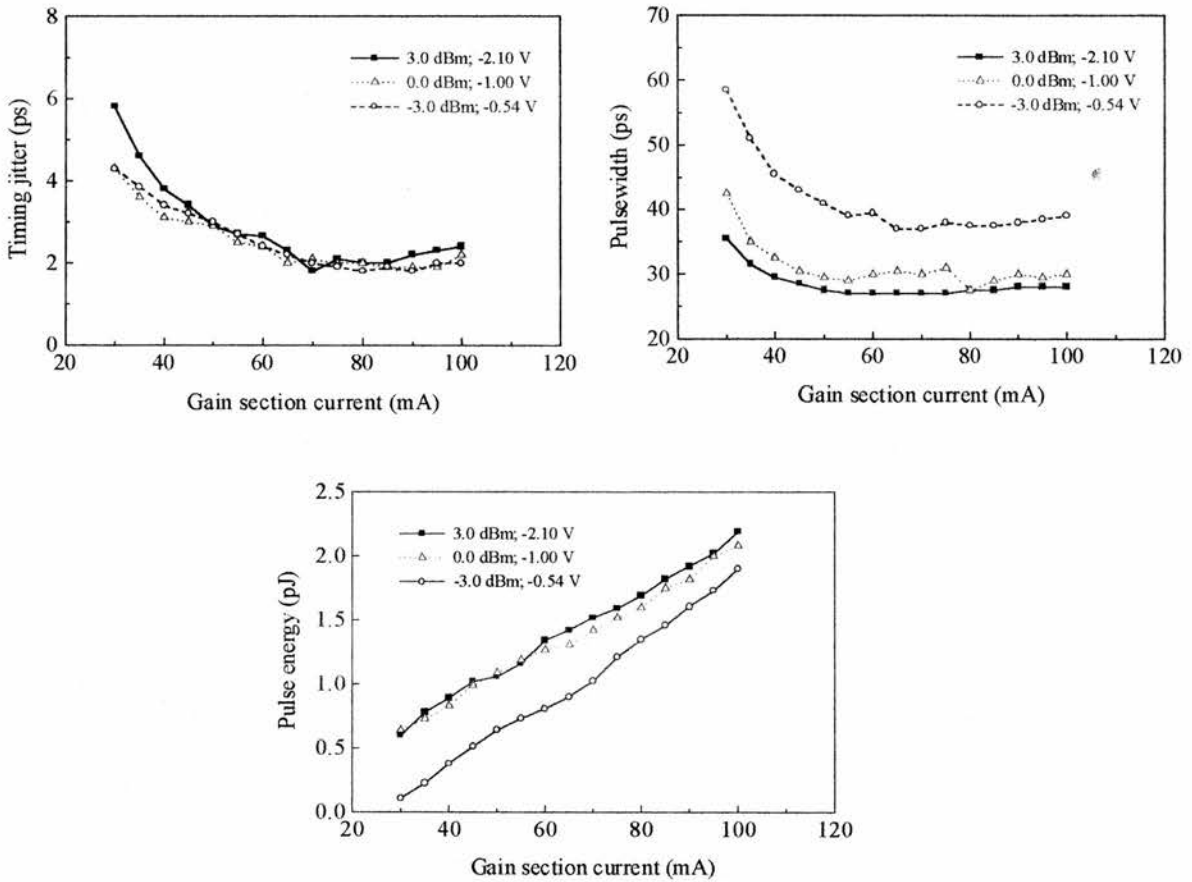


**Figure 7.12.** Timing jitter, pulse duration and pulse energy as a function of gain section bias current for a forced Q-switched 2-contact MQW InGaAsP FP laser. Contact geometry was 300/100 $\mu\text{m}$  and the modulation frequency 650 MHz.



### 7.4.7 Forced Q-switched 2-contact (300/100 $\mu\text{m}$ ) MQW InGaAsP FP device

Uncorrelated timing jitter was assessed as a function of gain section bias current for three values of RF power at both 650 MHz (Figure 7.12) and 1309 MHz (Figure 7.13). Correlated timing jitter was bias independent and negligible for the Anritsu signal generator. Over the frequency range 50 - 500Hz and 0.5 - 5kHz uncorrelated jitter was evaluated at 65fs and 35fs respectively.

From Figure 7.12 it is clear that timing jitter initially decreased from 4 - 6ps to ~2ps with increasing gain section bias as ever greater levels of spontaneous emission were coupled into the cavity laser modes. However as the cavity gain was increased the

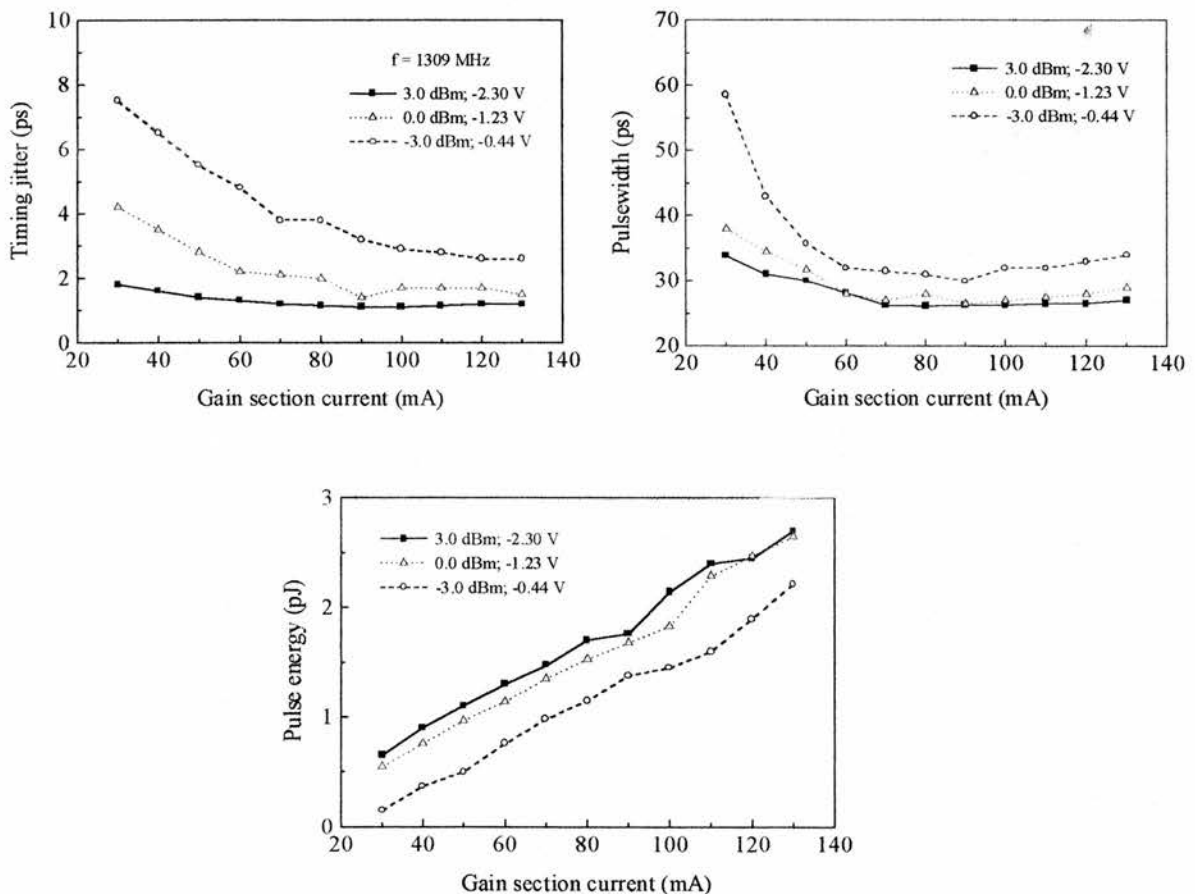


**Figure 7.13.** Timing jitter, pulse duration and pulse energy as a function of gain section bias current for a forced Q-switched 2-contact MQW InGaAsP FP laser. Contact geometry was 300/100 $\mu\text{m}$  and modulation frequency 1309 MHz.

main pulse power saturated and the jitter stabilised at  $\sim 2$ ps. Further pumping resulted in the formation of a subpulse or tail which influenced subsequent pulses and led to decreased stability at high bias conditions. The application of increased reverse bias to the absorber contact eliminated the subpulse, but degraded the jitter performance as shown in the figure where jitter began to increase at high bias levels. The jitter shows little variation with increased RF amplitude. These figures compare well with those obtained by Hughes *et al*<sup>18</sup> for forced Q-switching of multi-contact InGaAsP devices (1-3ps)

Pulse duration decreased with increased cavity gain and with increased RF power reaching a minimum of 27ps above 60mA at 3dBm. Pulse energies of up to 2pJ were possible at high bias levels. However for optimum temporal and jitter performance (27ps and 2.0ps respectively) pulse energies were typically  $\sim 1.5$ pJ as shown in Figure 7.12.

Operation at 1309MHz (Figure 7.13) resulted in higher pulse energies (up to 2.8pJ). Pulse duration was largely unchanged from values obtained at 650MHz (26ps at 3dBm, 80mA). Timing jitter showed a significant decrease to 1.2ps at high bias (3dBm, 100mA) although there was a marked increase ( $\sim 3 - 4$ ps) at lower RF amplitudes.

#### 7.4.8 Forced Q-switching of multi-contact multi-quantum well lasers at high RF frequency

The jitter performance of two MQW devices are examined. Five InGaAs wells with InGaAsP barriers formed the active layers of both devices.

- i) a three-contact (100/200/100 $\mu$ m) InGaAsP Fabry-Perot laser, the two end contacts connected off-chip to form the gain section. The central contact formed the absorber section. No AR coatings were applied.
- ii) a three-contact (200/200/200 $\mu$ m) InGaAsP DFB device. The centre contact supplied absorption and the two end contacts were pumped to provide gain.

Second order gratings were used with a central  $\lambda/4$  shift and the device was applied with AR coatings of better than 0.1%.

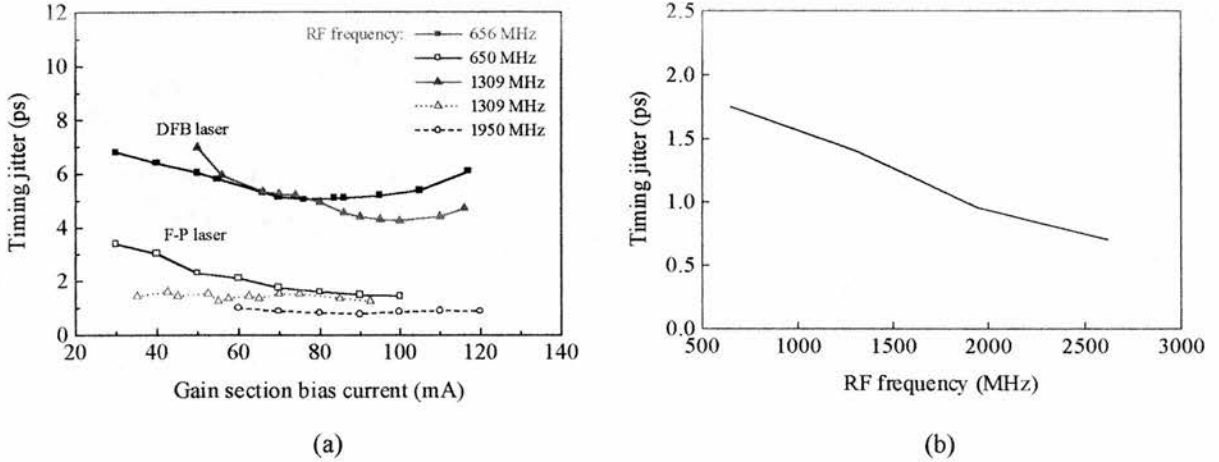


**Figure 7.14.** (a) Timing jitter as a function of gain section bias current for i) a 3-contact (200/200/200 $\mu\text{m}$ ) MQW DFB InGaAsP laser Q-switched at 1309MHz; ii) a 3-contact (100/200/100 $\mu\text{m}$ ) MQW FP InGaAsP laser Q-Switched at 656 MHz, 1309 MHz and 1950 MHz. (b) Timing jitter is reduced as the repetition rate is increased.  $\sigma_{\tau} \leq 1\text{ps}$  at  $f \geq 2\text{GHz}$  for FP devices.

The dependence of timing jitter on both gain section bias current and RF modulation frequency is shown in Figure 7.14(a). For the DFB laser (modulated at 656MHz), timing jitter was reduced with increasing bias current as a result of increased levels of spontaneous emission coupling into the laser mode before pulse initiation. Jitter decreases from 7ps to a minimum of 5ps at 80mA. Further pumping resulted in the formation of a subpulse or tail and the subsequent application of a reverse dc bias to the absorber section to eliminate satellite pulsation produced an increase in the level of jitter. Increasing the repetition rate to 1309MHz resulted in a reduction in jitter from 7ps to a minimum of 4ps at 100mA. At higher bias levels the jitter increased due to satellite pulsation.

The lower level of timing jitter produced by the Fabry-Perot device is a consequence of the larger spontaneous emission capture by the multiple FP modes prior to pulse turn on. Measurements for the FP device at 656MHz indicate a similar increase in timing jitter with decreasing gain section bias current. Jitter was minimised at 1.5ps

for single pulse operation. At a repetition rate of 1309MHz, jitter was independent of bias current (assuming no reverse bias on the absorber contact) and typical values of 1.4ps were obtained. A further increase in the repetition rate to 1950MHz produced a bias independent jitter level of 800fs. This very short value compares well with that obtained by Williams *et al*<sup>23</sup> for high-frequency Q-switching of multi-contact InGaAsP devices (1ps). In general, as the gain section bias was increased, the pulse became increasingly asymmetric until secondary pulsation and relaxation oscillations eventually became apparent. Thus, at low RF frequencies, lower levels of gain section bias were required to realise symmetric pulses. Figure 7.14(b) shows the linear decrease in timing jitter with increasing repetition rate due to the enhancement of pulse build-up times. For FP devices, sub-picosecond jitter levels were realised for repetition rates greater than 2GHz. Typical pulse duration varied between 20 - 30ps over a wide range of bias conditions with pulse energies in the 1 - 2pJ range.

#### 7.4.9 Timing jitter in forced Q-switched bulk GaAs lasers

The bulk FP device characterised in Chapter 6 (Figure 6.11) was assessed for jitter performance. This was a three-contact (100/40/100 $\mu$ m) bulk active layer Fabry-Perot device with a 5 $\mu$ m waveguide. The two end contacts were connected together off-chip and were pumped to provide gain. The central 40 $\mu$ m section formed the absorber contact, giving a gain to absorber contact ratio of 5:1. Output wavelength was 885nm. Figure 6.11 shows that the relatively short (15 - 25ps) symmetrical pulses produced by bulk GaAs devices were a direct consequence of the significantly lower levels of nonlinear gain in these lasers compared with DQW GaAs devices or bulk or MQW InGaAsP diodes. Reduced levels of nonlinear gain suppression mean that bulk GaAs can sustain much higher levels of gain bias current before the onset of satellite pulsation. Figures 6.11 (i)(a) & (iii)(a) show that satellite pulses were removed entirely at higher RF frequencies and amplitudes. However, timing jitter showed significant increase and pulse energy was reduced at extreme RF amplitudes. Optical spectra were broadly chirped and highly multimode with a typical full width at half maximum of 3nm.

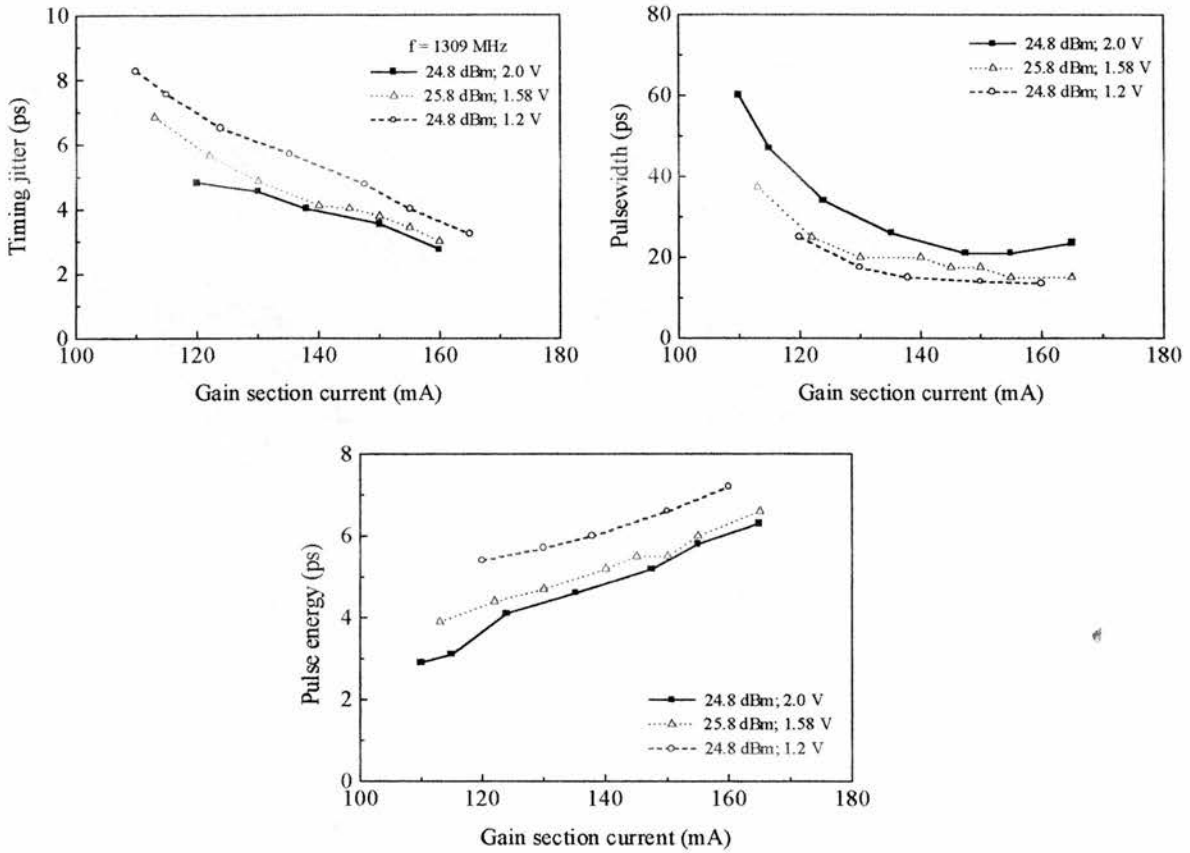


**Figure 7.16.** Timing jitter, pulse duration and pulse energy as a function of gain section bias current for a forced Q-switched 3-contact bulk GaAs FP laser. Contact geometry was 100/40/100 $\mu\text{m}$  with the 100 $\mu\text{m}$  contacts joined together off-chip to form the gain section. The modulation frequency was 1309 MHz.

Spectral control may be achieved by placing the Q-switched FP device in a grating cavity, the length of which is tuned to the relevant modulation frequency. Single longitudinal mode operation is possible although pulse energies and peak powers are drastically reduced.

Figures 7.15 and 7.16 indicate that timing jitter values of 4 - 6ps were produced at a modulation frequency of 656MHz. Operation at 1309MHz, however, resulted in a reduction in jitter to 3ps. Williams *et al*<sup>23</sup> reported similar levels of jitter (>4ps) for forced Q-switched multi-contact GaAs devices. These levels of timing jitter were considerably higher than those generated by InGaAsP devices and result primarily from the effects of reduced gain suppression which in turn produced large variations in peak

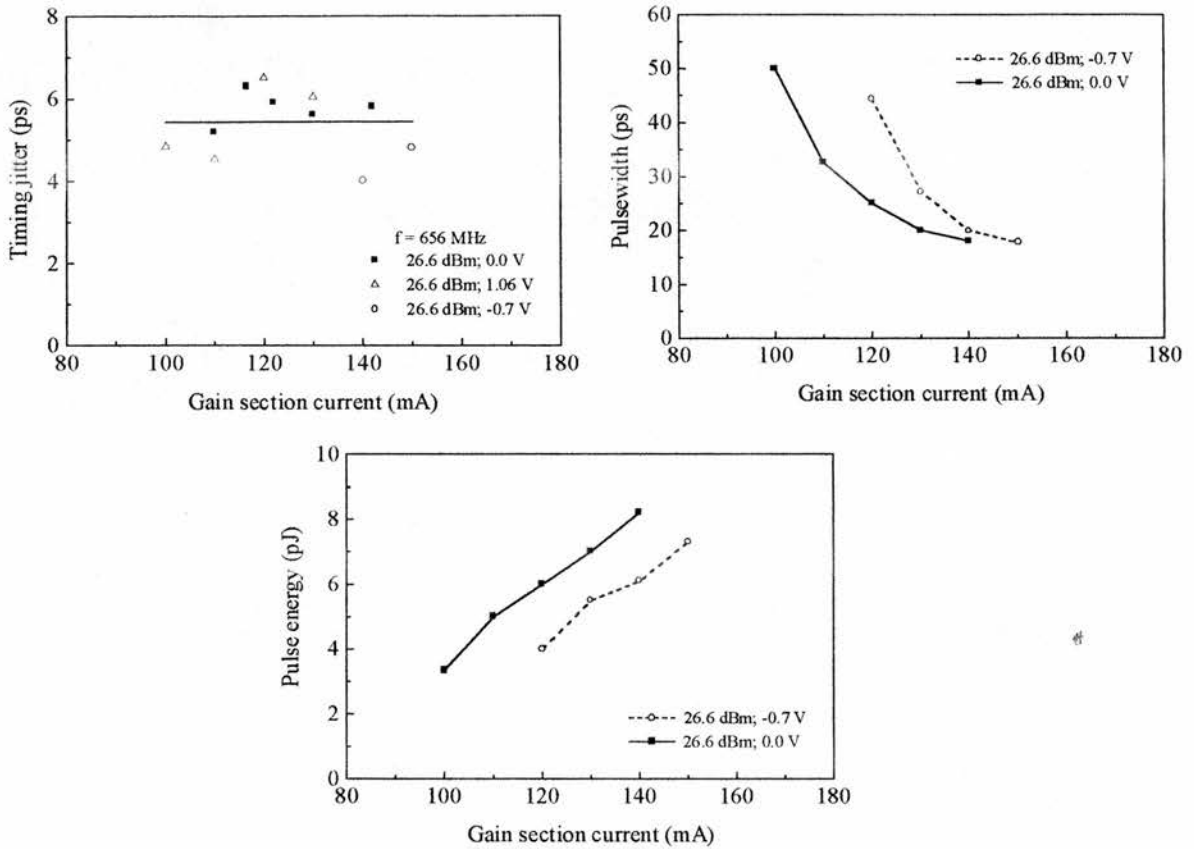


**Figure 7.15.** Timing jitter, pulse duration and pulse energy as a function of gain section bias current for a forced Q-switched 3-contact bulk GaAs FP laser. Contact geometry was 100/40/100 $\mu\text{m}$  with the 100 $\mu\text{m}$  contacts joined together off-chip to form the gain section. The modulation frequency was 656 MHz.

power. These deviations manifested themselves in the form of increased amplitude noise which resulted in increased levels of phase noise via cavity refractive index modulation. For GaAs devices, pulsewidth reduction with increasing gain bias displayed a similar trend to that shown by InGaAsP lasers. However pulse durations of  $\sim 20\text{ps}$  were universally lower than the typical 25 - 30ps available from 1550nm devices. The reduction in pulsewidth is attributable to the faster turn on, gain depletion and then pulse turn off which results from the reduced photon dependent saturation effects in bulk devices produced by the higher gains produced before optical turn on. Pulse energies in the range 4 - 8ps were easily attained at both 656MHz and 1309MHz, although these values were significantly higher than those obtained from InGaAsP devices.

## 7.5 Jitter reduction

Figure 7.17 shows the main physical processes involved in the production of ultrashort pulses in semiconductor diode lasers. The most important mechanism in the sequence in terms of timing jitter is spontaneous emission. It is the stochastic character of the spontaneous emission which creates an uncertainty in the temporal position (with respect to the modulation waveform) of the emitted pulse and results in timing jitter.

Gain-switched devices exhibit poor jitter performance, consequently, timing jitter may be reduced by

- (a) using forced Q-switching. Q-switched devices are capable of generating high peak powers. Peak power is directly proportional to carrier concentration, as is spontaneous emission;
- (b) increasing the bias current;
- (c) increasing the RF modulation frequency. Jitter is reduced as a direct consequence of the increased gradient of the electrical transient at optical turn-on;
- (d) increasing the spontaneous emission coupling to the laser mode via
  - (i) multi-mode oscillation rather than SLM. Fabry-Perot lasers are therefore preferable to DFB devices;

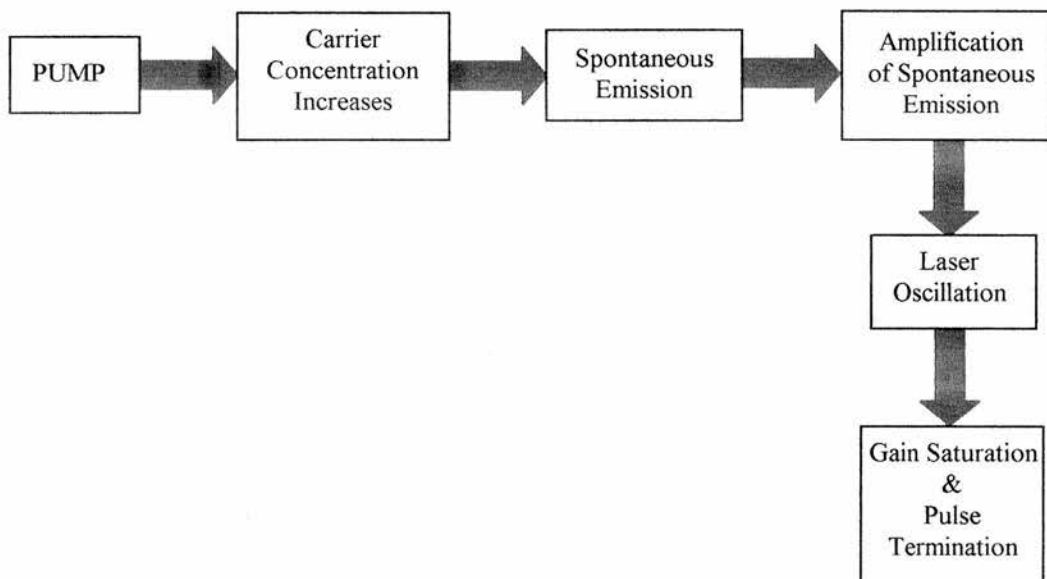


**Figure 7.17.** Picosecond pulse production in semiconductor diode lasers.



(ii) use of devices with higher spontaneous emission coupling coefficients;

(c) eliminating the need for spontaneous emission for pulse initiation, that is, by injection seeding. Jitter may be reduced by maximising the injection rate of the seed laser. However, the pulse shape is preserved by minimising the injection rate. Therefore a compromise must be made between jitter and pulse performance.

## 7.6 Conclusions

In this chapter, a theoretical treatment of both correlated and uncorrelated timing jitter was outlined. Values of timing jitter were determined for a variety of laser devices under modelocked, gain-switched and Q-switched regimes at both low and high modulation rates. For gain-switching and forced Q-switching, pulse timing jitter was found to decrease with increasing gain current, with increasing RF power and with increasing modulation frequency. Although FP lasers displayed lower timing jitter (<5ps) than DFB devices (>20ps), gain-switched devices generally exhibited poor jitter performance. Q-switched single mode DFB lasers produced bias dependent jitter in the 5 - 15ps range whereas Fabry-Perot devices showed reduced levels of 1 - 5ps due to the greater coupling of spontaneous emission into the laser modes. High frequency (1950MHz) modulation of forced-Q-switched multi-contact MQW InGaAsP Fabry-Perot lasers was found to produce the lowest levels of jitter (0.8ps). However spectral control was problematic for such devices.

While low timing jitter is an extremely desirable quality in any laser system, it cannot be treated in isolation. Other device characteristics must be taken into consideration such as pulsewidth, spectral performance (bandwidth limited pulses) and peak power. Pursuit of low jitter levels invariably means that one or more of these features is compromised since it is impossible at present to achieve optimum performance for all of the above simultaneously. Thus the various properties contributing to overall device performance must be prioritised.



## 7.7 References

1. P. Spano, A. D'Ottavi, A. Meozzi, and B. Diano, *Appl. Phys. Lett.* **52**, 2203 (1988).
2. A. D'Ottavi, A. Meozzi, P. Spano and S. Piazzolla, *Appl. Phys. Lett.* **53**, 2362 (1988).
3. E.H. Bottcher, K. Ketterer and D. Bimberg, *J. Appl. Phys.* **63**, 2469 (1988).
4. E.H. Bottcher and D. Bimberg, *Appl. Phys. Lett.* **54**, 1971 (1989).
5. A.G. Weber, W. Ronghan, E.H. Bottcher, M. Schell and D. Bimberg, *IEEE J. Quantum Electron.* **QE-28**, 441 (1992).
6. A.J. Taylor, J.M. Wiesenfeld, G. Eisenstein and R.S. Tucker, *Appl. Phys. Lett.* **49**, 681 (1986).
7. J. Kluge, D. Wicbert and D. von der Linde, *Opt. Comm.*, **51**, 271 (1984).
8. D. von der Linde, *Appl. Phys. B* **39**, 201 (1986).
9. M.J.W. Rodwell, D.M. Bloom and K.J. Weingarten, *IEEE J. Quantum Electron.* **QE-25**, 817 (1989).
10. D. Burns, A. Finch, W. Sleat and W. Sibbett, *IEEE J. Quantum Electron.* **QE- 26**, 1860 (1990).
11. D.J. Derickson, R.J. Helkey, A. Mar, J.R. Karin, G. Wasserbauer and J.E. Bowers, *IEEE J. Quantum Electron.* **QE- 28**, 2186 (1992).
12. D.A. Leep and D.A. Holm, *Appl. Phys. Lett.* **60**, 2451 (1992).
13. M. Jinno, *IEEE Photon. Technol. Lett.*, **5**, 1140 (1993).
14. P. Pepeljugoski, D. Cutrer and K. Lau, *Electron. Lett.* **30**, 491 (1994).
15. K. A. Williams, D. Burns, I.H. White, W. Sibbett and M.J. Fice, *IEEE Photon. Technol. Lett.*, **5**, 867 (1993).
16. K. A. Williams, I.H. White, D. Burns and W. Sibbett, in *LEOS Proc.*, Boston, MA, IEEE Press (1994).
17. I.H. White, K. A. Williams, D.M. Hughes, D. Burns and W. Sibbett, *CLEO Europe Proc.*, Amsterdam, The Netherlands, paper CTuL1 (1994).
18. D.M. Hughes, D. Burns, W. Sibbett, K. A. Williams and I.H. White, *CLEO Proc.*, Anaheim, CA, paper CWN4 (1994).
19. D.J. Derickson, A. Mar and J.E. Bowers, *Electron. Lett.* **26**, 2026 (1990).
20. D.J. Derickson, A. Mar, J.E. Bowers and R.L. Thornton, *Appl. Phys. Lett.* **59**, 3372 (1991).
21. P.J. Delfyett, D.H. Hartman and Z. Ahmeds, *IEEE J. Lightwave Technol.*, **9**, 1646 (1991).

22. K.J. Weingarten, M.J.W. Rodwell and D.M. Bloom, *IEEE J. Quantum Electron.* **QE-22**, 198 (1988).
23. K.A. Williams, I.H. White, D. Burns and W. Sibbett, *IEEE J. Quantum Electron.* **QE-32**, 188 (1996).

# Chapter 8

## GENERAL CONCLUSIONS

### 8.1 Ultrashort pulse semiconductor diode lasers

This thesis describes three methods of generating ultrashort light pulses in semiconductor diode lasers: modelocking, gain-switching and Q-switching. The strengths and weaknesses of each method have been outlined and simple, powerful computer models were constructed to provide a strong theoretical framework to complement and support the experimental data. Timing jitter in all three regimes was examined and routes towards jitter reduction were outlined. Two novel external-cavity modelocked laser systems were presented.

A major handicap throughout the course of this work was the non-availability of laser devices for experimental work. It proved impossible to construct a logical series of experiments with which to further the development of multi-contact semiconductor lasers. Device supply was rather haphazard and often non-existent. Consequently, at an early stage, development of multi-contact devices was abandoned. Equipment failure and lack of resources also meant that device characterisation facilities were no longer available. As a result, the scope of this thesis was severely limited and it has proved difficult to draw accurate general conclusions from experimental results based on a restricted range of devices.

A theoretical treatment of modelocking was presented in Chapter 2 as a precursor to the novel external-cavity systems described in subsequent chapters. Active modelocking was considered in detail and the performance of this method was assessed by computer simulation. Multiple-pulse formation and methods for the suppression of this phenomenon were also examined.

The dual-wavelength laser described in Chapter 3 was a simple and elegant application of the external-cavity actively modelocked InGaAsP laser. Dual-

wavelength output was demonstrated over a continuously tuneable wavelength range of 0.5 to 55nm.

A second novel modelocked laser system was described and characterised in Chapter 4: the multiple-pulse laser. Several composite external-cavity geometries were investigated and pulse frequencies over a 6 - 23GHz tuning range were achieved for low-frequency modulation rates.

The dual-wavelength laser and the multiple-pulse laser were only briefly examined and both would benefit greatly from further research. In particular, the operating principles of multi-pulsing lasers are not well understood and deserve further scrutiny, perhaps with the aid of a computer model.

Gain-switching techniques were addressed in Chapter 5. An effective theoretical model was developed to assess the temporal performance of gain-switched devices. Bulk DFB and Fabry-Perot devices were characterised. Pulse width and was limited to 20 - 30ps for low-energy ( $\sim 1 - 2\text{pJ}$ ) single feature operation.

Forced Q-switching of multi-contact diode lasers was described in Chapter 6. The physical processes involved in Q-switching were examined and important operational parameters were identified. Their relative importance was assessed using a powerful computer model based on nonlinear rate equations. Using this simulation, a wide range of operating conditions were considered and their effect on both pulsewidth and peak power were examined. InGaAsP and GaAs devices were compared experimentally and it was found that the higher peak powers available from GaAs devices were a direct consequence of increased levels of gain compression in gallium arsenide. In addition, nonradiative (Auger) recombination showed reduced levels in GaAs due to the wider band gap of this material. Peak powers of up to 90mW were obtained from Q-switched GaAs devices at 1.3GHz, an order of magnitude greater than those available from comparable InGaAsP devices.

Chapter 7 examined the origin and nature of phase noise or timing jitter. Correlated and uncorrelated timing jitter were described theoretically and the relationship between and significance of both variants explained. The stability of modelocked, gain-switched and Q-switched devices was assessed. Jitter in modelocked lasers was found to be largely correlated (to the drive electronics) and values as low as 49fs were determined for the dual-wavelength external-cavity system

described in Chapter 3. For the gain-switched lasers characterised in Chapter 5, it was found that Fabry-Perot devices exhibited lower levels of timing jitter ( $<5\text{ps}$ ) than DFB lasers ( $>20\text{ps}$ ) due to the highly multimode nature of the FP spectrum. Timing jitter was also found to decrease with both increasing RF modulation and frequency. High-frequency modulation (1950MHz) of multiple-contact forced Q-switched InGaAsP FP lasers produced jitter levels of 800fs with still lower levels predicted at higher repetition rates. GaAs devices displayed considerably higher levels of timing jitter ( $<3\text{ps}$ ) under similar operating conditions due to the effects of reduced gain suppression in these devices.

## 8.2 High-power ultrashort pulse lasers

The search for semiconductor laser structures exhibiting ever greater peak powers and pulse energies is inexorable and is a major research activity. Angled-stripe travelling wave<sup>1</sup> and large-area diffraction-limited tapered semiconductor amplifiers<sup>2,3</sup> are at the forefront of scientific interest and they are regarded as most promising sources of high power ultrashort pulse generation. Two such devices which warrant future investigation are the bow-tie laser and the vertical-cavity surface-emitting laser.

### 8.2.1 Bow-tie lasers

Tapered broad-area lasers offer the possibility peak powers and pulse energies at least one order of magnitude greater than those obtainable from conventional straight guide lasers under Q-switched operation. Tapered waveguide laser devices are a direct development of tapered semiconductor laser amplifiers<sup>2,3</sup>.

The flared-geometry or 'bow-tie' laser is shown schematically in Figure 8.1. A rib waveguide is formed by ion etching tapers from  $10\mu\text{m}$  in the centre to  $45\mu\text{m}$  at the end facets. The relatively large area of the end facets contribute significantly to the reduction of optical facet damage. Flared geometry lasers may be Q-switched to provide picosecond pulse generation<sup>4</sup>.

As with all other laser devices, supply of bow-tie lasers suitable for non-pulsed operation was problematic. The GaAs devices examined were of poor quality and of

such short operational lifetime that spectral and temporal characterisation was incomplete. Jitter analysis was not considered because of insufficient amplification. The theoretically more robust InGaAsP bow-tie devices were unavailable. As a result, bow-tie lasers do not feature in this thesis and it would appear at time of writing that

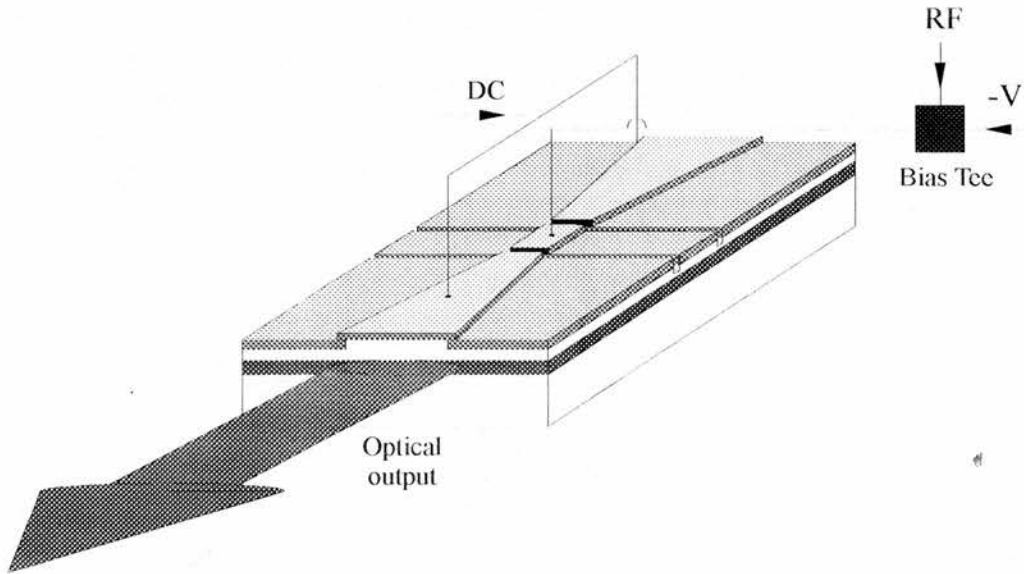


**Figure 8.1.** Schematic representation of a double tapered waveguide bow-tie laser. A three-contact laser is shown under Q-switched operation: the two end contacts are joined together off-chip and are forward biased to provide gain. The narrow central waveguide is driven via a strong RF modulation superimposed onto a reverse dc bias and provides saturable absorption and transverse mode filtering.

further research into straight and tapered guide multiple-contact semiconductor lasers has been totally abandoned. Given the severe shortage of operational devices and an overall shortage of resources, it would appear that this outcome was inevitable. However, given an alternative source of laser devices and adequate diagnostic hardware, there is no reason why this promising avenue of research could not be successfully resurrected.

### 8.2.2 Vertical-cavity surface-emitting lasers

Another promising area of high-power ultrashort pulse research is the vertical-cavity surface-emitting laser (VCSEL)<sup>5</sup>. These devices boast wide aperture, single longitudinal mode operation and find widespread use in optical computing and high-speed optoelectronic IC applications<sup>6</sup>. VCSELs have been shown to produce

pulsewidths of 17 - 30ps at low RF frequency (~8GHz) using gain-switching although such pulses exhibit strong wavelength chirp. However these devices have potentially very high modulation bandwidths which suggests that they can be operated at extremely high frequencies.

### 8.3 Pulsewidth reduction techniques

Along with drive for high output power, the second most important goal in diode laser research is that of pulsewidth reduction. Pulse durations in the 0.5 - 1.0ps range are the shortest currently available. However, optical pulsewidths of less than 50fs should in theory be possible given diode laser bandwidths of 15 - 20nm. Achieving such short pulsewidth in practice is problematic.

External-cavity modelocked systems would appear to offer the prospect of the shortest pulsewidths. In particular, coupled-cavity modelocked devices promise pulsewidths as short as 50 to 500fs.

Pulse compression techniques may also have the potential to reduce optical pulsewidths to less than 100fs. Gain-switched DFB lasers in conjunction with soliton-effect pulse compressors have generated pulses as short as 590fs with a peak powers of over 30W<sup>7</sup>.

Cross-phase modulation techniques<sup>8</sup> also show great promise as a method of pulsewidth reduction. Using this technique, 12ps modelocked pulses have been compressed down to 4.6ps at a repetition rate of 5GHz.

### 8.4 Low jitter in ultrashort pulse lasers

Jitter reduction would also appear to be a promising area of future research. A number of feedback techniques have been proposed for the reduction of timing jitter. These include optoelectronic feedback<sup>9-12</sup> in which the laser is electrically modulated via amplification of the optical pulse information incident on a photodetector, optical feedback<sup>9,13,14</sup> whereby pulse production is optically induced via reflection into the laser cavity of an optical pulse from a previous modulation cycle and electrical feedback<sup>9</sup> where a microwave directional coupler is used to modulate the amplified

forward voltage fluctuation of a laser junction. Of the three schemes, optoelectronic feedback offers the simplest and most effective means of jitter reduction. The feedback scheme illustrated in Figure 8.2 was implemented for a self Q-switched three-contact InGaAsP DFB laser. Here, shot noise from the dc biased gain-section was fed back into the subthreshold biased absorber contact via a bias tee. RF modulation of the absorber was not required since conditions in the feedback loop determined the frequency of operation of the system. Despite significant input, the feedback scheme was not successfully implemented due to insufficient levels of amplification in the feedback loop. This would be a fruitful area of future research and indeed the whole area of jitter characterisation deserves further investigation since previous efforts in this regard were terminated by equipment failure.

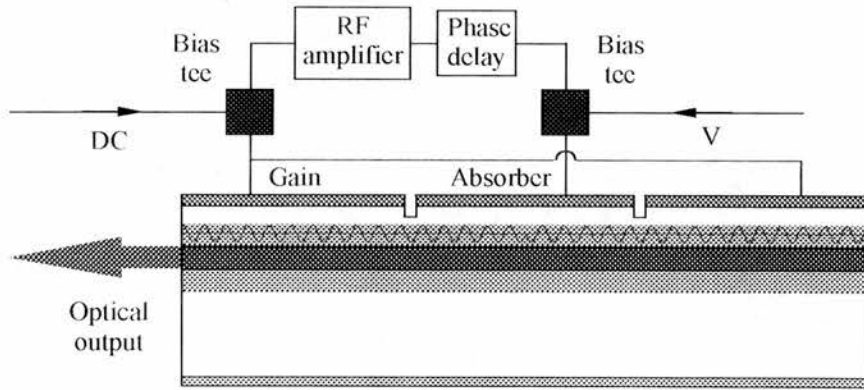


**Figure 8.2.** Schematic representation of integrated optoelectronic feedback for a three-contact DFB laser.



**8.4 References**

1. P.J. Delfyett, L.T. Florez, N. Stoffel, T. Gmitter, C. Andreakis, Y. Silverberg, J.P. Heritage and G.A. Alphonse, *IEEE J. Quantum Electron.*, **28**, 2203 (1992).
2. D. Mchuy, D.F. Welch and L. Goldberg, *Electron. Lett.*, **28**, 1944 (1992).
3. D.F. Welch, R. Parke, D. Mchuy, A. Hardy, R. Lang, S. O'Brien and S. Scifres, *Electron. Lett.*, **28**, 2011 (1992).
4. P.P. Vasil'ev, *IEEE J. Quantum Electron.*, **24**, 2386 (1988).
5. K. Iga, F. Koyama and S. Kinoshita, *IEEE J. Quantum Electron.*, **24**, 1845 (1988).
6. L.G. Meleer, J.R. Karin, R. Nagarajan and J.E. Bowers, *IEEE J. Quantum Electron.*, **27**, 1417 (1991).
7. J.T. Ong, R. Takahashi, M. Tsuchiya, S.-H. Wong, R.T. Sahara, Y. Ogawa and T. Kamiya, *IEEE J. Quantum Electron.*, **29**, 1701 (1993).
8. A.D. Ellis and D.M. Patrick, *Electron. Lett.*, **29**, 149 (1993).
9. T.L. Paoli and J.E. Ripper, *IEEE J. Quantum Electron.*, **6**, 335 (1970).
10. J.B. Georges, L. Buckman, D. Vassilovski, J. Park, M.-H. Kiang, O. Solgaard and K.L. Lau, *Electron. Lett.*, **30**, 69 (1994).
11. K. Lau and A. Yariv, *Appl. Phys. Lett.*, **45**, 124 (1984).
12. C. Yan, K.P.J. Reddy, R.K. Jain and J.C. McInerney, *IEEE Photon. Technol. Lett.*, **5**, 494 (1993).
13. D. Huhse, M. Schell, M. Kaessner and D. Bimberg, *Electron. Lett.*, **30**, 157 (1994).
14. O. Solgaard and K.Y. Lau, *IEEE Photon. Technol. Lett.*, **5**, 1264 (1993).

## Appendices

### 1. Semiconductor Laser Rate Equations

#### PHYSICAL DIMENSIONS

$$\text{Length} = 400 \cdot 10^{-6}$$

$$\text{Vol} = \text{Length} \cdot \text{width} \cdot \text{depth}$$

$$\text{width} = 3.5 \cdot 10^{-6}$$

$$\text{Vol} = 2.52 \cdot 10^{-16} \cdot \text{m}^3$$

$$\text{depth} = 0.18 \cdot 10^{-6}$$

#### CONFINEMENT FACTOR

$$\Gamma = 0.3$$

#### REFRACTIVE INDEX

$$\mu = 3.$$

#### SPONTANEOUS EMISSION COUPLING COEFFICIENT

$$\beta = 1 \cdot 10^{-4}$$

#### SPEED OF LIGHT

$$c = 3.0 \cdot 10^8 \cdot \text{m} \cdot \text{sec}^{-1}$$

#### ELECTRONIC CHARGE

$$e = 1.602 \cdot 10^{-19} \cdot \text{coul}$$

#### NONRADIATIVE RECOMBINATION RATE

$$A = 1 \cdot 10^8 \cdot \text{sec}^{-1}$$

#### RADIATIVE RECOMBINATION RATE

$$B = \frac{1 \cdot 10^{10} \cdot \text{cm}^3 \cdot \text{sec}^{-1}}{\text{Vol}}$$

#### AUGER COEFFICIENT

$$C = \frac{1.3 \cdot 10^{28} \cdot \text{cm}^6 \cdot \text{sec}^{-1}}{\text{Vol}^2}$$

#### TRANSPARENCY CARRIER DENSITY

$$T = 1.1 \cdot 10^{18} \cdot \text{cm}^{-3}$$

#### MIRROR LOSS

$$\alpha_{\text{mirror}} = 45 \cdot \text{cm}^{-1}$$

#### INTERNAL LOSS

$$\alpha_{\text{int}} = 40 \cdot \text{cm}^{-1}$$

#### TOTAL LOSS

$$\gamma = \frac{c}{\mu} \cdot (\alpha_{\text{mirror}} + \alpha_{\text{int}})$$

#### PHOTON LIFETIME

$$\rho = \gamma^{-1}$$

$$\rho = 1.451 \cdot 10^{-12} \cdot \text{sec}$$

LINEAR GAIN  $G: 3.0 \cdot 10^{-16} \cdot \text{cm}^2$

GAIN SUPPRESSION FACTOR  $\epsilon: \frac{1.0 \cdot 10^{-17} \cdot \text{cm}^3}{\text{Vol}}$   
 $\epsilon = 3.968 \cdot 10^{-8}$

MEASUREMENT INTERVAL IN ps Measurementint = 550  
 $t: 0.. \text{Measurementint}$

MODULATION FREQUENCY IN Hz  $f: 1.25 \cdot 10^9 \cdot (1 \cdot 10^{-12})$

TIME STEP  $\Delta t: 1 \cdot 10^{-12} \cdot \text{sec}$

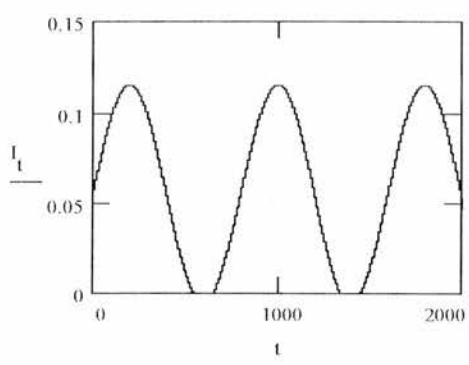
INITIAL VALUES OF PHOTON AND CARRIER NUMBER  
 $P_1:$   
 $N_1:$

DRIVE CURRENT

$I_t: \text{if}(t < \text{Measurementint}, (Rf \cdot \sin(2 \cdot \pi \cdot f \cdot t) + IC) \cdot \Phi(Rf \cdot \sin(2 \cdot \pi \cdot f \cdot t) + IC), 0 \text{ amp})$

COMPONENTS OF DRIVE CURRENT

$$\begin{pmatrix} P_{t+1} \\ N_{t+1} \end{pmatrix} = \begin{pmatrix} P_t \cdot \left[ 1 - \frac{\Gamma \cdot c \cdot G}{\mu} \cdot \frac{N}{V_0} \cdot T \right] \cdot (1 - \epsilon P_t) - \gamma \cdot P_t - \frac{\beta N}{I} \cdot \Delta t \cdot \Phi(P_t) \\ N_t \cdot \left[ 1 - \frac{\Gamma \cdot c \cdot G}{\mu} \cdot \frac{N}{V_0} \cdot T \right] \cdot (1 - \epsilon P_t) - P_t \cdot \frac{I_c}{e} \cdot \Delta t \cdot \Phi(N) \end{pmatrix} + \begin{pmatrix} I_t \cdot \Delta t \\ I_c \cdot \Delta t \end{pmatrix}$$



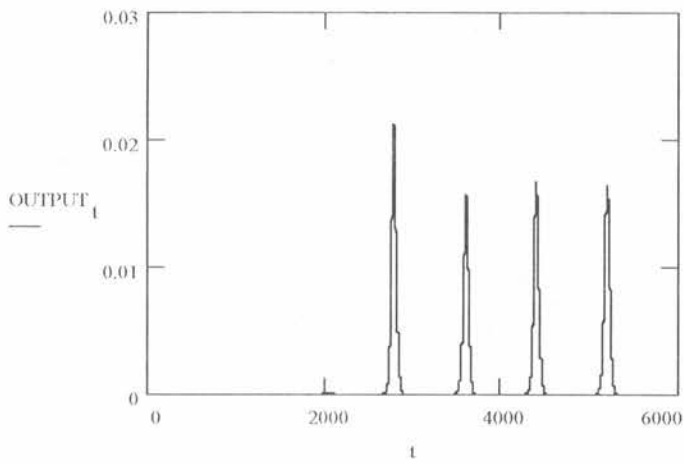
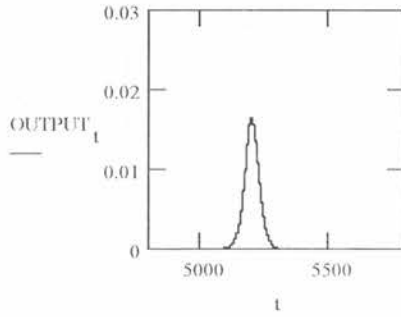
$Rf: 0.06 \text{ am}$   
 $IC: 0.055 \text{ am}$   
 $\lambda: 1500 \cdot 10^9$   
 $v: \frac{c}{\lambda}$

$$\nu = 2 \cdot 10^{14} \text{ sec}^{-1}$$

$$h = 6.63 \cdot 10^{-34} \text{ joule} \cdot \text{sec}$$

$$\text{OUTPUT}_t = \frac{1}{2} \cdot h \cdot \nu \cdot \frac{c}{\mu} \cdot \alpha \cdot \text{mirror} \cdot P_t$$

### OUTPUT POWER IN WATTS



## 2. Semiconductor Laser Rate Equations: Modelocking

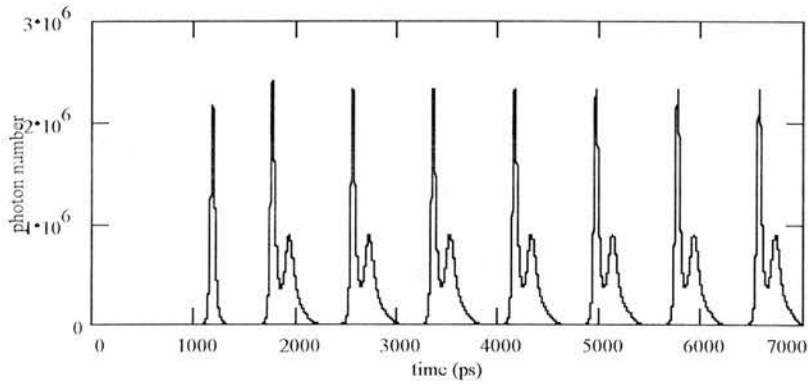
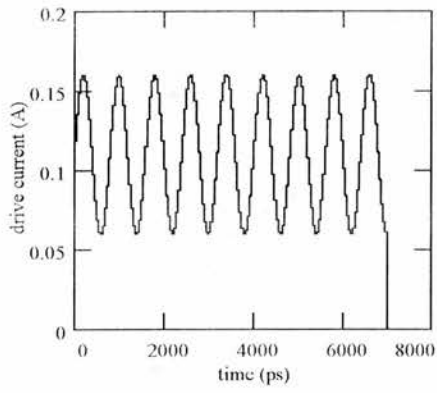
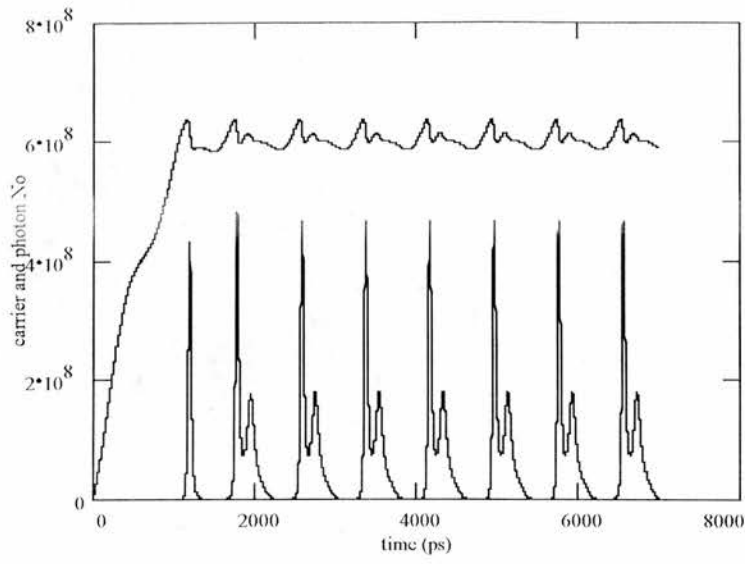
Single-mode rate equations with injection for single contact laser  $-1/(1+eP)$  type saturation  $-\beta BN^2$  type spontaneous emission.

```

Length = 500*10-6·m
Vol = Length·width·depth
width = 3.5*10-6·m
Vol = 3.15*10-16·m3
depth = 0.18*10-6·m
αmirror = 45·cm-1
Γ = 0.35
γ =  $\frac{c}{\mu}$ ·(αmirror + αint)
αint = 40·cm-1
μ = 3.7
ρ = γ-1
ρ = 1.451*10-12·sec
β = 1*10-4
B =  $\frac{1*10^{10}·cm^3·sec^{-1}}{Vol}$ 
G = 3.0*10-16·cm-2
c = 3.0*108·m·sec-1
λ = 1500*10-9·m
v =  $\frac{c}{\lambda}$ 
v = 2*1014·sec-1
C =  $\frac{1.3*10^{28}·cm^6·sec^{-1}}{Vol^2}$ 
e = 1.602*10-19·coul
h = 6.63*10-34·joule·sec
A = 1*108·sec-1
T = 1.1*1018·cm-3
t = 0., Measurementint
f = 1.25*109·(1*10-12)
Al = 5*10-12·sec
PI = 0
NI = 0
II = if(t<Measurementint, (RF·sin(2·π·f·t) + IC)·Φ(RF·sin(2·π·f·t) + IC), 0·amp)
eI = E
vI = Vol
e = 3.175*10-8

```





### 3. Semiconductor Laser Rate Equations: Gain-switching

Single-mode rate equations for single contact laser- $(1+\epsilon P)^{-1/2}$  type saturation  $-\beta B N^2$  type spontaneous emission

$$\Lambda : 1 \cdot 10^8 \cdot \text{sec}^{-1}$$

$$\mu\text{m} : 1 \cdot 10^6$$

$$\text{Length} : 250 \cdot \mu$$

$$\alpha_m : 45 \cdot \text{cm}^{-1}$$

$$\text{ps} : 1 \cdot 10^{12} \cdot \text{sec}$$

$$B : 1 \cdot 10^{10} \cdot \text{cm}^3 \cdot \text{sec}^{-1}$$

$$\text{width} : 2.0 \cdot \mu$$

$$\alpha_i : 40 \cdot \text{cm}^{-1}$$

$$\text{ns} : 1 \cdot 10^9 \cdot \text{sec}$$

$$\text{depth} : 0.2 \cdot \mu$$

$$C : 3 \cdot 10^{29} \cdot \text{cm}^6 \cdot \text{sec}^{-1}$$

$$\text{mW} : 1 \cdot 10^{-3} \cdot \text{watt}$$

$$\gamma_p = \frac{c}{\mu_g} \cdot (\alpha_m + \alpha_i)$$

$$\text{Vol} = \text{Length} \cdot \text{width} \cdot \text{depth}$$

$$\lambda : 1.5 \cdot \mu$$

$$\text{Hz} : \frac{1}{1 \cdot \text{sec}}$$

$$\text{Vol} = 100,000 \mu\text{m}^3$$

$$\tau_p = \gamma_p^{-1}$$

$$v = \frac{c}{\lambda}$$

$$\mu_g = 4$$

$$\gamma_p = 6.371 \cdot 10^{11} \cdot \text{sec}^{-1}$$

$$v = 1.999 \cdot 10^{14} \cdot \text{m} \cdot \text{sec}^{-1}$$

$$c = 299792458 \text{m} \cdot \text{sec}^{-1}$$

$$\tau_p = 1.5697 \text{ps}$$

$$e = 1.60217733 \cdot 10^{-19} \cdot \text{coul}$$

$$h = 6.62607551 \cdot 10^{-34} \cdot \text{joule} \cdot \text{sec}$$

$$G = 2.5 \cdot 10^{16} \cdot \text{cm}^{-2}$$

$$\Delta t = X \cdot \text{ps}$$

$$I = 0$$

$$P_1 =$$

$$N_1 =$$



$$\frac{c \cdot G \Gamma}{\mu_g \text{Vol}} = 5.621 \cdot 10^3 \cdot \text{sec}^{-1}$$

$$\beta = 1.0 \cdot 10^{-4}$$

$$N_o = 1.0 \cdot 10^{18} \cdot \text{cm}^{-3} \cdot \text{Vol}$$

$$G \Gamma = 7.500 \cdot 10^{-5} \cdot \text{m}^{-1}$$

$$\text{Vol}$$

t : 0, X.. Measurementint

$$I_t := \text{if}(t < \text{Measurementint}, (Rf \cdot \sin(2 \cdot \pi \cdot f \cdot t) + IC) \cdot \Phi(Rf \cdot \sin(2 \cdot \pi \cdot f \cdot t) + IC), 0 \cdot \text{amp})$$

$$\begin{pmatrix} P_{t,x} \\ N_{t,x} \end{pmatrix} = \begin{pmatrix} P_t \cdot \left| \frac{\frac{c \cdot G \Gamma}{\mu_g \text{Vol}} (N_t - N_o)}{\sqrt{1 + s \cdot P_t}} \right| \cdot \gamma_p \cdot P_t + \beta \cdot \frac{B}{\text{Vol}} \cdot (N_t)^2 \cdot \Delta t \cdot \Phi \cdot P_t \cdot \left| \frac{\frac{c \cdot G \Gamma}{\mu_g \text{Vol}} (N_t - N_o)}{\sqrt{1 + s \cdot P_t}} \right| \cdot \gamma_p \cdot P_t + \beta \cdot \frac{B}{\text{Vol}} \cdot (N_t)^2 \cdot \Delta t}{N_t \cdot \left| \frac{\frac{c \cdot G \Gamma}{\mu_g \text{Vol}} (N_t - N_o)}{\sqrt{1 + s \cdot P_t}} \right| \cdot \frac{I_t}{c} \cdot \Delta t \cdot \Phi \cdot N_t \cdot \left| \frac{\frac{c \cdot G \Gamma}{\mu_g \text{Vol}} (N_t - N_o)}{\sqrt{1 + s \cdot P_t}} \right| \cdot \frac{I_t}{c} \cdot \Delta t} \cdot \frac{I_t}{c} \cdot \Delta t \end{pmatrix}$$

$$\text{OUTPUT}_t := \frac{1}{2} \cdot h \cdot v \cdot \frac{c}{\mu_g} \cdot \alpha_m \cdot P_t$$

$$\text{threshold} := \frac{\gamma_p}{c \cdot G \Gamma} \cdot \frac{N_o}{\mu_g \text{Vol}}$$

$$P_{av} := \text{mean}(\text{OUTPUT})$$

$$P_p := \text{max}(\text{OUTPUT})$$

$$\text{threshold} = 2.133 \cdot 10^8$$

$$P_{ave} := \sum_{t=6000}^{\text{Measurementint}} \frac{\text{OUTPUT}_t \cdot X}{\text{Measurementint} - 6000}$$

$$s = 0.2 \cdot 10^6$$

$$N_o = 1.000 \cdot 10^8$$

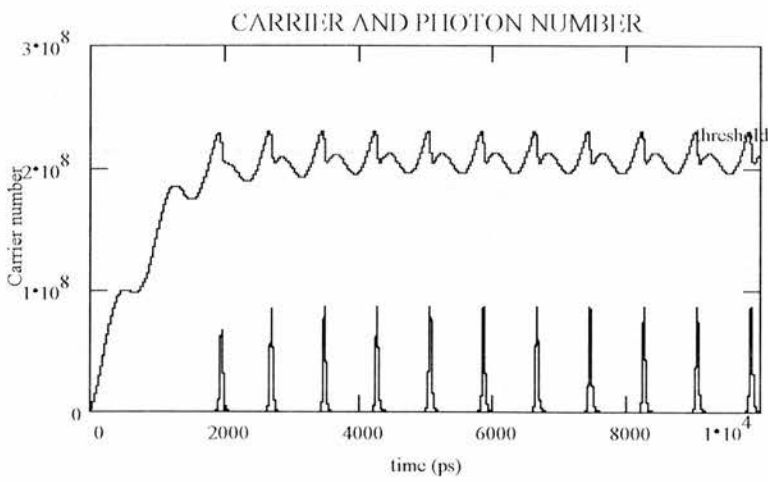
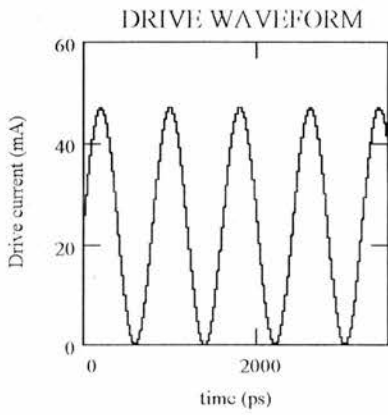
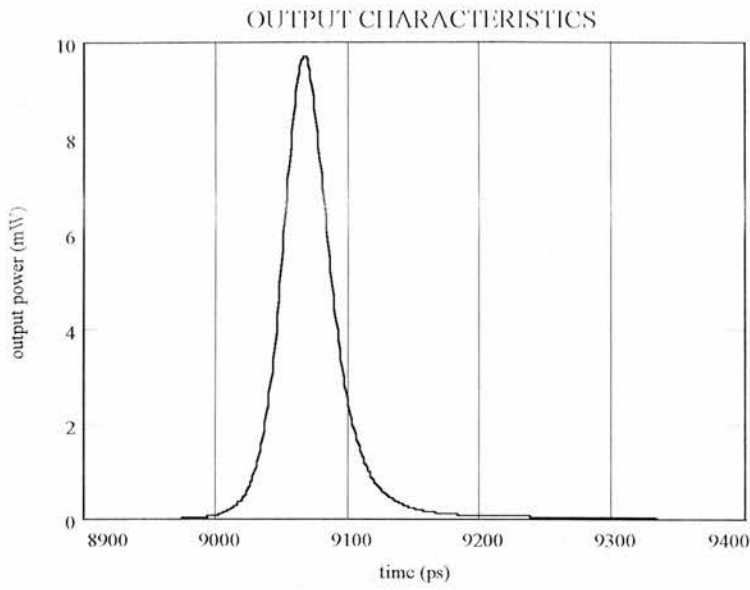
$$Rf = 0.0235 \text{ am}$$

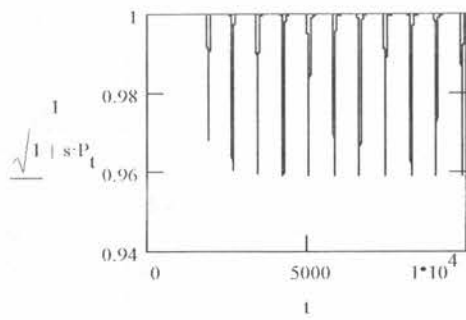
$$f = 1.25 \cdot 10^9 \cdot (1 \cdot 10^{12})$$

$$IC = 0.0235 \text{ am}$$

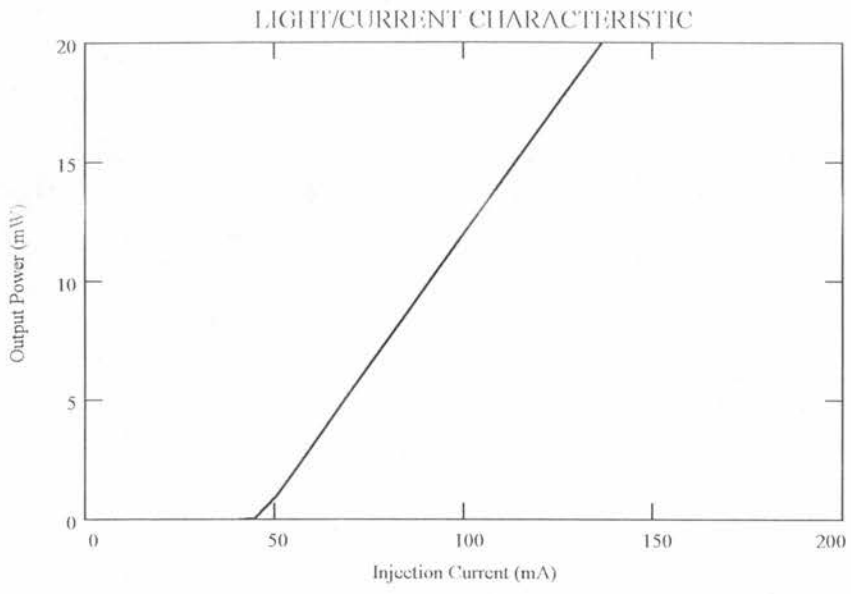
X

$$\text{Measurementint} = 1000$$





- $i : 0..$
- $j : 0..$
- $\Lambda_{0,0} : 1$
- $\Lambda_{0,1} : 1$
- $\Lambda_{1,0} : 2$
- $\Lambda_{1,1} : 1$
- $\Lambda_{2,0} : 2$
- $\Lambda_{2,1} : 1$
- $\Lambda_{3,0} : 2$
- $\Lambda_{3,1} : 1$
- $\Lambda_{4,0} : 4$
- $\Lambda_{4,1} : 0.00$
- $\Lambda_{5,0} : 4$
- $\Lambda_{5,1} : 0.04$
- $\Lambda_{6,0} : 5$
- $\Lambda_{6,1} : 0.97$
- $\Lambda_{7,0} : 10$
- $\Lambda_{7,1} : 11.97$
- $\Lambda_{8,0} : 40$
- $\Lambda_{8,1} : 78.79$



#### 4. Semiconductor Rate Equations: Q-switching

Single-mode rate equation for two-contact laser -(1-eP) type saturation –  $\beta N^2$  type spontaneous emission.

$$\text{Length}_1 = 300 \cdot 10^{-6}$$

$$\alpha_{\text{mirror}} = 45 \text{ cm}^{-1}$$

$$\text{Length}_2 = 100 \cdot 10^{-6}$$

$$\text{Vol}_1 = \text{Length}_1 \cdot \text{width} \cdot \text{depth}$$

$$\alpha_{\text{int}} = 40 \text{ cm}^{-1}$$

$$\text{width} = 3.5 \cdot 10^{-6}$$

$$\text{Vol}_1 = 1.89 \cdot 10^{-10} \text{ cm}^3$$

$$\gamma = \frac{c}{\mu} (\alpha_{\text{mirror}} + \alpha_{\text{int}})$$

$$\text{depth} = 0.18 \cdot 10^{-6}$$

$$\text{Vol}_2 = \text{Length}_2 \cdot \text{width} \cdot \text{depth}$$

$$I = 0.3$$

$$\mu = 3$$

$$\text{Vol}_2 = 6.3 \cdot 10^{-11} \text{ cm}^3$$

$$\rho = \gamma^{-1}$$

$$\beta = 1 \cdot 10^{-4}$$

$$\rho = 1.45 \cdot 10^{12} \text{ sec}$$

$$c = 3.0 \cdot 10^8 \text{ m sec}^{-1}$$

$$B_1 = \frac{1 \cdot 10^{10} \text{ cm}^3 \text{ sec}^{-1}}{\text{Vol}_1}$$

$$G = 3.0 \cdot 10^{16} \text{ cm}^2$$

$$e = 1.602 \cdot 10^{-19} \text{ coul}$$

$$\Lambda = 1 \cdot 10^8 \text{ sec}^{-1}$$

$$C_1 = \frac{1.3 \cdot 10^{28} \text{ cm}^6 \text{ sec}^{-1}}{\text{Vol}_1^2}$$

$$v = \frac{c}{\lambda}$$

$$v = 2 \cdot 10^{14} \text{ sec}^{-1}$$

$$T = 1.1 \cdot 10^{18} \text{ cm}^3$$

$$\lambda = 1500 \cdot 10^{-9}$$

$$B_2 = \frac{1 \cdot 10^{10} \text{ cm}^3 \text{ sec}^{-1}}{\text{Vol}_2}$$

$$h = 6.63 \cdot 10^{-34} \text{ joule sec}$$

$$e_1 = \frac{E}{\text{Vol}_1}$$

$$C_2 = \frac{1.3 \cdot 10^{28} \cdot \text{cm}^{-6} \cdot \text{sec}^{-1}}{\text{Vol}_2^2}$$

$$\epsilon_1 = 1.058 \cdot 10^{-7}$$

$$\epsilon_2 = \frac{1}{\text{Vol}_2}$$

$$\epsilon_2 = 3.175 \cdot 10^{-7}$$

t : 0, X... Measurementint

$$f = 1.25 \cdot 10^9 \cdot (1 \cdot 10^{-12})$$

$$\Lambda t = 1 \cdot 10^{-12} \cdot \text{sec}$$

$$P_1 = 0$$

$$N_{1_1} = 0$$

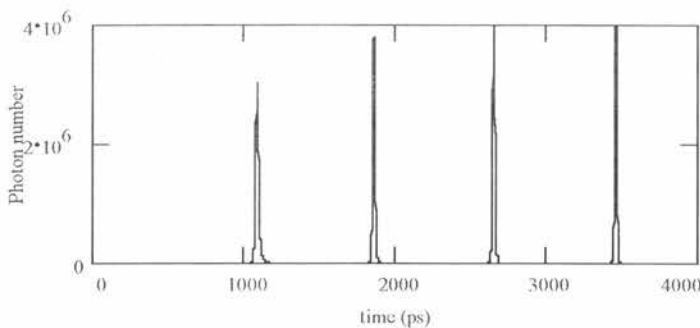
$$N_{2_1} = 0$$

$$I_{2_t} = \text{if} [ t < \text{Measurementint}, (R_1 \cdot \sin(2 \cdot \pi \cdot f \cdot t) + IC_2), 0 \cdot \text{amp} ]$$

$$I_{1_t} = IC_1 \cdot \text{amp}$$

$$\begin{pmatrix} P_{1,t+1} \\ N_{1,t+1} \\ N_{2,t+1} \end{pmatrix} = \begin{pmatrix} P_1 \cdot \left[ \frac{c \cdot G}{\mu} \left( \frac{N_1}{\text{Vol}_1} \right) \cdot T \cdot (1 - \epsilon_1 \cdot P_1) - \gamma + \frac{c \cdot G}{\mu} \left( \frac{N_2}{\text{Vol}_2} \right) \cdot T \cdot (1 - \epsilon_2 \cdot P_1) \right] \cdot P_1 + \beta \cdot B_1 \cdot (N_1)^2 \cdot \Lambda t - \Phi \cdot P_1 + \left[ \frac{c \cdot G}{\mu} \left( \frac{N_1}{\text{Vol}_1} \right) \cdot T \cdot (1 - \epsilon_1 \cdot P_1) - \gamma + \frac{c \cdot G}{\mu} \left( \frac{N_2}{\text{Vol}_2} \right) \cdot T \cdot (1 - \epsilon_2 \cdot P_1) \right] \cdot P_1 + \beta \cdot B_1 \cdot (N_1)^2 \cdot \Lambda t \\ N_1 \cdot \left[ \frac{c \cdot G}{\mu} \left( \frac{N_1}{\text{Vol}_1} \right) \cdot T \cdot (1 - \epsilon_1 \cdot P_1) \right] \cdot P_1 - \frac{I_{1_t}}{c} \cdot \Lambda t - \Phi \cdot N_1 + \frac{N_1}{\Lambda + B_1 \cdot N_1 + C_1 \cdot (N_1)^2} \cdot \left[ \frac{c \cdot G}{\mu} \left( \frac{N_1}{\text{Vol}_1} \right) \cdot T \cdot (1 - \epsilon_1 \cdot P_1) \right] \cdot P_1 - \frac{I_{1_t}}{c} \cdot \Lambda t \\ N_2 \cdot \left[ \frac{c \cdot G}{\mu} \left( \frac{N_2}{\text{Vol}_2} \right) \cdot T \cdot (1 - \epsilon_2 \cdot P_1) \right] \cdot P_1 - \frac{I_{2_t}}{c} \cdot \Lambda t - \Phi \cdot N_2 + \frac{N_2}{\Lambda + B_2 \cdot N_2 + C_2 \cdot (N_2)^2} \cdot \left[ \frac{c \cdot G}{\mu} \left( \frac{N_2}{\text{Vol}_2} \right) \cdot T \cdot (1 - \epsilon_2 \cdot P_1) \right] \cdot P_1 - \frac{I_{2_t}}{c} \cdot \Lambda t \end{pmatrix}$$

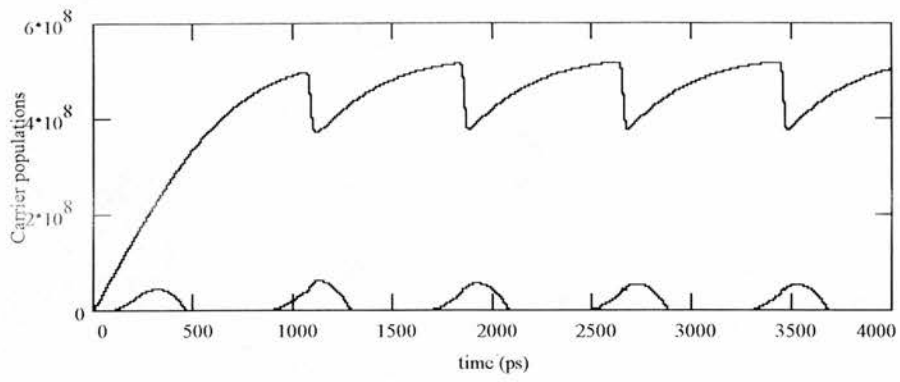
$$\text{OUTPUT}_t = \frac{1}{2} \cdot h \cdot \nu \cdot \frac{c}{\mu} \cdot \alpha_{\text{mirror}} \cdot P_t$$



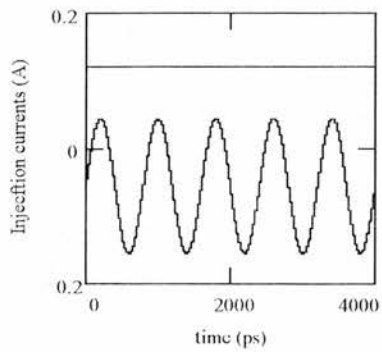
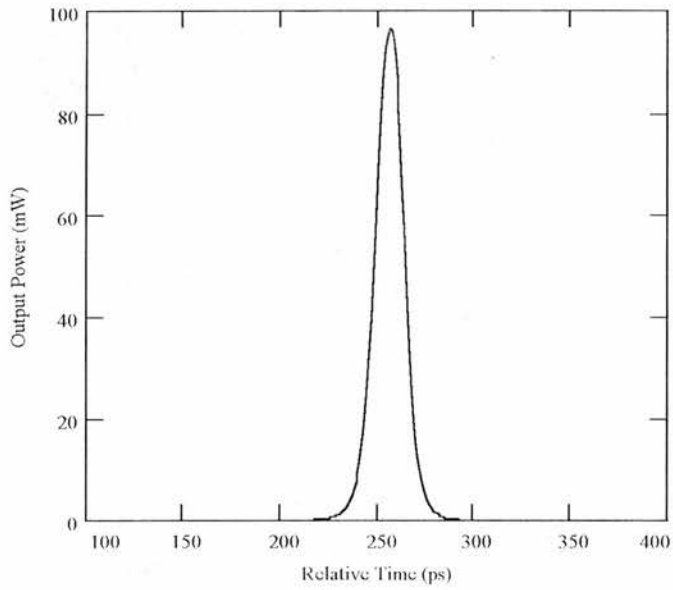
X 1

Measurementint 4000

$$B = 2.0 \cdot 10^{17} \cdot \text{cm}^3$$



RF: 0.1 am  
 IC<sub>1</sub>: 0.1  
 IC<sub>2</sub>: 0.055 am



## Publications

*Ultrashort pulse semiconductor lasers with improved timing jitter*, D.M. Hughes, D. Burns, W. Sibbett, K.A. Williams and I.H. White, CLEO Proc., Anaheim, CA, paper CWN4 (1994).

*High power picosecond pulse generation in multicontact diode lasers using modified Q-switching techniques*, I.H. White, K.A. Williams, D.M. Hughes, D. Burns and W. Sibbett, CLEO Europe Proc., Amsterdam, The Netherlands, paper TuL1 (1994).



## Acknowledgements

It is a real pleasure to acknowledge the unstinting support, encouragement and patience of my supervisor Professor Wilson Sibbett during the lengthy and often troubled course of this project.

I am indebted to Dr David Burns for introducing me into the mysteries of the semiconductor laser.

Profuse thanks should be directed towards Professor Ian White and Dr Kevin Williams, both of Bristol University, for their for the unlimited supply of laser devices and their selfless acknowledgement of my contribution to their published work.

Thanks should also be extended to

Bill Sleat for his streak camera expertise and electronics sorcery.

Carl Yelland for his ever-present optimism and virtuoso guitar skills.

Gareth Valentine for his computer know-how and beer drinking abilities.

Graham Friel for his good humour and acrobatic prowess.

Gordon Kennedy for his many useful discussions and sound advice on the pitfalls of diode lasers.

Gordon Hay for his early work on dual-wavelength and multi-pulsing lasers and for seeing the light a lot earlier than I did.

I would also like to extend thanks to BNR Europe Limited for their financial input in the form of a CASE award, and the Engineering and Physical Sciences Research Council for their personal financial support.

And finally last, but not least, Barbara Spinoula for believing in me when no-one else did. Nothing would have been possible without your support.